

THE STRATIGRAPHY AND GEOCHEMISTRY OF THE RAPITAN IRON FORMATION,
NORTHWEST TERRITORIES AND YUKON, CANADA

by

Geoffrey James Baldwin

A thesis submitted in partial fulfillment
of the requirements for the degree of
Doctor of Philosophy (PhD) in Mineral Deposits and Precambrian Geology

The School of Graduate Studies
Laurentian University
Sudbury, Ontario, Canada

© Geoffrey James Baldwin, 2014

THESIS DEFENCE COMMITTEE/COMITÉ DE SOUTENANCE DE THÈSE

Laurentian Université/Université Laurentienne
School of Graduate Studies/École des études supérieures

Title of Thesis Titre de la thèse	THE STRATIGRAPHY AND GEOCHEMISTRY OF THE RAPITAN IRON FORMATION, NORTHWEST TERRITORIES AND YUKON, CANADA	
Name of Candidate Nom du candidat	Baldwin, Geoffrey James	
Degree Diplôme	Doctor of Philosophy	
Department/Program Département/Programme	Mineral Deposits and Precambrian Geology	Date of Defence Date de la soutenance April 28, 2014

APPROVED/APPROUVÉ

Thesis Examiners/Examineurs de thèse:

Dr. Elizabeth Turner
(Supervisor/Directrice de thèse)

Dr. Balz Kamber
(Committee member/Membre du comité)

Dr. Darrel G. F. Long
(Committee member/Membre du comité)

Dr. Philip Fralick
(External Examiner/Examineur externe)

Dr. Stefan Siemann
(Internal Examiner/Examineur interne)

Approved for the School of Graduate Studies
Approuvé pour l'École des études supérieures
Dr. David Lesbarrères
M. David Lesbarrères
Director, School of Graduate Studies
Directeur, École des études supérieures

ACCESSIBILITY CLAUSE AND PERMISSION TO USE

I, **Geoffrey James Baldwin**, hereby grant to Laurentian University and/or its agents the non-exclusive license to archive and make accessible my thesis, dissertation, or project report in whole or in part in all forms of media, now or for the duration of my copyright ownership. I retain all other ownership rights to the copyright of the thesis, dissertation or project report. I also reserve the right to use in future works (such as articles or books) all or part of this thesis, dissertation, or project report. I further agree that permission for copying of this thesis in any manner, in whole or in part, for scholarly purposes may be granted by the professor or professors who supervised my thesis work or, in their absence, by the Head of the Department in which my thesis work was done. It is understood that any copying or publication or use of this thesis or parts thereof for financial gain shall not be allowed without my written permission. It is also understood that this copy is being made available in this form by the authority of the copyright owner solely for the purpose of private study and research and may not be copied or reproduced except as permitted by the copyright laws without written authority from the copyright owner.

Abstract

The Neoproterozoic was a time of major change in Earth's surficial history, including a major rise in atmospheric oxygen, the first appearance of complex metazoan life, and a series of worldwide glaciations. A particularly interesting element of these so-called "snowball Earth" glacial deposits is the presence of iron formation, a distinctive Precambrian rock type that is largely absent from the post-Paleoproterozoic record. Despite being relatively poorly studied with respect to their geochemistry and sedimentology, Neoproterozoic iron formations are used to support many models for the record of oxygen concentrations of the Earth. The classical example of Neoproterozoic iron formation is the Rapitan iron formation of northwestern Canada. This hematite-jasper iron formation is associated with glaciogenic turbidites and diamictites. Despite being the archetype, the Rapitan iron formation has not been studied in the context of recent ideas about the Neoproterozoic. In this thesis, the stratigraphy, geochemistry, and basin architecture of the Rapitan iron formation are reassessed. Using the REE+Y and the redox-sensitive elements Mo and U, it is shown that the Rapitan iron formation was deposited in a partially restricted basin from biogenically reduced iron under variable redox conditions. Elemental Re and Mo isotopes further show that although oxic and ferruginous conditions predominated during deposition of the iron formation, a transition towards a sulfidic water column locally terminated deposition. Finally, regional stratigraphy and geochemistry show that the iron formation was preferentially deposited in deep, newly formed basins that were protected from significant siliciclastic sedimentation. These basins were delimited by inferred crustal-scale faults trending roughly perpendicular to the axis of the rift basin, and allowed significant changes in thickness and sedimentological character over short distances along strike. These factors help build an overall geotectonic regime under which Neoproterozoic iron formations were deposited: young, deep rift basins that had undergone marine incursion, and were intermittently sealed by an ice shelf, allowing for the generation of an anoxic, iron-rich water column. The absence of the Eu anomaly and the heavy Mo isotopic signature indicate that the open ocean was fully oxygenated at the time of Rapitan iron formation deposition, as opposed to ferruginous as previously suggested.

Co-Authorship Statement

Several collaborators, some listed as coauthors, contributed to the work presented herein, providing supervision, scientific guidance and sample analysis. These collaborators provided excellent scientific discussions about stratigraphic principles, rare earth element, redox, and stable isotope geochemistry throughout the research for this thesis. As a result, these collaborators have been credited with co-authorship on each of the manuscripts contained in this dissertation. As first author, I measured all of the stratigraphic sections and gathered field data, collected the samples, prepared the samples for geochemical analysis, performed the primary interpretations of the stratigraphic, geochemical, and isotopic data, wrote the first drafts of the manuscripts, and communicated with the journal editors. All of my collaborators helped direct and refine my ideas and helped edit these manuscripts. Some specific sections of these manuscripts have been written by these collaborators, specifically the methodology sections in chapter 3. The rhenium analytical methods were written by Dr. Balz Kamber, one of my co-supervisors, as I did not conduct the lab analysis personally, and for the same reason the Mo isotopic methodology section was co-written by Dr. Thomas Nægler and Nicholas Greber of Universität Bern, Switzerland. These latter collaborators also added detail into the systematics of the Mo isotopic system beyond what I had written, but the ideas remained those I originally wrote. Dr. Kamber and Dr. Elizabeth Turner also edited and provided extensive feedback on the ideas and writing style for chapters 2 through 4, and are listed as co-authors for this reason

Acknowledgements

This thesis would not have been possible without the help and support I've received over the past four and a half years from my family, friends, and colleagues. Without such a strong supporting group, it would not have been possible.

I could not have asked for a better pair of supervisors than Drs. Elizabeth Turner and Balz Kamber. You both have provided outstanding support, guidance, and just the right balance of tough love and sympathetic support throughout this processes. Thank you both so much.

Without their diligent lab work and attention to detail, chapter 3 would not have been possible without my coauthors Thomas Nägler and Nicholas Greber. Without your analysis and help fitting my ideas within the proper Mo isotopic nomenclature, that manuscript would never have happened.

Support from the governments of the Northwest Territories and Yukon, specifically the Northwest Territories Geoscience Office (NTGO) and Yukon Geological Survey (YGS) was essential in completing this project, both from a funding a guidance standpoint. In particular, I wish to thank several people at the NTGO, namely Edith Martel, Carl Ozyer, and Luke Ootes, for their support in the field (Carl), financially (Edith), and in numerous helpful discussions about the Rapitan iron formation (Luke). I would also like to thank John Ketchum and Hendrick Falck for providing support for this project as well. At the YGS, my most sincere thanks goes to Joyia Chakungal and Venessa Bennett, both of whom provided support in the field and helped facilitate funding for helicopter support. Thanks also go to Carolyn Relf, Maurice Colpron, Steve Israel, and Lara Lewis, for providing financial support for helicopter time and ID-TIMS detrital zircon analysis.

I would also like to thank the opportunities presented to me by Aurora Geosciences and their clients, Coltstar Resources and Copper North. Dave White, Gary Vivien, and Robin Wyllie had the faith in me to give me opportunities well above my experience level, which helped in both my career, my confidence, and even with my degree. Without the chance to see so much more of the Mackenzie Mountains and Rapitan Group while working for Aurora, chapter 4 would not have been possible. I would also like to thank Dave Dupree of Coltstar Resources and Sally

Eyre of Copper North for allowing me to publish data and observations collected while working on their properties.

Without the eternally upbeat field assistance from Tiffany Chevrier, I never would have survived the 2010 field season, Tif, I owe so much of this thesis to our friendship. Likewise, I cannot thank nor apologize enough to Kirsti Medig for making her go through dealing with that terrible drill. Friends do not let friends do paleomag sampling. Despite our differences in the field, I got a lot out of working with Sean O'Hare, and although I would not do it again, thank you for what patience you had for me. Lastly, although their time in the field with me was short, I cannot thank Henry Ngo, Brandon Webster, and Parker Schachtel enough for their help.

Helpful correspondence with several other researchers, namely Nic Beukes and Gary Yeo was very helpful in figuring out small problems in this thesis. On a larger scale, the numerous discussions with Jack Milton, as well as the opportunity to share field camps and work together, were absolutely invaluable to the completion of this project. Jack, you have been both a good colleague and a great friend ever since we started our PhDs.

In the lab at Laurentian University, I cannot thank Thomas Ulrich, Kirk Ross, Joe Petrus, and Annette Gladu enough. Your help and support (occasionally emotional) was amazing. Likewise, the staff of the Ontario Geolabs, specifically Natalie Chrétien, Nathan Remeikis, and Nag Elwaer provided excellent support, both in allowing me to be involved in my own XRF analysis, and later helping expedite my final batch of samples despite massive delays in the labs.

To my many officemates over the years, Kirk Ross, Rob Lodge, Mike Babechuk, Sean O'Hare, Jordan Matheiu, Craig Stewart, and Taus Joergensen, thank you for being there to support me, tolerate me, and provide a consistent and effective sounding board to my ideas. I hope I never cost any of you too much productivity.

Caroline and Charlie Gordon, you have been the best roommates and friends I could have wanted over the last three years. I cannot thank you enough for your support and friendship, and am eternally grateful that you two have been there for me. Good luck raising my replacement; you will be such good parents.

Mike Babechuk, your friendship and support as a colleague was vital to me while you were still here. Thank you.

I cannot even count the many friends who have helped me along the way that I haven't listed, but I thank all of you. This would not have been the same without any of you.

Last, I could not have survived this degree without the lasting and unwavering support of my family. Mom, Dad, Drew, Tristan, I love you all. Thanks for being there for me. I never would have been here without you.

Table of Contents

<i>Thesis Defense Committee</i>	<i>ii</i>
<i>Abstract</i>	<i>iii</i>
<i>Co-Authorship Statement</i>	<i>iv</i>
<i>Acknowledgements</i>	<i>v</i>
<i>Table of Contents</i>	<i>viii</i>
<i>List of Figures</i>	<i>xii</i>
<i>List of Tables</i>	<i>xiv</i>
<i>Chapter 1: Introduction to the Thesis</i>	<i>1</i>
1.1 Statement of Problem	1
1.2 Regional geological history	2
1.3 Previous Work	4
1.4 Field and analytical methods	6
1.5 Structure of the thesis	7
1.6 Statement of original contributions	9
1.7 References	11
<i>Chapter 2: A new depositional model for glaciogenic Neoproterozoic iron formation: Insights from the chemostratigraphy and basin configuration of the Rapitan iron formation</i>	<i>19</i>
2.1 Abstract	19
2.2 Introduction	20
2.3 Geological Setting	22
2.4 Stratigraphy	24
2.5 Methods	27
2.6 Results	28
2.6.1 REE+Y systematics.....	28
2.6.2 Mo-U systematics.....	34

2.7 Basin Reconstruction	38
2.7.1 Highly restricted basins	39
2.7.2 Zones of upwelling and high productivity	39
2.7.3 Silled basins.....	40
2.7.4 Nature of the redox chemocline	41
2.7.5 Nature of the sill.....	43
2.7.6 A new model for Neoproterozoic iron formation.....	44
2.7.7 Oxidation state of the Neoproterozoic open ocean	47
2.8 Summary	48
2.9 Acknowledgements.....	49
2.10 Figures	51
2.11 References	67
2.12 Supplementary Data	78
2.12.1 Detailed Methods	78
2.12.2 Supplementary Figures.....	81
2.12.3 Supplementary Tables	83
2.12.4 Supplementary references	92
<i>Chapter 3: Mo isotopic composition of the mid-Neoproterozoic ocean: an iron formation perspective</i>	<i>93</i>
3.1 Abstract	93
3.2 Introduction	94
3.3 Sampling and analytical methods	96
3.3.1 Stratigraphy and sample selection.....	96
3.3.2 Digestion and trace element analysis	97
3.3.3 Rhenium	97
3.3.4 Mo isotopes	98
3.4 Results	99
3.4.1 Rhenium	99
3.4.2 Mo isotopes	100
3.5 Discussion.....	102
3.5.1 Metal enrichments, Re and $\delta^{98}\text{Mo}$	102
3.5.2 Implications for Neoproterozoic iron formation	106
3.5.3 Mo isotopic composition of the Neoproterozoic ocean	107
3.6 Conclusions	111

3.7 Acknowledgements.....	111
3.8 Figures	113
3.9 Tables.....	118
3.10 References	119
3.11 Supplementary Data	124
<i>Chapter 4: Paleogeographic controls on the distribution and sedimentological character of the Rapitan iron formation, Northwest Canada</i>	<i>126</i>
4.1 Abstract	126
4.2 Introduction	127
4.3 Geological Background.....	129
4.4 Stratigraphy	133
4.4.1 Snake River Basin	134
4.4.2 Redstone Basin.....	135
4.4.3 Regional observations	137
4.5 Rare earth element geochemistry	138
4.5.1 Iron Creek.....	140
4.5.2 Discovery Creek.....	142
4.5.3 Cranswick River.....	144
4.5.4 Hayhook North.....	145
4.5.5 Hayhook South.....	145
4.5.6 Sources of REE+Y variability.....	147
4.6 Discussion.....	151
4.6.1 Basins and faults.....	154
4.6.2 A revised correlation scheme for the Rapitan Group.....	160
4.6.3 Implications for the rifting of northwestern Laurentia.....	161
4.7 Conclusions	163
4.8 Acknowledgments.....	165
4.9 Figures	166
4.10 Tables.....	188
4.11 References	195
<i>Chapter 5: Conclusions.....</i>	<i>205</i>
5.1 Unanswered questions and suggestions for future work	207

5.2 References	209
<i>Appendix A: Lithofacies and lithostratigraphic correlation potential of the Rapitan iron formation, Snake River area (NTS 106F), Yukon</i>	210
A.1 Abstract	210
A.2 Introduction	210
A.3 Previous Work	211
A.4 Rapitan iron formation stratigraphy	212
A.4.1 Discovery Creek	212
A.4.2 Iron Creek	215
A.5 Discussion	218
A.5.1 Correlation	218
A.5.2 Copper mineralization	220
A.5.3 Comparison with previous work	221
A.6 Future Work	223
A.7 Acknowledgements	223
A.8 Figures	225
A.9 References	232

List of Figures

Figure 2.1: Distribution of Proterozoic strata in the northern cordillera.....	51
Figure 2.2: Generalised Neoproterozoic stratigraphy of the Mackenzie Mountains.....	52
Figure 2.3: Stratigraphic section of the Rapitan iron formation at Cranswick River.....	53
Figure 2.4: Photographs of the Rapitan iron formation at Cranswick River.....	54
Figure 2.5 A-C: REE+Y diagrams.....	56
Figure 2.6 A-B: Y/Ho vs. Gd/Gd*, Al ₂ O ₃	58
Figure 2.7 A-C: Eu/Eu* vs. Y/Ho, Gd/Gd*, Al ₂ O ₃	59
Figure 2.8: Histogram of La/La* normalised to MuQ and granite.....	60
Figure 2.9 A-B: Mo (ppb) vs. Fe ₂ O ₃ and MnO (wt%).....	61
Figure 2.10: Stratigraphic distribution of Mo _{EF} , U _{EF} , and W _{EF}	62
Figure 2.11: Mo _{EF} vs. U _{EF}	64
Figure 2.12: Schematic depositional model for Rapitan iron formation.....	65
Figure 2.S1: Counts per second vs. Time of Mo and U by LA-ICP-MS.....	81
Figure 2.S2: Mo standard concentration vs. ICP-MS signal intensity.....	82
Figure 3.1 (A-C): Regional geology and photographs.....	113
Figure 3.2 (A-C): Photographs of nodules and bedding relationships.....	115
Figure 3.3: Stratigraphic distribution of Mo _{EF} , U _{EF} , Re (ppt), Re/Mo, and δ ⁹⁸ Mo.....	116
Figure 3.4 (A-D): δ ⁹⁸ Mo vs. Mo (ppb), Mo _{EF} , Re (ppt), and Re/Mo.....	117
Figure 3.S1: Mo by ICP-MS vs. Mo by ID-ICP-MS.....	125
Figure 4.1: Regional geology and location maps.....	166
Figure 4.2: Neoproterozoic stratigraphy of the Mackenzie Mountains.....	167
Figure 4.3: Six measured stratigraphic sections.....	168
Figure 4.4: Photographs from the Snake River basin.....	169

Figure 4.5: Photographs from the Redstone basin.....	171
Figure 4.6: Photographs from regional sites visited.....	173
Figure 4.7: REE+Y chemostratigraphy of Iron Creek.....	174
Figure 4.8: REE+Y chemostratigraphy of Discovery Creek.....	175
Figure 4.9: REE+Y chemostratigraphy of Cranswick River.....	176
Figure 4.10: REE+Y chemostratigraphy of Hayhook North.....	177
Figure 4.11: REE+Y chemostratigraphy of Hayhook South.....	178
Figure 4.12: Fe/Al vs Pr_{MUQ}/Yb_{MUQ}, Eu/Eu*, Y/Ho, and Gd/Gd*.....	179
Figure 4.13: Ba/Sr chemostratigraphy of Discovery Creek.....	180
Figure 4.14: Locations of basin-forming faults.....	181
Figure 4.15: Basin Profile.....	182
Figure 4.16: Interpreted basin fill history for the Rapitan Group.....	184
Figure 4.17: Correlation scheme for the Rapitan Group.....	186
Figure A1: Study Location map on NTS 106F.....	225
Figure A2: Stratigraphic column of section Discovery Creek 2.....	226
Figure A3 (A-D): Photographs of section Discovery Creek 2.....	227
Figure A4: Stratigraphic column of section Iron Creek 1.....	228
Figure A5 (A-F): Photographs of section Iron Creek 1.....	229
Figure A6: Stratigraphic column of section Iron Creek 3.....	230
Figure A7 (A-D): Photographs of section Iron Creek 3.....	231

List of Tables

Table 2.S1: Concentrations in rock standards via standard addition.....	83
Table 2.S2: Selected Major (wt%) and Trace (ppb) element results.....	84
Table 3.1: Results and errors for $\delta^{98}\text{Mo}$ and Re (ppt).....	118
Table 3.S1: Mo concentration by different techniques.....	124
Table 4.1: Locations of study sites.....	188
Table 4.2: Stratigraphic descriptions of Sayunei Formation.....	189
Table 4.3: Major (wt%) and trace (ppb) element results.....	190

Chapter 1: Introduction to the Thesis

1.1 Statement of Problem

One of the most unusual and enigmatic rock types is Precambrian banded iron formation. These sedimentary rocks, consisting of chert and various iron minerals, are found in the geological record from the Eoarchean through to the Neoproterozoic (Bekker et al., 2010; Kamber, 2010), with the majority deposited in the Neoproterozoic and Paleoproterozoic. Depositing sedimentary iron in the impressive volumes found in iron formations is assumed to have required an anoxic water column capable of containing dissolved, reduced iron (Holland, 1984), which would explain why iron formation is not deposited in the modern, fully oxic ocean. Furthermore, little iron formation was deposited between 1.8 and 0.7 Ga, a time span of over a billion years, prior to a sudden, large pulse of iron formation deposition in the Neoproterozoic (Ilyin, 2009). This observation has resulted in numerous different models for the evolution of the redox state of the Proterozoic ocean, with various authors suggesting that the ocean was either oxic (Holland, 1992), sulfidic (Canfield, 1998), or still ferruginous (Poulton and Canfield, 2011), but with a limited supply of marine iron for various reasons (Kump and Seyfried Jr., 2005; Bekker et al., 2010). In any case, the sudden resumption of iron formation deposition in the Neoproterozoic is significant, because it coincided with a major increase in marine and atmospheric oxygen content (Neoproterozoic oxygenation event, NOE), which, although dwarfed in scale by its Paleoproterozoic counterpart (the Great Oxygenation Event, GOE) (Bekker et al., 2004), was still critical in the development of the modern surficial system of the Earth (Och and Shields-Zhou, 2012).

Neoproterozoic iron formation is distinct from older iron formations in that it is almost exclusively associated with glaciogenic deposits associated with the purportedly global “snowball Earth” glacial event (Hoffman et al., 1998). The relationship between these glacial events and iron formation deposition has been hotly debated, with several different models for the relationship between ice cover and iron formation deposition (e.g., Klein and Beukes, 1993; Halverson et al., 2011; Hoffman et al., 2011). Perhaps the best studied Neoproterozoic iron

formation is the Rapitan iron formation of the northern Canadian cordillera (Northwest Territories and Yukon). The Rapitan iron formation is considered the archetypical Neoproterozoic iron formation, and has been episodically studied since the 1960s (e.g., Gross, 1965; Gross, 1993). It has not, however, been studied in great detail since the early 1980s (Yeo, 1984), and there is a paucity of both modern stratigraphic and geochemical work on this geologically important iron formation. New studies in both of these areas should greatly improve the understanding of this unusual rock type, and the critical time in Earth history in which it was deposited. This thesis aims to establish the depositional history of the Rapitan iron formation, the basinal and global redox conditions that contributed to its deposition, and the paleogeography and configuration of the basin in which it was deposited. This was done using numerous newly measured stratigraphic sections, a large trace and major element geochemical dataset for iron formation samples, and Mo isotopic data, to develop a comprehensive analysis of the depositional controls of the Rapitan iron formation.

1.2 Regional geological history

The Mackenzie Mountains (Northwest Territories and Yukon, Canada) are a Mesozoic-Tertiary fold-thrust belt in the northern Canadian cordillera. These mountains expose sedimentary rocks deposited on the northwestern margin of Laurentia from the mid-Neoproterozoic through to the Permian (Gabrielse et al., 1973), with unexposed but presumably underlying Paleo- and Mesoproterozoic sedimentary rocks preserved to the northwest in the Wernecke Mountains, Yukon (Thorkelson et al., 2005). Proterozoic rocks of the Mackenzie Mountains outcrop in an arcuate belt (Gabrielse, 1967; Aitken and Long, 1978), the architecture of which reflects the sedimentary basin configuration, controlled by several crustal-scale structures (Aitken and Pugh, 1984) visible in geophysical surveys. The oldest rock unit in the general region, the Paleoproterozoic Wernecke Supergroup, is a suite of metasedimentary rocks that have been deformed repeatedly since deposition, including at 1.6 Ga in the Rackla Orogeny, during which the volcanic terrain Bonnetia was obducted over them (Furlanetto et al., 2013; Nielsen et al., 2013). The Wernecke Supergroup is unconformably overlain by the Mesoproterozoic Pinguicula

Group (Thorkelson et al., 2005), which is in turn unconformably overlain by the Mackenzie Mountains Supergroup (Turner, 2011).

The Mackenzie Mountains Supergroup contains the oldest Neoproterozoic strata in the Mackenzie Mountains, consisting of the Dolores Creek, Tarn Lake, Black Canyon Creek, Tabasco, and Tsezotene Formations, and the overlying Katherine and Little Dal Groups (Turner, 2011; Long and Turner, 2012; Turner and Long, 2012). These consist predominantly of shale, siltstone, shallow to deep water carbonate rocks, shallow marine sandstone and minor evaporite. The Mackenzie Mountains Supergroup was gently deformed in the Corn Creek “orogeny”, an extensional event that predated Windermere Supergroup deposition (Thorkelson et al., 2005). The Mackenzie Mountains Supergroup is unconformably overlain by the Windermere Supergroup, which consists of three formalised groups: the Coates Lake, Rapitan, and Hay Creek Groups, and an informal ‘upper’ group (Green and Godwin, 1963; Yeo, 1978; Aitken, 1989; Jefferson and Parrish, 1989).

The basal package of the Windermere Supergroup is the Coates Lake Group, which is a continental rift succession consisting of continental tholeiitic basalt, continental siltstone, evaporite, conglomerate, and carbonate rocks, and is host to the Coates Lake stratiform copper deposit (Kupferschiefer-type) (Jefferson, 1983; Rose et al., 1986; Jefferson and Ruelle, 1987; Jefferson and Parrish, 1989). The basal tholeiitic basalts are assumed to be the extrusive equivalents of sills and dykes intruding the underlying Mackenzie Mountains Supergroup, and have been dated at 780-770 Ma, making them part of the Gunbarrel mafic igneous event (Armstrong et al., 1982; Harlan et al., 2003). The Coates Lake Group is unconformably overlain by the Rapitan Group, which consists of the basal, regionally limited diamictites of the Mt. Berg Formation, fine-grained turbidites of the Sayunei Formation, and massive diamictites of the Shezal Formation (Eisbacher, 1978). All three formations of the Rapitan Group have been shown to be glaciogenic in origin (Yeo, 1981), and are presumed to belong to the Sturtian glaciation, the oldest of the three Neoproterozoic “snowball Earth” glacial episodes (Hoffman and Halverson, 2011). The Sayunei Formation is locally capped by hematite-jasper iron formation, which can be up to 120 m thick, forming the Crest iron deposit (Klein and Beukes, 1993). The Rapitan Group is conformably overlain by the Hay Creek Group, which consists of mudstone, siltstone and

wacke of the Twitya Formation, shallow-water limestone and sandstone of the Keele Formation, diamictite of the Ice Brook Formation, and cap carbonate of the Teepee dolostone (Yeo, 1978; Aitken, 1991a; Aitken, 1991b; James et al., 2001; Day et al., 2004; James et al., 2005). The Hay Creek Group is suggested to be the first of three “grand cycles” that make up the upper Windermere Supergroup, each with an up-section transition from basinal shale to platformal carbonate, capped by a major flooding surface (Narbonne and Aitken, 1995; Yeo et al., 1978). The latter two of these “grand cycles” are contained within the unnamed “upper group”, consisting of the Sheepbed (shale), Gametrail (limestone), Blueflower (shale), and Risky (limestone) formations (Aitken, 1989). An unconformity is present at the top of the Risky Formation, which marks the top of the Windermere Supergroup in the Mackenzie Mountains, and which is overlain by the lower Cambrian Ingta and Backbone Ranges formations and lower to middle Paleozoic rocks. During the Paleozoic, the region developed into two depositional regions, the Mackenzie Platform, where predominantly shallow water carbonates were deposited, and the Selwyn Basin, a deep marine shale basin. Both contain sedimentary-hosted Zn-Pb deposits (Mississippi-Valley type [MVT] on the platform, Sedimentary hosted exhalative [SEDEX] in the basin) of late Cambrian to Devonian age, and it has been suggested that these are of a cogenetic origin (Nelson et al., 2002), although the MVT deposits may be much younger. All rocks of the Mackenzie Mountains were variably thrust and folded during the Mesozoic-Tertiary cordilleran orogeny.

1.3 Previous Work

It was first proposed in the middle of the twentieth century that apparently glaciogenic deposits, a common, world-wide feature in Neoproterozoic sedimentary basins, may record a global glaciation (Harland, 1964). Much later, with the advantage of paleomagnetic data, it was observed that many of these glacial deposits were apparently deposited at low latitudes, giving rise to the concept of a true global glaciation, coined “snowball Earth”, in which it was envisioned that the entire planet was glaciated down to the equator (Kirschvink, 1992). With more detailed study, it was established that there were three distinct glacial intervals in the

Neoproterozoic, which are commonly referred to as the Sturtian (~700 Ma), the Marinoan (~635 Ma) and the Gaskiers/Ediacaran (~585 Ma) glaciations (Hoffman, 2009). Several unusual lithologies were found to be stratigraphically associated with these glacial deposits, namely cap carbonates and iron formation, which were accepted as evidence for total glacial cover due to their unusual stratigraphic and temporal implications (Hoffman et al., 1998). Indeed, several of the cap carbonates are well-documented as having unusual textures (e.g., James et al., 2001) and chemistries (e.g., Huang et al., 2011), when compared to most other contemporary carbonate rocks. The iron formation, associated almost exclusively with the Sturtian glaciation (Macdonald et al., 2010), has proven much more confounding. Iron formation is predominantly associated with the Archean and Paleoproterozoic, over one billion years before the Neoproterozoic “snowball Earth” (Klein, 2005). Other than these Neoproterozoic examples, there are very few iron formations younger than 1.8 billion years old, although there are both Mesoproterozoic (e.g., Slack et al., 2007) and Phanerozoic (e.g., Peter et al., 2003) examples directly associated with submarine hydrothermal activity. This apparent disparity has been explained through proposed variations in the redox state of the ocean (e.g., Canfield, 1998; Holland, 1984), or through changes in the global hydrothermal and volcanic flux (e.g., Kump and Seyfried Jr., 2005; Bekker et al., 2010). Most models, however, place much more emphasis on the proposed glaciation associated with these iron formations (Klein and Beukes, 1993; Hoffman, 2009; Hoffman and Li, 2009; Hoffman et al., 2011).

The Rapitan iron formation of the Windermere Supergroup (Northwest Territories and Yukon, Canada), is the archetypical example of Neoproterozoic iron formation (Gross, 1993), although prominent examples are also present in Brazil (Klein and Ladeira, 2004), South Australia (Lottermoser and Ashley, 2000), Namibia (Le Heron et al., 2013), and elsewhere worldwide (e.g., Hoffman and Li, 2009; Ilyin, 2009). Iron formation was first reported in the Snake River area, Yukon, during the Klondike gold rush (Keele, 1906), and discovered in the Mackenzie Mountains, NWT soon after (Keele, 1910). Siliciclastic rocks associated with the iron formation were identified as glaciogenic by Ziegler (1959), and iron formation of substantial thickness was discovered in 1961 (Stuart, 1963). The thick iron formation was the subject of extensive exploration by Crest Exploration, Ltd., a subsidiary of Standard Oil of California (now Chevron Corp.) in the 1960s, and a 5.6 billion tonne iron deposit with 42.7% Fe was reported

over an area of 25.9 km² in the northern Mackenzie Mountains near the NWT-YT border (Stuart, 1963), but was found to be sub-economic due to remoteness and metallurgical concerns. Intensive field mapping studies conducted by the Geological Survey of Canada in the 1970s confirmed the glaciogenic origin of the Rapitan Group (as designated by Green and Godwin, 1963), and its component formations, the Mt. Berg, Sayunei, and Shezal formations (e.g., Condon, 1964; Upitit, 1966; Gabrielse et al., 1973; Eisbacher, 1976; Young, 1976; Eisbacher, 1978; Yeo, 1978; Eisbacher, 1981a; Eisbacher, 1981b; Yeo, 1981; Yeo, 1984; Eisbacher, 1985; Yeo, 1986). The most in-depth of these studies concluded that the iron formation was probably the product of interaction between hydrothermal activity and glacial cover (Yeo, 1981), which was in agreement with some of the earliest work on the deposit (Gross, 1965), and in agreement with several later workers (e.g., Klein and Beukes, 1993; Halverson et al., 2011; Hoffman et al., 2011), and consistent with iron formation depositional models overall (e.g., Derry and Jacobsen, 1990; Isley, 1995; Isley and Abbott, 1999; Clout and Simonson, 2005; Bekker et al., 2010).

1.4 Field and analytical methods

Excellent and often near-complete exposure of the Rapitan Group, on exposed ridges and in creek beds, greatly facilitated the study of its stratigraphy and its implications for basin reconstruction. Stratigraphic sections were measured at a metre-scale using a 1.5 m range pole fitted with a clinometer set to the measured dip of the stratigraphy to ensure measurement of true thickness. The lack of structural deformation, apart from a relatively gentle dip resulting from Mesozoic-Tertiary thrusting (Eisbacher, 1981b) greatly facilitated this effort. Attention was paid to sedimentary structures, grain size in siliciclastic rocks, clast composition in diamictite, and the texture and mineralogy of iron formation. Furthermore, the relative proportions of hematite and jasper beds, as well as the proportions of jasper beds and nodules, were given great importance. Samples and photographs of the strata were taken where appropriate, both of which were collected at especially high density in iron formation intervals.

Eighty-nine polished thin sections were prepared for petrographic investigation of chert and iron formation samples. These materials were examined to identify microstructures in the chert beds and nodules, as the first stage towards selecting samples for geochemical analysis. Jasper beds that were found to be texturally homogeneous were then pre-screened for chemical homogeneity by Laser Ablation Inductively coupled plasma mass spectrometer (LA-ICP-MS) at Laurentian University following the protocol described by Baldwin et al. (2011). Jasper bands that were found to be chemically homogeneous were sub-sampled for high-precision total-dissolution trace element geochemical analysis, and analysed at Laurentian University (94 samples) for a suite of 46 trace elements (see Baldwin et al., 2012, online supplement for analytical methods). Major elements were either analyzed by ICP-MS (22 samples) at Laurentian University, or by x-ray fluorescence (XRF) at the Ontario Geoscience Laboratories (72 samples). Twenty-two samples were selected to be analysed for the elemental Re concentration by isotope-dilution ICP-MS at Laurentian University, using the same digestions as the full trace element suite (Baldwin et al., 2013). Of those 22 samples, 11 were sent to Thomas Nägler's isotope geochemistry lab at Institut für Geologie, Universität Bern, Switzerland for Mo isotope analysis.

1.5 Structure of the thesis

This dissertation is presented in five chapters. Chapters 2-4 are written as manuscripts for publication in refereed scientific journals. Frequently, these chapters overlap in their introduction, due to their preparation as individual papers. Furthermore, due to their sequential publication, each successive chapter contains reference to those preceding it.

A number of collaborators provided supervision and scientific guidance during various stages of the preparation of this dissertation, some of whom are included as co-authors. These collaborations provided invaluable scientific discussions on the stratigraphic and basin controls on Rapitan iron formation, the role and scale of the “snowball Earth” glaciations, and on the systematics and application of the rare earth elements plus yttrium (REE+Y), redox-sensitive trace metals, and Mo isotopes in the reconstruction of the basin chemistry and its implications for

the Neoproterozoic ocean as a whole. Despite these contributions, as first author, I conducted all of the field work and measured the stratigraphic sections, digitized and compared these sections across the basin, prepared (and in some cases, analyzed) samples for trace and major element geochemical analysis, made the primary interpretations of all data, prepared the first drafts of each manuscript, and communicated with the journal editors.

Chapter 1 introduces the reader to the purpose and objectives of this project, as well as an overview of the methodology, background geology and structure of the thesis.

Chapter 2 is written as a manuscript entitled “**A new depositional model for glaciogenic Neoproterozoic iron formation: Insights from the chemostratigraphy and basin configuration of the Rapitan iron formation**” (Published 2012, *Canadian Journal of Earth Sciences*, vol. 49, p. 455-476). This paper presents a detailed stratigraphic and trace element study of a single well-exposed exposure of the Rapitan iron formation, with emphasis on the behavior of the REE+Y, as well as the redox-sensitive transition metals Mo and U. Using these data, it proposes an updated depositional model for the deposition of Neoproterozoic iron formation, as well as insight into the global redox state of the Neoproterozoic ocean.

The coauthors on this publication are: Turner, E.C. and Kamber, B.S., Department of Earth Sciences, Laurentian University, 935 Ramsey Lake Rd, Sudbury, ON P3E 2C6 (current address for Kamber, B.S.; Department of Geology, Trinity College Dublin, Dublin 2, Ireland). This manuscript is also Northwest Territories Geoscience Office contribution 0052.

Chapter 3 is written as a manuscript entitled “**The Mo isotopic composition of the mid-Neoproterozoic ocean: an iron formation perspective**” (Published 2013, *Precambrian Research*, vol. 230, p. 168-178). This paper supplies the first published Mo isotopic and elemental Re compositions of iron formation of any age, which are used to improve the interpretations made in chapter 2, as well as identify a mechanism for the end of the deposition of the Rapitan iron formation, and its implications for the $\delta^{98}\text{Mo}$ composition of the Neoproterozoic ocean.

The coauthors of this publication are: Nägler, T.F., Greber, N.D., Institut für Geologie, Universität Bern, Baltzerstr. 1, 3012 Bern, Switzerland; Turner, E.C., Department of Earth

Sciences, Laurentian University, Sudbury, ON, P3E 2C6; and Kamber, B.S., Department of Geology, Trinity College Dublin, Dublin 2, Ireland.

Chapter 4 is written as a manuscript entitled “**Paleogeographic controls on the distribution and sedimentological character of the Rapitan iron formation, northwest Canada**” (to be submitted to *Precambrian Geology*). It uses a several stratigraphic sections, a large REE+Y dataset, and regional geological observations to explain syn-depositional fault and basin controls on the distribution and thickness of the Rapitan iron formation, as well as provide a revised stratigraphic correlation scheme for the Rapitan Group.

The coauthors on this manuscript are: Turner, E.C., Department of Earth Sciences, Laurentian University, Sudbury, Ontario, P3E 2C6; and Kamber, B.S., Department of Geology, Trinity College Dublin, Dublin 3, Ireland.

Chapter 5 presents the overall conclusions of the thesis.

Appendix A contains a report written for the Yukon Geological Survey entitled: “**Lithofacies and lithostratigraphic correlation potential of the Rapitan iron formation, Snake River area (NTS 106F), Yukon**” (Published 2012, *Yukon exploration and Geology 2011*, K.E. MacFarlane and P.J. Sack (eds.), p. 1-15). It contains preliminary stratigraphic findings and field observations, which are referenced in chapters 3 and 4.

The coauthor of this publication is: Turner, E.C., Department of Earth Sciences, Laurentian University, Sudbury, ON P3E 2C6.

1.6 Statement of original contributions

The following points outline the original contributions made in this study:

- 1) Documents detailed stratigraphy through the Sayunei Formation and Rapitan iron formation from numerous sites across the Mackenzie and Wernecke Mountains for the first

time; previous studies have not reported this many measured sections nor as much sedimentological and stratigraphic detail.

- 2) Provides a large and modern, precise trace element geochemical suite of 46 elements for 94 iron formation samples collected from five different stratigraphic sections, as well as major element data for all samples.
- 3) Provides the first detailed REE+Y characterisation of the Rapitan iron formation using the full 15-element suite analysed by ICP-MS, using these to characterise the basin's connectivity with the open ocean and differentiate between chemical and siliciclastic sedimentation.
- 4) Presents the first usage of Mo and U enrichment factors to elucidate the redox state of the Rapitan basin and establish the depositional basin type.
- 5) Presents a new depositional model for Neoproterozoic iron formation in the context of the trace element geochemistry and partial basin connectivity with the open ocean.
- 6) Presents the first elemental Re and Mo isotopic data for iron formation, and uses this to refine the above depositional model.
- 7) Using Re, Mo isotopes, and the lack of a Eu anomaly to establish an oxic Neoproterozoic open ocean with a near-modern $\delta^{98}\text{Mo}$ composition.
- 8) Provides a detailed proposal on a system of pre- and syn-sedimentary faults that controlled the distribution, thickness, and character of the Sayunei Formation and Rapitan iron formation.
- 9) Establishes a set of criteria for the deposition of thick, hematite-rich iron formation that may be useful in exploration in the future
- 10) Provides the first detailed and comprehensive sedimentary, stratigraphic, and basin analysis study of any Neoproterozoic glacial succession in the world.
- 11) Provides the first defensible correlation scheme for the Rapitan Group.

1.7 References

- Aitken, J.D., 1989. Uppermost Proterozoic formations in central Mackenzie Mountains, Northwest Territories. Geological Survey of Canada, Bulletin 368: 1-26.
- Aitken, J.D., 1991a. The Ice Brook Formation and post-Rapitan, Late Proterozoic Glaciation, Mackenzie Mountains, Northwest Territories. Geological Survey of Canada Bulletin, 404: 1-43.
- Aitken, J.D., 1991b. Two late Proterozoic glaciations, Mackenzie Mountains, northwestern Canada. *Geology*, 19: 445-448.
- Aitken, J.D. and Long, D.G.F., 1978. Mackenzie tectonic arc- reflection of early basin configuration? *Geology*, 6: 626-629.
- Aitken, J.D. and Pugh, D.C., 1984. The Fort Norman and Leith Ridge structures: major, buried, Precambrian features underlying Franklin Mountains and Great Bear and Mackenzie Plains. *Bulletin of Canadian Petroleum Geology*, 32(2): 139-146.
- Armstrong, R.L., Eisbacher, G.H. and Evans, P.D., 1982. Age and stratigraphic-tectonic significance of Proterozoic diabase sheets, Mackenzie Mountains, northwestern Canada. *Canadian Journal of Earth Sciences*, 19: 316-323.
- Baldwin, G.J., Nägler, T.F., Greber, N.D., Turner, E.C. and Kamber, B.S., 2013. Mo isotopic composition of the mid-Neoproterozoic ocean: an iron formation perspective. *Precambrian Research*, 230: 168-178.
- Baldwin, G.J., Thurston, P.C. and Kamber, B.S., 2011. High-precision rare earth element, nickel, and chromium chemistry of chert microbands pre-screened with in-situ analysis. *Chemical Geology*, 285: 133-143.
- Baldwin, G.J., Turner, E.C. and Kamber, B.S., 2012. A new depositional model for glaciogenic Neoproterozoic iron formation: insights from the chemostratigraphy and basin configuration of the Rapitan iron formation. *Canadian Journal of Earth Sciences*, 49: 455-476.

- Bekker, A., Slack, J. Planavsky, N., Krapež, B., Hofmann, A., Konhauser, K.O., and Rouxel, O.J. 2010. Iron formation: The sedimentary product of a complex interplay among mantle, tectonic, oceanic, and biospheric processes. *Economic Geology*, 105: 467-508.
- Bekker, A., Wang, P.-L., Rumble III, D., Stein, H.J., Hannah, J.L., Coetzee, L.L., and Beukes, N.J. 2004. Dating the rise of atmospheric oxygen. *Nature*, 427: 117-120.
- Canfield, D.E., 1998. A new model for Proterozoic ocean chemistry. *Nature*, 396: 450-453.
- Clout, J.M.F. and Simonson, B.M., 2005. Precambrian Iron Formations and Iron Formation-Hosted Iron Ore Deposits. *Economic Geology 100th Anniversary Volume*: 643-680.
- Condon, F., 1964. Geology of the North Nahanni iron formation, District of Mackenzie, Northwest Territories. B.Sc. thesis Thesis, University of British Columbia, Vancouver, 28 pp.
- Day, E.S., James, N.P., Narbonne, G.M. and Dalrymple, R.W., 2004. A sedimentary prelude to Marinoan glaciation, Cryogenian (middle Neoproterozoic) Keele Formation, Mackenzie Mountains, northwestern Canada. *Precambrian Research*, 133: 223-247.
- Derry, L.A. and Jacobsen, S.B., 1990. The chemical evolution of Precambrian seawater: Evidence from REEs in banded iron formations. *Geochimica et Cosmochimica Acta*, 54(11): 2965-2977.
- Eisbacher, G.H., 1976. Proterozoic Rapitan Group and Related Rocks, Redstone River Area, District of Mackenzie. *Geological Survey of Canada Paper*, 76(1A): 117-125.
- Eisbacher, G.H., 1978. Re-definition and subdivision of the Rapitan Group, Mackenzie Mountains. *Geological Survey of Canada Paper*, 77(35): 1-21.
- Eisbacher, G.H., 1981a. Late Precambrian tillites of the northern Yukon-Northwest Territories region, Canada. In: M.J. Hambrey and W.B. Harland (Editors), *Earth's pre-Pleistocene glacial record*. Cambridge University Press, Cambridge, pp. 724-727.
- Eisbacher, G.H., 1981b. Sedimentary tectonics and glacial record in the Windermere Supergroup, Mackenzie Mountains, Northwestern Canada. *Geological Survey of Canada Paper*, 80(27): 1-41.
- Eisbacher, G.H., 1985. Late Proterozoic rifting, glacial sedimentation, and sedimentary cycles in the light of Windermere deposition, western Canada. *Palaeogeography, Palaeoclimatology, Palaeoecology*, 51: 231-254.

- Furlanetto, F., Thorkelson, H.D., Marshall, D.D., Rainbird, R.H., Davis, W.J., Crowley, J.L., and Vervoort, J.D. 2013. Late Paleoproterozoic terrane accretion in northwestern Canada and the case for circum-Columbian orogenesis. *Precambrian Research*, 224: 512-528.
- Gabrielse, H., 1967. Tectonic evolution of the northern Canadian cordillera. *Canadian Journal of Earth Sciences*, 4: 271-298.
- Gabrielse, H., Blusson, S.L. and Roddick, J.A., 1973. Geology of Flat River, Glacier Lake, and Wrigley Lake map-areas, District of Mackenzie and Yukon Territory. Geological Survey of Canada Memoir 366, 153 pp.
- Green, L.H. and Godwin, C.I., 1963. Mineral Industry of Yukon Territory and southwestern District of Mackenzie, 1962. *Geological Survey of Canada Paper*, 63(38): 15-18.
- Gross, G.A., 1965. Iron-formation, Snake River area, Yukon and Northwest Territories. In: S.E. Jenness (Editor), Report of Activities: Field, 1964, Geological Survey of Canada paper 65-1, pp. 143.
- Gross, G.A., 1993. Industrial and genetic models for iron ore in iron-formations. In: R.V. Kirkham, W.D. Sinclair, R.I. Thorpe and J.M. Duke (Editors), Mineral deposit modelling: Geological Association of Canada, Special Paper no. 40, Ottawa, pp. 151-170.
- Halverson, G.P., Poitrassen, F., Hoffman, P.F., Nédeléc, A., Montel, J.-M., and Kirby, J., 2011. Fe isotope and trace element geochemistry of the Neoproterozoic syn-glacial Rapitan iron formation. *Earth and Planetary Science Letters*, 309(1-2): 100-112.
- Harlan, S.S., Heaman, L., LeCheminant, A.N. and Premo, W.R., 2003. Gunbarrel mafic magmatic event: A key 780 Ma time marker for Rodinia plate reconstructions. *Geology*, 31(12): 1053-1056.
- Harland, W.B., 1964. Critical evidence for a great infra-Cambrian glaciation. *Geologische Rundschau*, 54(1): 45-61.
- Hoffman, P.F., 2009. Pan-glacial- a third state in the climate system. *Geology Today*, 25(3): 100-107.
- Hoffman, P.F. and Halverson, G.P., 2011. Chapter 36 Neoproterozoic glacial record in the Mackenzie Mountains, northern Canadian Cordillera. In: E. Arnaud, G.P. Halverson and G. Shields-Zhou (Editors), The geological record of Neoproterozoic glaciations. Geological Society of London, London, pp. 397-411.

- Hoffman, P.F., Kaufman, A.J., Halverson, G.P. and Schrag, D.P., 1998. A Neoproterozoic Snowball Earth. *Science*, 281: 1342-1346.
- Hoffman, P.F. and Li, Z.X., 2009. A paleogeographic context for Neoproterozoic glaciation. *Palaeogeography, Palaeoclimatology, Palaeoecology*, 277: 158-172.
- Hoffman, P.F., Macdonald, F.A. and Halverson, G.P., 2011. Chapter 5 Chemical sediments associated with Neoproterozoic glaciation: iron formation, cap carbonate, barite, and phosphate. In: E. Arnaud, G.P. Halverson and G. Shields-Zhou (Editors), *The geological record of Neoproterozoic Glaciations*. Geological Society of London, London, pp. 67-80.
- Holland, H.D., 1984. *The chemical evolution of the atmosphere and oceans*. Princeton University Press, Princeton, 598 pp.
- Holland, H.D., 1992. Chemistry and evolution of the Proterozoic ocean. In: J.W. Schopf and C. Klein (Editors), *The Proterozoic Biosphere: a multidisciplinary study*. Cambridge University Press, Cambridge, pp. 169-172.
- Huang, J., Chu, X., Jiang, G., Feng, L. and Chang, H., 2011. Hydrothermal origin of elevated iron, manganese and redox-sensitive trace elements in the c. 635 Ma Doushantuo cap carbonate. *Journal of the Geological Society, London*, 168: 805-815.
- Ilyin, A.V., 2009. Neoproterozoic banded iron formations. *Lithology and Mineral Resources*, 44(1): 78-86.
- Isley, A.E., 1995. Hydrothermal Plumes and the Delivery of Iron to Banded Iron-Formation. *Journal of Geology*, 103(2): 169-185.
- Isley, A.E. and Abbott, D.H., 1999. Plume-related mafic volcanism and the deposition of banded iron formation. *Journal of Geophysical Research*, 104: 15461-15477.
- James, N.P., Narbonne, G.M., Dalrymple, R.W. and Kyser, T.K., 2005. Glendonites in Neoproterozoic low-latitude, interglacial, sedimentary rocks, northwest Canada: Insights into the Cryogenian ocean and Precambrian cold-water carbonates. *Geology*, 33(1): 9-12.
- James, N.P., Narbonne, G.M. and Kyser, T.K., 2001. Late Neoproterozoic cap carbonates: Mackenzie Mountains, northwestern Canada: precipitation and global glacial meltdown. *Canadian Journal of Earth Sciences*, 38: 1229-1262.
- Jefferson, C.W., 1983. *The upper Proterozoic Redstone copper belt, Mackenzie Mountains, N.W.T.*, University of Western Ontario, London, 445 pp.

- Jefferson, C.W. and Parrish, R.R., 1989. Late Proterozoic stratigraphy, U-Pb zircon ages, and rift tectonics, Mackenzie Mountains, northwestern Canada. *Canadian Journal of Earth Sciences*, 26: 1784-1801.
- Jefferson, C.W. and Ruelle, J.C.L., 1987. The late Proterozoic Redstone copper belt, Mackenzie Mountains, Northwest Territories. In: J.A. Morin (Editor), *Mineral Deposits of the northern Cordillera*. Canadian Institute of Mining and Metallurgy Special Vol. 37, pp. 154-168.
- Kamber, B.S., 2010. Archean mafic-ultramafic volcanic landmasses and their effect on ocean atmosphere chemistry *Chemical Geology*, 274(1-2): 19-28.
- Keele, J., 1906. Upper Stewart River region, Yukon. *Geological Survey of Canada Annual Report 1904*, 16: 5-23.
- Keele, J., 1910. Reconnaissance across the Mackenzie Mountains on the Pelly, Ross, and Gravel Rivers, Yukon and Northwest Territories. *Geological Survey of Canada Report No. 1097*.
- Kirschvink, J.L., 1992. Late Proterozoic low-latitude global glaciation: the Snowball Earth. In: J.W. Schopf and C. Klein (Editors), *The Proterozoic biosphere: A multidisciplinary study*. Cambridge University Press, Cambridge, pp. 51-52.
- Klein, C., 2005. Some Precambrian banded iron-formations (BIFs) from around the world: Their age, geologic setting, mineralogy, metamorphism, geochemistry, and origin. *The American Mineralogist*, 90: 1473-1499.
- Klein, C. and Beukes, N.J., 1993. Sedimentology and geochemistry of the glaciogenic late Proterozoic Rapitan iron-formation in Canada. *Economic Geology*, 88: 542-565.
- Klein, C. and Ladeira, E.A., 2004. Geochemistry and mineralogy of Neoproterozoic banded iron-formations and some selected, siliceous manganese formations from the Urucum District, Mato Grosso Do Sul, Brazil. *Economic Geology*, 99: 1233-1244.
- Kump, L.R. and Seyfried Jr., W.E., 2005. Hydrothermal Fe fluxes during the Precambrian: Effect of low oceanic sulfate concentrations and low hydrostatic pressure on the composition of black smokers. *Earth and Planetary Science Letters*, 235: 654-662.
- Le Heron, D.P., Busfield, M.E., Le Ber, E. and Kamona, A.F., 2013. Neoproterozoic ironstones in northern Namibia: Biogenic precipitation and cryogenian glaciation. *Palaeogeography, Palaeoclimatology, Palaeoecology*, 369: 48-57.

- Long, D.G.F. and Turner, E.C., 2012. Formal definition of the Neoproterozoic Mackenzie Mountains Supergroup (Northwest Territories), and formal stratigraphic nomenclature for terrigenous clastic units of the Katherine Group. Geological Survey of Canada Open File, 7713: 1-40.
- Lottermoser, B.G. and Ashley, P.M., 2000. Geochemistry, petrology and origin of Neoproterozoic ironstones in the eastern part of the Adelaide Geosyncline, South Australia. *Precambrian Research*, 101: 49-67.
- Macdonald, F.A., Strauss, J.V., Rose, C.V., Dudás, F.Ö. and Schrag, D.P., 2010. Stratigraphy of the Port Nolloth Group of Namibia and South Africa and implications for the age of Neoproterozoic iron formations. *American Journal of Science*, 310: 862-888.
- Narbonne, G.M. and Aitken, J.D., 1995. Neoproterozoic of the Mackenzie Mountains, northwestern Canada. *Precambrian Research*, 73: 101-121.
- Nelson, J., Paradis, S., Christensen, J. and Gabites, J., 2002. Canadian Cordilleran Mississippi Valley-type deposits: a case for Devonian-Mississippian back-arc hydrothermal origin. *Economic Geology*, 97: 1013-1030.
- Nielsen, A.B., Thorkelson, D.J., Gibson, H.D. and Marshall, D.D., 2013. The Wernecke igneous clasts in Yukon, Canada: Fragments of the Paleoproterozoic volcanic arc terrane Bonnetia. *Precambrian Research*, 238: 78-92.
- Och, L.M. and Shields-Zhou, G.A., 2012. The Neoproterozoic oxygenation event: Environmental perturbations and biogeochemical cycling. *Earth-Science Reviews*, 110: 26-57.
- Peter, J.M., Goodfellow, W.D. and Doherty, W., 2003. Hydrothermal Sedimentary Rocks of the Heath Steele Belt, Bathurst Mining Camp, New Brunswick: Part 2. Bulk and Rare Earth Element Geochemistry and Implications for Origin. In: W.D. Goodfellow, S.R. McCutcheon and J.M. Peter (Editors), *Economic Geology Monograph 11: Massive Sulfide Deposits of the Bathurst Mining Camp, New Brunswick, and Northern Maine*. *Economic Geology Monograph*. Society of Economic Geologists, pp. 391-415.
- Poulton, S.W. and Canfield, D.E., 2011. Ferruginous conditions: a dominant feature of the ocean through Earth's history. *Elements*, 7: 107-112.
- Rose, A.W., Smith, A.T., Lustwerk, R.L., Ohmoto, H. and Hoy, L.D., 1986. Geochemical aspects of stratiform and red-bed copper deposits in the Catskill Formation (Pennsylvania, USA)

- and Redstone Area (Canada). Sequence of mineralization in sediment-hosted copper deposits (Part 3). In: G.H. Friedrich (Editor), *Geology and Metallogeny of Copper Deposits*. Springer-Verlag, Berlin, pp. 414-421.
- Slack, J.F., Grenne, T., Bekker, A., Rouxel, O.J. and Lindberg, P.A., 2007. Suboxic deep seawater in the late Paleoproterozoic: Evidence from hematitic chert and iron formation related to seafloor-hydrothermal sulfide deposits, central Arizona, USA. *Earth and Planetary Science Letters*, 255: 243-256.
- Stuart, R.A., 1963. *Geology of the Snake River Iron deposit*. D.I.A.N.D. Assessment Files, Yellowknife, N.W.T.: 18 p.
- Thorkelson, D.J. et al., 2005. Early and Middle Proterozoic evolution of Yukon, Canada. *Canadian Journal of Earth Sciences*, 42: 1045-1071.
- Turner, E.C., 2011. Stratigraphy of the Mackenzie Mountains Supergroup in the Wernecke Mountains, Yukon. In: K.E. MacFarlane, L.H. Weston and C. Relf (Editors), *Yukon Exploration and Geology 2010*. Yukon Geological Survey, pp. 207-231.
- Turner, E.C. and Long, D.G.F., 2012. Formal definition of the Neoproterozoic Mackenzie Mountains Supergroup (Northwest Territories), and formal stratigraphic nomenclature for its carbonate and evaporite formations. *Geological Survey of Canada Open File*, 7712(1-57).
- Upitis, U., 1966. *The Rapitan Group, southeastern Mackenzie Mountains, Northwest Territories*. M.S. Thesis, McGill University, Montreal, 70 pp.
- Yeo, G.M., 1978. Iron-formation in the Rapitan Group, Mackenzie Mountains, Yukon and Northwest Territories. *DIAND Mineral Industry Report 1975, NWT Economic Geology Series 1978-5*: 170-175.
- Yeo, G.M., 1981. The late Proterozoic Rapitan glaciation in the northern Cordillera. In: F.H.A. Campbell (Editor), *Proterozoic Basins of Canada*. Geological Survey of Canada Paper 81-10, pp. 25-46.
- Yeo, G.M., 1984. *The Rapitan Group: Relevance to the global association of late Proterozoic glaciation and iron-formation*. Ph.D. Thesis, University of Western Ontario, London, 603 pp.

- Yeo, G.M., 1986. Iron-formation in the late Proterozoic Rapitan Group, Yukon and Northwest Territories. In: J.A. Morin (Editor), Mineral Deposits of the Northern Cordillera: Canadian Institute of Mining and Metallurgy Special Vol. 37, pp. 142-153.
- Yeo, G.M., Delaney, G.D. and Jefferson, C.W., 1978. Two major Proterozoic unconformities, northern Cordillera: Discussion. Current Research Part B, Geological Survey of Canada Paper, 78-1B: 225-230.
- Young, G.M., 1976. Iron-formation and glaciogenic rocks of the Rapitan Group, Northwest Territories, Canada. Precambrian Research, 3: 137-158.
- Ziegler, P.A., 1959. Frühpaläozoische Tillite im östlichen Yukon-Territorium (Kanada). *Ecologiae Geologicae Helveticae*, 52: 735-741.

Chapter 2: A new depositional model for glaciogenic Neoproterozoic iron formation: Insights from the chemostratigraphy and basin configuration of the Rapitan iron formation

2.1 Abstract

Neoproterozoic iron formations record an unusual and apparently final recurrence of this sediment type after a hiatus of more than one billion years. Despite the unusual environmental conditions that led to their formation, specifically their association with glaciogenic deposits, Neoproterozoic iron formations have strongly influenced models for the Precambrian Earth's surficial evolution and iron formation in general. A suite of high-quality trace element data for 42 samples from the Rapitan iron formation in northwestern Canada were used to reconstruct the configuration and redox evolution of the Rapitan basin. Complete REE+Y patterns demonstrate that the Rapitan basin was hydrologically connected to the open ocean, but that local catchments of an evolved, possibly granitic composition supplied dissolved REE+Y, suggesting partial basin restriction. Molybdenum and U systematics are consistent and indicate a partly restricted, or 'silled' basin. In contrast to modern analogues for such basins, such as the Cariaco Basin, the stratigraphic association with glaciogenic clastic rocks requires ice cover to be considered in basin reconstruction. Accordingly, the Rapitan iron formation was deposited through a complex interplay of processes: during intervals of ice cover, glacially-sourced iron oxy-hydroxides were bacterially reduced to dissolved ferrous iron, which was subsequently oxidised to ferric iron following ice withdrawal. During this time, extreme primary productivity in the shallow water column drove eutrophication at middle water depths and the production of a three-tiered stratified water column with ferruginous deep water, a thin euxinic wedge at middle depths, and oxic surface water. Regardless of the basinal redox conditions and depositional constraints, the absence of a positive Eu anomaly in the Rapitan iron formation suggests that the global ocean was fully oxygenated by the Neoproterozoic.

2.2 Introduction

Neoproterozoic iron formations remain one of the most enigmatic rock types in the geologic record. Deposited during the last major pulse of Precambrian iron formation, these deposits have played a major role in the development of models for Earth's atmospheric and oceanic evolution. Neoproterozoic iron formations mark the re-emergence of iron formation after roughly one billion years in which very few were deposited, and have been interpreted to represent the termination of the controversial episode known as the "Canfield ocean". The observation that little to no iron formation was deposited during the Mesoproterozoic, with the exception of those in direct association with hydrothermal vent sites (e.g., Slack et al. 2007), paired with a shift to heavier sulphur isotopes, led some workers to suggest that the Mesoproterozoic deep ocean was euxinic (e.g., Canfield 1998; Farquhar et al. 2010), and that the reappearance of iron formation in the Neoproterozoic records the termination of that condition. In addition to the absence of iron formation during the Mesoproterozoic, the first series of redox condition studies of shale basins, using iron speciation (e.g., Shen et al. 2002; 2003; Poulton et al. 2004), and molybdenum isotopes (Arnold et al. 2004), argued in favour of a euxinic ocean, although each of these basins has been independently shown to have been restricted from the open ocean (e.g., Pufahl et al. 2010). Shales deposited in such basins are thus unlikely to record open-marine conditions. More recent studies that have good spatial and stratigraphic control both in the latest Paleoproterozoic (Poulton et al. 2010) and in the Neoproterozoic (Canfield et al. 2008; Johnston et al. 2010; Li et al. 2010), have shown that limited euxinia existed in shallow, coastal waters, whereas ferruginous conditions dominated deeper basins. This suggests that a true 'Canfield ocean', as originally defined, may never have existed, and that the stratified water column more closely resembled the conditions reported in the more recent studies (Poulton and Canfield 2011). If the Mesoproterozoic ocean was not euxinic, the relative lack of iron formation during that time requires a new explanation. Kump and Seyfried (2005) suggested that there was a major change in the composition and flux of hydrothermal vent fluids, whereas Bekker et al. (2010) observed that the Mesoproterozoic was a time of relatively few mantle plume events. Neither of these explanations fully address why so little iron formation was deposited in an otherwise ferruginous ocean. Others have proposed that the deposition of Neoproterozoic iron formation was the result of a Neoproterozoic oxygenation event ("NOE") that had significant

influence on the chemical and biological development of the planet prior to the Cambrian explosion, including triggering a final pulse of iron formation deposition (Shields-Zhou and Och 2011).

The universal association of Neoproterozoic iron formation with glacial deposits attributed to the “snowball” Earth interval has led some workers to suggest that iron formation may have been closely associated with glacial episodes throughout the Precambrian (Young 1988; 2002), despite the lack of glacial deposits associated with most of the largest Paleoproterozoic iron formations. In this context, it is important to recall that the overwhelming majority of Neoproterozoic iron formations are associated with a single glaciation, the Sturtian glaciation (e.g., Hoffman and Li 2009; Macdonald et al. 2010b). A few iron deposits have poor age constraints and are believed to be of Marinoan age (e.g., Trompette et al. 1998; Kianian and Khakzad 2008). Only one is associated with the much later Ediacaran/Gaskiers glaciation (Pecoits et al. 2008). Another common attribute of the Neoproterozoic glaciogenic deposits, and therefore the iron formations themselves, is their close spatial link with rift basins that are associated with the initial break-up of Rodinia (Young 1992), which some have suggested were the direct cause of the glaciations (Young 2002; Eyles 2008). In summary, due to the conflicting views on the significance of geochronological and paleoenvironmental data for both the glacial events and iron formation deposition, the nature of the relationship between Neoproterozoic iron formation and glaciation remains largely unresolved.

A surprising concern is that in spite of the numerous outstanding questions that remain about the geodynamic, chemical, and oceanic constraints on Neoproterozoic iron formations, modified versions of the early depositional models for Neoproterozoic iron formation, such as that of Klein and Beukes (1993), continue to be applied to Archean iron formation (e.g., Beukes and Klein 1992). As a consequence, the geological implications of past studies of Neoproterozoic iron formation may far exceed the direct significance of the rocks themselves.

Specialised chemical and isotopic data extracted from Neoproterozoic iron formation are widely used in reconstructions of the Earth’s surficial evolution, regardless of the fact that they are poorly understood compared to their older counterparts (e.g., Frei et al. 2009; Konhauser et al. 2009; Planavsky et al. 2010b). One of the core reasons for this lack of understanding is the

relative paucity of comprehensive geochemical data for the Neoproterozoic iron formations. Previous geochemical studies (e.g., Klein and Beukes 1993; Lottermoser and Ashley 2000; Klein and Ladeira 2004), were limited by the quality of the trace element data available. Because of the use of instrumental neutron activation analysis (INAA) in previous studies, only limited trace element datasets were obtained. The inability of this technique to measure many different trace elements, most notably the mono-isotopic rare earth elements (REE), has hitherto precluded an in-depth analysis of the marine chemistry controlling the deposition of the iron formation. With the advent of improved quadrupole ICP-MS techniques that allow for the precise analysis of suites of more than 40 trace elements, including all of the REE, it is crucial to revisit the geochemistry of Neoproterozoic iron formations to properly understand the geochemical and oceanographic conditions that influenced their deposition.

This study addresses the Rapitan iron formation, one of the most prominent and archetypical Neoproterozoic iron formations, using the REE, with the addition of yttrium, to assess the general chemical nature of the basin. The redox evolution and configuration of the basin are interpreted using recent advances in understanding the behaviour of redox-sensitive trace metals, such as Mo and U, in modern basins. A proper understanding of the Rapitan iron formation's depositional basin, as well as those of other Neoproterozoic iron formations, is critical to using these deposits to model the evolution of Earth-surface environments.

2.3 Geological Setting

The Rapitan Group (lower Windermere Supergroup) is exposed in the northern Canadian Cordillera, in the Northwest Territories and Yukon (Fig. 2.1). In the Mackenzie Mountains, the Windermere Supergroup consists of the basal Coates Lake Group, the Rapitan Group, the Hay Creek Group (Yeo 1978; James et al. 2001), and several ungrouped late Neoproterozoic formations (Aitken 1989; Narbonne and Aitken 1995) (Fig. 2.2). In Yukon, the Coates Lake Group is absent, and the Rapitan Group lies directly on strata of the early Neoproterozoic Mackenzie Mountains supergroup. This thick (~4-5 km) succession consists of shallow-marine carbonate rocks, fluvial quartz arenite, marine siltstone and minor shale, and evaporite rocks (Long et al. 2008).

The Rapitan Group is underlain by the Coates Lake Group in the Redstone River - Mountain River region of the Mackenzie Mountains, and by the Little Dal Group in the Snake River region of the Northwest Territories and Yukon (Yeo 1981) (Fig. 2.2). Both the Coates Lake and Rapitan groups were deposited in extensional settings associated with the initial rifting of the supercontinent Rodinia (Young 1992), and there is local evidence for a slight angular unconformity between the two groups, as well as within the Rapitan Group (Helmstaedt et al. 1979). The sedimentological evidence of pronounced lateral thickness and lithofacies, combined with the observed angular unconformities indicate that these groups were deposited on an actively rifting margin, which would have generated fault grabens, promoted basin restriction, and possibly caused glaciation (Eyles 2008; Young 2002). The Coates Lake Group consists of the “Little Dal basalt”, the Thundercloud, Redstone River, and Coppercap formations; sedimentary-hosted copper deposits are associated with the Redstone River-Coppercap contact (e.g., Rose et al. 1986; Jefferson and Ruelle 1987; Jefferson and Parrish 1989; Narbonne and Aitken 1995). The stratigraphic affiliation of the Coates Lake Group has been the subject of dispute: some authors suggest that it belongs to neither the Mackenzie Mountains supergroup nor the Windermere Supergroup (Jefferson and Parrish 1989). The current consensus, however, is that it represents the basal Windermere Supergroup (e.g., Narbonne and Aitken 1995; Long et al. 2008). Overlying the Rapitan Group in the Redstone River region (Fig. 2.1A) is the Hay Creek Group (Yeo 1978; James et al. 2001), the lowermost formation of which is the Twitya Formation, which contains disc-shaped impressions that are purported to be the oldest documented physical evidence of metazoans (Hofmann et al. 1990). The Hay Creek Group is conformably overlain by several ungrouped formations of the upper Windermere Supergroup, which extends through to the lower Cambrian (Aitken 1989). In the Snake River region (Fig. 2.1B), the Rapitan Group is unconformably overlain by the lower Paleozoic Franklin Mountain and Mount Kindle formations.

The Rapitan Group was established by Green and Godwin (1963) for a succession of diamictite and iron formation, although the presence of iron formation in the Snake River region had been known as early as the Yukon gold rush (Keele 1906), and was identified elsewhere in the Mackenzie Mountains soon after (Keele 1910). Siliciclastic rocks associated with the iron formation were first interpreted to be of glaciogenic origin by Ziegler (1959), a conclusion that

was later confirmed by other authors (e.g., Eisbacher 1976; 1978; 1981a; 1981b; 1985; Young 1976; Yeo 1981). The stratigraphy of the Rapitan Group was studied extensively by Eisbacher (1978), who established type sections for the Sayunei and Shezal formations in the Redstone River region. The Sayunei Formation consists of dark red to maroon, deep-water, fine-grained turbidites, locally capped by thin jaspilitic iron formation in the Redstone River area, and is overlain by green, grey or tan diamictite of the Shezal Formation (Eisbacher 1978; Yeo 1981). In the Snake River region, the iron formation is significantly thicker (up to 120 m), and was the target of extensive exploration for iron ore in the 1960s (Stuart 1963). The stratigraphic position of the iron formation in this region is the subject of some dispute. Klein and Beukes (1993) contend that it is at the top of the Sayunei Formation, as is the case to the southeast in the Redstone Plateau area, whereas Yeo (1981) placed it in the lowermost Shezal Formation. Diamictite of the aeri ally limited Mount Berg Formation underlies the Sayunei Formation only in the southernmost part of the Rapitan exposure area (Eisbacher 1978; Yeo 1981).

A granitic dropstone from the lower Sayunei Formation yielded a U-Pb zircon age of 755 ± 18 Ma, providing a maximum depositional age for the Rapitan Group (Ross and Villeneuve 1997). Macdonald et al. (2010a) obtained a U-Pb zircon age of 716.47 ± 0.24 Ma from a felsic tuff interbedded with the possibly equivalent upper Mount Harper Group of the central Ogilvie Mountains, western Yukon (Yeo 1981), which was interpreted to imply that volcanism and iron formation were coeval within the larger basinal context. These ages are consistent with the estimated age of the Sturtian glaciation, the oldest of the major glacial episodes associated with the “snowball” Earth hypothesis (e.g., Kirschvink 1992; Hoffman et al. 1998). The Sturtian affiliation of the Rapitan Group is indirectly supported by the presence of another Neoproterozoic glaciogenic unit higher in the Windermere Supergroup, the Ice Brook Formation, which is attributed to the Marinoan glacial event (Aitken 1991a; 1991b; James et al. 2001).

2.4 Stratigraphy

A detailed stratigraphic section of the Rapitan iron formation was measured near the Cranswick River, Northwest Territories (Fig. 2.3). This easternmost exposure of the Snake River

deposit of the Rapitan iron formation (65°12.856'N and 132°22.105'W), contains approximately 30 metres of hematite-jasper iron formation. Most of this deposit (called the Crest or Snake River deposit) is located in Yukon. Good exposure in the NWT is limited to a series of incised canyons along the mountainsides east of the Cranswick River, one of which contains a complete exposure of the iron formation, as well as variable exposure of the under- and overlying clastic, glaciogenic rocks.

Attempts to use the iron-formation textural classification scheme of Beukes and Gutzmer (2008) proved ineffective. Rapitan iron formation lithofacies are best referred to as hematite-jasper felutite (Nicolas J. Beukes, pers. comm., 2010). Here, however, a Rapitan-specific classification scheme is used. The iron formation rocks are generally either layered jasper and hematite (i.e., BIF) or nodular iron formation, which consists of massive hematite and sub-spherical to elongate, zoned jasper nodules (Fig. 2.4A, B). The most elongate of the nodules have been referred to as 'lenticles' (Yeo 1981) or lenses, can be up to a metre in lateral extent, and may be of either syn-depositional or very early diagenetic origin (Fig. 2.4C). These two types of iron formation are end-members, and most units are transitional between the two; each unit is classified according to whether beds or nodules are the dominant form of jasper. The term 'jasper' is quite useful for these rocks, because Rapitan cherts exhibit a considerable range in iron content, and vary in colour from yellow-orange to purple.

The iron formation is underlain by a polymictic, clast-supported, channel-fill conglomerate containing predominantly carbonate and quartz arenite clasts derived from the underlying Mackenzie Mountains supergroup, as well as scattered basaltic clasts of uncertain provenance. Clasts are pebble- to cobble-grade, and rare boulders are present. The intergranular space contains carbonate cement and scattered quartz sand grains. The conglomerate has variable lateral thickness and continuity, and is hosted in a friable, clast-rich, purple intermediate diamictite with clast lithologies that are similar to those of the conglomerate. The contact between the conglomerate/diamictite and the iron formation is in a thin covered interval, above which is a two-metre-thick succession of siltstone and sandy siltstone. These clastic layers are hematite-cemented and contain scattered dropstones, predominantly of carbonate composition,

weak normal grading, and faint cross-bedding. Similar units recur throughout the iron formation, but are rarely more than a few tens of centimetres thick.

Above the basal clastic interval, the iron formation consists of variably interbedded BIF and nodular iron formation units. Continuous jasper beds are common in nodular units, particularly in the thicker intervals of this rock type. Ubiquitous dropstones are typically of carbonate composition, and generally deform only 1-2 cm of underlying iron formation, if any (Fig. 2.4D). Some iron formation intervals are very dropstone-rich, containing more than 70% dropstones of mixed composition (mostly carbonate) in a predominantly hematitic matrix, with dropstone grain sizes ranging from granules to large pebbles (this lithofacies is here referred to as ‘dropstone-rich IF’). The iron formation contains irregular bedding in some intervals, and local slump folds. Slump folds are most conspicuous in the vicinity of a large slump scar that is between 5 and 10 metres above the base of the iron formation. The surface cross-cuts up to 3 metres of strata and is associated with considerable reworking and folding in its lateral equivalents. A few intervals in the main measured section are extensively reworked, such that they no longer resemble typical iron formation, and the primary relationships between the folded and disjointed jasper beds, hematite beds, and jasper nodules are not clearly discernible; these units are referred to as ‘slumped or reworked IF’.

The relative ratio of BIF to nodular iron formation increases in the uppermost 15 metres of the iron formation, although nodular iron formation remains abundant, as do nodular layers in the BIF. Unlike the lower part of the section, the upper part of the iron formation contains jasper nodules in jasper beds; these nodules are generally not zoned, and commonly have a fairly subtle colour difference from the host jasper. Consequently, although these units are referred to as bedded jasper, or BIF, units, a strong case can be made for their classification as nodular iron formation, because a far greater proportion of the jasper is in the nodules than in the bands (Fig. 2.4E). The uppermost jasper bed, at the contact between the iron formation and overlying diamictite, contains greenish-tan chert nodules in a jasper matrix; this is the only non-jaspilitic chert in the section (Fig. 2.4F).

Overlying the iron formation are at least 15 metres of texturally and compositionally variable diamictite. These are dominated by grey-green to tan, carbonate-rich, sandy clast-rich

pebble diamictite, commonly with a fissile, scaly weathering style that is typical of Shezal Formation diamictite. The exception to this is a roughly two-metre-thick unit of well-indurated red diamictite containing abundant jasper clasts, many of which show evidence of resedimentation prior to lithification. Some elongate clasts are vertically oriented, which may be evidence of either rapid sedimentation or reworking of locally derived iron formation. Based on the sedimentological evidence offered by the siliciclastic rocks that under- and overlie the iron formation at this site, the stratigraphic position of the iron formation is entirely within the Shezal Formation, as per Yeo (1981), but further work is needed in the area to confirm this.

2.5 Methods

Forty-two jasper samples were analysed for major and trace element geochemistry. Following the procedures outlined by Baldwin et al. (2011) and Ulrich et al. (2009), exploratory LA-ICP-MS analyses were performed on both jasper bands and nodules to screen for homogeneity. Jasper bands are highly homogeneous, whereas the nodules exhibit both concentric and discordant chemical zoning, and were therefore considered less suitable for the purpose of this study. Furthermore, because the nodules are undoubtedly of an early diagenetic origin, they probably do not record true basinal seawater conditions. It has been suggested that chert beds in iron formations containing ferrous iron species, such as siderite and magnetite, could also be diagenetic in origin (Fischer and Knoll 2009), but this idea has not been extended to hematite-jasper iron formations.

Trace elements were analysed by quadrupole ICP-MS at Laurentian University, following the digestion methods of Babechuk et al. (2010) and Baldwin et al. (2011), and a mass spectrometric approach similar to that of Eggins et al. (1997), using modifications reported in Kamber (2009) and Babechuk et al. (2010). Element concentrations were externally calibrated using multiple solutions of the USGS standard W-2. The international rock standards JA-2, JB-2, and IF-G were analysed as unknowns and compared to the laboratory long-term reproducibility (e.g., Kamber 2009). Weight percent major element oxides were measured using XRF at the Ontario GeoLabs for 20 samples, and by ICP-MS for the remaining 22 samples at Laurentian University. Samples measured by ICP-MS lack data for SiO₂ and LOI due to the digestion

methods used. More detail about methods, full data tables, and related figures are available in supplementary materials.

2.6 Results

2.6.1 REE+Y systematics

There is a surprising lack of modern high-quality chemical data, especially the REE+Y, for Neoproterozoic chemical sediments (including iron formation), which contrasts with a rich literature on comparable Archean and Paleoproterozoic materials. This is unfortunate, because the behaviour of the rare earth elements and yttrium (REE+Y) in modern seawater is well understood. Depletion of the light rare earth elements (LREE) relative to the heavy rare earth elements (HREE), superchondritic Y/Ho ratios, and positive anomalies of both La and Gd are all characteristic of modern seawater (e.g., Zhang and Nozaki 1996), and have been reported for hydrogenous sediments from the entire geological record (e.g., Bau and Dulski 1996; Nothdurft et al. 2004; Alexander et al. 2008; Planavsky et al. 2010a), which points to the extreme antiquity of the hydrological cycle (Kamber 2010). Although some authors have contended that the REE composition of seawater has changed significantly over time (e.g., Picard et al. 2002), others point out that these reported changes in the marine REE budget are an artefact of using marine phosphates as a seawater proxy, which inherently fractionate the REE from ambient seawater compositions (Shields and Webb 2004). There is little doubt that changes in the overall slope of the normalised REE pattern and the size of the Y, La and Gd anomalies may have changed over time (Kamber 2010) but the only substantial temporal deviations exist for the redox-sensitive Ce and Eu (as explained below). The remarkable similarity of the REE patterns in modern seawater and normal marine hydrogenous rocks from throughout time (Fig. 2.5C) is interpreted to reflect the extreme antiquity of the marine REE cycle. The diagnostic features of the marine REE pattern have been demonstrated to be generated during the introduction of dissolved REE+Y from riverine sources into the ocean. In an estuary, LREE are more readily removed by adsorption to organometallic complexes than are the HREE, Y, La and Gd (Elderfield et al. 1990; Lawrence and Kamber 2006). It is noteworthy that seawater-type REE patterns can form in saline aquifers

(Johannesson et al. 2006), but such a setting clearly does not apply to sediment of proven marine origin. In addition to these features, europium (Eu) and cerium (Ce) are critical tools for understanding Precambrian seawater because they deviate from normal trivalent REE behaviour. Europium can be used as a proxy for the contribution of hydrothermal fluids to ocean water, due to the large positive Eu anomalies of modern high-temperature hydrothermal fluids (e.g., Bau and Dulski 1999). The presence of positive Eu anomalies even in shallow-water Paleoproterozoic iron formation and microbial carbonate strongly suggests long-distance transport of Eu^{2+} through an anoxic ocean (e.g., Derry and Jacobsen 1990). Due to differences in particle adhesion between Ce^{3+} and the oxidised ion Ce^{4+} , the Ce anomaly is a common proxy for oceanic paleoredox conditions. This behaviour typically results in negative Ce anomalies in oxidised seawater, but excess Ce in anoxic water below a chemocline (e.g., Ohta et al. 1999; Kato et al. 2006; Planavsky et al. 2010a). In summary, proper assessment of REE+Y systematics is an important starting point when examining any hydrogenous sedimentary rock.

In this study, REE plus yttrium data were normalised to upper-continental-crust using the modern alluvial sediment average MuQ (Mud from Queensland, Kamber et al. 2005), which was produced with the same analytical protocol as the present study. Normalised data were initially screened for patterns demonstrating the two most diagnostic features of seawater REE+Y patterns: LREE depletion and a superchondritic Y/Ho ratio ($\text{Y}/\text{Ho} > 26$). Most of the dataset ($n = 33$) exhibits these characteristics, but nine samples deviated from typical marine patterns (Fig. 2.5A, B). Of these nine samples, seven produced REE+Y patterns that were distinct from typical seawater in their overall shape or slope, and two demonstrated significantly greater LREE-depletion than is expected for seawater: in the latter two samples the HREE were enriched by more than two orders of magnitude relative to the LREE, whereas the HREE are typically enriched by approximately one order of magnitude in the rest of the dataset (Fig. 2.5B). A basic assessment of other diagnostic trace element concentrations, such as Th, showed that these two samples were strongly influenced by a non-hydrogenous source, and so do not reflect seawater chemistry, despite some similarities.

The patterns that do not reflect pure, hydrogenous chert (see Fig. 2.5C for examples) have limited use for reconstructing basin water chemistry. The nine samples may be influenced either

by elevated phosphate mineral contents, which can cause non-trivalent fractionation of the otherwise non-anomalous REE, by detrital material whose trace element budget overwhelms the chert, or by late, low-temperature hydrothermal veins (primarily calcite). In view of the relative uniformity of all of the other patterns, no further effort was made to understand the nine incongruent patterns and these samples are excluded from further discussion.

Cerium can be an interesting and direct window into the paleoredox conditions of the depositional basin in which a chemocline existed, and in which particle transport involved Mn-oxy-hydroxides. Much like other REE studies of Neoproterozoic iron formation (e.g., Klein and Beukes 1993; Lottermoser and Ashley 2000; Klein and Ladeira 2004; Kato et al. 2006), the new data show that the Rapitan iron formation displays only limited variability in Ce/Ce* (see Lawrence et al. 2006 for formula), with values ranging from 0.8 to 1.07 for 33 samples, 19 of which fall between 0.95 and 1.05, indicating the absence of a significant Ce anomaly. Of the remaining 14 samples, seven fall between 0.8 and 0.95, and seven are between 1.05 and 1.07, demonstrating that the majority of the dataset (n=26) has either no statistically significant Ce anomaly or a very small negative anomaly. This suggests that seawater conditions were anoxic to very weakly oxic with respect to Ce. It is also critical to note the absence of a positive Ce anomaly. Planavsky et al. (2010a) demonstrated a tendency for some late Paleoproterozoic iron formations (e.g., Gunflint iron formation) to produce flat to positive Ce anomalies. They interpreted this tendency to reflect a Mn-particle shuttle across a redoxcline. Below such a redoxcline, Mn particles dissolve and Ce⁴⁺, which was preferentially scavenged relative to the trivalent REE from the oxidised upper water column, was released, thereby producing an overabundance of Ce below the redoxcline. This can result in pronounced positive Ce anomalies in BIF deposited in such settings. The absence of any meaningful positive Ce anomaly in the new Rapitan data suggests that any particulate shuttle in the Rapitan basin was not dominated by Mn-oxides, and was probably defined by an iron shuttle and redoxcline, similar to that suggested for Archean and early Paleoproterozoic iron formations (Planavsky et al. 2010a).

Despite its origin from high-temperature hydrothermal vent fluids, a Eu anomaly is common in most Archean and Paleoproterozoic hydrogenous sediments, including iron formation and shallow-water microbial carbonate. This characteristic has led to oceanic circulation models

that involve a sufficiently anoxic ocean to allow for the long-distance transport of Eu^{2+} , and therefore Fe^{2+} , from its most important source, vent systems along mid-ocean ridges (Derry and Jacobsen 1990; Isley 1995). An alternative explanation is the proposed relationship of iron formation deposition and mantle plume events (e.g., Isley and Abbott 1999; Bekker et al. 2010); unusually large volumes of hydrothermally-sourced Eu and Fe are postulated to have been released into the ocean during such events. The lack of a positive Eu anomaly in the majority of samples studied here is clearly inconsistent with these models for iron formation genesis and with the source of the iron. Only two samples have Eu/Eu^* values above 1.1, whereas the bulk of the dataset ($n=25$) has Eu/Eu^* values of 1.0 or less. This consistent lack of a Eu anomaly is significant and imposes strong constraints on depositional models. In brief, the simplest explanation for the missing Eu anomaly is that the open ocean was sufficiently oxygenated in the Neoproterozoic that long-distance transport of Eu was inhibited through co-precipitation with Fe-oxide phases (Bau and Dulski 1999). The only plausible alternative explanation is that the basin was almost completely isolated from the open ocean, meaning that its sediment would be inappropriate for reconstructing global oceanic conditions, or inferring a global sheet of sea-ice. Both of these explanations are incompatible with a hydrothermal iron source for the Rapitan iron formation, because hydrothermal Fe^{2+} and the positive Eu anomaly are cogenetic features in iron formation.

The new Rapitan data express three of the most common and meaningful REE+Y features: HREE-enrichment, a positive Gd anomaly, and a Y anomaly (expressed as Y/Ho). HREE-enrichment, indicated by a positive overall slope in the REE+Y pattern, is best calculated as the $\text{Pr}_{\text{SN}}/\text{Yb}_{\text{SN}}$ ratio, because these are the lightest and heaviest elements that behave in a manner that is strictly determined by ionic radius (La, Ce, and possibly Lu behave differently in marine systems). Hydrogenous sediment precipitated from normal seawater should demonstrate very low $\text{Pr}_{\text{SN}}/\text{Yb}_{\text{SN}}$ ratios, because Yb should have a much greater normalised abundance than Pr. The samples studied here show a fairly tight range of very low $\text{Pr}_{\text{SN}}/\text{Yb}_{\text{SN}}$ ratios (~ 0.05 - 0.2), indicating strong enrichment of the HREE relative to the LREE. Similarly, superchondritic Y/Ho ratios are a ubiquitous feature in such rocks, with any values greater than $\text{Y}/\text{Ho}=26$ considered indicative of quantifiable hydrogenous influence on a detrital REE pattern. The new data show a fairly wide range of superchondritic values, ranging from 29.9 to 42.5, as well as relatively

variable but consistently positive Gd anomalies ($Gd/Gd^* = 1.04-1.19$). All three of these features (low Pr_{SN}/Yb_{SN} ratios, superchondritic Y/Ho ratios, and positive Gd anomalies) are hallmarks of normal marine seawater, and despite their individual variability, suggest that the Rapitan basin must have been connected to the open ocean, an assertion further reinforced by the reasonably strong positive correlation between the Y/Ho ratio and the Gd/Gd^* values ($r^2 = 0.72$; Fig. 2.6A). The rather large but strongly correlated range of these values, particularly the Y/Ho ratio, points to some variability either in the degree of clastic contamination or in the basin water chemistry. The most common mechanism for causing such ranges is dilution of the seawater signature by detrital material such as clay minerals (e.g., Baldwin et al. 2011). The flat shale-normalised REE patterns of clays and their much higher overall REE concentrations (relative to hydrogenous sediments), combine to dilute recorded seawater anomalies, such as Y/Ho ratios, even with as little as 1-2% by weight clastic contamination. This can be easily addressed, however, by plotting the Y/Ho ratios against the concentration of an immobile lithophile element, such as Al (Fig. 2.6B). The complete lack of a relationship between the Y/Ho ratio and Al, as well as several other immobile elements (e.g., Ti, Th, Ga) indicates that the documented variability in the Y/Ho ratio is not a function of the amount of detrital input. The variation was therefore probably the result of variable water chemistry (over the duration of the Rapitan deposition) caused by moderate but variable degrees of basin restriction, in which the basin had sufficient connectivity with the open ocean to maintain a strong correlation between Y/Ho and Gd/Gd^* , while simultaneously being restricted enough to allow for considerable variability in the same values.

Neither the Y/Ho ratio nor the Gd anomaly correlates clearly with the Eu anomaly (Fig. 2.7A, B). Instead, there are two weakly developed trends of inverse correlation, but no well-defined trend exists for the entire dataset. The few samples that have more elevated Eu anomalies show smaller Gd anomalies and relatively low Y/Ho ratios, indicating that the few positive Eu anomalies present are not of an open-marine origin. Furthermore, the samples with the largest positive Eu anomalies contain elevated concentrations of Al relative to the bulk of the dataset (Fig. 2.7C). This suggests that the largest positive Eu anomalies resulted from the input of older detrital material that was over-enriched in Eu (e.g., feldspar), which is consistent with the observations of Klein and Beukes (1993) that positive Eu anomalies were only present in samples containing volcanoclastic detritus. Naturally, not all samples with elevated Al also demonstrated

positive Eu anomalies, because not all of the detrital material supplied would have been from Eu-rich phases, and indeed the samples with the highest Al have Eu/Eu* values that are consistent with the majority of the sample suite, indicating that most detrital input was from Eu-poor clay minerals. Therefore, regardless of whether an open-marine signal was modified in the Rapitan basin by a more local water mass, the lack of positive Eu anomalies in the samples with the highest Y/Ho and strongest positive Gd anomalies constitutes firm evidence that the Neoproterozoic ocean no longer had a positive Eu anomaly.

The final REE+Y feature associated with seawater is a positive La anomaly. Lanthanum is fractionated from its neighbouring REE because of its empty 4f-orbital, which limits adhesion to particles during the introduction of dissolved REE from freshwater into the marine system (Bau 1996; 1999), thereby causing it to be over-enriched in seawater, and in hydrogenous precipitates that form in equilibrium with seawater (e.g., Bolhar et al. 2004). Samples from the Rapitan iron formation, however, do not consistently produce positive La anomalies. The surprising finding is that several samples (n=8) have La/La* values of less than one, or in other words, slightly negative La anomalies (Fig. 2.8). This is clear evidence for an artefact of normalisation, because there are no known processes that can negatively fractionate La from the other LREE. When a water body is under the influence of a local, very LREE-enriched source, normalisation to average upper crust may not show a La anomaly (Kamber et al. 2004). This is in part because the MuQ upper continental crust composite is from a drainage that samples heavily from an intra-plate basalt province, and is not especially enriched in the LREE, and thus normalisation to a local granitic source may be more appropriate for the Rapitan basin. The drainage area of the Rapitan basin is poorly constrained, but to explore the possibility of a granitic catchment, the data were normalised to the USGS granite standard GSP-2. This pulled all of the La/La* values above one (La/La*= 1.03-1.65) (Fig. 2.8), thereby eliminating the seemingly negative La anomalies that had been produced by normal crustal normalisation. This solution suggests that a local source of roughly granitic composition may have contributed dissolved REE into the Rapitan basin. This possibility is supported by the presence of granitic ‘stranger stones’ in the lower Sayunei Formation (Ross and Villeneuve 1997), as well as the abundance of quartz arenite in the Katherine Group of the lower Mackenzie Mountains supergroup (e.g., Long et al. 2008), which was probably produced by the weathering of granitoid rocks on the Canadian

Shield and Grenville Province to the east. The quartz arenite was probably the main source of quartz-rich clastic material in the glaciogenic deposits of the Sayunei and Shezal formations, and its sub-glacial weathering would probably have introduced significant amounts of La into the basin. The influence of a local granitic input is most pronounced in La because in the chert it is the relatively most depleted REE, whereas in the granite, it is the relatively most enriched REE.

The combined analysis of the various REE+Y features suggests that the Rapitan iron formation formed in a basin that received dissolved REE both from the open ocean as well as from local drainage. These two seemingly diametric oceanographic conditions can coexist in partially restricted basins. Such partially restricted basins are referred to as ‘silled basins’, in reference to a subaqueous topographic high that restricts water exchange with the open ocean, while also allowing moderate exchange across shallow water depths.

2.6.2 Mo-U systematics

Two of the most useful features in diagnosing different basin types are the redox conditions and stratification of the water column. These phenomena leave distinctive geochemical signatures in the sediment, which can be used to aid in basin reconstruction. Many of the transition metals have multiple redox states and record oceanic and diagenetic conditions (e.g., Tribovillard et al. 2006). Among the most useful redox-sensitive metals are molybdenum and uranium. Both of these metals exhibit conservative behaviour in modern seawater and have very long residence times. Unlike some other redox proxies, both Mo and U are evenly distributed throughout the open ocean relative to both area and depth, making them more practical tools than many other metals. Molybdenum and U are strongly over-enriched in seawater relative to their crustal abundances; Mo is the most abundant transition metal in the modern oxygenated ocean (Algeo and Maynard 2008), but its estimated concentration in the ocean changed significantly over the course of the Precambrian (Scott et al. 2008).

Molybdenum is soluble in oxic conditions as the molybdate ion, MoO_4^{2-} , which is slowly removed from seawater through scavenging by Mn-oxides. Under euxinic conditions it can form thiomolybdate ($\text{MoO}_x\text{S}_{4-x}^{2-}$; $x=0-3$), which is highly particle-reactive and is scrubbed from the water column at much greater rates through adsorption onto Fe-sulphides, Fe and Mn-oxides, organic material, and clay minerals (Algeo and Tribovillard 2009). Alternatively, it may form Fe-

Mo-S complexes similar to mackinawite under conditions with moderately low dissolved H₂S. These complexes then adhere to larger particles (Helz et al. 2011). Either of these two Mo-fixation methods requires the presence of H₂S in the water column, and thus at least mildly euxinic conditions. Uranium, in contrast, exists in oxic seawater as highly soluble uranyl carbonate (UO₂(CO₃)₃⁴⁻), and is reduced to less-soluble U-oxides (e.g., UO₂, U₃O₇, and U₃O₈) under anoxic conditions (Algeo and Tribovillard 2009; and refs. therein). These more-reduced U species are removed from the water column by direct transfer across the sediment-seawater interface and attendant precipitation or slow adsorption, a process quite distinct from those affecting Mo. Besides their preferred fixation mechanisms, each of these metals reacts under different redox conditions: U is fixed under all anoxic conditions, completely independent of the presence of dissolved sulphide, whereas Mo requires at least mildly euxinic (i.e., sulphidic) conditions (Morford and Emerson 1999; Morford et al. 2005; Tribovillard et al. 2006; Algeo and Maynard 2008; Algeo and Tribovillard 2009). The characteristic redox pathways make the enrichment of these two metals relative to one another an excellent geochemical tool in basin analysis.

Although most of the systematics for the redox behaviour of Mo and U have been worked out using a combination of modern redox-sensitive basins and Paleozoic shales, the basic principles of their behaviour should be similar for iron formation environments. Due in large part to the limited number of modern analogues for an iron-rich basin (e.g., Crowe et al. 2008b; Mikucki et al. 2009), the behaviour of these metals must be extrapolated from these other, better understood systems. Although several factors may directly influence their fixation rates, chiefly the generation of large volumes of iron oxy-hydroxides (Tribovillard et al. 2006), our working hypothesis is that, the behaviour, and more importantly the relative ratios of the deposited metals, would not be significantly affected.

The role of Mn and Fe oxy-hydroxides in the fixation of Mo is fairly well documented (e.g., Algeo and Tribovillard 2009; Goldberg et al. 2009). Due to the ability of Mn-oxides, and to a much lesser degree, Fe-oxides, to scavenge the molybdate ion from oxic seawater, a strong relationship between these metals, especially in iron formation, may indicate Mo enrichment without euxinic conditions; a strong correlation would suggest that increased Fe deposition

controlled Mo fixation rather than changes in the redox conditions of the basin. The lack of any strong correlation between Mo and Fe₂O₃ (Fig. 2.9A), across the full range of compositions, demonstrates that iron deposition rates were not a limiting factor in Mo enrichment, although the development of a correlation in mid-range concentrations of both Mo and Fe₂O₃ suggests that an iron particulate shuttle was an important but not limiting factor. Furthermore, Mo shows no correlation with MnO (Fig. 2.9B), essentially eliminating the possibility of a particulate shuttle that fixed Mo as molybdate, and that some free H₂S was needed to drive Mo fixation. Although it could be argued that a Mn-oxide was still the driving factor in Mo shuttling across a redoxcline through subsequent Mn-reduction, dissolution, and Mo release in anoxic bottom waters (e.g., Algeo and Tribovillard 2009), such a possibility can be eliminated because of the absence of a positive Ce anomaly, as discussed above. The high reactivity of Mo-S compounds allows easy adhesion to clay particles, organic material, or even amorphous silica colloids, as well as to the more widely discussed Fe-oxides. All of these, in varying amounts, would have been significant components of any particle shuttle operating during the deposition of the Rapitan iron formation.

One of the limitations commonly faced when using redox-sensitive trace metals as paleoredox proxies is that detrital sediment supplied to the basin can mask the concentrations contained in authigenic phases. Several approaches have been employed to address this issue, most commonly the normalisation of the metal of interest to Al, expressed as the [metal]/Al ratios (e.g., Morford and Emerson 1999; Lyons et al. 2003; Cruse and Lyons 2004; Tribovillard et al. 2004). The same approach has also been applied using other immobile trace elements, such as Th (e.g., Meyer et al. 2008; Pollack et al. 2009). Such straightforward correction fails to illustrate properly the true degree of authigenic enrichment in many sediments (Van der Weijden 2002). For example, although Th is of great utility when assessing U, due to their strong relationship, it becomes ineffective when comparing the enrichment of U to a metal with dissimilar behaviour, such as Mo, thus necessitating the use of an element whose behaviour differs from that of both Mo and U. Simple Al normalisation can also produce inaccuracies if the sediment contains a very small detrital component or exceedingly low Al concentrations relative to other immobile elements, such as Ti (e.g., Tribovillard et al. 2006). An alternative approach is double normalisation to a shale standard and an immobile element (e.g., Van der Weijden 2002; Meyer et al. 2008; Algeo and Tribovillard 2009). Such an approach can establish the degree of

enrichment over crustal averages, expressed as unitless ‘enrichment factors’ as described, for example, by Algeo and Tribovillard (2009). These calculations most commonly use Al as the detrital proxy, and the Post-Archean Australian Shale (PAAS) of Taylor and McLennan (1985) as the shale standard. The standard used in the present work is MuQ (Kamber et al. 2005), because it, unlike shale, provides an upper-crustal average that has not been influenced by diagenesis. The original alluvial sediment dataset from which MuQ was calculated lacks Mo data, but this has been supplemented with a much larger, new dataset for similar alluvial sediment, with an average Mo content of 485.3 ppb from Marx and Kamber (2010). Aluminum is used as the proxy for the detrital component because it demonstrates a hyperbolic correlation with both Mo and U, whereas other immobile elements (e.g., Sc, Ti, Ga, Zr, Nb, Th) were less consistent in this regard. Several of the other possible normalisers were rejected for reasons such as strong correlations with U, but not Mo (Zr, Th), unusually high Nb/Ta ratios, and commensurately strong correlations between Ti and both Nb and Ta, suggesting that these three elements are controlled by the same mineral phases in this depositional environment. Both U and Mo show weak relationships with loss on ignition (when available), indicating that neither is strongly related to low-Al phases such as carbonate or organic carbon, which also addresses the concerns expressed by Van der Weijden (2002) regarding Al normalisations.

The enrichment factors of several metals are plotted against stratigraphy in Figure 2.10. Each of these metals (Mo, U, W) shows distinct stratigraphic variation relative to the others. Mo and U do not show strong covariance with respect to stratigraphy, and U enrichment, although somewhat variable, averages to a fairly constant low enrichment throughout the section. This is to be expected, because U is removed from the water-column at steady rates under anoxic conditions, and would show sustained changes in its authigenic enrichment only during intervals of oxicity. Therefore, it can be inferred that anoxic bottom-water prevailed for the duration of iron formation deposition. Molybdenum is most strongly enriched in the lowermost and uppermost parts of the iron formation stratigraphy. This distribution indicates sulphidic (euxinic) conditions were present in the water column during deposition of strata at the base and top of the iron formation, but were absent during the middle of the depositional interval, where Mo enrichment is closer to presumed background levels.

The aqueous behaviour of W under reducing conditions is poorly understood (Johannesson et al. 2000; Seiler et al. 2005), but its systematics in the studied Rapitan section are included here to show that it demonstrates transitional behaviour between Mo and U. The relationship between Mo and W in numerous other systems, including microbiology, is well documented (Kletzin and Adams 1996; Arnórsson and Óskarsson 2007). The biogeochemical behaviour of these elements is also known to be somewhat similar to that of V, another redox-sensitive trace metal (Johannesson et al. 2000). Under oxic conditions, W behaves very much like Mo, but it does not react with H₂S under euxinic conditions (Arnórsson and Óskarsson 2007). This apparent resistance to forming sulphides, despite the similarity of the valence states of W and Mo, may help to explain why the stratigraphic distribution of W enrichment is transitional between that of Mo and U. Caution must be used in applying this insight, however, until the aqueous redox behaviour of this metal is better constrained.

The distinct redox behaviours of Mo and U makes plotting these two elements against one another of great utility for evaluating basinal redox conditions and basin configuration. This can be done most effectively using their enrichment factors (Fig. 2.11). The relatively tight clustering and well-developed trend demonstrates the effectiveness of this approach, as compared to plots of absolute Mo vs. U concentration, which show considerable scatter in a broad, fan-shaped array. The trend formed by the enrichment factors rises with a steep slope from the origin with relatively little deviation. Many other redox-sensitive elements, including W, Ni, Co, Sb, and Pb, are similarly correlated with either Mo or U, although V does not correlate with either element. Reconstruction of the Rapitan basin in the following section will focus on the established correlation between Mo and U and the REE+Y systematics, because their behaviour in the modern setting is well understood.

2.7 Basin Reconstruction

Using MO_{EF} vs. U_{EF} covariance plots, Algeo and Tribovillard (2009) were able to distinguish three types of modern redox-sensitive basin: (i) zones of marine upwelling and high primary productivity (e.g., eastern tropical Pacific); (ii) highly restricted basins (e.g., Black Sea); and (iii) partially restricted, silled basins (e.g., Cariaco Basin). Each of these basin types develops

a distinct Mo_{EF} vs. U_{EF} trend that is controlled by a combination of the redox stratification and evolution of the basin, the degree of connectivity with the open ocean, and the refreshing rate of the basinal waters.

2.7.1 Highly restricted basins

The most distinctive of the three modern basin types, the highly restricted Black Sea, typically forms Mo_{EF} vs. U_{EF} trends that are flat overall, showing greater U enrichment over Mo, although at near-constant elevated Mo enrichment. This is because such highly restricted basins develop long-term, persistent euxinia at depth, which promotes the reduction of molybdate to thiomolybdate, and thus elevates Mo removal rates from seawater. Over time, a reservoir effect develops, in which Mo, through prolonged draw-down in the euxinic parts of the basin, becomes supply-limited. This effect also implies pronounced basin restriction that limits mixing of the basin water with the open ocean to only the shallowest water depths, and even then with only limited water-mass exchange. In contrast, U does not develop a significant reservoir effect because of its steady fixation rate, and it continues to be enriched well after the Mo supply has been depleted. This allows for the development of flat Mo_{EF} vs. U_{EF} trends with somewhat elevated Mo enrichment (Algeo and Tribovillard 2009) (Fig. 2.11, BS). The much steeper slope shown in the Rapitan samples indicates that the Rapitan basin was not nearly as restricted as the modern Black Sea. A highly restricted basin was already considered unlikely based on the REE+Y data, which indicate considerable connectivity with the open ocean, showing consistently elevated Y/Ho ratios, positive Gd/Gd* values, and a strongly developed positive REE slope overall.

2.7.2 Zones of upwelling and high productivity

At the other end of the spectrum are open-marine settings characterised by deep-water upwelling that causes high primary productivity near the top of the water column, such as in the eastern tropical Pacific along the western coasts of North and South America. Nutrient-rich deep water is upwelled into the photic zone in these areas, creating a bloom in biological activity. This increased productivity results in prolific export of organic material to the seafloor, the decomposition of which causes anoxic conditions to develop in sediment pore waters and, rarely, in seawater just above the sediment-seawater interface (e.g., Morford et al. 2005; Pattan and

Pearce 2009). Uranium is commonly markedly over-enriched relative to Mo in sediment from these areas, because suboxic to anoxic bottom and pore waters are sufficient to cause its enrichment. Water-column euxinia is rare in these zones, because O₂-deficiency is generally limited to pore waters, where it is not sufficient to promote Mo removal from the water column. The combined effect leads to shallow slopes on Mo_{EF} vs. U_{EF} diagrams for most sediment deposited in these environments (Algeo and Tribovillard 2009) (Fig. 2.11, ETP). These trends are different from that of the Rapitan iron formation. In the rare occurrence of water-column euxinia in an upwelling zone, steep Mo enrichment can develop, but the steep trend in such a situation would trend away from already elevated U enrichment levels due to persistent U enrichment in all conditions, whereas the trend discovered in this study extends from the origin. This suggests that the Rapitan basin was probably not a zone of oceanic upwelling and high productivity. The REE+Y patterns also suggest a degree of restriction in the system, which is inconsistent with this type of redox-sensitive marine area. Consequently, a basin as open to the global ocean as this can be eliminated from consideration for the Rapitan basin.

2.7.3 Silled basins

The third type of redox-sensitive environment is a partially restricted, ‘silled’ basin, such as the Cariaco Basin off the Caribbean coast of Venezuela. This basin type features a deep-water depression protected by a series of bathymetric highs (“sills”), that limit mixing of the deepest waters of the basin with the open-marine realm, while allowing most of the water column to remain well-mixed with the open ocean (Lyons et al. 2003). Silled basins are distinct from Black-Sea-type basins because the latter are almost completely cut off from the open ocean at depth, and experience only limited exchange of surface waters, whereas silled basins have full connectivity at all but the deepest parts of the basins (Fig. 2.12A). If a pronounced redoxcline is established, silled basins can develop long-term euxinia in their bottom waters, which allows for the fixation of Mo through the generation of Fe-Mo-S compounds of variable stoichiometry (Helz et al. 2011). Unlike the Black Sea, however, the high connectivity of the upper parts of the water column helps prevent Mo exhaustion, because the metal budget of the euxinic bottom waters can be maintained through slow exchange across the redoxcline, episodic spillover of extrabasinal ocean water, or a Mn/Fe particulate shuttle. The nearly constant Mo supply in these systems allows for steep Mo enrichment relative to U, which is fixed at the same rates as in any

other redox-sensitive basin (Algeo and Tribovillard 2009) (Fig. 2.11, CB). The steep slopes in the Mo_{EF} vs. U_{EF} covariance plots generated by modern basins of this type is closely mirrored by the slope defined by the Rapitan iron formation, indicating that the Rapitan basin may have been similarly silled. The REE+Y systematics, which also indicate a hybrid source of dissolved species, further support this basin type.

The basin configuration emerging from the geochemical data is consistent with the basinal architecture that was established using sedimentological and stratigraphic evidence. The Rapitan Group was deposited in an incipient rift basin (Yeo 1981; Eisbacher 1985), a dynamic tectonic setting that is capable of producing bathymetric sills, such as the uplifted edges of graben systems. The geologically ephemeral tectonic regime of a rift system could also limit the longevity of the silled basin through continued rift subsidence. This may help to explain why iron formation was deposited during only a brief stage of Rapitan Group deposition, and why thick iron formation is of limited geographic extent. It also helps explain why the Rapitan Group is divided into a series of sub-basins across the Mackenzie Mountains (Yeo 1981). The limited distribution of iron formation within each sub-basin also conforms to the typical view of rift systems, which commonly consist of a series of topographic lows that are not necessarily well interconnected.

2.7.4 Nature of the redox chemocline

A drawback of using the modern silled basin model for the Rapitan basin is that one of the most important processes in such basins today is the role of a Mn-oxide particulate shuttle. In the modern Cariaco Basin, apart from intermittent spillover of water from the open ocean into the basin, the principal mechanism for the transport of Mo and other metals into the euxinic zone is through Mn redox cycling (Algeo and Tribovillard 2009). In modern basins, the oxidation of dissolved Mn^{2+} to Mn oxy-hydroxides occurs in the oxic zone. Molybdate ions readily adsorb to Mn oxides, providing the primary mechanism for Mo removal from oxic seawater (Morford and Emerson 1999; Morford et al. 2005; Tribovillard et al. 2006). In a stratified basin in which the upper water column is well connected to the open ocean, Mn oxides would readily form in the upper water column, but would re-dissolve upon settling below the redoxcline into more reduced waters, releasing all adsorbed material such as Mo and Ce. This process keeps the metal supply in

these basins almost constant, and can lead to over-enrichment of some metals in the anoxic bottom waters (Algeo and Tribovillard 2009; Planavsky et al. 2010a). Strong evidence against this process is present in the Rapitan basin: one of the characteristic signs of this process is a positive Ce anomaly, a phenomenon documented in some late Paleoproterozoic iron formation and in bottom-waters from modern redox-sensitive basins, but not present in the Rapitan, where normalised Ce is either flat or shows a slight negative anomaly. The absence of a Mn shuttle does not preclude the silled basin model: the oxidation of dissolved Mn^{2+} to Mn oxy-hydroxides is common in modern settings, but, due to the complexities of the redox and chemical state of the Neoproterozoic ocean, may not have been in effect at that time.

An iron particulate shuttle across an oxic-ferruginous redoxcline was probably in operation in the Rapitan basin, as opposed to a Mn-oxide shuttle. This process would not generate a positive Ce anomaly, but would allow for a nearly constant marine metal budget in the suboxic to anoxic water masses. Redox stratification of the basin during deposition of the Rapitan iron formation was a critical component of the classic depositional model of Klein and Beukes (1993). The nature of the redox stratification in that model is, however, overly simplistic. Given that significant Mo enrichment relative to U requires at least mildly euxinic conditions, it can be inferred that the Rapitan basin had at least three different water masses, defined by their redox conditions. Euxinic water in the basin would have been, by necessity, quite limited in extent. In order to generate large volumes of ferric iron oxides (hematite or its precursors), much of the basin, including the bottom waters, must have been under ferruginous conditions and transitioning towards oxic conditions, because pervasive euxinia would promote the formation of pyrite and inhibit the build-up of sufficient dissolved ferrous iron to generate iron formation. Consequently, the Rapitan basin was highly redox-stratified, and probably consisted of oxic surface waters, highly ferruginous deep waters (iron enrichment of sufficient levels to form large iron formations), and intermittent, weakly euxinic middle water depths. This type of stratification differs strongly from most modern redox-stratified basins, such as the Black Sea and Cariaco Basin, and more closely resembles ferruginous lakes, such as Lake Matano, Indonesia (Crowe et al. 2008b), of which there are far fewer modern examples.

2.7.5 Nature of the sill

A major difference between the Rapitan and Cariaco basins, besides the established redox water column stratigraphy, is the largely unknown influence of ice cover. Capping of the ocean by thick sea ice, as would have been the case in the classic model for snowball Earth (e.g., Kirschvink 1992; Hoffman et al. 1998; Hoffman 2009), plays a major role in the BIF model of Klein and Beukes (1993). Evidence for the presence of glaciers and either sea ice or an ice shelf is present throughout the Rapitan Group, in the form of diamictites and abundant dropstones in the iron formation. The full scope of the influence of sea ice on the redox stratification in a Neoproterozoic basin remains to be fully explored. Currently, the most detailed proposal hypothesises that prolonged ice cover would promote stagnation and the buildup of dissolved ferrous iron in the basin waters (e.g., Klein and Beukes 1993). Furthermore, in a modern example of sub-glacial stagnation from Antarctica, in the McMurdo dry valleys, strong redox stratification develops in some of the sub-glacial lakes. There, the REE+Y evidence points towards a Mn particulate shuttle, as demonstrated by positive Ce anomalies observed at depth (De Carlo and Green 2002). Other basins in the region have developed high concentrations of dissolved ferrous iron, primarily through anaerobic bacterial activity and complete isolation from the atmosphere and ocean, and have been suggested as possible analogues to Neoproterozoic basins that contain iron formation and glaciogenic siliciclastic rocks (Mikucki et al. 2009). These modern examples are imperfect analogues, because they are lakes, not restricted oceanic basins, but they do help to demonstrate that glacial ice can induce water column stratification and redox stagnation.

The redox stratigraphy of modern basins is maintained through the formation of hydrological barriers that are generally independent of the redox state of the basin. These are most commonly temperature gradients (thermocline) and salinity gradients (halocline). These features commonly occur together, as is the case in the Cariaco basin, where colder, more saline water underlies a combined halo- and thermocline that forms the barrier between oxic and anoxic water (Lyons et al. 2003). Either of these features is easily formed in a glaciomarine environment, where glacial outwash injects cold, fresh water into the basin, commonly contributing to the formation of either a thermo- or halocline (although such a system would be associated with clastic sedimentation that would inhibit the deposition of chemogenic iron formation). This process could allow for the development of glacially triggered water-column

stratification, which, when coupled with basin restriction, would aid in preservation of strong redox stratification of the water column, and greatly inhibit mixing and dilution of distinct basinal water masses.

In order to maintain long-lived redox stratification in a basin, physical barriers between the deeper basin water and the open ocean are needed. As discussed above, active movement along normal faults (Helmstaedt et al. 1979) during Rapitan deposition associated with early rift formation could easily have generated a well-defined sill along the rift margin. Furthermore, because there was active subsidence and rifting, continued movement along the normal faults would maintain accommodation space in the basin over much longer intervals, and would prevent the basin from shallowing and gradually increasing its overall degree of connectivity to the open ocean.

2.7.6 A new model for Neoproterozoic iron formation

The presence of ice-transported sediment in the Rapitan basin clearly limits the extent to which the Cariaco-type silled basin model can serve as an analogue for the Neoproterozoic, because sea-ice has the ability to isolate the system from the atmosphere and possibly from the open ocean. Any proposed model for the Rapitan basin must therefore consider the effect of ice. A bathymetric sill, formed by a hanging-wall block, is without question capable of creating a partially restricted basin. The structural and sedimentological evidence for a rifted graben environment also helps to explain the geographically variable thickness of iron formation throughout the Rapitan Group exposure area. However, the relative roles of ice-capping versus bathymetric sill in promoting the buildup of sufficient iron to deposit the thick iron formation unit of the Snake River region are difficult to assess.

Here we envisage a silled basin that, during extended intervals of ice-cover and concomitant sea-level lowstand, would have been isolated from the atmosphere and restricted from the open ocean (Fig. 2.12B). At times, the basin could have been completely isolated from the ocean, when the thick ice shelf was grounded on the sill at the outboard edge of the basin. Isolation from the atmosphere, as well as inhibition of photosynthesis due to ice cover, would have resulted in the rapid drawdown of free oxygen in the shallow water column, allowing ferruginous conditions, already prevalent in the deep basin (e.g., Johnston et al. 2010), to become

the dominant redox state at all water depths (Fig. 2.12B). During this time, large amounts of clastic material would have been introduced to the basin through sub-glacial outwash, generating fine-grained turbidite deposits. In our model, this is the setting in which the turbidite-dominated Sayunei Formation (Yeo 1981) was deposited. In addition to clastic sediment, there would have been a small supply of dissolved sulphate generated through oxic weathering of sulphide-bearing rocks and mechanical weathering of sedimentary sulphates under the wet-based glacier. Due to low productivity levels, the dissolved sulphate would have gradually built up to saturation levels, causing the precipitation of small amounts of sulphate minerals, such as glauberite (now preserved as dolomite pseudomorphs), within clastic strata (Young 1976). In addition to clastic material and sulphate, glaciers have been documented as the dominant iron supply to the modern open ocean (Raiswell et al. 2006). Thus, it can be envisaged that highly reactive ferric iron oxy-hydroxide nano-particles such as lepidocrocite (Fe_{nano}), which are both readily bioavailable and easily reduced and dissolved under ferruginous marine conditions, were supplied by the ice sheet (Fig. 2.12B). Iron-reducing bacteria have been documented in modern ice-capped, restricted basin settings, such as Blood Falls, Antarctica (Mikucki et al. 2009), where they reduce these particles to ferrous iron while auto-recycling sulphur and carbon, allowing for minimal organic carbon burial and H_2S production. Prolonged intervals in which such microbially mediated iron reduction was taking place would have enabled the buildup of enough dissolved iron in the basin to eventually form the large iron deposits of the Snake River region. Additional iron could also have entered the basin through limited exchange with ferruginous seawater from the deep open (Fig. 2.12B).

Upon glacial retreat and subsequent sea-level rise, the iron-rich basin waters would have become simultaneously exposed to both atmospheric oxygen and sunlight (Fig. 2.12C). Due to the relatively high concentration of nutrients, such as Fe^{2+} , and SO_4^{2-} , that had been able to build up in the basin during ice cover, primary productivity in the upper water column would have exponentially increased, resulting in the rapid sequestration of large volumes of organic carbon in shallow to middle water depths. Burial of this carbon, combined with the elevated dissolved sulphate concentrations in the water column, would have enabled bacterially-mediated sulphate reduction (BSR) to generate sulphidic conditions in deeper shallow to median depth water, generating a euxinic wedge that migrated outwards from the lower shelf to upper slope. This

condition is similar to what has been proposed in several recent models for other intervals in the Paleo- and Neoproterozoic (e.g., Johnston et al. 2010; Li et al. 2010; Poulton et al. 2010; Poulton and Canfield 2011).

During times of maximum BSR, the euxinic wedge would extend far out into the basin along the chemocline between oxic surface waters and ferruginous deep water. It is unlikely that this wedge would ever have been strongly euxinic, due to the large amount of Fe^{2+} in the water column, which would have generated large quantities of iron sulphides and quickly exhausted the supply of dissolved H_2S . Importantly, however, strong euxinic conditions may not be necessary for Mo fixation. According to new models for Mo fixation, strong Mo removal under euxinic conditions can occur at much lower H_2S concentrations than previously suggested, through the formation of FeMoS compounds in lieu of the generation of thiomolybdates, as is the traditionally accepted mechanism for Mo fixation in euxinic environments (Helz et al. 2011). In this model, Mo removal from the water column is primarily dependent on the availability of ferrous iron and pH, with dissolved H_2S merely needing to be present to remove dissolved MoO_4^{2-} from the water column. It has been suggested that Mo fixation can be driven by iron removal alone (Crowe et al. 2008a), but in that example the zone of strongest Mo removal corresponds with that of the highest concentrations of H_2S . When applying these new findings to our model for the Rapitan iron formation, we propose that FeMoS compounds would have been shuttled from the euxinic wedge in middle water depths by newly oxidised iron oxy-hydroxides that had formed through the upwelling of dissolved ferrous iron into the oxic surface waters and its subsequent oxidation (Fig. 2.12C). The iron supply to the basin would be quickly drawn down through the progressive oxidation of the water column, although there may have been continued refreshment of dissolved Fe^{2+} through either upwelling of non-hydrothermal iron from deep waters outboard of the sill, or through the continued supply of Fe_{nano} into the basin by the combination of glacial outwash and icebergs (Raiswell et al. 2006), whose presence can be inferred from the abundant dropstones in the iron formation (Fig. 2.12C). Larger iron resupply events would have happened during colder times in which persistent sea ice, or potentially ice shelf re-advance, caused the basin to become isolated from the atmosphere again, which may be recorded by the thin interbeds of siltstone in the iron formation.

It is important to note that the basin configuration and water chemistry during deposition of the ferruginous clastic rocks of the Sayunei Formation and the chemogenic iron formation may not have been dramatically different; the main or only difference may have been the supply rate of clastic sediment. The turbiditic rocks of the lower Sayunei Formation have a very high Fe content (average 12.4 wt% Fe₂O₃; Yeo 1981), but clastic supply was very high. By contrast, in order to deposit true iron formation, clastic sedimentation had to be nearly or completely shut off in the deep basin (Klein and Beukes 1993). Here we envisage that due to the sea-level highstand that followed glacial retreat, much of the clastic sediment deposited in the proglacial environment would have been trapped in shallow water on the upper shelf (Fig. 2.12C). The combination of rising sea level, isostasy, and subsidence along rift-margin normal faults would prevent significant volumes of clastic material from reaching the deep basin. Consequently, with the exception of the delivery of coarse material into the basin in the form of ice-rafted debris, dropstones, and infrequent, brief episodes of silt and fine sandstone deposition (distal turbidites), chemical sedimentation would dominate in the deep basin, allowing for the formation of large volumes of 'true' hydrogenous iron formation. The most probable cause for the termination of iron formation deposition is therefore the loss of accommodation space. As other authors have reported, the top of the iron formation locally contains granular iron formation (GIF), which is evidence of shallow-water deposition (Klein and Beukes 1993), and is overlain by ferruginous glacioclastic rocks. This suggests that although the dissolved iron supply locally remained high well after the end of iron formation deposition, shallowing water, and eventually clastic sedimentation, drove the cessation of hydrogenous iron formation deposition.

2.7.7 Oxidation state of the Neoproterozoic open ocean

The REE+Y patterns in the Rapitan iron formation are a combination of open-marine and local (LREE-enriched) sources. The strong correlation of REE+Y features is not a function of terrigenous contamination but probably reflects varying importance of the two major dissolved REE+Y sources to the basin. The data thus suggest variable connectivity with the open ocean. The most surprising finding in this regard is the absence of a positive Eu anomaly in most Rapitan samples. If, as is widely postulated, the late Neoproterozoic deep ocean was sulphidic or ferruginous, it would clearly be expected that high-temperature hydrothermal vent fluids would have imparted a positive Eu anomaly to the ocean water. However, the Rapitan iron formation

lacks such an anomaly, suggesting that the open ocean may already have been quite well oxygenated by the late Neoproterozoic.

The few other published REE patterns for Neoproterozoic iron formations (e.g., Lottermoser and Ashley 2000; Klein and Ladeira 2004) from different localities (e.g., South Adelaide Geosyncline, South Australia; Urucum district, Brazil) also lack evidence for positive Eu anomalies, although this is not readily evident in those studies due to incomplete REE data. The missing anomaly is significant. According to the widely cited theory that for most of the Proterozoic, the deep ocean was sulphidic (i.e., stagnant Meso- to Neoproterozoic ocean), hydrothermally sourced iron would be expected to be removed from the water column through the formation of pyrite (Canfield 1998), and the REE would remain dissolved (Bau and Dulski 1999). Sequestration of REE into pyrite would be unable to match the dissolved hydrothermal REE flux into the ocean, and so the ocean as a whole would carry a significant positive Eu anomaly, as did the Archean ocean, for which this phenomenon is well established. Similarly, widespread ferruginous conditions in the open ocean would also preserve the Eu anomaly, because hydrothermal REE would stay in solution as long as the iron did, suggesting that even suboxic, ferruginous conditions in the Neoproterozoic open ocean were implausible. The absence of the Eu anomaly requires widespread oceanic ventilation at the time of Rapitan Group deposition. This conflicts with Mo concentration data from black shales, which remained very low until *after* the Neoproterozoic glaciations (Scott et al. 2008). The information from the REE and from Mo are mutually inconsistent and will require better study of the elemental supply to Neoproterozoic iron formations and further studies of Neoproterozoic black shale.

2.8 Summary

High-quality trace element analyses of jasper samples from the Rapitan iron formation enable detailed reconstruction of the depositional basin and oceanic conditions. The REE+Y demonstrate that although the basin maintained a considerable degree of water-mass exchange with the open ocean, local REE+Y sources also supplied a significant flux of dissolved load from geologically localised and chemically distinct sources. Collectively, this indicates some degree of basin restriction. The near-absence of the Eu anomaly shows that the open ocean was not only

Eu-deficient, but that hydrothermally sourced Fe was not important for the Rapitan iron formation, indicating instead that the primary iron source may have been glacially sourced iron oxy-hydroxide nano-particles that were subsequently bacterially reduced under ferruginous conditions. Evidence from Mo and U suggests that the basin was partially restricted (silled), which is consistent with evidence obtained from the REE+Y. Although the traditional model for silled basins cannot be applied to the Rapitan iron formation without modification, due to the presence of glacial ice, an alternative model proposes prolonged ice-capping of a silled basin, which allowed for the development of strongly ferruginous conditions. Upon ice retreat, this iron-rich basin would be gradually oxidised from above, triggering high primary productivity and eutrophication on the deep shelf and upper slope, establishing a weakly euxinic wedge in middle water depths. Oxidation of upwelling dissolved ferrous iron into ferric iron oxy-hydroxides would provide a shuttle for FeMoS compounds during the intervals of most persistent euxinia, causing Mo enrichments of over an order of magnitude greater than background levels.

This new model for the configuration of the Rapitan basin and depositional controls on the iron formation suggest that the Neoproterozoic open ocean was at least partially oxygenated, inhibiting the long-distance transport of Eu. Oceanic ventilation is not compatible with the sulphidic Proterozoic ocean model, nor is it compatible with newer models for a ferruginous Proterozoic deep ocean. Furthermore, the close analogies drawn between Archean-Paleoproterozoic iron formation and Neoproterozoic examples, and *vice versa*, are inappropriate, at least when discussing the iron source.

2.9 Acknowledgements

This paper is NTGO contribution 0052. This project was funded by the Northwest Territories Geoscience Office (NTGO) and the Yukon Geological Survey (YGS). Additional substantial funding was from NSERC Discovery Grants to B.S. Kamber and E.C. Turner, as well as a SEG- Foundation student research grant to G.J. Baldwin. The authors would like to thank E. Martel, C. Ozyer, J. Ketchum and H. Falck of the NTGO. J. Chakungal and V. Bennett of the YGS are also thanked for their insight in the field. Chevron Canada Ltd. is thanked for granting access to the Crest iron deposit. The handling editor M. Colpron, as well as journal reviewers

P.W. Fralick and F.A. Macdonald are also thanked for their helpful comments and reviews. Field assistance was provided by T. Chevrier, H. Ngo, and K. Medig. Thanks also go to A. Gladu and J. Petrus of Laurentian University for their assistance with sample preparation and analysis. L. Griffiths is thanked for performing the standard addition experiments. N. Elwaer and N. Chrétien of the Ontario Geolabs are thanked for their work in obtaining major element XRF data.

2.10 Figures

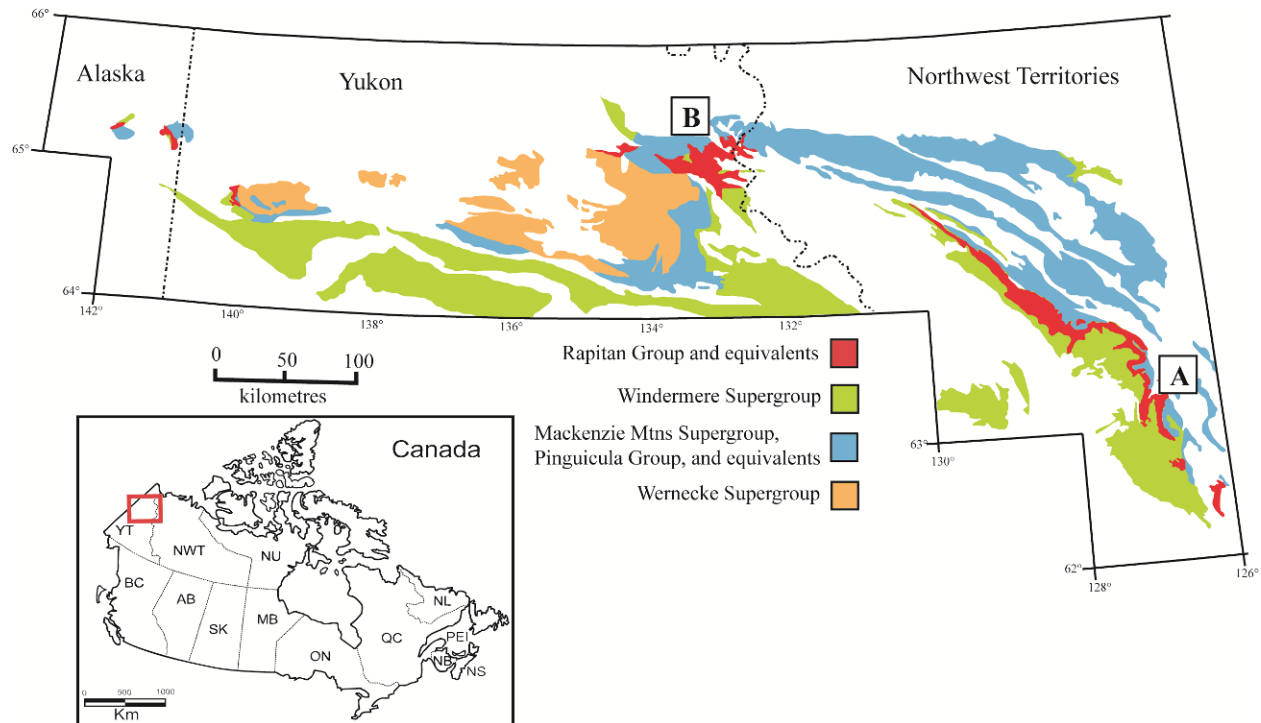
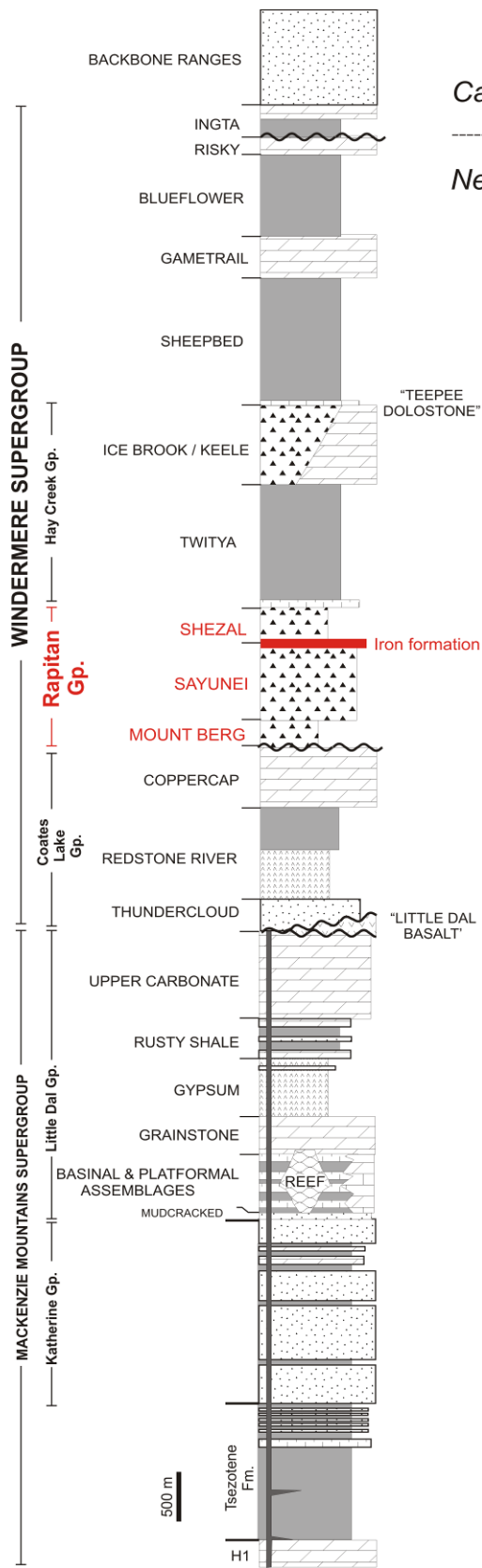


Figure 2.1: Geological map of the approximate distribution of Proterozoic strata of northwestern Canada and eastern Alaska. Inset map shows the location of the geological map. The Rapitan Group and its equivalents in the Ogilvie Mountains (western Yukon and eastern Alaska) are in red. The Redstone River region (A) and the Snake River region (B) are indicated (modified from Yeo 1981).



Cambrian

Neoproterozoic

Figure 2.2: Generalised Neoproterozoic stratigraphy of the Mackenzie Mountains, Northwest Territories and Yukon, showing the stratigraphic position of the Rapitan Group in the Windermere Supergroup and its position relative to the older Mackenzie Mountains supergroup and the Neoproterozoic-Cambrian boundary.

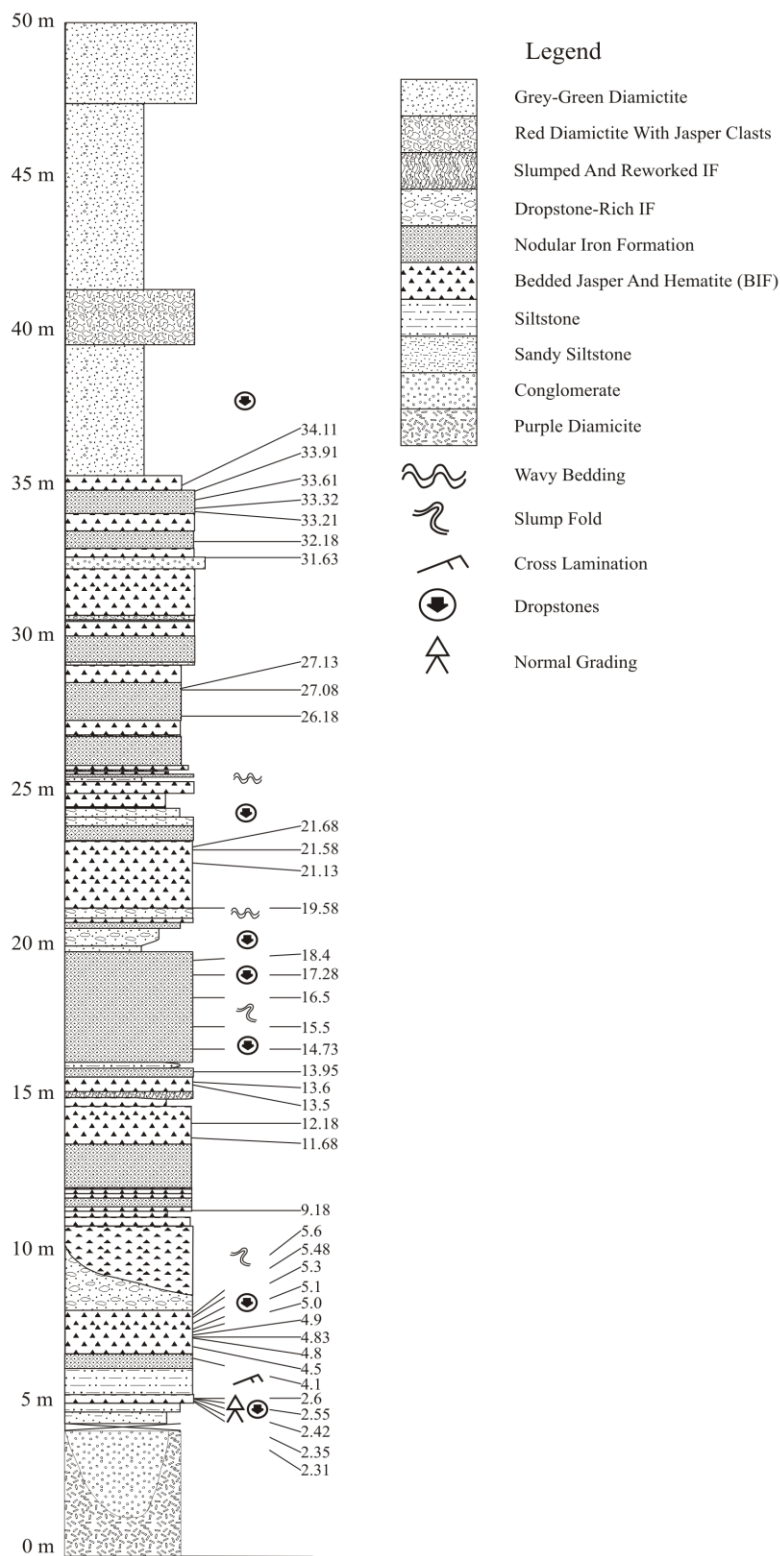


Figure 2.3: Stratigraphic column of the Rapitan iron formation at Cranswick River, NWT. Inset map shows location of measured section (star) in the Mackenzie Mountains, Northwest Territories, Canada. Sample numbers that correspond with stratigraphic position are located on the right side of the column. Lithofacies listed in the legend correspond to those referred to in the text.

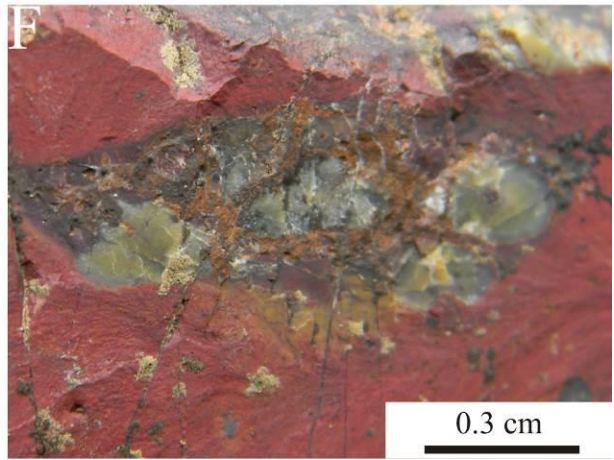
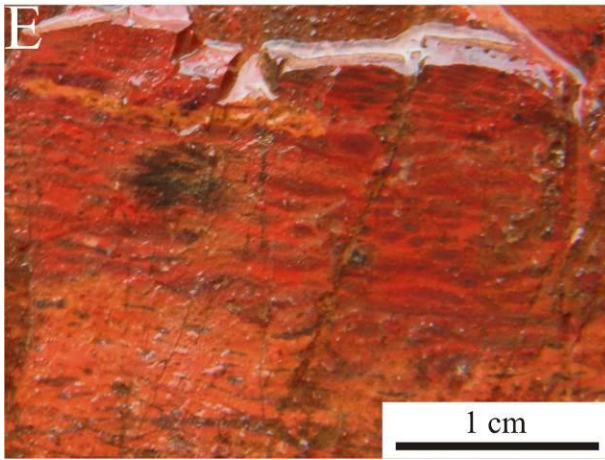
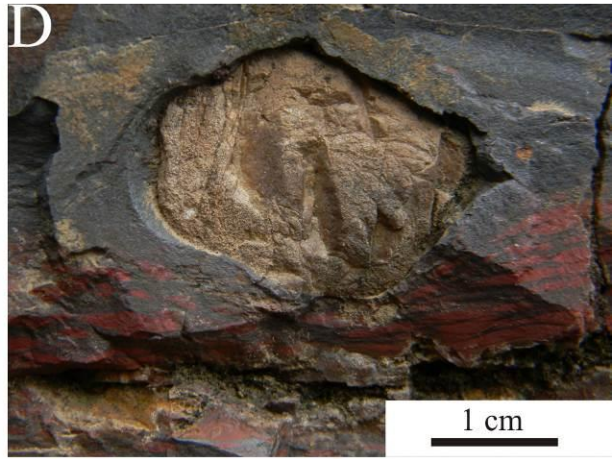
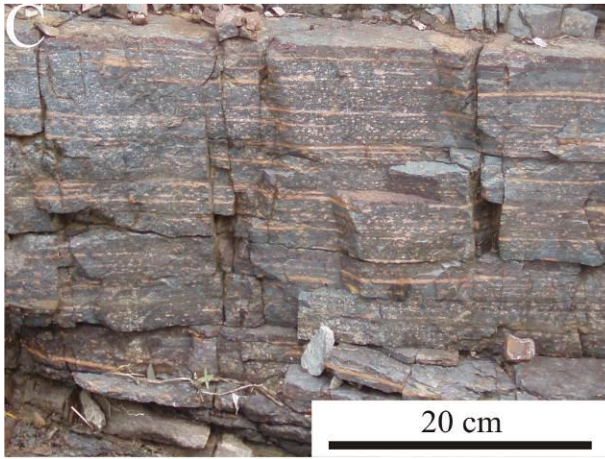
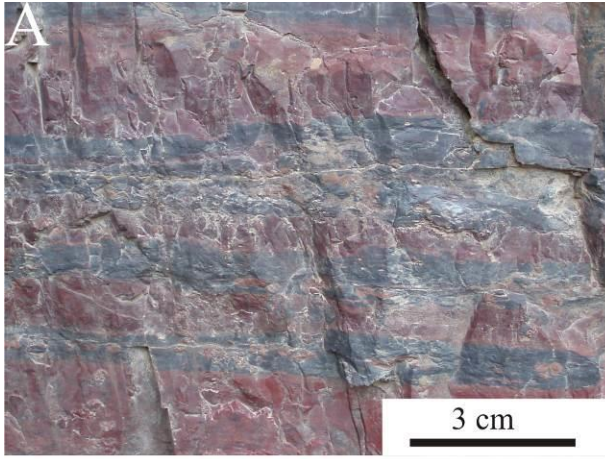


Figure 2.4: (A) Typical bedded jasper and hematite ‘BIF’ that was the primary sampling target. (B) Zoned jasper nodules are ubiquitous in the Rapitan iron formation, here in a matrix of massive hematite. (C) Elongate, lenticular nodules, or ‘lenticles’ in a thick package of hematite and nodules with very few true jasper bands. (D) Dropstones, predominantly of resedimented carbonate clasts, deform only a maximum of a few millimetres of underlying sediment. (E) Jasper nodules can also be hosted in jasper bands, a potential hazard when sampling for geochemical analysis. (F) Grey-green chert nodules are present only in the uppermost jasper band of the iron formation.

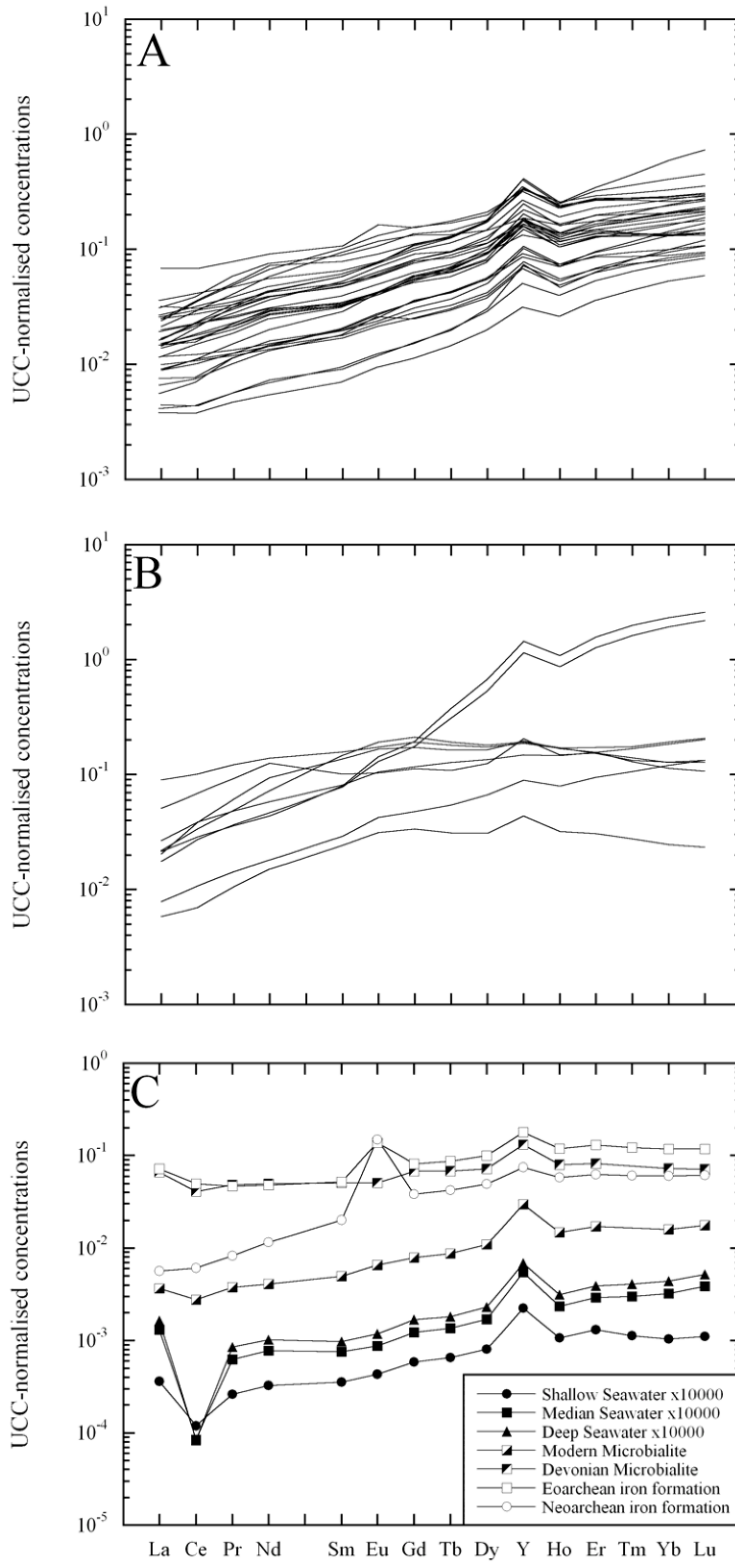


Figure 2.5: Shale-normalised REE+Y diagrams of jasper samples from the Rapitan iron formation. (A) Most of the samples (n=34) demonstrate fairly uniform, consistent, seawater-type patterns with pronounced positive slopes, small negative to flat Ce anomalies, positive Gd anomalies, and superchondritic Y/Ho ratios. (B) Nine other samples show non-seawater-type REE+Y patterns, commonly with unusual patterns that have not been interpreted, and have accordingly been eliminated from further discussion. These nine samples are identified in Table S2. (C) Compilation of REE+Y data for seawater and hydrogenous sedimentary rocks through time. Modern shallow, median, and deep seawater compiled by Kamber (2010), showing deep negative Ce anomalies and positive La, Gd, and Y anomalies. Modern (Webb and Kamber 2000) and Devonian (Nothdurft et al. 2004) microbial carbonates show positive La and Y anomalies with small negative Ce anomalies. Eoarchean (Bolhar et al. 2004) and Neoproterozoic (Baldwin et al. 2011) iron formation also show positive La, Gd, and Y anomalies, but without statistically significant Ce anomalies, and with pronounced positive Eu anomalies, showing that these (Ce/Ce^* and Eu/Eu^*) are the only attributes of the REE+Y systematics of seawater that have changed significantly over Earth history. Comparison of the patterns in (A) with those in (C) demonstrates that they record the REE+Y composition of seawater that has remained largely unchanged throughout Earth history, and are thus the most appropriate samples to include in a study of the basinal seawater chemistry of the Rapitan iron formation.

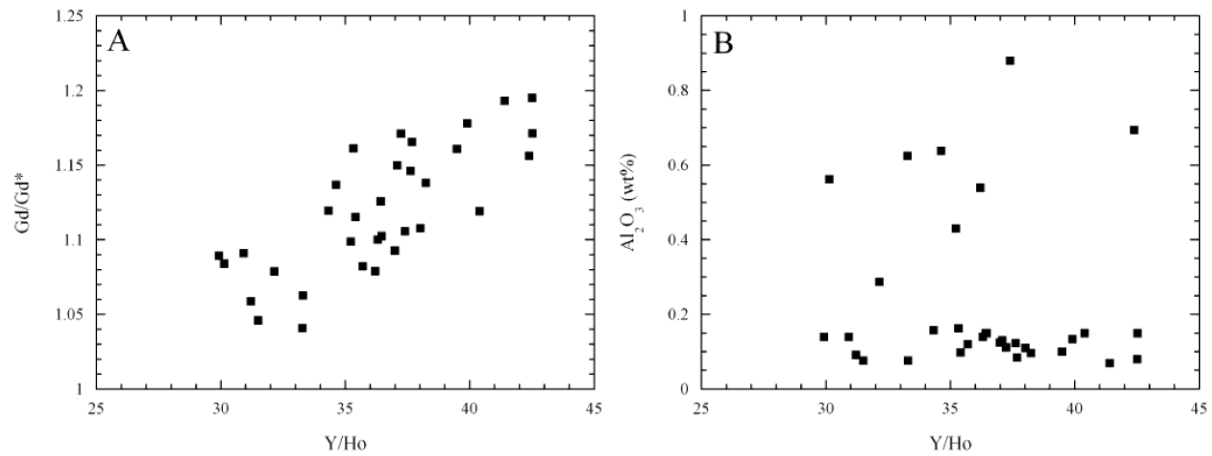


Figure 2.6: (A) Y/Ho ratios plotted against the Gd anomaly (Gd/Gd*). Y/Ho and Gd/Gd* are strongly correlated, with $r^2 = 0.71$. (B) Y/Ho ratios plotted against Al₂O₃ concentrations (wt%). Al₂O₃ does not have a relationship with the Y/Ho ratio, with the full range of Y/Ho values occurring at near-constant Al₂O₃ concentrations. Samples with elevated Al₂O₃ show a wide range of Y/Ho ratios, indicating that detrital input exerted minimal control on the Y/Ho ratio. The variability in Y/Ho and the Gd anomaly therefore reflects the existence of distinctive water chemistries in the basin, and not detritally controlled variability.

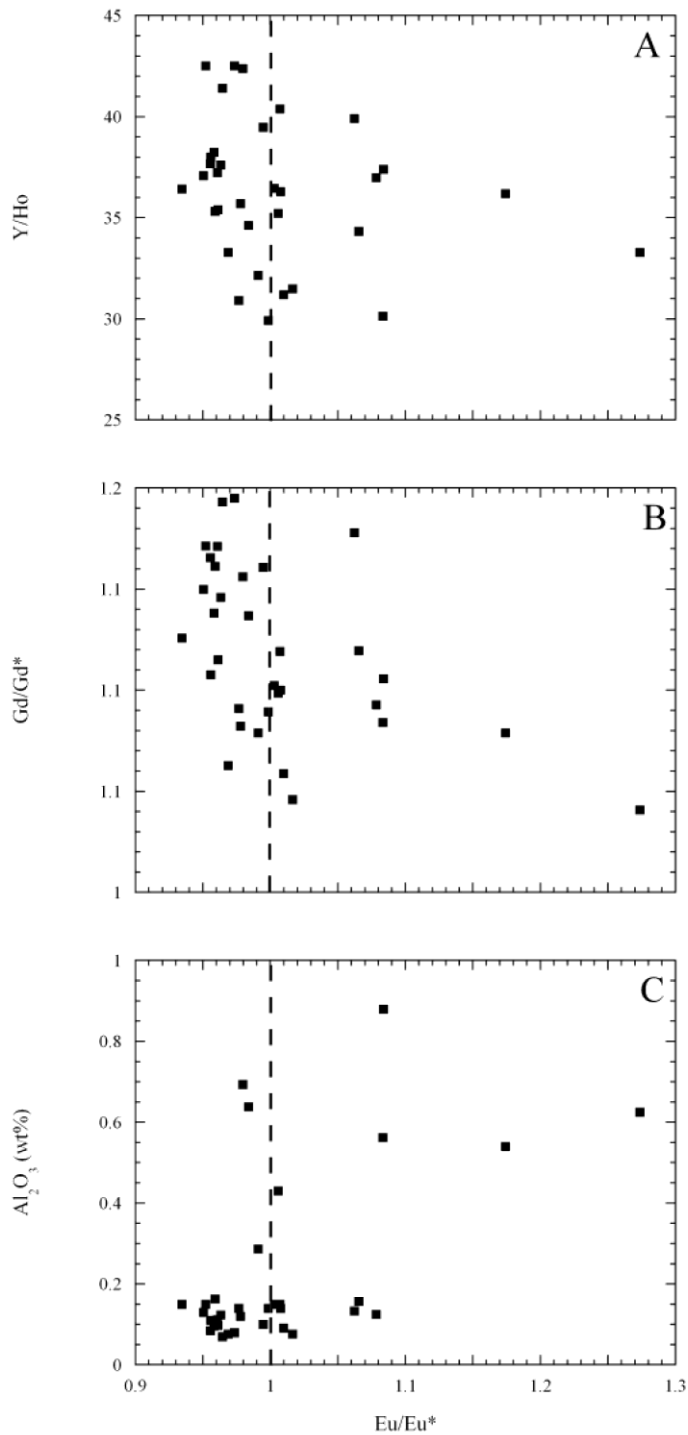


Figure 2.7: The Eu anomaly (Eu/Eu^*) plotted against (A) Y/Ho , (B) Gd/Gd^* , and (C) Al_2O_3 . No statistically significant correlation is found between the Eu anomaly and either Y/Ho or Gd/Gd^* . Dotted lines indicate $\text{Eu}/\text{Eu}^*=1$, or the threshold for the Eu anomaly. This indicates that positive Eu anomalies are not of open-marine origin, and that the wider ocean did not carry a positive Eu anomaly. Samples with Eu/Eu^* values greater than the statistically significant 1.1 also contain elevated Al_2O_3 concentrations relative to the majority of the dataset. This suggests that the positive Eu anomalies can be attributed to input of older detritus with positive Eu anomalies (e.g. feldspar) into the iron formation, rather than from a contemporaneous hydrothermal source, as noted by Klein and Beukes (1993).

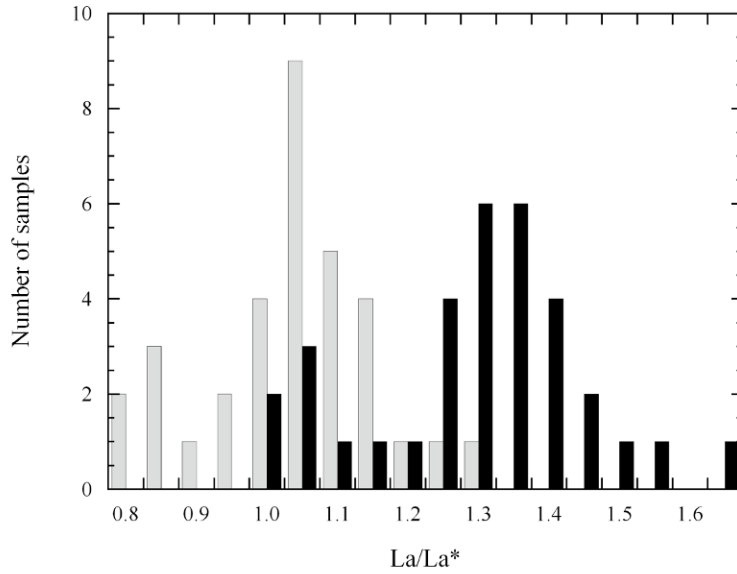


Figure 2.8: Histogram showing the distribution of La/La^* values normalised to MuQ (grey) and the USGS granitoid standard GSP-2 (black). Both have bimodal distributions, but when normalised to GSP-2, the entire dataset is shifted into positive La anomalies, whereas the lower mode in the MuQ-normalised dataset produces apparent negative La anomalies. No negative La anomalies are known from rocks, and so this finding implies that the local dissolved REE+Y supply originated from catchment areas dominated by LREE-rich rocks, possibly of granitoid composition.

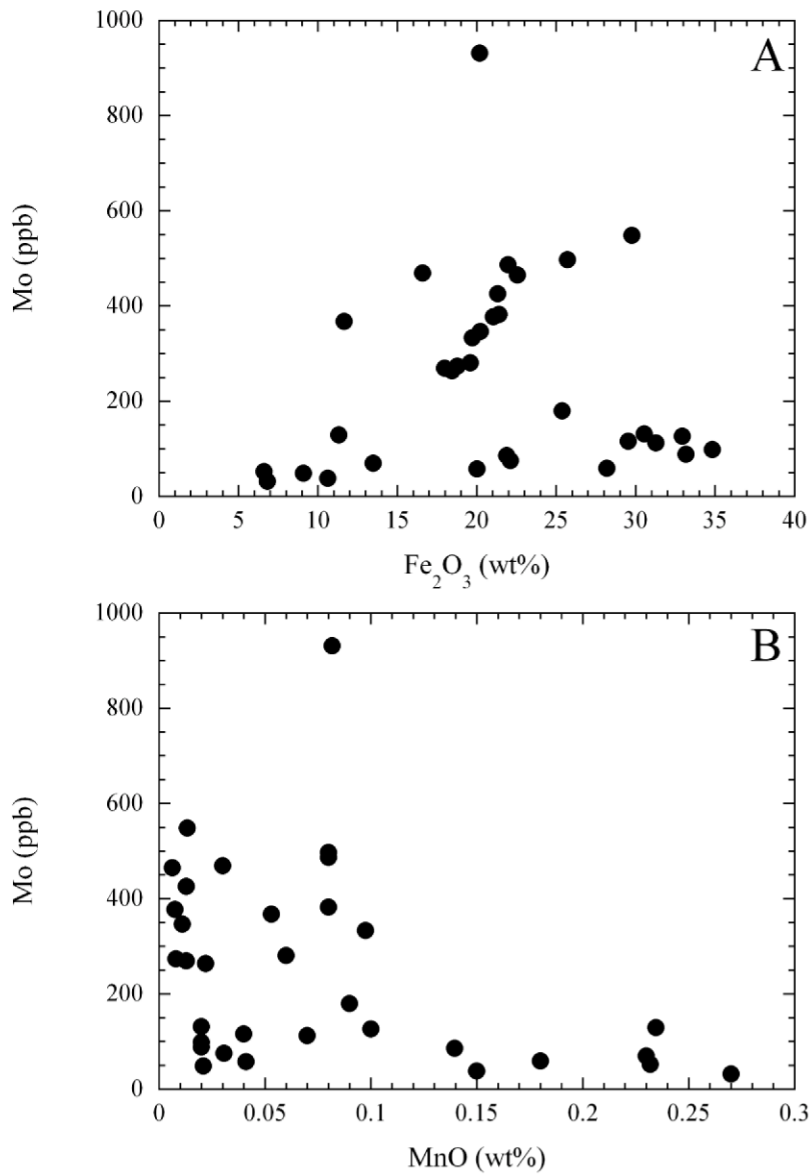


Figure 2.9: Covariance diagrams of elemental Mo (ppb) and Fe₂O₃ and MnO (wt%). (A) Molybdenum does not correlate with Fe₂O₃, indicating that increased iron deposition did not directly influence Mo fixation rates, although the strong correlation for samples at mid-range Mo and Fe₂O₃ concentrations suggests that iron particles may have nonetheless been an important particle shuttle for Mo at moderate concentrations. (B) No correlation between Mo and MnO is seen, indicating that a Mn particulate shuttle was

not a factor in Mo fixation.

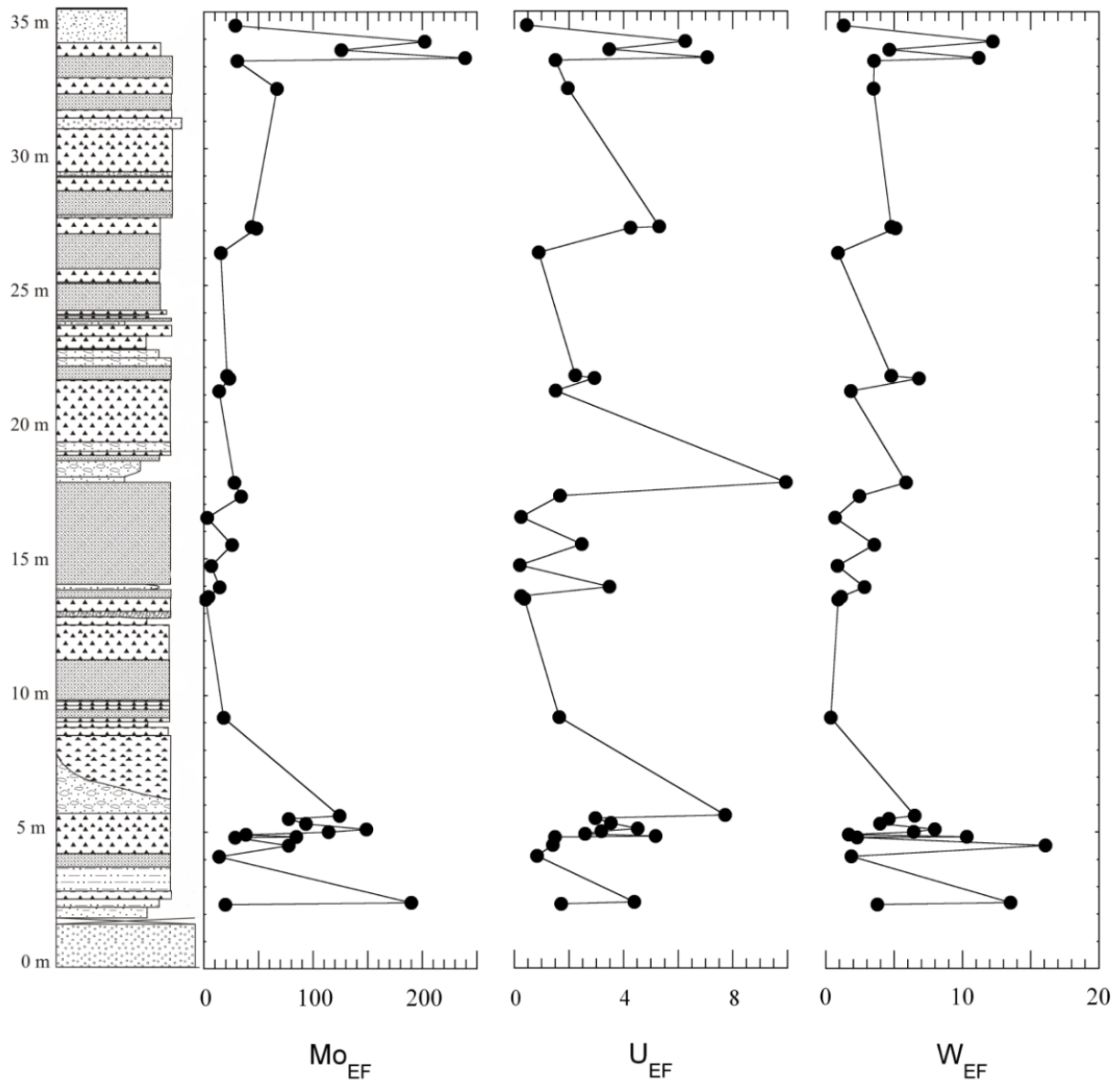


Figure 2.10: Stratigraphic distributions of the enrichment factors for Mo, U, and W. Stratigraphic column on the left is the iron formation interval from Fig. 3. Molybdenum is significantly more enriched in the upper and lower parts of the iron formation, indicating stronger mechanisms for Mo fixation, whereas U is more constant throughout the section. Tungsten is transitional between Mo and U, showing relative enrichment at the base and top of the section like Mo, albeit with much smaller enrichment factors. See text for further discussion.

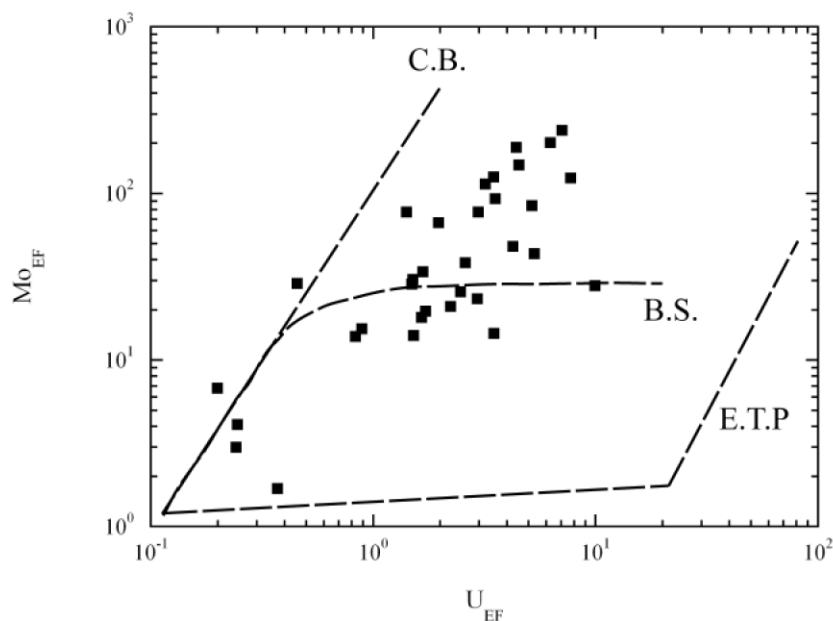


Figure 2.11: Covariance plot of Mo_{EF} and U_{EF} . These elements show good covariance with stronger absolute enrichment of Mo than U. Similar relationships exist between both of these metals and Ni, Co, Pb, and Sb, but not with V. Dotted lines show the expected trends in Mo_{EF} - U_{EF} space for the modern Cariaco Basin (C.B.), Black Sea (B.S.), and Eastern Tropical Pacific (E.T.P.).

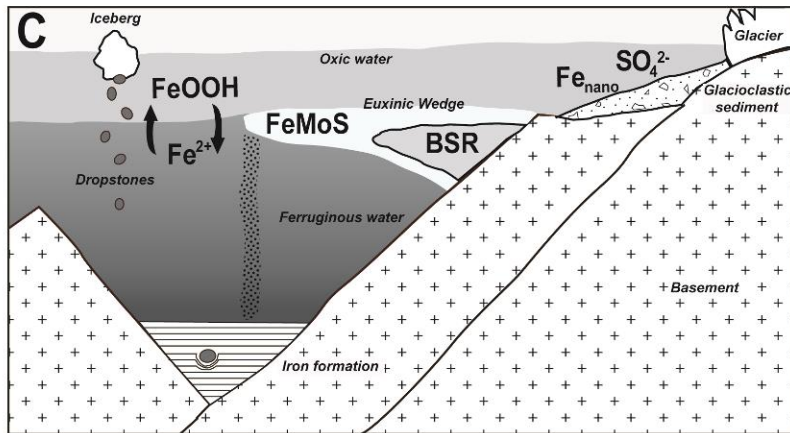
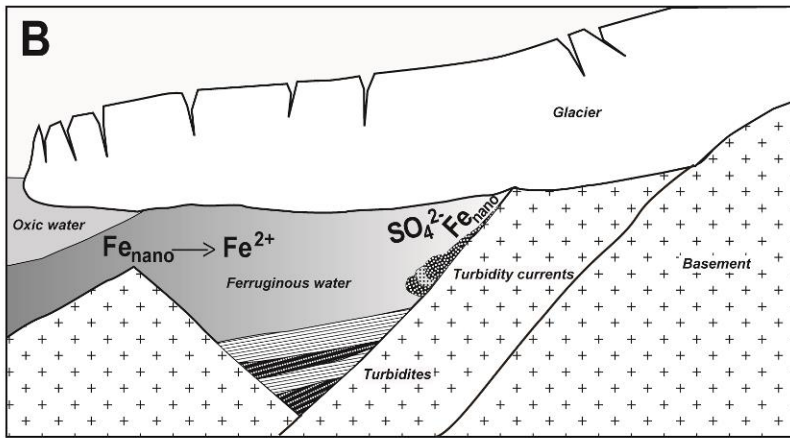
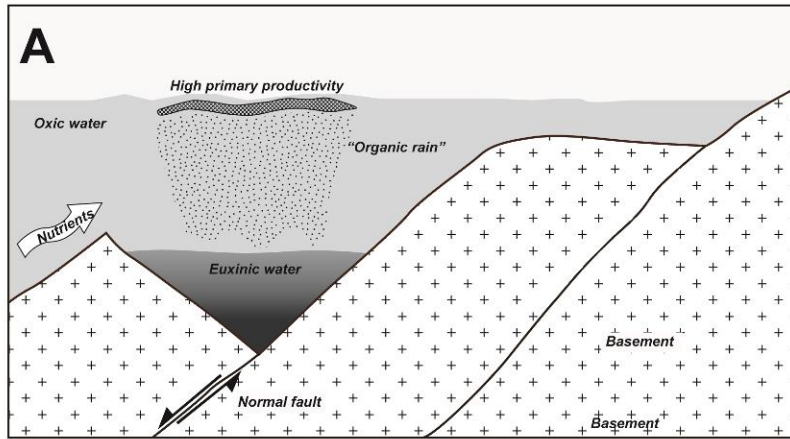


Figure 2.12: Schematic diagrams of three partially restricted basin models for a rift basin setting. (A) In the classic silled basin model, based on the Cariaco basin (after Lyons et al. 2003), a bathymetric sill, formed for example by a down-dropped fault block, limits water exchange between the deep basin and the open ocean, with stratification controlled by the development of a chemocline. The upper water mass has unrestricted exchange with the open ocean, allowing for a steady supply of dissolved metals to the basin. The lower part of the water column ... This model cannot be applied directly to the Rapitan basin because it does not account for ice cover. (B) In a rift basin with widespread ice cover, free oxygen in the upper water column of the basin would be limited, allowing the pre-existing ferruginous deep water to become the dominant redox state of the basin. During this time, clastic sediment and dissolved sulphate produced by limited chemical weathering beneath a wet-based glacier would be introduced into the basin through sub-glacial outwash, depositing the thick turbidites of the lower Sayunei Formation and raising the dissolved sulphate concentration in the basin to glauberite saturation. Simultaneously, glacially derived, highly reactive iron oxy-hydroxide nano-particles (Fe_{HR}) would be introduced into the basin and reduced to soluble Fe^{2+} by iron-reducing bacteria, gradually increasing the dissolved iron content in the ice-capped basin to levels that could deposit iron formation. (C) Upon glacial retreat from a previously ice-covered rift basin and exposure of the basin water to atmospheric oxygen and sunlight, high primary productivity occurs, generating sufficient organic material in anoxic shallow to middle water depths to initiate bacterial sulphate reduction (BSR) and produce a mildly euxinic 'wedge' in middle water depths. Dissolved MoO_4^- is converted to FeMoS compounds at relatively low H_2S concentrations, which adsorb to the surface of flocculating iron oxy-hydroxides that form through the oxidation of dissolved Fe^{2+} in the oxic upper water column. The relative position of the wedge dictates either strong Mo enrichment (solid line) or weaker enrichment (dashed line). The basinal iron supply may be refreshed through the input of additional glaciogenic Fe_{HR} nano-particles, or via upwelling of non-hydrothermal iron from extrabasinal sources. Iron formation deposition occurs only during sea-level highstand, when most glaciogenic clastic sediment is trapped in shallow, proglacial estuaries. At this time, the primary source of clastic sediment to the basin is dropstones from icebergs.

2.11 References

- Aitken, J.D. 1989. Uppermost Proterozoic formations in central Mackenzie Mountains, Northwest Territories. Geological Survey of Canada, Bulletin 368, 1-26.
- Aitken, J.D. 1991a. The Ice Brook Formation and post-Rapitan, Late Proterozoic Glaciation, Mackenzie Mountains, Northwest Territories. Geological Survey of Canada Bulletin, 404: 1-43.
- Aitken, J.D. 1991b. Two late Proterozoic glaciations, Mackenzie Mountains, northwestern Canada. *Geology*, 19: 445-448.
- Alexander, B.W., Bau, M., Andersson, P. and Dulski, P. 2008. Continentally-derived solutes in shallow Archean seawater: Rare earth element and Nd isotope evidence in iron formation from the 2.9 Ga Pongola Supergroup, South Africa. *Geochimica et Cosmochimica Acta*, 72: 378-394.
- Algeo, T.J. and Maynard, J.B. 2008. Trace-metal covariation as a guide to water-mass conditions in ancient marine environments. *Geosphere*, 4: 872-887.
- Algeo, T.J. and Tribovillard, N. 2009. Environmental analysis of paleoceanographic systems based on molybdenum-uranium covariation. *Chemical Geology*, 268: 211-225.
- Arnold, G.L., Anbar, A.D., Barling, J. and Lyons, T.W. 2004. Molybdenum isotope evidence for widespread anoxia in mid-Proterozoic oceans. *Science*, 304: 87-90.
- Arnórsson, S. and Óskarsson, N. 2007. Molybdenum and tungsten in volcanic rocks and in surface and <100°C ground waters in Iceland. *Geochimica et Cosmochimica Acta*, 71: 284-304.
- Babechuk, M.G., Kamber, B.S., Greig, A., Canil, D. and Kodolanyi, J. 2010. The behavior of tungsten during mantle melting revisited with implications for planetary differentiation time scales. *Geochimica et Cosmochimica Acta*, 74: 1448-1470.
- Baldwin, G.J., Thurston, P.C. and Kamber, B.S. 2011. High-precision rare earth element, nickel, and chromium chemistry of chert microbands pre-screened with in-situ analysis. *Chemical Geology*, 285: 133-143.
- Bau, M. 1996. Controls on the fractionation of isovalent trace elements in magmatic and aqueous systems: Evidence from Y/Ho, Zr/Hf, and lanthanide tetrad effect. *Contributions to Mineralogy and Petrology*, 123: 323-333.

- Bau, M. 1999. Scavenging of dissolved yttrium and rare earths by precipitating iron oxyhydroxide: Experimental evidence for Ce oxidation, Y-Ho fractionation, and lanthanide tetrad effect. *Geochimica et Cosmochimica Acta*, 63: 67-77.
- Bau, M. and Dulski, P. 1996. Distribution of yttrium and rare-earth elements in the Penge and Kuruman iron-formations, Transvaal Supergroup, South Africa. *Precambrian Research*, 79: 37-55.
- Bau, M. and Dulski, P. 1999. Comparing yttrium and rare earths in hydrothermal fluids from the Mid-Atlantic Ridge: implications for Y and REE behaviour during near-vent mixing and for the Y/Ho ratio of Proterozoic seawater. *Chemical Geology*, 155: 77-90.
- Bekker, A., Slack, J.F., Planavsky, N., Krapež, B., Hofmann, A., Konhauser, K.O. and Rouxel, O.J. 2010. Iron formation: The sedimentary product of a complex interplay among mantle, tectonic, oceanic, and biospheric processes. *Economic Geology*, 105: 467-508.
- Beukes, N.J. and Gutzmer, J. 2008. Origin and paleoenvironmental significance of major iron formations at the Archean-Paleoproterozoic boundary. *Reviews in Economic Geology*, 15: 5-47.
- Beukes, N.J. and Klein, C. 1992. Models for iron-formation deposition. *In The Proterozoic biosphere: a multidisciplinary approach. Edited by J.W. Schopf and C. Klein. Cambridge University Press, Cambridge. pp. 147-151.*
- Bolhar, R., Kamber, B.S., Moorbath, S., Fedo, C.M. and Whitehouse, M.J. 2004. Characterisation of early Archaean chemical sediments by trace element signatures. *Earth and Planetary Science Letters*, 222: 43-60.
- Canfield, D.E. 1998. A new model for Proterozoic ocean chemistry. *Nature*, 396: 450-453.
- Canfield, D.E., Poulton, S.W., Knoll, A.H., Narbonne, G.M., Ross, G., Goldberg, T. and Strauss, H. 2008. Ferruginous conditions dominated later Neoproterozoic deep-water chemistry. *Science*, 321: 949-952.
- Crowe, S.A., Fowle, D.A., Katsev, S., Sundby, B., Mucci, A. and Haffner, G.D. 2008. Geochemistry of Mo in a modern Archean ocean analogue. *Geochimica et Cosmochimica Acta*, 72: A190.
- Crowe, S.A., Jones, C., Katsev, S., Magen, C., O'Neill, A.H., Sturm, A., Canfield, D.E., Haffner, G.D., Mucci, A., Sundby, B. and Fowle, D.A. 2008b. Photoferrotrophs thrive in an

- Archean ocean analogue. *Proceedings of the National Academy of Sciences of the United States of America*, 105: 15938-15943.
- Cruse, A.M. and Lyons, T.W. 2004. Trace metal records of regional paleoenvironmental variability in Pennsylvanian (Upper Carboniferous) black shales. *Chemical Geology*, 206: 319-345.
- De Carlo, E.H. and Green, W.J. 2002. Rare earth elements in the water column of Lake Vanda, McMurdo Dry Valleys, Antarctica. *Geochimica et Cosmochimica Acta*, 66: 1323-1333.
- Derry, L.A. and Jacobsen, S.B. 1990. The chemical evolution of Precambrian seawater: Evidence from REEs in banded iron formations. *Geochimica et Cosmochimica Acta*, 54: 2965-2977.
- Eggins, S.M., Woodhead, J.D., Kinsley, L.P.J., Mortimer, G.E., Sylvester, P., McCulloch, M.T., Hergt, J.M. and Handler, M.R. 1997. A simple method for the precise determination of ≥ 40 trace elements in geological samples by ICPMS using enriched isotope internal standardisation. *Chemical Geology*, 134: 311-326.
- Eisbacher, G.H. 1976. Proterozoic Rapitan Group and Related Rocks, Redstone River Area, District of Mackenzie. *Geological Survey of Canada Paper*, 76: 117-125.
- Eisbacher, G.H. 1978. Re-definition and subdivision of the Rapitan Group, Mackenzie Mountains. *Geological Survey of Canada Paper*, 77: 1-21.
- Eisbacher, G.H. 1981a. Late Precambrian tillites of the northern Yukon-Northwest Territories region, Canada. *In Earth's pre-Pleistocene glacial record. Edited by M.J. Hambrey and W.B. Harland. Cambridge University Press, Cambridge. pp. 724-727.*
- Eisbacher, G.H. 1981b. Sedimentary tectonics and glacial record in the Windermere Supergroup, Mackenzie Mountains, Northwestern Canada. *Geological Survey of Canada Paper*, 80: 1-41.
- Eisbacher, G.H. 1985. Late Proterozoic rifting, glacial sedimentation, and sedimentary cycles in the light of Windermere deposition, western Canada. *Palaeogeography Palaeoclimatology Palaeoecology*, 51: 231-254.
- Elderfield, H., Upstill-Goddard, R. and Sholkovitz, E.R. 1990. The rare earth elements in rivers, estuaries, and coastal seawaters: processes affecting crustal input of elements to the

- oceans and their significance to the composition of seawater. *Geochimica et Cosmochimica Acta*, 54: 971-991.
- Eyles, N. 2008. Glacio-epochs and the supercontinent cycle after ~3.0 Ga: Tectonic boundary conditions for glaciation. *Palaeogeography Palaeoclimatology Palaeoecology*. 258: 89-129.
- Farquhar, J., Wu, N., Canfield, D.E. and Oduro, H. 2010. Connections between sulfur cycle evolution, sulfur isotopes, sediments, and base metal sulfide deposits. *Economic Geology*, 105: 509-533.
- Fischer, W.W. and Knoll, A.H. 2009. An iron shuttle for deepwater silica in Late Archean and early Paleoproterozoic iron formation. *GSA Bulletin*, 121: 222-235.
- Frei, R., Gaucher, C., Poulton, S.W. and Canfield, D.E. 2009. Fluctuations in Precambrian atmospheric oxygenation recorded by chromium isotopes. *Nature*, 461: 250-253.
- Goldberg, T., Archer, C., Vance, D. and Poulton, S.W. 2009. Mo isotope fractionation during adsorption to Fe (oxyhydr)oxides. *Geochimica et Cosmochimica Acta*, 73: 6502-6516.
- Green, L.H. and Godwin, C.I. 1963. Mineral Industry of Yukon Territory and southwestern District of Mackenzie, 1962. Geological Survey of Canada Paper, 63: 15-18.
- Helmstaedt, H., Eisbacher, G.H. and McGregor, J.A. 1979. Copper mineralization near an intra-Rapitan unconformity, Nite copper prospect, Mackenzie Mountains, Northwest Territories, Canada. *Can J Earth Sci*, 16: 50-59.
- Helz, G.R., Bura-Nakić, E., Mikac, N. and Ciglencčki, I. 2011. New model for molybdenum behavior in euxinic waters. *Chemical Geology*, 284: 323-332.
- Hoffman, P.F., Kaufman, A.J., Halverson, G.P. and Schrag, D.P. 1998. A Neoproterozoic Snowball Earth. *Science*, 281: 1342-1346.
- Hoffman, P.F. 2009. Pan-glacial- a third state in the climate system. *Geology Today*, 25: 100-107.
- Hofmann, H.J., Narbonne, G.M. and Aitken, J.D. 1990. Ediacaran remains from intertillite beds in northwestern Canada. *Geology*, 18: 1199-1202.
- Isley, A.E. 1995. Hydrothermal Plumes and the Delivery of Iron to Banded Iron-Formation. *Journal of Geology*, 103: 169-185.

- Isley, A.E. and Abbott, D.H. 1999. Plume-related mafic volcanism and the deposition of banded iron formation. *Journal of Geophysical Research*, 104: 15461-15477.
- James, N.P., Narbonne, G.M. and Kyser, T.K. 2001. Late Neoproterozoic cap carbonates: Mackenzie Mountains, northwestern Canada: precipitation and global glacial meltdown. *Canadian Journal of Earth Sciences*, 38: 1229-1262.
- Jefferson, C.W. and Ruelle, J.C.L. 1987. The late Proterozoic Redstone copper belt. *In Mineral Deposits of the northern Cordillera. Edited by J.A. Morin. Canadian Institute of Mining and Metallurgy Special Vol. 37*, pp. 154-168.
- Jefferson, C.W. and Parrish, R.R. 1989. Late Proterozoic stratigraphy, U-Pb zircon ages, and rift tectonics, Mackenzie Mountains, northwestern Canada. *Canadian Journal of Earth Sciences*, 26: 1784-1801.
- Johannesson, K.H., Lyons, W.B., Graham, E.Y. and Welch, K.A. 2000. Oxyanion concentrations in eastern Sierra Nevada Rivers- 3. Boron, molybdenum, vanadium, and tungsten. *Aquatic Geochemistry*, 6: 19-46.
- Johannesson, K.H., Hawkins, D.L. and Cortes, A. 2006. Do Archean chemical sediments record ancient seawater rare earth element patterns? *Geochimica et Cosmochimica Acta*, 70: 871-890.
- Johnston, D.T., Poulton, S.W., Dehler, C., Porter, S., Husson, J., Canfield, D.E. and Knoll, A.H. 2010. An emerging picture of Neoproterozoic ocean chemistry: Insights from the Chuar Group, Grand Canyon, USA. *Earth and Planetary Science Letters*, 290: 64-73.
- Kamber, B.S., Bolhar, R. and Webb, G.E. 2004. Geochemistry of late Archean stromatolites from Zimbabwe: evidence for microbial life in restricted epicontinental seas. *Precambrian Research*, 132: 379-399.
- Kamber, B.S., Greig, A. and Collerson, K.D. 2005. A new estimate for the composition of weathered young upper continental crust from alluvial sediments, Queensland, Australia. *Geochimica et Cosmochimica Acta*, 69: 1041-1058.
- Kamber, B.S. 2009. Geochemical fingerprinting: 40 years of analytical development and real world applications. *Applied Geochemistry*, 24: 1074-1086.
- Kamber, B.S. 2010. Archean mafic-ultramafic volcanic landmasses and their effect on ocean atmosphere chemistry *Chemical Geology*, 274: 19-28.

- Kato, Y., Yamaguchi, K.E. and Ohmoto, H. 2006. Rare earth elements in Precambrian banded iron formations: Secular changes of Ce and Eu anomalies and evolution of atmospheric oxygen. *In* GSA Memoir 198: Evolution of Earth's Atmosphere, Hydrosphere, and Biosphere- Constraints from Ore Deposits. *Edited by* S.E. Kesler and H. Ohmoto. The Geological Society of America, Boulder. pp. 269-289.
- Keele, J. 1906. Upper Stewart River region, Yukon. Geological Survey of Canada Annual Report 1904, 16: 5-23.
- Keele, J. 1910. Reconnaissance across the Mackenzie Mountains on the Pelly, Ross, and Gravel Rivers, Yukon and Northwest Territories. Geological Survey of Canada Report No 1097,
- Kianian, M. and Khakzad, A. 2008. Geochemistry of glaciogenic Neoproterozoic banded iron formations from the Kerma District (Iran). 33rd International Geological Congress, Session CGC-04:
- Kirschvink, J.L. 1992. Late Proterozoic low-latitude global glaciation: the Snowball Earth. *In* The Proterozoic biosphere: A multidisciplinary study. *Edited by* J.W. Schopf and C. Klein. Cambridge University Press, Cambridge. pp. 51-52.
- Klein, C. and Beukes, N.J. 1993. Sedimentology and geochemistry of the glaciogenic late Proterozoic Rapitan iron-formation in Canada. *Economic Geology*, 88: 542-565.
- Klein, C. and Ladeira, E.A. 2004. Geochemistry and mineralogy of Neoproterozoic banded iron-formations and some selected, siliceous manganese formations from the Urucum District, Mato Grosso Do Sul, Brazil. *Economic Geology*, 99: 1233-1244.
- Kletzin, A. and Adams, M.W.W. 1996. Tungsten in biological systems. *FEMS Microbiology Reviews*, 18: 5-63.
- Konhauser, K.O., Pecoits, E., Lalonde, S.V., Papineau, D., Nisbet, E.G., Barley, M.E., Arndt, N.T., Zahnle, K. and Kamber, B.S. 2009. Oceanic nickel depletion and a methanogen famine before the Great Oxidation Event. *Nature*, 458: 750-753.
- Kump, L.R. and Seyfried Jr. W.E. 2005. Hydrothermal Fe fluxes during the Precambrian: Effect of low oceanic sulfate concentration and low hydrostatic pressure on the composition of black smokers. *Earth and Planetary Science Letters*, 235: 654-662.

- Lawrence, M.G., Greig, A., Collerson, K.D. and Kamber, B.S. 2006. Rare earth element and yttrium variability in South East Queensland waterways. *Aquatic Geochemistry*, 12: 39-72.
- Lawrence, M.G. and Kamber, B.S. 2006. The behaviour of the rare earth elements during estuarine mixing-revisited. *Marine Chemistry*, 100: 147-161.
- Li, C., Love, G.D., Lyons, T.W., Fike, D.A., Sessions, A.L. and Chu, X. 2010. A stratified redox model for the Ediacaran ocean. *Science*, 328: 80-83.
- Long, D.G.F., Rainbird, R.H., Turner, E.C. and MacNaughton, R.B. 2008. Early Neoproterozoic strata (Sequence B) of mainland northern Canada and Victoria and Banks islands: a contribution to the Geological Atlas of the North Canadian Mainland Sedimentary Basin. Geological Survey of Canada, Open File 5700, 24 p.
- Lottermoser, B.G. and Ashley, P.M. 2000. Geochemistry, petrology and origin of Neoproterozoic ironstones in the eastern part of the Adelaide Geosyncline, South Australia. *Precambrian Research*, 101: 49-67.
- Lyons, T.W., Werne, J.P., Hollander, D.J. and Murray, R.W. 2003. Contrasting sulfur geochemistry and Fe/Al and Mo/Al ratios across the last oxic-to-anoxic transition in the Cariaco Basin, Venezuela. *Chemical Geology*, 195: 131-157.
- Macdonald, F.A., Schmitz, M.D., Crowley, J.L., Roots, C.F., Jones, D.S., Maloof, A.C., Strauss, J.V., Cohen, P.A., Johnston, D.T. and Schrag, D.P. 2010a. Calibrating the Cryogenian. *Science*, 327: 1241-1243.
- Macdonald, F.A., Strauss, J.V., Rose, C.V., Dudás, F.Ö. and Schrag, D.P. 2010b. Stratigraphy of the Port Nolloth Group of Namibia and South Africa and implications for the age of Neoproterozoic iron formations. *American Journal of Science*, 310: 862-888.
- Marx, S.K. and Kamber, B.S. 2010. Trace-element systematics in the Murray-Darling Basin, Australia: Sediment provenance and paleoclimate implications of fine scale heterogeneity. *Applied Geochemistry*, 25: 1221-1237.
- Meyer, E.E., Burgreen, B.N., Lackey, H., Landis, J.D., Quicksall, A.N. and Bostick, B.C. 2008. Evidence for basin restriction during syn-collisional basin formation in the Silurian Arisaig Group, Nova Scotia. *Chemical Geology*, 256: 1-11.

- Mikucki, J.A., Pearson, A., Johnston, D.T., Turchyn, A.V., Farquhar, J., Schrag, D.P., Anbar, A.D., Prisco, J.C. and Lee, P.A. 2009. A contemporary microbially maintained subglacial ferrous "ocean". *Science*, 324: 397-400.
- Morford, J.L. and Emerson, S. 1999. The geochemistry of redox sensitive trace metals in sediments. *Geochimica et Cosmochimica Acta*, 63: 1735-1750.
- Morford, J.L., Emerson, S.R., Breckel, E.J. and Kim, S.H. 2005. Diagenesis of oxyanions (V,U,Re, and Mo) in pore waters and sediments from a continental margin. *Geochimica et Cosmochimica Acta*, 69: 5021-5032.
- Narbonne, G.M. and Aitken, J.D. 1995. Neoproterozoic of the Mackenzie Mountains, northwestern Canada. *Precambrian Research*, 73: 101-121.
- Nothdurft, L.D., Webb, G.E. and Kamber, B.S. 2004. Rare earth element geochemistry of Late Devonian reefal carbonate, Canning Basin, Western Australia: confirmation of a seawater REE proxy in ancient limestones. *Geochimica et Cosmochimica Acta*, 68: 263-283.
- Ohta, A., Ishii, S., Sakakibara, M., Mizuno, A. and Kawabe, I. 1999. Systematic correlation of the Ce anomaly with the Co/(Ni+Cu) ratio and Y fractionation from Ho in distinct types of Pacific deep-sea nodules. *Geochemical Journal*, 33: 399-417.
- Pattan, J.N. and Pearce, N.J.G. 2009. Bottom water oxygenation history in southeastern Arabian Sea during the past 140 ka: Results from redox-sensitive elements. *Palaeogeography, Palaeoclimatology, Palaeoecology*, 280: 396-405.
- Pecoits, E., Gingras, M., Aubet, N. and Konhauser, K. 2008. Ediacaran in Uruguay: palaeoclimatic and palaeobiological implications, *Sedimentology*, 55: 689-719.
- Picard, S., Lécuyer, C., Barrat, J.-A., Garcia, J.P., Dromart, G. and Sheppard, S.M.F. 2002. Rare-earth element contents of Jurassic fish and reptile teeth and the potential relation to seawater composition (Anglo-Paris basin, France and England). *Chemical Geology*, 186: 1-16.
- Planavsky, N., Bekker, A., Rouxel, O.J., Kamber, B., Hofmann, A., Knudsen, A. and Lyons, T.W. 2010a. Rare earth element and yttrium compositions of Archean and Paleoproterozoic Fe formations revisited: New perspectives on the significance and mechanisms of deposition. *Geochimica et Cosmochimica Acta*, 74: 6387-6405.

- Planavsky, N., Rouxel, O.J., Bekker, A., Lalonde, S.V., Konhauser K.O., Reinhard, C.T., and Lyons, T.W. 2010b. The evolution of the marine phosphate reservoir. *Nature*, 467; 1088-1090
- Pollack, G.D., Krogstad, E.J. and Bekker, A. 2009. U-Th-Pb-REE systematics of organic-rich shales from the ca. 2.15 Ga Sengoma Argillite Formation, Botswana: Evidence for oxidative continental weathering during the Great Oxidation Event. *Chemical Geology*, 260: 172-185.
- Poulton, S.W., Fralick, P.W. and Canfield, D.E. 2010. Spatial variability in oceanic redox structure 1.8 billion years ago. *Nature Geoscience*, 3: 486-490.
- Poulton, S.W. and Canfield, D.E. 2011. Ferruginous conditions: a dominant feature of the ocean through Earth's history. *Elements*, 7: 107-112.
- Pufahl, P.K. Hiatt, E.E. and Kyser, T.K. 2010. Does the Paleoproterozoic Animikie Basin record the sulfidic ocean transition? *Geology*, 38: 659-662.
- Raiswell, R., Tranter, M., Benning, L.G., Siegert, M., De'ath, R., Huybrechts, P. and Payne, T. 2006. Contributions from glacially derived sediment to the global iron (oxyhydr)oxide cycle: implications for iron delivery to the oceans. *Geochimica et Cosmochimica Acta*, 70: 2765-2780.
- Rose, A.W., Smith, A.T., Lustwerk, R.L., Ohmoto, H. and Hoy, L.D. 1986. Geochemical aspects of stratiform and red-bed copper deposits in the Catskill Formation (Pennsylvania, USA) and Redstone Area (Canada). Sequence of mineralization in sediment-hosted copper deposits (Part 3). *In Geology and Metallogeny of Copper Deposits. Edited by G.H. Friedrich. Springer-Verlag, Berlin. pp. 414-421.*
- Ross, G.M. and Villeneuve, M.E. 1997. U-Pb geochronology of stranger stones in Neoproterozoic diamictites, Canadian Cordillera: implications for provenance and ages of deposition. *Radiogenic Age and Isotopic Studies: Report 10; Geological Survey of Canada, Current Research 1997-F*, 141-155.
- Scott, C., Lyons, T.W., Bekker, A., Shen, Y., Poulton, S.W., Chu, X. and Anbar, A.D. 2008. Tracing the stepwise oxygenation of the Proterozoic ocean. *Nature*, 452: 456-459.

- Seiler, R.L., Stollenwerk, K.G. and Garbarino, J.R. 2005. Factors controlling tungsten concentrations in ground water, Carson Desert, Nevada. *Applied Geochemistry*, 20: 423-441.
- Sheilds-Zhou, G. and Och, L. 2011. The case for a Neoproterozoic oxygenation event: geochemical evidence and biological consequences. *GSA Today*, 21: 4-11.
- Sheilds, G.A. and Webb, G.E. 2004. Has the REE composition of seawater changed over geological time? *Chemical Geology*, 204: 103-107.
- Slack, J.F., Grenne, T. Bekker, A., Rouxel, O.J. and Lindberg, P.A. 2007. Suboxic deep seawater in the late Paleoproterozoic: Evidence from hematitic chert and iron formation related to seafloor-hydrothermal sulfide deposits, central Arizona, USA. *Earth and Planetary Science Letters*, 255: 243-256.
- Stuart, R.A. 1963. Geology of the Snake River Iron deposit. DIAND Assessment Files, Yellowknife, NWT, 18 p.
- Taylor, S.R. and McLennan, S.M. 1985. *The continental crust: its composition and evolution*. Blackwell, Oxford. pp. 312.
- Tribouillard, N., Riboulleau, A., Lyons, T. and Baudin, F. 2004. Enhanced trapping of molybdenum by sulfurized marine organic matter of marine origin in Mesozoic limestones and shales. *Chemical Geology*, 213: 385-401.
- Tribouillard, N., Algeo, T.J., Lyons, T. and Riboulleau, A. 2006. Trace metals as paleoredox and paleoproductivity proxies: An update. *Chemical Geology*, 232: 12-32.
- Trompette, R., De Alvarenga, C.J.S. and Walde, D. 1998. Geological evolution of the Neoproterozoic Corumbá graben system (Brazil). Depositional context of the stratified Fe and Mn ores of the Jacadigo Group. *Journal of South American Earth Sciences*, 11: 587-597.
- Ulrich, T., Kamber, B.S., Jugo, P.J. and Tinkham, D.K. 2009. Imaging element-distribution patterns in minerals by laser ablation - inductively coupled plasma - mass spectrometry (LA-ICP-MS). *Canadian Mineralogist*, 47: 1001-1012.
- Van der Weijden, C.H. 2002. Pitfalls of normalisation of marine geochemical data using a common divisor. *Marine Geology*, 184: 167-187.

- Yeo, G.M. 1978. Iron-formation in the Rapitan Group, Mackenzie Mountains, Yukon and Northwest Territories. DIAND Mineral Industry Report 1975, NWT Economic Geology Series 1978-5: 170-175.
- Yeo, G.M. 1981. The late Proterozoic Rapitan glaciation in the northern Cordillera. *In* Proterozoic Basins of Canada. *Edited by* F.H.A. Campbell. Geological Survey of Canada Paper 81-10, pp. 25-46.
- Young, G.M. 1976. Iron-formation and glaciogenic rocks of the Rapitan Group, Northwest Territories, Canada. *Precambrian Research*, 3: 137-158.
- Young, G.M. 1988. Proterozoic plate tectonics, glaciation and iron-formations. *Sedimentary Geology*, 58: 127-144.
- Young, G.M. 1992. Late Proterozoic stratigraphy and the Canada-Australia connection. *Geology*, 20: 215-218.
- Young, G.M. 2002. Stratigraphic and tectonic settings of Proterozoic glaciogenic rocks and banded iron-formations: relevance to the snowball Earth debate. *Journal of African Earth Science*, 35: 451-466.
- Zhang, J. and Nozaki, Y. 1996. Rare earth elements and yttrium in seawater: ICP-MS determinations in the East Caroline, Coal Sea, and South Fiji basins of the western South Pacific Ocean. *Geochimica et Cosmochimica Acta*, 60: 4631-4644.
- Ziegler, P.A. 1959. Frühpaläozoische Tillite im östlichen Yukon-Territorium (Kanada). *Ecologiae Geologicae Helveticae*, 52: 735-741.

2.12 Supplementary Data

2.12.1 Detailed Methods

Forty-two jasper samples were carefully cleaned of adhering modern sediment. When necessary, samples were briefly immersed in an HCl bath to eliminate late-diagenetic to sub-recent calcite veins and surface precipitates. Cleaned samples were then carefully examined to determine the suitability of the jasper band for trace element analysis, with the most nodule-rich bands being excluded from the study due to their extreme heterogeneity. In some cases, chert bands needed to be mechanically separated from the associated hematite bands using a water-cooled lapidary saw.

To test the possibility of chert heterogeneity (e.g., Baldwin et al. 2011), thin sections of several samples underwent exploratory *in situ* analysis for Mo, U, and Al by LA-ICP-MS, using a Resonetics RESolution M-50-LR 193 nm laser ablation system operating at 12.4 J/cm², with a repetition rate of 5 Hz. Analyses were performed as a longitudinal traverse of the jasper bands with a spot size of 89 μm and a scan rate of 20 μm/s. These analyses demonstrated excellent homogeneity across the thickness of jasper bands for all analyzed elements, as expressed by counts per second (cps) over time (Fig. 2.S1). It was thus concluded that the chert bands were sufficiently chemically homogenous. By contrast, 2 dimensional trace element maps of chert nodules, obtained using the methodology described by Ulrich et al. (2009), exposed great chemical gradients and complex zonations. These elemental gradients are likely secondary and make it impossible to sample nodules on a representative scale.

The selected samples were crushed to pebble-sized grains in a Sturtivant steel jaw crusher that was thoroughly cleaned of all residue between samples with a nylon brush and ethanol. The crushed material was then carefully picked under a dissecting microscope to ensure that only pure jasper was sampled, and to avoid such impurities as weathering surfaces, veins, massive hematite, and jasper nodules. Avoiding the nodules was especially critical due to their probable early diagenetic origin. The picked grains were rinsed in ethanol, dried, and crushed in an agate mortar and pestle.

Samples for trace element analysis were weighed as 100 mg aliquots for digestion in a 4:1 mixture of 2 mL of distilled, ultra-pure, concentrated HF, and 0.5 mL of sub-boiling, triple-distilled concentrated HNO₃ in 29 mL Savillex Teflon beakers. Digestion was achieved in tightly sealed beakers at 140°C for 72 hours, after which samples were dried-down at 110°C, volatilizing all Si as SiF₄. Remaining fluoride complexes were converted to nitrates using repeated treatments of 1 mL pure HNO₃. The converted residue was then taken up into a 10 mL stock solution of 20% HNO₃ by dissolving it in closed beakers overnight at 140°C. The stock solutions were diluted to nominal dilution factors of approximately 2,600x. In reality, the dilution factors were much lower, due to the substantial loss of Si as SiF₄.

Sample dilutions were prepared for analysis by the addition of an internal standard mixture containing the enriched isotopes ⁶Li and ²³⁵U, as well as pure elemental Re, Rh, and Bi. A suite of 46 trace elements was analyzed using a Thermo X Series II quadrupole ICP-MS with a quartz spray chamber, externally calibrated using multiple solutions of the USGS standard W-2. Additionally, the USGS standards JA-2 and JB-2 were analyzed as laboratory unknowns, as well as the iron formation reference material IFG, which was run as a procedural unknown, all three of which were compared to the laboratory long-term reproducibility (e.g., Kamber 2009). The production of oxides and oxide interferences by the ICP-MS (e.g., BaO) was tracked and corrected using the procedure described by Ulrich et al. (2010).

The preferred concentrations of elements in the calibration standard (W-2) have been listed and explained in previous publications (e.g., Kamber et al. 2003; Babechuk et al. 2010) but for this study, standard addition experiments were performed to verify the preferred concentration for the important metal Mo, alongside three other siderophile and/or redox-sensitive metals (As, Sb and Tl). For this purpose, four 100 mg digestions were produced from 4 international rock standards (W-2, BHVO-1, JA-2 and JA-3). The separate digestions of each standard were diluted to a factor of 2,500 and spiked with internal standards, as were the regular samples. One dilution was analyzed pure, but to the other three dilutions a mixed tracer of combined Mo, As, Sb and Tl was added. This tracer was prepared from certified 10,000 ppm pure metal solutions. The approximate tracer concentrations in the first spiked dilution were 0.088 ppb Mo, 0.55 ppb As, 0.07 ppb Sb and 0.05 ppb Tl. The second and third spiked dilutions contained 5 and 10 times

higher concentrations, respectively. Plots of blank, internal standard, and dilution-factor-corrected signal intensity (raw counts) vs. added standard concentrations were produced. Linear regressions were calculated from these plots, yielding r^2 of better than 0.9995, attesting to the internal consistency of the experiments (Fig. S2). One such plot (for Mo) is shown in Figure 2.S2. From the slope and intercept of these regression lines, the metal concentration can be calculated (Table 2.S1). The Mo concentration was calculated for three isotopes and those of Sb and Tl for two isotopes. The errors listed in Table 2.S1 for these elements represent the one-sigma standard deviation of the individual estimates. The error for As was calculated from the propagated error in slope, intercept and blank subtraction. Importantly, the previously preferred concentration of Mo in W-2 (423.4 ppb) was reproduced in this experiment (424.4 ± 2.1 ppb) within error, and the data reported here are thus consistent with earlier data from the same laboratory.

Major elements were analyzed in two different ways. For twenty samples, a representative but less carefully picked split of the material was pulverized in a tungsten carbide puck mill for analysis by XRF at the Ontario GeoLabs, where loss on ignition (LOI) was also determined. The remaining 22 samples were analyzed for major elements (except Si) by ICP-MS. The same stock solutions used for the trace elements were diluted by factors of 16,000-19,000x to bring the major element concentrations of these elements within the upper detection limits of the ICP-MS. Otherwise, the operating parameters for these analyses were very similar to those for the trace element analysis, with the same internal standards and external calibration with W-2. The USGS standards BHVO-2 and BCR-2 were run as unknowns and results compared favorably with the certified major-element values published by the USGS. Samples measured by the ICP-MS lack data for SiO_2 and LOI, due to the loss of both Si and volatile phases during the drydown phase of digestion, but the data correspond exactly to the material analyzed for trace elements. Major and trace element results are reported in Table 2. S2.

2.12.2 Supplementary Figures

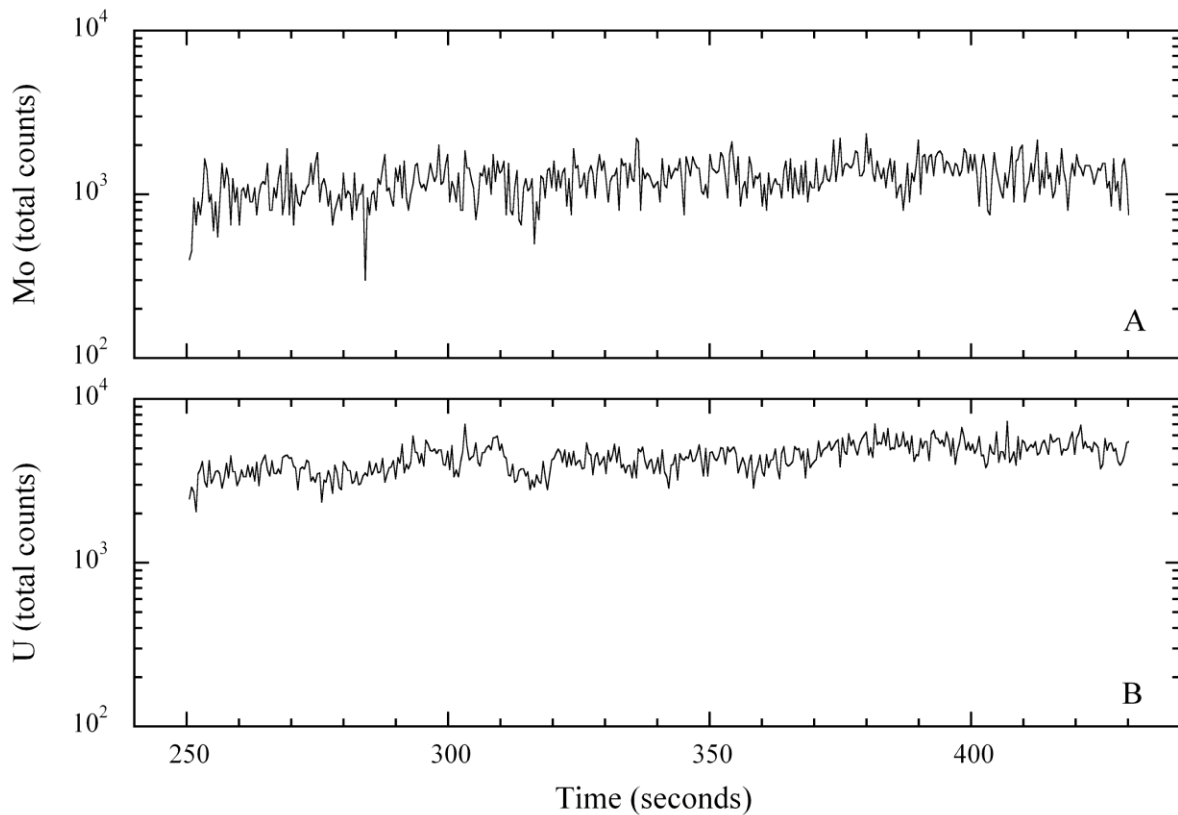


Figure 2.S1: Time-resolved LA-ICP-MS signals (counts per second) for Mo and U from a traverse across a jasper band. Fairly uniform levels of both Mo (A) and U (B) were obtained throughout the thickness of the band. The absence of concentration spikes clearly argues against nugget effects, and the uniform distribution shows that both elements are genuinely hosted by the jasper. Uranium is more homogeneously distributed than Mo, but not by a statistically significant amount. Similar profiles were obtained from other jasper bands in traverses both across and along different jasper bands, indicating that the jasper is chemically homogeneous.

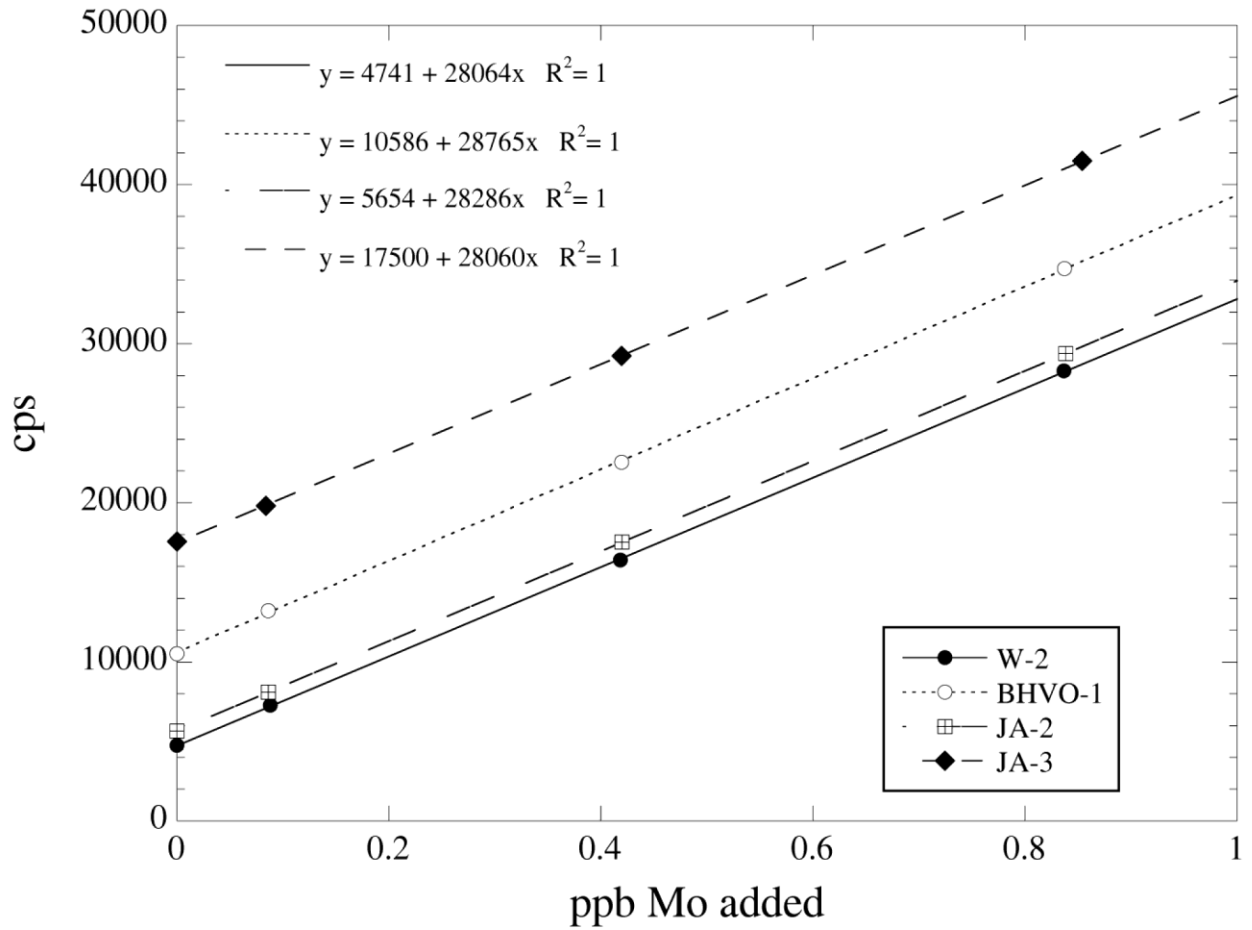


Figure 2.S2: Plot of added Mo standard concentration vs. signal intensity (corrected for blank and adjusted to a constant dilution factor of 2,500 and internal standard concentration of 4.4 ppb). Note excellent co-linearity of unspiked and three spiked dilutions for all four standards. Intercepts and slopes of regression lines were used to calculate metal concentration in rock standards as listed in Table 1.

2.12.3 Supplementary Tables

Table 2.S1: Concentrations (ppb) in international rock standards obtained via standard addition

	ppb As	ppb Mo	ppb Sb	ppb Tl
W-2	1260±64	424±2	800±13	94±1
BHVO-1	829±34	909±4	126±0.3	42±1
JA-2	849±29	475±8	129±2	307±2
JA-3	4472±128	1,567±17	278±2	203±1

Table 2.S2: Major (wt%) and trace (ppb) element geochemical results

Table S2: Major (wt%) and trace (ppb) element geochemical results						
	W-2 Preferred values	JB-2	JA-2	IFG	2.31 ^a	2.35
SiO ₂ ^b	52.68					
Al ₂ O ₃	14.45				1.18	0.56
Fe ₂ O ₃	10.83				18.94	19.74
MnO	0.167				0.10	0.10
MgO	6.37				1.17	1.24
CaO	10.86				3.07	3.26
K ₂ O	0.626				0.13	0.02
Na ₂ O	2.2				0.03	0.03
P ₂ O ₅	0.14				0.06	0.11
LOI ^b						
Sc	36074	55694	19356	364	4693	2612
Ti	6354611	6929251	3964792	25655	224344	137628
V	261597	578201	120349	1945	39204	19108
Co	44526	37036	29810	33692	3201	4186
Ni	69993	13669	139523	29139	10922	11812
Ga	17424	16380	16450	753	5001	3033
Y	20113	22223	15904	10398	5960	5973
Zr	87866	45030	105825	514	14368	5047
Nb	7275	485	9091	111	1124	494
Mo	423	944	549	578	233	333
Sb	709	201	131	596	393	390
La	10521	2251	15614	3410	2900	692
Ce	23216	6560	32699	4923	7184	2084
Pr	3025	1154	3726	535	1031	350
Nd	12911	6303	14153	2145	4577	1917
Sm	3266	2267	3003	463	1088	647
Eu	1094	826	879	422	274	184
Gd	3708	3233	3008	798	1221	849
Tb	615	581	477	130	178	133
Dy	3808	3934	2899	922	1024	863
Ho	803	884	612	240	208	198
Er	2222	2576	1723	733	581	594
Tm	327	392	259	107	89	94
Yb	2058	2549	1661	670	625	661
Lu	301	385	248	106	101	110
Hf	2356	1430	2748	14	251	100
Ta	454	35	654	201	29	21
W	240	269	1205	262931	233	196
Pb	7528	4976	18477	2709	2598	722
Th	2104	249	4686	50	258	181
U	505	156	2238	23	115	158
Pr/Yb					0.63	0.20
La/La*					0.95	1.02
Ce/Ce*					0.95	1.00
Eu/Eu*					1.04	1.08
Gd/Gd*					1.03	1.08
Y/Ho					28.6	30.1

^aEliminated from interpretation due to non-seawater REE+Y pattern. See Fig. 5B.

^bNo data available for samples measured by ICP-MS

Table S2: Major (wt%) and trace (ppb) element geochemical results (cont.)

	2.42	2.55 ^a	2.6 ^a	4.1	4.5	4.8
SiO ₂ ^b			68.63			
Al ₂ O ₃	0.16	0.58	0.44	0.12	0.16	0.15
Fe ₂ O ₃	20.20	21.53	25.87	6.61	11.66	11.33
MnO	0.08	0.11	0.07	0.23	0.05	0.23
MgO	0.77	0.93	0.73	2.06	0.41	2.44
CaO	1.55	2.66	1.45	5.59	1.49	5.47
K ₂ O	0.04	0.03	0.05	0.03	0.04	0.04
Na ₂ O	0.05	0.04	<0.01	0.04	0.06	0.07
P ₂ O ₅	0.09	0.15	0.07	0.22	0.25	0.31
LOI ^b			2.82			
Sc	1384	3131	5774	2333	710	1551
Ti	59035	110653	157343	41494	61312	49010
V	10098	33960	30909	10604	16209	10608
Co	1925	2193	2197	1284	793	1211
Ni	11543	9605	11162	1637	3345	1541
Ga	631	4316	4150	312	288	168
Y	5707	6097	4753	10844	5733	7921
Zr	2738	11185	16908	4340	2832	1448
Nb	194	536	471	106	222	96
Mo	931	301	238	52	368	129
Sb	283	223	319	87	162	347
La	1035	712	859	775	550	812
Ce	2170	2383	2749	2502	1562	1950
Pr	297	416	412	415	236	265
Nd	1402	2384	1921	2216	1199	1266
Sm	352	1015	556	700	366	347
Eu	94	301	166	209	111	101
Gd	503	1342	744	999	576	516
Tb	84	189	126	168	95	93
Dy	618	1059	799	1176	670	719
Ho	162	209	180	293	167	196
Er	539	517	528	905	501	667
Tm	93	68	86	139	71	110
Yb	678	417	600	924	435	779
Lu	115	65	99	148	67	129
Hf	34	131	89	34	37	24
Ta	6	13	8	4	4	3
W	204	370	403	22	234	32
Pb	883	1108	1134	754	1126	510
Th	55	130	148	65	65	29
U	117	125	221	17	36	37
Pr/Yb	0.17	0.38	0.26	0.17	0.21	0.13
La/La*	1.33	0.97	0.78	0.92	1.03	1.20
Ce/Ce*	1.05	1.01	0.95	0.98	1.03	1.07
Eu/Eu*	0.96	1.17	1.09	1.08	1.07	1.01
Gd/Gd*	1.16	1.04	0.97	1.09	1.12	1.12
Y/Ho	35.3	29.1	26.5	37.0	34.3	40.4

^aEliminated from interpretation due to non-seawater REE+Y pattern. See Fig. 5B.

^bNo data available for samples measured by ICP-MS

Table S2: Major (wt%) and trace (ppb) element geochemical results (cont.)

	4.83	4.9	5	5.1	5.3	5.48
SiO ₂ ^b	71.51	68.79				75.15
Al ₂ O ₃	0.15	0.43	0.12	0.08	0.10	0.12
Fe ₂ O ₃	21.41	25.72	21.33	21.05	18.77	19.61
MnO	0.08	0.08	0.01	0.01	0.01	0.06
MgO	0.86	0.69	0.07	0.03	0.06	0.44
CaO	2.15	1.46	0.48	0.45	0.45	1.51
K ₂ O	0.04	0.05	0.02	0.02	0.02	0.02
Na ₂ O	<0.01	<0.01	0.02	0.05	0.02	<0.01
P ₂ O ₅	0.17	0.07	0.21	0.33	0.29	0.23
LOI ^b	3.36	2.83				1.95
Sc	683	1065	782	491	495	1171
Ti	49643	110933	40048	38442	38156	58642
V	17546	19486	11685	9297	8581	9352
Co	630	2367	960	706	715	1220
Ni	1988	3899	1244	1224	708	1133
Ga	281	278	167	130	97	106
Y	2475	2281	3384	5666	5072	5298
Zr	2260	4346	2160	1951	2189	2558
Nb	124	219	101	91	109	139
Mo	382	497	426	378	274	280
Sb	1124	566	232	512	264	238
La	296	322	289	476	448	495
Ce	789	767	721	1183	1201	1283
Pr	105	101	105	172	183	182
Nd	471	445	529	883	946	907
Sm	123	117	137	219	232	223
Eu	36	34	40	63	67	66
Gd	179	161	230	369	377	355
Tb	32	30	41	67	69	68
Dy	248	236	327	541	540	535
Ho	68	65	90	150	143	148
Er	229	232	288	483	460	501
Tm	38	42	44	70	70	83
Yb	261	307	286	427	439	583
Lu	43	53	46	65	69	99
Hf	32	53	21	16	17	21
Ta	3	7	1	1	1	2
W	143	67	74	62	36	51
Pb	1060	812	319	479	266	287
Th	33	52	33	32	43	50
U	127	182	65	62	56	58
Pr/Yb	0.16	0.13	0.14	0.16	0.16	0.12
La/La*	0.97	1.08	1.18	1.25	1.12	1.16
Ce/Ce*	1.02	1.03	1.05	1.08	1.04	1.07
Eu/Eu*	1.00	1.01	0.96	0.96	0.96	0.98
Gd/Gd*	1.10	1.10	1.15	1.17	1.12	1.08
Y/Ho	36.5	35.2	37.6	37.7	35.4	35.7

^aEliminated from interpretation due to non-seawater REE+Y pattern. See Fig. 5B.

^bNo data available for samples measured by ICP-MS

Table S2: Major (wt%) and trace (ppb) element geochemical results (cont.)

	5.6	9.18	11.68 ^a	12.18 ^a	13.5	13.6
SiO ₂ ^b	72.49	79.64	70.4	68.26		
Al ₂ O ₃	0.13	0.07	1.77	0.87	0.63	0.69
Fe ₂ O ₃	21.97	10.64	20.91	28.54	6.83	21.89
MnO	0.08	0.15	0.09	0.04	0.27	0.14
MgO	0.7	0.95	0.83	0.35	2.67	0.82
CaO	1.46	2.95	1.93	0.64	6.18	6.05
K ₂ O	0.03	0.01	0.03	0.02	0.09	0.02
Na ₂ O	<0.01	<0.01	<0.01	<0.01	0.03	0.04
P ₂ O ₅	0.05	0.04	0.06	0.04	0.11	0.20
LOI ^b	2.61	4.39	4.16	2.18		
Sc	1079	3003	16615	11307	6918	5767
Ti	74294	14069	749723	574084	214646	275979
V	15468	5763	223928	143453	11406	38006
Co	2072	297	2691	2461	1235	2113
Ni	3464	553	12409	12625	2829	10936
Ga	403	82	14090	8519	682	3655
Y	3231	2363	46191	36753	10445	13131
Zr	3822	486	339358	273230	4121	9130
Nb	195	19	7047	4246	354	408
Mo	486	38	149	364	32	86
Sb	458	33	244	168	93	171
La	380	144	699	575	2240	467
Ce	870	310	2037	1930	4840	1507
Pr	113	48	304	310	665	268
Nd	499	241	1444	1537	2991	1420
Sm	135	63	549	534	737	400
Eu	38	19	225	205	258	120
Gd	196	99	1239	1119	979	701
Tb	36	20	374	306	175	129
Dy	298	179	3943	3156	1238	1048
Ho	87	57	1323	1053	314	310
Er	323	216	5303	4291	982	1167
Tm	59	41	1010	826	157	229
Yb	468	324	7474	6234	1069	1924
Lu	83	59	1266	1063	174	358
Hf	42	6	13345	10055	117	236
Ta	5	0	19	27	41	13
W	78	2	97	91	53	72
Pb	1027	301	12033	6046	809	1498
Th	49	18	1761	1204	604	101
U	164	19	198	165	38	28
Pr/Yb	0.09	0.06	0.02	0.02	0.24	0.05
La/La*	1.13	1.28	0.90	0.78	1.17	0.84
Ce/Ce*	1.04	0.98	0.98	0.95	1.00	0.91
Eu/Eu*	0.95	0.96	1.05	1.04	1.27	0.98
Gd/Gd*	1.15	1.19	0.91	0.99	1.04	1.16
Y/Ho	37.1	41.4	34.9	34.9	33.3	42.4

^aEliminated from interpretation due to non-seawater REE+Y pattern. See Fig. 5B.

^bNo data available for samples measured by ICP-MS

Table S2: Major (wt%) and trace (ppb) element geochemical results (cont.)

	13.95	14.73	15.5	16.5	17.28	17.78
SiO ₂ ^b		67.31			64.01	60.9
Al ₂ O ₃	0.11	0.88	0.10	0.64	0.11	0.15
Fe ₂ O ₃	9.09	25.38	22.12	20.01	31.28	32.93
MnO	0.02	0.09	0.03	0.04	0.07	0.1
MgO	0.22	0.71	0.25	0.13	0.62	0.63
CaO	0.87	2.02	1.22	0.62	1.43	2.34
K ₂ O	0.01	0.03	0.02	0.03	0.02	0.02
Na ₂ O	0.02	<0.01	0.03	0.05	<0.01	<0.01
P ₂ O ₅	0.34	0.16	0.41	0.06	0.23	0.55
LOI ^b		3.55			2.14	2.42
Sc	2007	3736	742	719	1277	1124
Ti	113272	274385	54396	57263	94533	59694
V	9963	37129	10779	11769	11995	11845
Co	820	2190	641	595	1269	2038
Ni	1982	16309	1237	1155	1530	2631
Ga	204	6403	133	211	145	217
Y	10712	4774	5935	7040	6477	10330
Zr	2049	11747	2483	2784	3481	2893
Nb	130	388	135	146	177	137
Mo	49	180	75	58	113	126
Sb	40	200	383	410	347	256
La	806	290	485	532	651	1205
Ce	2566	794	1326	1646	1628	3010
Pr	431	129	194	255	216	410
Nd	2376	664	962	1267	1001	1895
Sm	537	198	221	333	227	459
Eu	143	66	63	96	66	125
Gd	713	350	340	516	352	664
Tb	127	63	65	95	70	126
Dy	1021	473	548	760	588	1032
Ho	288	128	155	203	170	284
Er	932	427	539	665	597	934
Tm	142	73	89	103	105	146
Yb	902	525	632	671	788	951
Lu	141	92	103	105	135	154
Hf	40	265	26	29	54	34
Ta	12	11	3	3	5	4
W	29	70	32	40	25	82
Pb	566	1065	562	668	582	1072
Th	147	102	37	49	56	67
U	64	29	39	25	30	244
Pr/Yb	0.18	0.09	0.12	0.15	0.11	0.17
La/La*	0.98	1.03	1.05	0.89	1.11	1.08
Ce/Ce*	1.01	0.97	1.04	0.98	1.07	1.04
Eu/Eu*	0.96	1.08	0.96	0.98	0.96	0.93
Gd/Gd*	1.17	1.11	1.14	1.14	1.11	1.13
Y/Ho	37.2	37.4	38.2	34.6	38.0	36.4

^aEliminated from interpretation due to non-seawater REE+Y pattern. See Fig. 5B.

^bNo data available for samples measured by ICP-MS

Table S2: Major (wt%) and trace (ppb) element geochemical results (cont.)

	18.4 ^a	19.58 ^a	21.13	21.58	21.68	26.18
SiO ₂ ^b	80.57	80.15	60.23	62.54	64.31	70.93
Al ₂ O ₃	2.42	0.14	0.14	0.14	0.14	0.15
Fe ₂ O ₃	11.51	11.33	28.19	34.83	33.17	13.49
MnO	0.06	0.15	0.18	0.02	0.02	0.23
MgO	1.16	1.31	1.09	0.16	0.2	1.38
CaO	1.49	2.98	4.06	0.85	0.72	6.09
K ₂ O	0.14	0.02	0.02	0.02	0.04	0.03
Na ₂ O	<0.01	<0.01	<0.01	<0.01	0.15	<0.01
P ₂ O ₅	0.34	0.21	0.37	0.43	0.36	1.08
LOI ^b	2.66	4.29	5.09	0.71	0.76	6.62
Sc	5220	493	1236	1050	667	1114
Ti	182296	45014	48249	82750	64648	39606
V	88326	4841	6387	23097	16183	2769
Co	994	144	521	778	429	670
Ni	3422	366	914	1484	801	859
Ga	3331	81	86	182	142	62
Y	6254	6514	8679	5369	4345	13123
Zr	5276	1372	2934	4140	2459	1972
Nb	502	116	112	334	181	113
Mo	37	25	59	98	89	70
Sb	77	28	222	576	375	115
La	665	1668	545	858	648	896
Ce	2730	4877	1684	2153	1649	2308
Pr	521	782	285	286	227	333
Nd	3084	4135	1470	1313	1042	1605
Sm	942	693	410	334	277	430
Eu	263	161	121	94	80	122
Gd	1096	714	632	494	409	699
Tb	163	107	115	89	75	129
Dy	973	733	886	675	566	1061
Ho	206	182	239	174	145	309
Er	529	523	785	574	475	1107
Tm	66	72	127	97	79	188
Yb	368	416	892	691	554	1346
Lu	52	62	147	113	90	225
Hf	121	30	25	48	38	25
Ta	10	5	2	5	4	4
W	63	16	24	88	62	12
Pb	851	434	503	817	561	352
Th	130	54	48	81	68	46
U	26	21	35	67	51	22
Pr/Yb	0.54	0.72	0.12	0.16	0.16	0.10
La/La*	0.77	1.03	0.88	1.09	1.04	1.07
Ce/Ce*	0.95	1.01	0.93	1.06	1.02	1.02
Eu/Eu*	1.13	0.97	1.01	0.98	1.00	0.95
Gd/Gd*	1.05	1.19	1.10	1.09	1.09	1.17
Y/Ho	30.3	35.8	36.3	30.9	29.9	42.5

^aEliminated from interpretation due to non-seawater REE+Y pattern. See Fig. 5B.

^bNo data available for samples measured by ICP-MS

Table S2: Major (wt%) and trace (ppb) element geochemical results (cont.)

	27.08	27.13	31.63 ^a	32.18	33.21	33.32
SiO ₂ ^b	67.18	67.73				
Al ₂ O ₃	0.08	0.1	0.14	0.13	0.29	0.08
Fe ₂ O ₃	29.53	30.55	24.02	17.99	18.44	29.77
MnO	0.04	0.02	0.04	0.01	0.02	0.01
MgO	0.24	0.14	0.24	0.07	0.07	0.01
CaO	1.03	0.75	1.54	0.59	0.26	0.12
K ₂ O	0.02	0.02	0.02	0.03	0.02	0.02
Na ₂ O	<0.01	<0.01	0.04	0.08	0.04	0.05
P ₂ O ₅	0.27	0.38	0.81	0.31	0.07	0.11
LOI ^b	1.23	0.56				
Sc	613	812	3407	519	1308	518
Ti	40914	40800	144072	79155	76539	38929
V	8048	9883	83306	13842	25891	17770
Co	832	743	1319	794	1325	1459
Ni	991	1037	3871	997	3267	1833
Ga	80	85	3852	194	1206	165
Y	5825	11377	2823	5223	2981	2800
Zr	2416	2637	12854	1917	4857	2207
Nb	132	163	1403	160	262	125
Mo	116	131	110	269	264	548
Sb	254	296	199	250	158	281
La	493	1035	254	385	254	187
Ce	1149	2820	762	1094	568	515
Pr	195	508	122	162	99	98
Nd	1004	2540	599	839	484	494
Sm	242	624	199	221	143	145
Eu	68	171	67	68	43	45
Gd	386	888	304	338	229	225
Tb	65	147	54	59	43	43
Dy	494	1080	391	462	339	332
Ho	137	288	96	131	93	89
Er	448	915	318	444	324	303
Tm	70	139	54	68	57	49
Yb	459	862	392	436	437	331
Lu	75	135	66	69	76	54
Hf	24	26	447	25	44	20
Ta	2	2	8	6	4	2
W	38	44	123	43	94	79
Pb	337	2518	2274	899	8422	678
Th	24	30	89	48	42	26
U	56	87	53	43	71	88
Pr/Yb	0.16	0.23	0.12	0.14	0.09	0.11
La/La*	1.14	0.87	0.87	1.10	1.06	0.83
Ce/Ce*	0.92	0.85	0.94	1.07	0.86	0.81
Eu/Eu*	0.97	0.99	1.15	1.06	0.99	1.02
Gd/Gd*	1.19	1.16	1.06	1.18	1.08	1.05
Y/Ho	42.5	39.5	29.3	39.9	32.2	31.5

^aEliminated from interpretation due to non-seawater REE+Y pattern. See Fig. 5B.

^bNo data available for samples measured by ICP-MS

Table S2: Major (wt%) and trace (ppb) element geochemical results (cont.)

	33.61	33.91	34.11 ^a	34.5
SiO ₂ ^b				79.98
Al ₂ O ₃	0.09	0.08	0.12	0.54
Fe ₂ O ₃	20.24	22.56	9.71	16.6
MnO	0.01	0.01	0.01	0.03
MgO	0.00	0.01	0.01	0.17
CaO	0.05	0.03	0.13	0.12
K ₂ O	0.02	0.02	0.02	0.02
Na ₂ O	0.02	0.04	0.03	<0.01
P ₂ O ₅	0.04	0.04	0.07	0.03
LOI ^b				2.53
Sc	348	733	79	802
Ti	46383	38349	61272	66170
V	15616	14124	15047	21551
Co	668	985	85	1302
Ni	1080	877	468	3143
Ga	125	201	204	1238
Y	1027	1663	1399	2225
Zr	2432	2336	1075	2244
Nb	149	127	151	115
Mo	347	465	172	469
Sb	173	314	142	89
La	128	138	190	222
Ce	277	322	494	552
Pr	41	49	89	88
Nd	185	234	498	444
Sm	50	67	167	128
Eu	15	20	49	42
Gd	74	99	213	163
Tb	15	21	31	30
Dy	120	173	181	227
Ho	33	50	39	61
Er	124	186	103	217
Tm	23	34	14	38
Yb	177	248	80	279
Lu	30	42	11	46
Hf	22	22	17	30
Ta	2	1	2	3
W	39	86	77	65
Pb	343	655	453	624
Th	27	18	28	24
U	52	78	27	40
Pr/Yb	0.09	0.08	0.43	0.12
La/La*	1.09	1.10	1.14	1.09
Ce/Ce*	0.93	0.96	0.95	0.96
Eu/Eu*	1.01	0.97	1.14	1.17
Gd/Gd*	1.06	1.06	1.07	1.08
Y/Ho	31.2	33.3	36.1	36.2

^aEliminated from interpretation due to non-seawater REE+Y pattern. See Fig. 5B.

^bNo data available for samples measured by ICP-MS

2.12.4 Supplementary references

- Babechuk, M.G., Kamber, B.S., Greig, A., Canil, D. and Kodolanyi, J. 2010. The behavior of tungsten during mantle melting revisited with implications for planetary differentiation time scales. *Geochimica et Cosmochimica Acta*, 74: 1448-1470.
- Baldwin, G.J., Thurston, P.C. and Kamber, B.S. in press. Using in situ analytical techniques to identify chemical microbands in chert for high-precision total dissolution ICP-MS analysis of the rare earth elements. *Chemical Geology*, 285: 133-143.
- Kamber, B.S. 2009. Geochemical fingerprinting: 40 years of analytical development and real world applications. *Applied Geochemistry*, 24: 1074-1086.
- Kamber, B.S., Greig, A., Schoenberg, R. and Collerson, K.D. 2003. A refined solution to Earth's hidden niobium: implications for evolution of continental crust and mode of core formation. *Precambrian Research*, 126: 289-308.
- Ulrich, T., Kamber, B.S., Jugo, P.J. and Tinkham, D.K. 2009. Imaging element-distribution patterns in minerals by laser ablation - inductively coupled plasma - mass spectrometry (LA-ICP-MS). *Canadian Mineralogist*, 47: 1001-1012.
- Ulrich, T., Kamber, B.S., Woodhead, J.D. and Spencer, L.A. 2010. Long term observations of isotope ratio accuracy and reproducibility using quadrupole ICP mass spectrometry. *Geostandards and Geoanalytical Research*, 34: 161-174.

Chapter 3: Mo isotopic composition of the mid-Neoproterozoic ocean: an iron formation perspective

3.1 Abstract

The Neoproterozoic was a major turning point in Earth's surficial history, recording several widespread glaciations, the first appearance of complex metazoan life, and a major increase in atmospheric oxygen. Marine redox proxies have resulted in many different estimates of both the timing and magnitude of the increase in free oxygen, although the consensus has been that it occurred following the Marinoan glaciation, the second globally recorded "snowball Earth" event. A critically understudied rock type of the Neoproterozoic is iron formation associated with the Sturtian (first) glaciation. Samples from the <716 Ma Rapitan iron formation were analysed for their Re concentrations and Mo isotopic composition to refine the redox history of its depositional basin. Rhenium concentrations and Re/Mo ratios are consistently low throughout the bottom and middle of the iron formation, reflecting ferruginous to oxic basinal conditions, but samples from the uppermost jasper layers of the iron formation show significantly higher Re concentrations and Re/Mo ratios, indicating that iron formation deposition was terminated by a shift towards a sulfidic water column. Similarly, the $\delta^{98}\text{Mo}$ values are close to 0.0‰ throughout most of the iron formation, but rise to $\sim+0.7\text{‰}$ near the top of the section. The $\delta^{98}\text{Mo}$ from samples of ferruginous to oxic basinal conditions are the product of adsorption to hematite, indicating that the Neoproterozoic open ocean may have had a $\delta^{98}\text{Mo}$ of $\sim-1.8\text{‰}$. Together with the now well-established lack of a positive Eu anomaly in Neoproterozoic iron formations, these results suggest that the ocean was predominantly oxygenated at 700 Ma.

3.2 Introduction

The Neoproterozoic was a critical time in the Earth's surficial evolution. It witnessed the global "snowball Earth" glaciations (Kirschvink, 1992) and the subsequent appearance of the first complex metazoan life (e.g., Canfield et al., 2007). One of the most significant developments in the Neoproterozoic was a major rise in atmospheric oxygen content and the apparently concomitant increase in marine oxygenation (Och and Sheilds-Zhou, 2012). This ventilation of the ocean represents a major change from conditions earlier in the Proterozoic. Following the Great Oxygenation Event (GOE) between 2.4 and 2.3 Ga (Bekker et al., 2004), the ocean apparently remained unoxygenated at depth throughout the Paleo- and Mesoproterozoic. The precise redox conditions of the deep open ocean during this time are subject to considerable debate, and it has been suggested that the global deep ocean was sulfidic during this time (Canfield, 1998). Studies using both iron speciation (e.g., Shen et al., 2002; Poulton et al., 2004) and molybdenum isotopes (Arnold et al., 2004) initially supported this interpretation. More recent work has shown, however, that the deep ocean was probably ferruginous or even locally oxic during this interval (e.g., Slack et al., 2007; Poulton et al., 2010; Planavsky et al., 2011), and remained so into the early to middle Neoproterozoic (e.g., Johnston et al., 2010), and perhaps into the Ediacaran (e.g., Canfield et al., 2008; Li et al., 2010). The growing consensus is that the Proterozoic water column was oxygenated at shallow depths, had ferruginous deep water, and contained limited, near-shelf, mid-depth sulfidic conditions around areas with high biological primary productivity and organic carbon burial (Poulton and Canfield, 2011).

The gradual redox evolution of the ocean is reflected by several geochemical proxies, including Mo concentrations in black shales (e.g., Scott et al., 2008), which show a distinct, three-step increase over time, corresponding to the GOE and the late Neoproterozoic rise in oxygen ("NOE"), respectively. This gradual increase in Mo content in black shale and the implied commensurate rise in seawater Mo was explained as the result of more widespread anoxic and sulfidic water masses in the ocean than prevail today. Accordingly, the Mo inventory of seawater was limited prior to the NOE by Mo fixation into sediment below sulfidic water masses (Scott et al., 2008). Due to this increased Mo fixation rate, it is generally assumed that the $\delta^{98}\text{Mo}$ composition of Proterozoic seawater would have been isotopically light, because under high sulfide concentrations Mo is scavenged from ambient seawater without significant isotope

fractionation (Neubert et al., 2008). This behaviour would result in Proterozoic seawater being $\geq 1.0\%$ lighter than its modern counterpart, as has been observed in black shales of both Meso- (Arnold et al., 2004) and early Neoproterozoic age (Dahl et al., 2011). These interpretations rely on the assumption that the studied shales were deposited in basins with full connectivity to the open ocean and that other redox proxies can reliably distinguish between sulfidic, ferruginous, or oxic conditions. Their validity notwithstanding, these studies represent all but two data points covering a time interval in excess of one billion years, clearly indicating the need for further work in this area.

An additional, unusual attribute of the Neoproterozoic was the deposition of iron formation, which, with very few exceptions, had not occurred since the late Paleoproterozoic (Bekker et al., 2010). Although the ocean had apparently remained ferruginous throughout the Meso- and early Neoproterozoic, very little iron formation was deposited except during the <716 Ma Sturtian glaciation (Macdonald et al., 2010a; 2010b), with a few older (e.g., Slack et al., 2007) exceptions. Numerous models have been proposed to explain the causes for the return of iron formation, and the development of the widespread “snowball Earth” glacial events have been critical in the development of these models (e.g., Klein and Beukes, 1993; Baldwin et al., 2012). Equally important was the development of a complex water column redox stratigraphy, similar to that described by Poulton and Canfield (2011), which allowed for the build-up of significant dissolved iron in basins that deposited iron formations (Baldwin et al., 2012).

The least understood aspect of Sturtian iron formation is its apparently abrupt termination. Did a sudden influx of clastic detritus overwhelm deposition of hydrogenous sediment, or did water column chemistry change sufficiently to make the iron deposition impossible? Using trends in authigenic Mo enrichment, Baldwin et al. (2012) proposed that the water column was becoming more sulfidic towards the end of iron formation deposition, which eventually stopped the oxidation of dissolved ferrous iron to ferric iron oxy-hydroxides. This proposal was built on the elemental Mo proxy only. In the present study we set out to test this hypothesis more rigorously. Using jasper samples from the Rapitan iron formation, north-western Canada (Fig. 3.1A) that have already been characterised according to their sedimentology and their rare earth element (REE+Y), Mo, and U chemistry, we present $\delta^{98}\text{Mo}$ and Re elemental data to elucidate

the causes of the termination of iron formation deposition and provide insight into the $\delta^{98}\text{Mo}$ composition of middle Neoproterozoic seawater.

3.3 Sampling and analytical methods

3.3.1 Stratigraphy and sample selection

A continuous stratigraphic section through the Neoproterozoic Rapitan iron formation, Northwest Territories, Canada (Fig. 3.1A), was documented at centimetre-scale. Previously described by Baldwin et al. (2012), the iron formation at this location is 35 m thick, and is underlain by purple hematite- and clast-rich diamictite with localised channels of clast-supported tan polymictic conglomerate (Fig. 3.3). The iron formation is of the oxide-facies type, with the iron mineralogy consisting of jasper and hematite, and accessory calcite and dolomite present in small but variable abundances. Texturally, the iron formation is characterised by interbedded jasper and massive hematite beds, or banded iron formation (BIF), and is in nearly equal proportion to intervals of massive hematite with zoned, lensoidal jasper nodules 0.5-50 cm in diameter. Glacially derived dropstones are common throughout the iron formation, occurring in such high concentrations at several horizons as to constitute a hematite-matrix diamictite. Thin siliciclastic intervals of siltstone and polymictic conglomerate are also present (5-40 cm thick). The iron formation is sharply overlain by tan to grey, clast-poor diamictite (Fig. 1B, C), which contains a thin interval of hematite-bearing diamictite consisting of reworked iron formation clasts several metres above the uppermost intact iron formation layer (Fig. 3.1B). Textual evidence from dropstones indicates that, at a minimum, partial lithification occurred fairly early: even large dropstones (up to 15 cm) penetrate bedding by only a maximum of half the diameter of the dropstone (Fig. 3.2A). Similarly, textural evidence from hematite microbands shows that in addition to fairly early compaction and partial lithification, any primary iron mineralogy was converted to hematite very early in the diagenetic process, with bands at the sub-millimetre scale preserved both in outcrop (Fig. 3.2B) and at the microscopic scale (Fig. 3.2C).

Sampling focussed on jasper beds as opposed to nodular iron formation, for reasons explained in Baldwin et al. (2012). Jasper beds were mechanically separated from associated hematite beds, and all samples reported here are from jasper beds in the iron formation interval.

3.3.2 Digestion and trace element analysis

In view of the anticipated low Mo and Re concentrations, special care was taken to test reagents for blank levels prior to the analyses. The main source of blank was found to be HF, and for this reason, a dedicated batch of HF was produced by sub-boiling 5-fold distillation. The total procedural blank for Mo trace element analysis (i.e., digestion, dilution, and analysis) was determined in duplicate, and yielded 0.100 and 0.093 ng, respectively. Trace elements other than Re were determined by solution ICP-MS, and Mo analysis was calibrated with a dedicated standard-addition experiment (Baldwin et al., 2012). The accuracy of the Mo data was tested by comparison with data obtained by isotope dilution (see section 3.2.3) and was found to be excellent (Suppl. Fig. 3.1). Analyses took advantage of the high Si content (typically >65 wt%) of the samples, which results in low matrix load of the final solution (due to loss of Si as SiF₄). This afforded very low detection limits, as explained in Baldwin et al. (2011).

3.3.3 Rhenium

Sample stock solutions from trace element analysis of jasper samples used in Baldwin et al. (2012) were spiked with 20 pg of enriched ¹⁸⁵Re. The spiked solutions underwent a modified column separation chemistry after Fischer-Gödde et al. (2011) to remove elemental matrix for Re analysis. The purified Re solutions were analysed for isotope composition by isotope dilution inductively-coupled plasma mass spectrometry (ID-ICP-MS) on a Thermo X series II quadrupole ICP-MS at Laurentian University. Mass bias was estimated using the standard-sample-standard bracketing technique. Full errors in weights, spike composition, mass bias, and analysis were propagated (1-σ).

For the lowest-concentration samples the largest sources of uncertainty were the blank contribution (determined in triplicate to be 0.18±0.04 pg) and over-spiking. In the very lowest concentration samples, the blank contributed up to 40% of the total Re. The samples were spiked with 20 pg of ¹⁸⁵Re from an anticipated 800:1 mass ratio of Mo:Re, derived from exploratory

laser ablation ICP-MS (LA-ICP-MS) analysis of samples from the uppermost iron formation strata. These samples proved to be the ones with the lowest Mo:Re. Regardless of the large relative errors on the single-digit ppt data, the critical aspect of the data was that the majority of samples have exceedingly low Re contents. Rhenium concentrations were calculated based on the known natural isotopic abundances of ^{185}Re and ^{187}Re , and the recorded mass of added ^{185}Re .

Accuracy of the method was tested by analyses of the rock reference materials BHVO-1, BCR-2, and Sco-1. The Re concentrations obtained for these materials are slightly higher (6.5% for Sco-1, 6% for BHVO-2 and 19% for BCR-2) than those published by Meisel and Moser (2004), who did not digest with HF. According to Meisel et al. (2009), this outcome is because HF digests release Re held in silicates (e.g., clinopyroxene in the basaltic reference materials BHVO-1 and BCR-2).

3.3.4 Mo isotopes

The Mo-isotope data were obtained on aliquots of the same powder used for the trace element analysis. This had been carefully obtained from thin slices adjacent to thin sections. Between 0.63 and 1.44 g of powder aliquot was digested with a 4:1 mixture of 5-fold distilled HF and 3-fold distilled HNO_3 . The resulting solution was then spiked and split in two to allow for duplicate analyses. A ^{100}Mo - ^{97}Mo double spike was used to enable corrections for mass biases produced during chemical separation and MC-ICP-MS measurement. The use of a double-spike allows for the simultaneous determination of the Mo isotope composition and the Mo concentration using isotope dilution. The Mo concentration can be determined to a precision of $\pm 2\%$ (Greber et al. 2012). Molybdenum was separated from the sample matrix using a sequential procedure involving anion and cation exchange chromatography, as described in Wille et al. (2007). The anion chromatography was employed twice, to ensure total Fe removal. For each chemical separation step, 3x-distilled HCl and HNO_3 were used, resulting in a procedural blank of ≤ 1.5 ng Mo.

The $\delta^{98}\text{Mo}$ composition of all samples were analysed using a double-focussing Nu InstrumentsTM MC-ICP-MS system (Wrexham, Wales, UK). Measurement procedure and double-spike calibration are described in Greber et al. (2012), employing the double-spike mathematics outlined in Siebert et al. (2001). The precision under intermediate-precision

conditions is better than $\pm 0.1\%$ (2SD) for both liquid standards (see below) and the NIST SRM 610 and 612 glasses (see Table 1 and Greber et al. 2012). A Johnson Matthey ICP standard solution (lot 602332B) was used as reference material. Its $\delta^{98}\text{Mo}$ composition is 0.25‰ lower than the NIST SRM 3134 and 2.34‰ lower than the mean open ocean water Mo (Greber et al. 2012).

3.4 Results

3.4.1 Rhenium

Rhenium concentrations range from 2.3 to 358 parts per trillion (ppt), with a mean value of 39.8 ppt, and a median of 9.7 ppt, reflecting a strong bias in the dataset towards low concentrations. Eleven out of 22 samples have low concentrations of Re, with less than 10 ppt, whereas eight others have concentrations in the double-digit ppt. Only three samples contain >100 ppt Re, all from the top of the stratigraphic section, and all leaving reduced carbon stains in the digestion beakers. Single-digit Re concentrations are distributed throughout the section, whereas double-digit values are restricted to the bottom and middle of the succession. Recorded Re/Mo ratios, an extremely sensitive indicator of marine redox conditions (e.g., Crusius et al., 1996; Nameroff et al., 2002; Morford et al., 2005;), ranged from 6.49×10^{-6} to 1.02×10^{-3} (ppb/ppb), with mean values of 1.93×10^{-4} . Eighteen of 22 samples have Re/Mo ratios well below the average modern seawater ratio of 8.0×10^{-4} (Pattan and Pearce, 2009), whereas two of the three samples from the top of the section show higher Re/Mo ratios than modern seawater (Fig. 3.3).

Rhenium has a very low crustal abundance, and is rendered completely soluble during oxidative weathering, thus minimizing its detrital flux to the marine realm. Consequently, absolute concentrations can be used as a redox proxy in most sedimentary rock types without significant influence of detritally sourced Re. In clean hydrogenous sediment such as jasper, with very low Al content, the clastic mineral contribution to the total Re inventory is negligible. In the present dataset, there is no correlation between Re concentration and common clastic indicators such as Al, Sc, or Th. Under oxic marine conditions, Re is present as the highly soluble

perrhenate ion (ReO_4^-), but Re becomes reduced and more insoluble at oxygen levels just below the oxygen level at which U and Fe reduction take place, and well before the appearance of free H_2S (Morford and Emerson, 1999). In this context, the limited fixation rate throughout most of the iron formation implies predominantly oxic conditions. The appearance of significantly higher Re concentrations at the top of the section, however, records a pronounced shift towards increasingly anoxic conditions. This shift is also recorded by elevated Re/Mo ratios in the same samples. Typically, Re/Mo ratios well below those of modern seawater record oxic conditions, despite very low, depleted concentrations of both elements. This is due to the comparatively high (but absolutely very low) fixation rate of Mo through adsorption to Fe and Mn oxy-hydroxides in comparison to Re, which is unaffected by Fe and Mn cycling (Crusius et al., 1996; Morford and Emerson, 1999). Sedimentary Re/Mo ratios significantly greater than that of modern seawater, in turn, record suboxic to anoxic conditions due to strong Re fixation relative to Mo. Seawater-like ratios record sulfidic conditions due to strong fixation of both Re and Mo, thus preserving the ambient metal budget (Crusius et al., 1996). Samples from the top of the iron formation alternate between greater than and less than the modern seawater ratio, but clearly remain close to that value. This result suggests that, at the top of the section, the marine redox conditions were becoming increasingly anoxic, and possibly mildly sulfidic.

3.4.2 Mo isotopes

Molybdenum isotopic data, expressed as $\delta^{98}\text{Mo}$, range from -0.22 to +0.71‰, with errors in the range of 0.03-0.10‰. Throughout most of the stratigraphic section, $\delta^{98}\text{Mo}$ is at approximately crustal (0.0‰) to slightly negative values. One sample at 13.6 m is fractionated towards heavier $\delta^{98}\text{Mo}$, with a value of $0.37\text{‰} \pm 0.10\text{‰}$, but overlying samples show fractionation levels similar to those seen in lower strata. The uppermost three samples all have a significantly heavier Mo isotope signature, with $\delta^{98}\text{Mo}$ values of 0.51, 0.71, and 0.70‰.

Crustal $\delta^{98}\text{Mo}$ is approximately 0.0‰ (e.g., Barling et al., 2001), with crustal igneous rocks generally between -0.1‰ to +0.3‰ (Siebert et al., 2003). Published $\delta^{98}\text{Mo}$ values of crustal MoS_2 vary widely over a few per mil, but the average $\delta^{98}\text{Mo}$ value is $\sim 0.4\text{‰}$ (Greber et al., 2011). Modern open ocean water is homogeneous within $\leq \pm 0.2\text{‰}$ (2 SD), irrespective of ocean or water depth (e.g., Nakagawa et al., 2012; Siebert et al., 2003). Apparent variability between

other published $\delta^{98}\text{Mo}$ values for ocean water are probably due to different standards used in different laboratories, rather than a reflection of true ocean water heterogeneity (cf. Greber et al. 2012, Nakagawa et al., 2012). In the standardisation used here, the Mo isotope ocean water value is +2.34 ‰ (see Methods). Mo isotopes have been shown to fractionate negatively from modern ocean water ($\alpha_{\text{Mo}_{\text{sorb}} - \text{MoO}_4^{-2}} = 0.997$) down to $\delta^{98}\text{Mo}$ values of -0.1 to -0.8‰ through surface adsorption to Mn-oxides (e.g., Barling and Anbar, 2004). Fractionation on the surface of hematite, goethite or ferrihydrite (Goldberg et al., 2009) is somewhat smaller ($\alpha_{\text{Mo}_{\text{sorb}} - \text{MoO}_4^{-2}} = 0.998, 0.9985, \text{ and } 0.999$ respectively). By comparison, $\delta^{98}\text{Mo}$ signatures from modern sediments deposited under high sulfide concentrations show much less fractionation from modern seawater (Neubert et al., 2008), essentially preserving the seawater Mo isotopic composition.

The $\delta^{98}\text{Mo}$ values from samples low in the stratigraphic section (-0.22 to +0.06‰) show a range that would be expected from hematite-based Mo scavenging from ocean water with a modern Mo isotopic composition. The $\delta^{98}\text{Mo}$ signatures documented at the top of the iron formation (+0.51 to +0.71‰), however, fall firmly in the range for recent suboxic sediments that trend towards anoxic conditions (Poulson et al., 2006), and are significantly heavier than is expected in hematite-rich rocks.

According to scientific consensus, iron formation was formed by Fe^{2+} transformation to Fe^{3+} at a mixing zone with oxidizing seawater, precipitating as $\text{Fe}(\text{OH})_3$ -particles. The phase that most closely resembles this among the Fe-precipitates investigated by Goldberg et al. (2009) might therefore be goethite. However, the solid Fe-phase observed in the Rapitan IF is exclusively hematite. The basis for most models of oxide-facies IF is that the $\text{Fe}(\text{OH})_3$ -particles dehydrated to hematite prior to compaction. Therefore, oxide facies BIF should preserve pre-compaction particles of hematite (Krapež et al., 2003). Furthermore, the preservation of primary sedimentary textures in the hematite in samples analysed here suggests that the precursor mineral converted to hematite very early (Fig. 3.2A, B, C). Even if it does not form in the water column, but is the product of the transformation of an earlier metastable phase, hematite re-equilibrates with ocean water as long as it stays in contact with bottom water. Therefore, we consider hematite to be the relevant stable Fe-phase in further discussion. According to Goldberg et al.

(2009), the adsorption of Mo on hematite results in a negative fractionation of 1.8‰ to 2.0‰, unless extreme removal is assumed.

3.5 Discussion

3.5.1 Metal enrichments, Re and $\delta^{98}\text{Mo}$

A proper understanding of the implications of the documented Re and $\delta^{98}\text{Mo}$ compositions of the Rapitan iron formation requires direct comparison to other, simpler redox proxies, such as the authigenic elemental enrichments of the redox-sensitive Mo and U, expressed as unitless enrichment factors (Mo_{EF} and U_{EF} , respectively). In this study, enrichment factors were calculated by double-normalising Mo and U to the Al concentration and the upper continental crust composite MuQ (an alluvial sediment average, Kamber et al., 2005), using the formula $\text{EF} = ([\text{X}]_{\text{sample}}/\text{Al}_{\text{sample}})/([\text{X}]_{\text{MuQ}}/\text{Al}_{\text{MuQ}})$, X= either Mo or U concentrations (cf., Algeo and Tribovillard, 2009 and ref. within). Comparison to these elements is particularly useful, in that their behaviour in marine systems is well understood, and their redox sensitivities bracket those of Re, and also because enrichments of Mo and U have been a crucial line of evidence in the development of recent depositional models for Neoproterozoic IF (e.g., Baldwin et al., 2012).

The stratigraphic distribution of Re concentrations is similar to U enrichment factors throughout the thickness of the iron formation (Fig. 3). This covariation is because both elements are fixed under suboxic to non-sulfidic anoxic conditions, although Re requires slightly more reducing conditions for its fixation than does U. At the base and middle of the section, both elements show low to moderate enrichments (U) or concentrations (Re), but both values increase towards the top of the IF. Uranium, although only modestly enriched overall, shows its strongest enrichment at the bottom and in the middle of the section. Zones of increased U enrichment probably record open marine conditions at a redox level in the vicinity of Fe oxidation, because U and Fe oxidise at approximately similar O_2 levels, although below this threshold U fixation increases, whereas Fe solubility increases. Thus, horizons with the lowest U enrichment may record the zones of greatest iron oxidation and fixation. The general increase in U enrichment and substantial increase in Re concentration at the top of the iron formation indicate that marine conditions became more anoxic near the end of iron formation deposition.

Rhenium also roughly mirrors the distribution of the Mo_{EF} throughout much of the iron formation. The main difference is the elevated Mo enrichment at the base of the section, which has been interpreted to reflect brief, mildly sulfidic conditions at middle water depths immediately following glacial ice withdrawal (Baldwin et al., 2012), without driving significant Re fixation. Thus, it can also be assumed that adsorption of dissolved Mo and Mo-bearing phases onto Fe colloids may have been a factor. This is reflected by the weak correlation between Fe_2O_3 and Mo in samples with moderately high concentrations of both (Baldwin et al., 2012), resulting in elevated Mo enrichment at the bottom of the section without commensurate Re enrichment. The pronounced increase in both the Re/Mo ratio and $\delta^{98}Mo$, paired with very low Mo enrichment may at first seem counterintuitive. The most obvious explanation is that this arrangement could reflect a decrease in the oxidation state of the water column towards increased ferruginous conditions. Decreased production of Fe oxy-hydroxides would accompany an increase in ferruginous conditions and would limit both the Mo fixation rate (explaining the low Mo_{EF}), as well as the influence of hematite on the Mo isotopic budget, thereby allowing an increase in $\delta^{98}Mo$. This change would have been short-lived and fairly mild. Although the Re/Mo ratios show a strong increase, this is less driven by an increase in Re fixation, and much more strongly caused by the decrease in Mo fixation rates. Thus, this brief increase in Re/Mo and $\delta^{98}Mo$ can be explained as a decrease in the Fe oxy-hydroxide production rate due to a brief, slight decrease in oxygen availability in the water column. At the top of the iron formation, however, both Re concentrations and Mo_{EF} show a marked increase, which is coincident with elevated U_{EF} values and Re/Mo ratios that are comparable to those of modern seawater. The increased Mo enrichment at this stratigraphic level, paired with the seawater Re/Mo values, shows that marine conditions during deposition of the uppermost iron formation beds were rapidly transitioning from an oxic to suboxic/anoxic regime towards mildly sulfidic conditions.

If it is accepted that adsorption to hematite was the dominant fractionation process of Mo isotopes at the base and throughout most of the middle of the iron formation, an ocean water Mo isotope composition of around +1.8‰ can be inferred from the light $\delta^{98}Mo$ signatures in the jasper. The three stratigraphically highest samples, however, show higher $\delta^{98}Mo$ values, from +0.51 to +0.71‰. Other proxies from these samples (Mo_{EF} and Re/Mo) indicate mildly sulfidic conditions. This apparent mutual inconsistency between the $\delta^{98}Mo$ and trace element enrichments

could be resolved if deposition of significant volumes of hematite or other iron oxy-hydroxides continued at this stratigraphic level. In summary, the data are best explained if hematite deposition and (weakly) sulfidic water conditions coexisted.

Four hypotheses may help to explain the increased $\delta^{98}\text{Mo}$ values that accompany increasing anoxia at the top of the section:

- 1) Seawater $\delta^{98}\text{Mo}$ increased by $\sim 0.7\text{‰}$;
- 2) Diagenetic effects were imposed by the overlying diamictite;
- 3) The $\delta^{98}\text{Mo}$ of local water increased by 0.7‰ due to increased Mo sequestration (basin effect);
- 4) Alpha, (the fractionation factor) changed.

Considering hypothesis 1 first, we note that a general increase of the seawater $\delta^{98}\text{Mo}$ cannot be definitively tested using the present data set. However, a sudden increase by about 0.7‰ , coincident with a local change in redox conditions, appears to be an *ad hoc* assumption with relative low probability.

With regard to hypothesis 2, it is important to recall that the trend in all geochemical proxies towards an anoxic water column occurs exclusively in the uppermost metre of the iron formation. The iron formation is immediately overlain by non-hematitic glacioclastic sediment (Fig. 3.1B, C), which therefore do not have the strong negative Mo isotope fractionation to Fe-phases. The heavier $\delta^{98}\text{Mo}$ composition (and the rest of the chemical proxies) from the top of the section could be diagenetically mixed with the pore water of the glacioclastic sediment, which was shown to be possible in Goldberg et al. (2012). The possibility of diagenesis strongly influencing the $\delta^{98}\text{Mo}$ composition is deemed less probable, based on the fact that the top of the iron formation was mostly lithified before the diamictite was deposited, as shown by the presence of angular, reworked jasper clasts low in the diamictite.

Addressing hypothesis 3 (basin effect), the key criterion is that a $\delta^{98}\text{Mo}$ increase of the local water by 0.7‰ would require that the basin was becoming restricted and that significantly

more Mo was being sequestered. For example, Nägler et al. (2011) showed that in the Black Sea the anoxic water mass has a $\delta^{98}\text{Mo}$ composition of about 0.4 to 0.6‰ above mean open ocean water. However, for the IF studied here, REE+Y patterns (reported in Baldwin et al. 2012) do not change stratigraphically, and lack evidence for increasing water restriction overall. Hydrogenous sedimentary rocks from epi-continental basins have REE+Y patterns that are different from those of the open ocean (e.g., Kamber et al., 2004). Furthermore, covariance plots between $\delta^{98}\text{Mo}$ and several trace element proxies (Mo, Mo_{EF} , Re, and Re/Mo) clearly demonstrate that their enrichment is independent of the Mo isotopic composition: samples with elevated $\delta^{98}\text{Mo}$ ($\delta^{98}\text{Mo} > 0.20\text{‰}$) form a distinct sub-parallel to non-parallel trend with respect to each of these proxies from samples with lower $\delta^{98}\text{Mo}$ values (Fig. 3.4A-D). Not only does this support the independence of the trace element proxies from the processes that drove Mo isotopic fractionation, it also dissociates the $\delta^{98}\text{Mo}$ values from both the absolute Mo concentrations and relative Mo enrichment (Fig 3.4A, B). This strongly indicates that under all redox conditions, the $\delta^{98}\text{Mo}$ signature of the sediment was controlled by processes that were distinct from those that controlled the elemental redox proxies. These observations render the basin effect an improbable explanation for the documented Mo isotope stratigraphy.

Finally, concerning hypothesis 4, it is important to recall that in general terms the Mo isotope fractionation factor can vary based on the redox condition of the water (e.g., Nägler et al., 2011; Neubert et al., 2008; Poulson et al., 2006). However, most studies attribute such fractionation to the formation of authigenic Fe-sulfides in the water column or in pore waters under anoxic water columns. In the studied jasper, all samples are consistently composed of quartz and hematite, and so a change of the fractionation factor that is tied to changes in the mineral precipitate species can be excluded. It has to be considered, though, that Mo isotope fractionation factors for adsorption on hematite under reducing conditions are not known. Apparently, as the seawater at the time of the uppermost part of the Rapitan IF was turning anoxic, its $\delta^{98}\text{Mo}$ signature adjusted to the smaller Mo isotope fractionation factor that prevailed under such conditions.

In summary, the first three hypotheses are all counter-indicated to various extents by other evidence, leaving the fractionation factor model as the only possible explanation. Given the non-

actualistic formation of these sedimentary rocks, a firm conclusion on the mechanistic processes resulting in a change of the fractionation factor (hypothesis 4) cannot be drawn. However, this hypothesis is compatible with all observations made: it explains the documented shift in $\delta^{98}\text{Mo}$ based on observed changes in the water column, is not in conflict with the elemental redox proxies that record a shift towards anoxia, and results in Mo isotopic signatures that are significantly heavier than is typical for hematite adsorption, but which are also lighter than the ambient Mo isotopic composition of seawater.

3.5.2 Implications for Neoproterozoic iron formation

The trace element and Mo isotopic data show that throughout the majority of iron formation deposition, marine redox conditions in the basin were predominantly driven by a combination of oxic and ferruginous conditions, as reflected by the large volume of hematite deposited in the iron formation, together with the low Mo enrichments, Re concentrations, and Re/Mo ratios. At the top of the iron formation, however, all available proxies indicate that the basin conditions were becoming anoxic to slightly sulfidic. The marked increase in the fixation rates of U, Mo, and Re shows that the redox state of the water column dropped well below the oxygen levels required for the oxidation of Fe^{2+} to Fe^{3+} . This pattern is perhaps best illustrated by the elevated Re/Mo ratios, which are comparable to those of modern seawater. Furthermore, the shift towards markedly positive $\delta^{98}\text{Mo}$ values shows a decreased fractionation from presumed ambient seawater conditions, with a maximum $\delta^{98}\text{Mo}$ of +0.71‰. This value is only slightly lower than previous estimates for the Mo isotopic composition for Mesoproterozoic (0.8‰; Arnold et al., 2004) and early Neoproterozoic ($1.0 \pm 0.1\%$; Dahl et al., 2011) seawater. Sulfidic conditions were gradually driving more complete Mo fixation, with an evolving fractionation factor, thus recording different $\delta^{98}\text{Mo}$ than would be expected based on the continued deposition of large volumes of iron oxy-hydroxides. The most important aspect of this shift is the fact that the heavy Mo isotopes and seawater Re/Mo ratios are preserved in samples at the very top of the iron formation, which is immediately overlain by *non-hematitic* glacioclastic sediment (Fig 1B, C). The abrupt termination of hematite deposition suggests either that the Fe^{2+} inventory in the Rapitan basin had been drawn down such that there was insufficient supply to continue depositing sedimentary iron (as iron formation or hematitic clastic sediment), or that the recorded

shift towards increasingly anoxic conditions abruptly terminated the oxidation of dissolved Fe^{2+} to Fe^{3+} , thereby keeping the iron in solution. This second explanation is more plausible due to its consistency with the other redox proxy data.

The observed shift away from oxic and ferruginous conditions, as recorded by the elemental proxies (Mo enrichment and Re/Mo) was not responsible for the termination of iron formation deposition across the entire basin. In Yukon, west of the study site, the uppermost strata of the iron formation consists of granular iron formation (GIF) (Baldwin and Turner, 2012; Klein and Beukes, 1993), which is in turn overlain by hematitic glacioclastic rocks. This relationship indicates that in some areas, particularly where the preserved iron formation is thickest, loss of accommodation space was probably the driving force behind the cessation of pure iron formation deposition. As accommodation space diminished, the clastic sedimentation rate to the deep basin increased, which would have volumetrically overwhelmed the background iron and silica precipitation, forming hematitic clastic rocks in lieu of iron formation. Thus, deposition of thick iron formation represents a condition of a perfect balance of ferruginous to oxic basinal redox conditions, a limited clastic sediment supply, and ample accommodation space. Elimination of any of these features, even at the local scale, apparently caused the fairly abrupt cessation of iron formation deposition.

3.5.3 Mo isotopic composition of the Neoproterozoic ocean

It has been suggested that Proterozoic seawater had a significantly lighter Mo isotopic composition than the modern ocean (e.g., Dahl et al., 2011). This proposal was based on several studies of Meso- and Neoproterozoic black shales that have been shown to be sulfidic using other proxies (e.g., iron speciation). These studies have shown that sulfidic shales from this time have $\delta^{98}\text{Mo}$ values more than 1.0‰ lighter (Arnold et al., 2004; Dahl et al., 2011), than the modern seawater value of +2.34‰ (Siebert et al., 2003; Greber et al., 2012), suggesting that seawater $\delta^{98}\text{Mo}$ remained stable at approximately 1.0‰ throughout the Proterozoic. The explanation for this apparent difference in seawater isotope composition is that more widespread sulfidic conditions in the Proterozoic would have resulted in an overall depletion of ^{98}Mo in seawater, leaving a lighter ambient $\delta^{98}\text{Mo}$ composition in normal marine seawater, which in turn was recorded in sulfidic black shales. A few of the samples analysed here have values similar to those

of many samples reported in Dahl et al. (2011), which were interpreted to record sulfidic conditions based on iron speciation data, and were thought to record ambient seawater $\delta^{98}\text{Mo}$ values. Thus, these authors proposed that the $\delta^{98}\text{Mo}$ composition of Neoproterozoic seawater was approximately $1.0\pm 0.1\text{‰}$. This claim is problematic for two reasons. First, Dahl et al. (2011) used an unusually low threshold in their iron speciation data ($\text{Fe}_P/\text{Fe}_{\text{HR}} = 0.5$) to distinguish sulfidic from suboxic to anoxic shales, on the grounds that the majority of the reactive iron is pyrite. Conventionally, a higher threshold of 0.7-0.8 is applied, to help eliminate the influence of diagenetic sulfidisation (Poulton and Canfield, 2011). Very few of the samples analysed by Dahl et al. (2011) meet the conventional threshold for this ratio, making the bulk of the dataset indicative of ferruginous rather than sulfidic conditions. This allows for the possibility that very little of their data records the true seawater $\delta^{98}\text{Mo}$ signature. Furthermore, Dahl et al. (2011) do not address why they preferred to assume an ocean water composition of 1.0‰ , even though their own detritus-corrected data for true sulfidic samples ($\text{Fe}_P/\text{Fe}_{\text{HR}} > 0.7$) is 1.25 ± 0.40 . The second problem is that samples analysed by Dahl et al. (2011) with $\text{Fe}_P/\text{Fe}_{\text{HR}}$ significantly below the criterion for sulfidic conditions (down to 0.0), also show the same $\delta^{98}\text{Mo}$ data as those few samples that supposedly represent ocean water. As shown by earlier publications, Mo isotope fractionation inevitably occurs under anoxic, non-sulfidic conditions (e.g., Poulson et al. 2006) or conditions with $\text{H}_2\text{S}_{\text{aq}}$ below the threshold value of $11\ \mu\text{M}\ \text{H}_2\text{S}_{\text{aq}}$ (Neubert et al., 2008). For example, in the Black Sea, at 400 m water depth, including a 250 m-thick sulfidic layer, sediment still records a $\delta^{98}\text{Mo}$ of 0.7‰ below seawater values, due to insufficient H_2S concentration. The most plausible explanation would be that the whole sequence adjusted its $\delta^{98}\text{Mo}$ values during diagenesis under anoxic waters (indicated by the semi-constant $\text{Fe}_{\text{HR}}/\text{Fe}_{\text{T}}$), which would imply a coeval seawater value of 0.7‰ above the sedimentary average (Poulson et al. 2006). We here maintain that this interpretation of Dahl et al. (2011) is not unique and the data are not incompatible with coeval ocean water $\delta^{98}\text{Mo}$ of $\sim 1.8\text{‰}$.

Taken at face value, the $\delta^{98}\text{Mo}$ data from the most anoxic samples published here fall into a similar range as the samples used by Dahl et al. (2011) to establish their proposed Neoproterozoic seawater composition. Although some of these samples record probable sulfidic conditions, as indicated by the Mo_{EF} and Re/Mo data, they are also hematite-rich rocks (i.e., iron

formation and jasper). This geological constraint, together with the redox proxy data and the presence of primary to very early diagenetic hematite, has important implications. Namely, across the entire basin, iron formation deposition was not stratigraphically coherent. Instead, a subtle interplay between basin subsidence, the relative proportion of clastic and hydrogenous sediment supply, elemental inventories (i.e., Fe and S), and ice cover resulted in variable deposition of Fe-rich rocks. Unusual basinal redox situations existed at a local scale and may be represented by IF horizons, which are appropriate for geochemical investigations owing to the lack of interfering clastic sediment. Such unusual redox situations had a profound effect on the typical processes controlling Mo isotopic behaviour. Qualitatively at least, it is evident that Mo isotopes in rocks containing hydrogenous hematite (or other Fe-oxides) show lighter isotopic compositions than coeval seawater, as is clearly recorded throughout most of the lower part of the Rapitan iron formation. Jasper samples with relatively heavy Mo isotopic signatures, therefore, must similarly be negatively fractionated from ambient seawater, regardless of the basinal redox conditions. It is impossible to quantify the ocean water Mo isotope signature from these anoxic samples, because the corresponding fractionation factor cannot be independently defined.

Heavy $\delta^{98}\text{Mo}$ signatures in the Rapitan IF record the interplay between two opposing fractionation mechanisms. Although the ambient sulfidic conditions in the water column apparently limited the fractionation away from the seawater composition, the continued rain of iron oxide/oxy-hydroxide flocculates through the sulfidic part of the water column from overlying oxic waters (Baldwin et al., 2012) still preferentially fixed light Mo, even under conditions favourable to complete, unfractionated fixation. The net result of these processes would be a sedimentary $\delta^{98}\text{Mo}$ composition that is significantly lighter than that of seawater, but also much higher than would be recorded under oxic to ferruginous conditions during normal hematite deposition, as is seen in the samples from the top of the iron formation, which have $\delta^{98}\text{Mo}$ of +0.7‰. Thus, although the highest $\delta^{98}\text{Mo}$ values reported here are lower than the previously proposed $\delta^{98}\text{Mo}$ composition of the Neoproterozoic ocean ($1.0\pm 0.1\text{‰}$), they clearly indicate that the isotopic composition must have been still higher than that, and much closer to that of the modern ocean. Although the Rapitan iron formation was deposited in a partly restricted rift basin, REE+Y data show that there was significant connectivity between the Rapitan basin and the open ocean (Baldwin et al., 2012). It is reasonable to assume that a basin

with moderate to high connectivity with the open ocean would have had the same isotopic composition as the global ocean. Therefore, as a working hypothesis, it can be inferred that global mid-Neoproterozoic seawater had a $\delta^{98}\text{Mo}$ composition of approximately 1.8‰, which is not much lower than that of the modern ocean. If true, this analogy to modern oceans implies a homogeneous ocean water composition. On the surface, this assumption is challenged by the possibility that, during the Neoproterozoic, the residence time of Mo was significantly shorter owing to a limited Mo ocean inventory. However, even if the Neoproterozoic Mo inventory was only 10% of that of the modern ocean (as suggested by Scott et al., 2009), the residence time of Mo would still be at least 44 k.y., based on a residence time of Mo in modern seawater of 440 k.y. This latter value, put forward by Miller et al. (2011), is the lowest proposed in recent literature. To allow for significant heterogeneity of the ocean water in terms of Mo isotopic composition, the ocean mixing time would have to have been in the range of the Mo residence time. Of course the true mixing time of the Neoproterozoic oceans is not known. A mixing time of 44 k.y., however, would be about 30 times longer than that of modern oceans. This is hardly realistic if there was any connectivity among the Neoproterozoic oceans at all. Thus, even if the Neoproterozoic Mo inventory was only 10% of the modern ocean, the resulting shorter residence time does not challenge the assumption of a nearly uniform ocean water Mo isotopic composition.

A near-modern marine Mo isotopic composition in the middle Neoproterozoic indicates that the deep ocean was already ventilated at that time. If the Neoproterozoic weathering regime of Mo was comparable to that of today, the principal control on the $\delta^{98}\text{Mo}$ composition of seawater would have been the generation of Mn and Fe oxy-hydroxides, and the subsequent adsorption of isotopically light Mo to these particles. This stands in sharp contrast with arguments for a lighter seawater $\delta^{98}\text{Mo}$ composition in the Neoproterozoic, which require moderately extensive, nearshore sulfidic water masses to limit the amount of heavy Mo in seawater (Dahl et al., 2011). Thus, the data presented here suggest that sulfidic conditions in the open ocean during the middle Neoproterozoic could have been only slightly more pervasive than today. Taken together with the well-established absence of the positive Eu anomaly in Neoproterozoic iron formations (e.g., Baldwin et al., 2012; Klein and Beukes, 1993; Klein and Ladeira, 2004; Lottermoser and Ashley, 2000), it appears that in the middle Neoproterozoic the

open ocean was well oxygenated, and that ferruginous and sulfidic conditions were limited to restricted and semi-restricted basin environments. The strong evidence for pervasive anoxia in the Ediacaran ocean (e.g., Canfield et al., 2008) suggests a post-“snowball Earth” return to more widespread reduced marine conditions.

3.6 Conclusions

Evidence from Re concentrations, Re/Mo ratios, and Mo isotope ratios shows that the prevailing basin redox conditions during deposition of the Rapitan iron formation were ferruginous trending towards oxic. Rhenium concentrations and Re/Mo ratios are consistently low throughout most of the thickness of the iron formation. Near the top of the section, however, both values increase by several orders of magnitude, recording a shift away from oxic to ferruginous conditions and towards anoxic to sulfidic conditions. Similarly, most of the iron formation has negative to mildly positive $\delta^{98}\text{Mo}$ compositions, most likely because adsorption to hematite was the primary cause of Mo isotopic fractionation. At the top of the iron formation, the $\delta^{98}\text{Mo}$ composition increases to +0.7‰, which, when considered together with other redox proxies (Mo enrichment, Re concentrations, and Mo/Re), records sulfidic conditions. The observed shift to sulfidic conditions, paired with the presence of non-hematitic glacioclastic sediments above the iron formation, indicates that these conditions locally terminated the deposition of iron formation. Correcting the $\delta^{98}\text{Mo}$ value for the isotope fractionation that occurs during adsorption to iron oxy-hydroxides, the Mo isotope composition of the Neoproterozoic ocean was around 1.8‰. A middle Neoproterozoic ocean with such $\delta^{98}\text{Mo}$ values indicates that the open ocean may have been well oxygenated at 700 Ma.

3.7 Acknowledgements

This paper is Northwest Territories Geoscience Office contribution number 0065. Field work was supported by the Northwest Territories Geoscience Office (NTGO) and Yukon Geological Survey (YGS). Substantial funding was also provided by National Science and

Engineering Research Council of Canada (NSERC) Discovery Grants to ECT and BSK, as well as a Society of Economic Geologists (SEG) student research grant to GJB. This paper benefitted greatly from the comments of editor R.R. Parrish and an anonymous reviewer. A. Gladu and J.A. Petrus are thanked for their assistance in the lab at Laurentian University. The ^{185}Re metal spike was supplied by O.M. Burnham of the Ontario Geoscience Laboratories (GeoLabs).

3.8 Figures

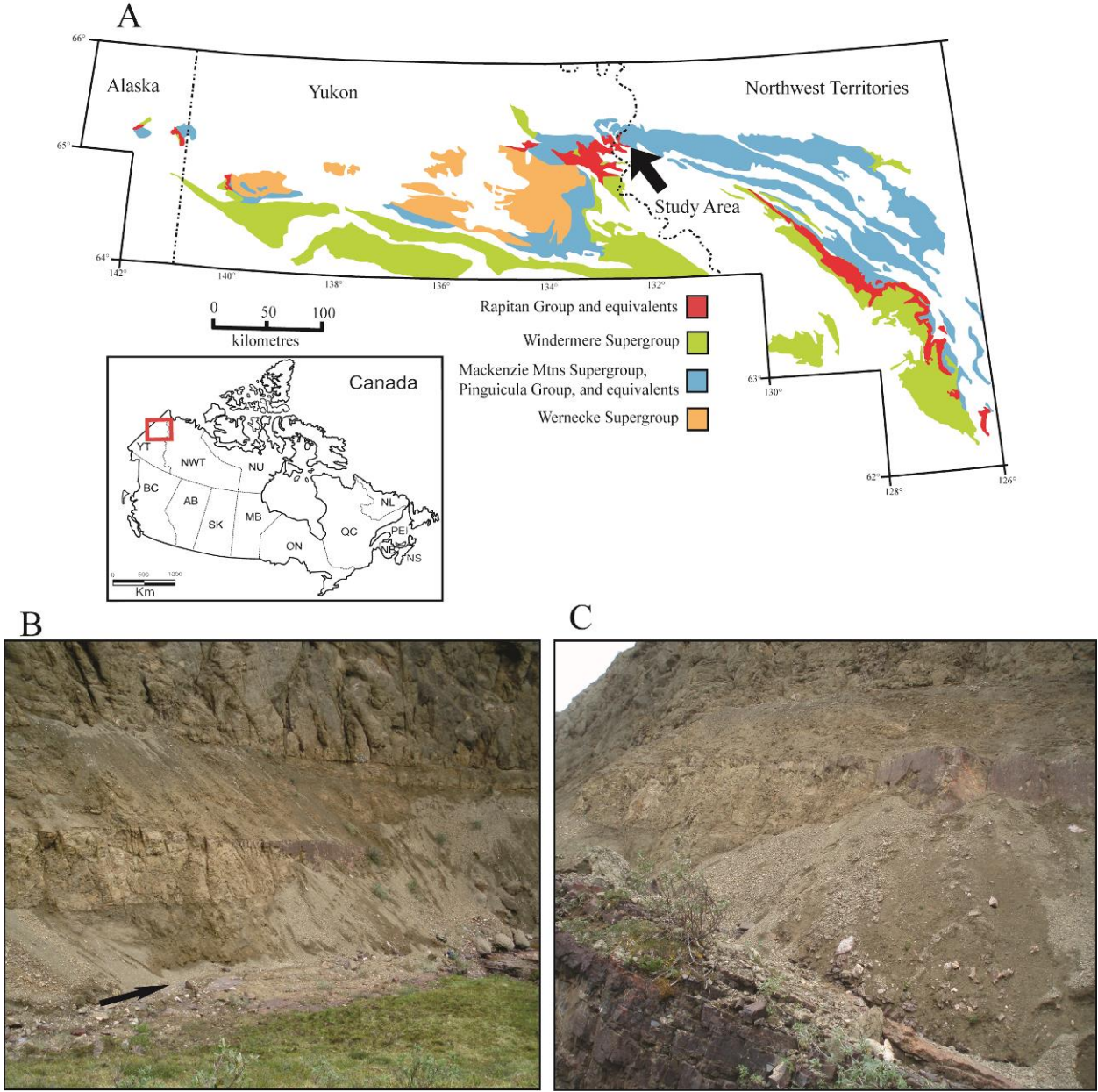


Figure 3.1: Map showing the distribution of Proterozoic sedimentary rocks in north-western Canada. The <716 Ma glaciogenic Rapitan Group is in red (from Baldwin et al., 2012), with an arrow indicating the location of the study area (A). Sharp upper contact between the Rapitan iron formation and the overlying non-hematitic glacioclastic rocks of the overlying Shezal Formation (B, C). The contact is partly obscured in each photo due to the recessive weathering character of the glacioclastics, but is indicated by an arrow in (B). Purple area on the cliff face in each photo is an area of reworked iron formation contained as a raft in the overlying glacioclastics; this unit is laterally discontinuous, as seen in each photograph.

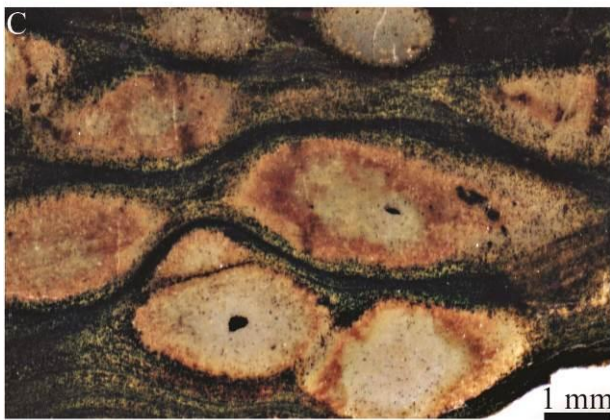


Figure 3.2: Photographs (A, B) and a photomicrograph (C) showing the preservation of primary sedimentary fabrics in hematite, suggesting a depositional or early diagenetic origin. Deformed bedding from a dropstone is preserved (A). Fine laminations in hematite visible on the outcrop scale (B) and sub-millimetre scale (C) around chert and carbonate nodules. Late conversion to hematite from precursor minerals would overprint some of these finer textures.

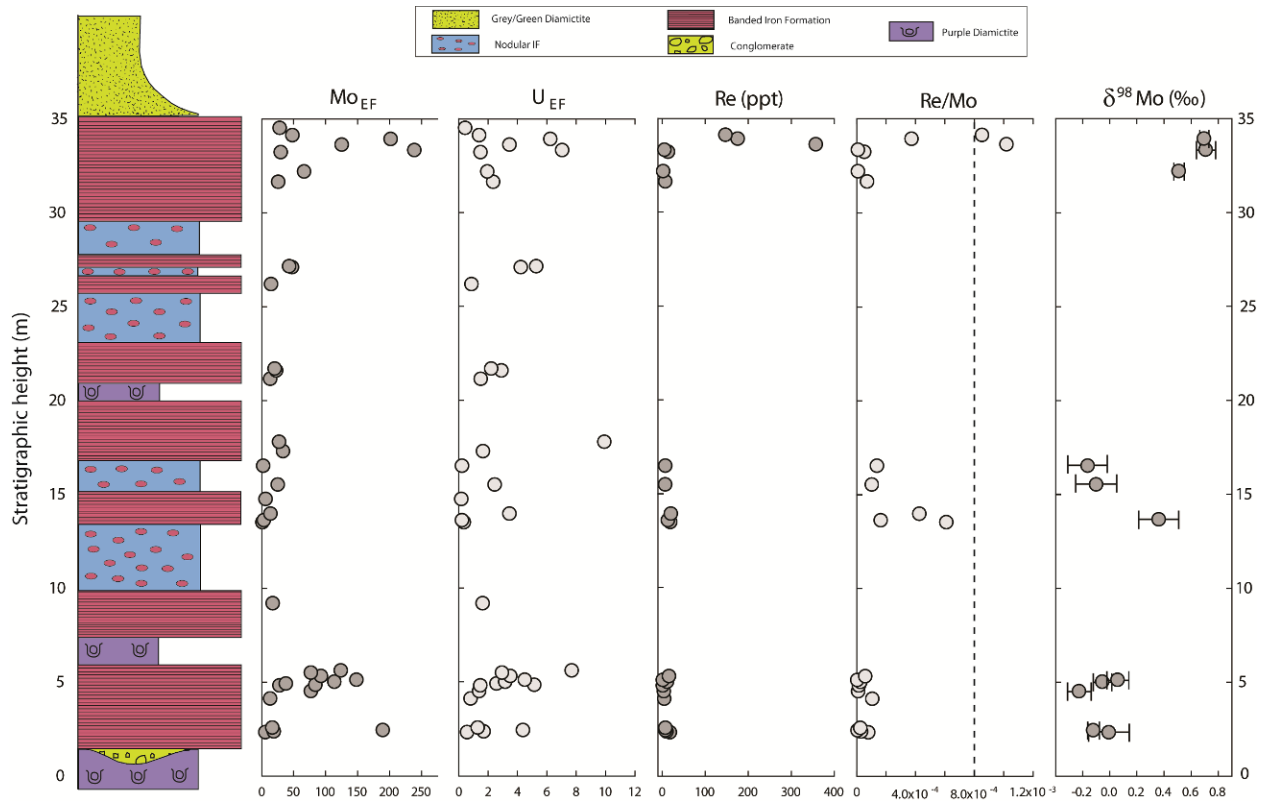


Figure 3.3: Simplified stratigraphic column of section CR1 (after Baldwin et al., 2012) with stratigraphic distributions of Mo_{EF} , U_{EF} , Re (ppt), Re/Mo, and $\delta^{98}Mo$ (‰). Mo, U, and Al concentration data (used to calculate enrichment factors and Re/Mo) are from Baldwin et al. (2012). With the exception of the moderate to strong Mo enrichment at the base of the section, Mo enrichment and Re concentration covary, both showing a pronounced increase at the top of the section. With the exception of the uppermost samples, the Re/Mo ratio is well below the modern seawater ratio of 8.0×10^{-4} (dashed line), but the uppermost samples are close to this value, recording sulfidic conditions. $\delta^{98}Mo$ (with 2σ error bars) is scattered between -0.2 and 0.1‰, recording sulfidic conditions paired with adsorption to hematite, except for a few higher values, most notably at the top of the section.

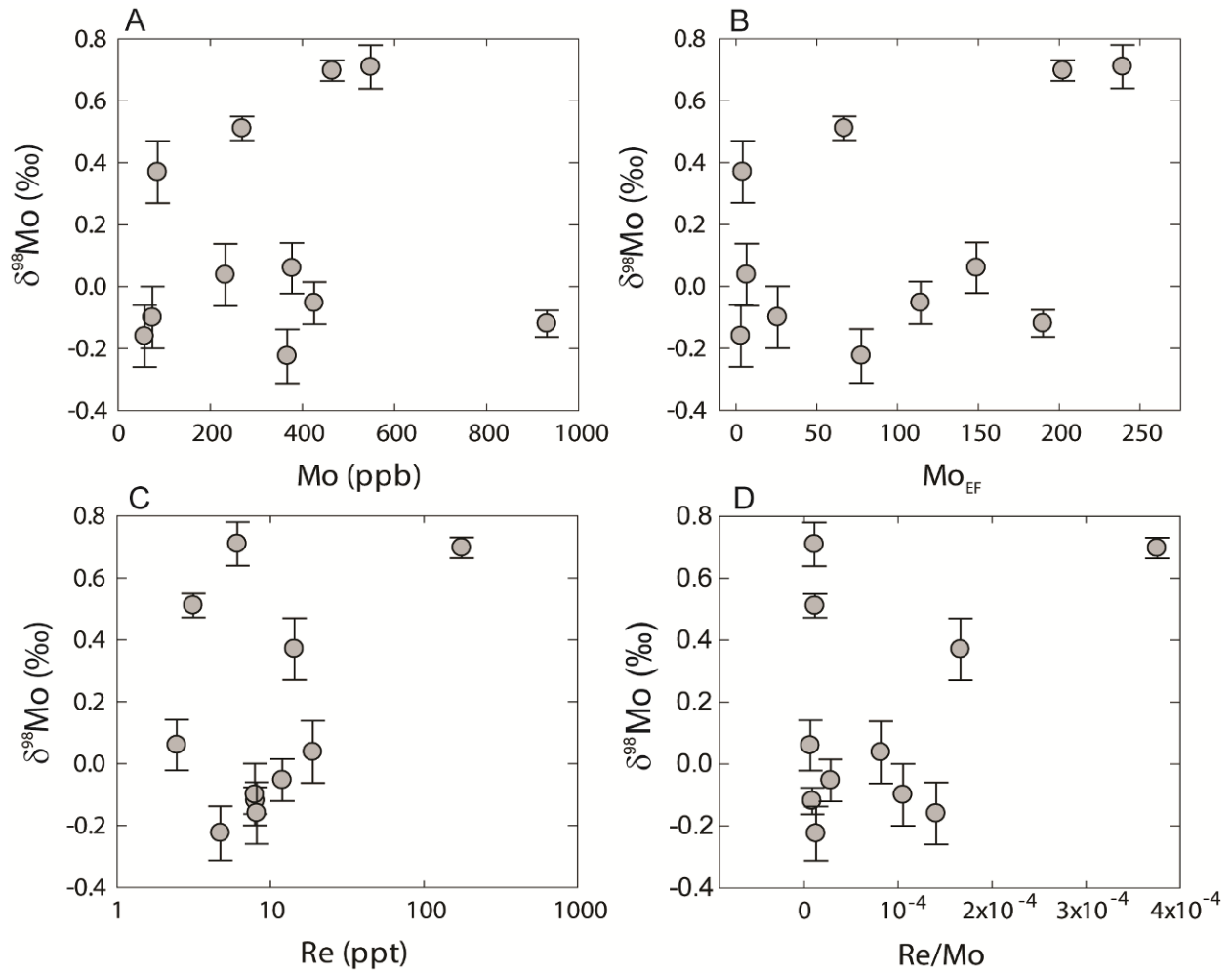


Figure 3.4: Covariance plots of $\delta^{98}\text{Mo}$ vs. Mo concentration (A), Mo enrichment (B), Re concentration (C), and Re/Mo (D). Samples with positive $\delta^{98}\text{Mo}$ form distinct trends relative to all other proxies from samples with near-zero to negative $\delta^{98}\text{Mo}$ values.

3.9 Tables

Table 3.1: Results and errors

Table 1: Results and errors												
Strat height	Sample type	¹ Mo (ppb)	¹ U (ppb)	Re (ppt)	+	-	¹ M _{OPF}	¹ U _{EF}	Re/Mo	$\delta^{98}\text{Mo}$	³ σ stdv	
2.31	Jasper band	231.5	113.8	18.9	1.8	1.8	6.5	0.59	8.15×10^{-5}	-0.03	0.10*	
2.35	Jasper band	335.7	158.8	11.1	1.7	1.7	19.7	1.72	3.3×10^{-5}			
2.42	Jasper band	933.7	117.4	8.0	1.2	1.2	189.9	4.40	8.54×10^{-6}	-0.12	0.04	
2.55	Jasper band	304.8	126.0	8.4	1.5	1.5	17.2	1.31	2.76×10^{-5}			
4.1	Jasper band	51.9	16.9	5.6	1.1	1.1	13.9	0.83	1.09×10^{-4}			
4.5	Jasper band	372.0	36.7	4.7	1.5	1.5	77.6	1.41	1.27×10^{-5}	-0.22	0.09	
4.8	Jasper band	130.4	36.9	2.3	1.0	1.0	28.6	1.49	1.76×10^{-5}			
5	Jasper band	426.3	64.6	12.0	1.5	1.5	114.2	3.19	2.81×10^{-5}	-0.05	0.07	
5.1	Jasper band	378.8	62.5	2.5	1.2	1.2	148.8	4.52	6.49×10^{-6}	0.06	0.08	
5.3	Jasper band	274.5	56.4	16.8	1.2	1.2	93.4	3.53	6.12×10^{-5}			
13.5	Jasper band	32.1	38.2	19.7	1.4	1.4	1.7	0.37	6.13×10^{-4}			
13.6	Jasper band	86.1	27.9	14.3	1.6	1.5	4.1	0.24	1.66×10^{-4}	0.37	0.10*	
13.95	Jasper band	48.9	64.1	21.0	1.6	1.6	14.4	3.48	4.29×10^{-4}			
15.5	Jasper band	75.3	39.2	7.9	1.4	1.4	25.8	2.47	1.05×10^{-4}	-0.10	0.10*	
16.5	Jasper band	58.0	25.3	8.1	1.0	1.0	3.0	0.24	1.40×10^{-4}	-0.16	0.10*	
31.63	Jasper band	110.1	53.1	8.1	1.4	1.4	26.6	2.36	7.36×10^{-5}			
32.18	Jasper band	270.8	43.1	3.1	1.1	1.1	67.0	1.96	1.16×10^{-5}	0.51	0.04	
33.21	Jasper band	265.9	71.3	14.4	1.6	1.6	30.5	1.51	5.43×10^{-5}			
33.32	Jasper band	551.4	88.5	6.1	1.3	1.3	239.2	7.07	1.11×10^{-5}	0.71	0.07	
33.61	Jasper band	350.4	52.6	357.8	6.3	6.2	125.8	3.48	1.02×10^{-3}			
33.91	Jasper band	469.5	78.9	176.3	4.4	4.4	202.2	6.26	3.75×10^{-4}	0.70	0.03	
34.11	Jasper band	173.0	27.2	147.9	3.8	3.8	48.8	1.41	8.55×10^{-4}			
Standards				Re (ppt)	+	-				$\delta^{98}\text{Mo}$	2σ stdv	
SCO-1				1076	44	41						
BHVO-1				578	24	23						
² BCR-2				14390	2689	1970						
⁴ NIST SRM 3134										0.25	0.09	
⁴ NIST SRM 610										0.31	0.09	
⁴ NIST SRM 612										0.29	0.10	

¹Data from Baldwin et al., 2012; samples without Re or ⁹⁸Mo analysis not included in table
²the error on BCR-2 was relatively high due to under-spiking
³Precision (2SD) under intermediate precision conditions of a single measurement (*: see text) or 2SD between 2 measurements
⁴NIST silicate glass standard reference materials, see Greber et al. (2012)

3.10 References

- Algeo, T.J. and Tribovillard, N., 2009. Environmental analysis of paleoceanographic systems based on molybdenum-uranium covariation. *Chemical Geology*, 268: 211-225.
- Arnold, G.L., Anbar, A.D., Barling, J. and Lyons, T.W., 2004. Molybdenum isotope evidence for widespread anoxia in mid-Proterozoic oceans. *Science*, 304: 87-90.
- Baldwin, G.J., Thurston, P.C. and Kamber, B.S., 2011. High-precision rare earth element, nickel, and chromium chemistry of chert microbands pre-screened with in-situ analysis. *Chemical Geology*, 285: 133-143.
- Baldwin, G.J. and Turner, E.C., 2012. Lithofacies and lithostratigraphic correlation potential of the Rapitan iron formation, Snake River area (NTS 106F), Yukon. In: K.E. Macfarlane and P.J. Sack (Editors), *Yukon Exploration and Geology 2011*. Yukon Geological Survey, pp. 1-15.
- Baldwin, G.J., Turner, E.C. and Kamber, B.S., 2012. A new depositional model for glaciogenic Neoproterozoic iron formation: insights from the chemostratigraphy and basin configuration of the Rapitan iron formation. *Canadian Journal of Earth Sciences*, 49: 455-476.
- Barling, J. and Anbar, A.D., 2004. Molybdenum isotope fractionation during adsorption by manganese oxides. *Earth and Planetary Science Letters*, 217: 315-329.
- Barling, J., Arnold, G.L. and Anbar, A.D., 2001. Natural mass-dependent variations in the isotopic composition of molybdenum. *Earth and Planetary Science Letters*, 193: 447-457.
- Bekker, A. et al., 2010. Iron formation: The sedimentary product of a complex interplay among mantle, tectonic, oceanic, and biospheric processes. *Economic Geology*, 105: 467-508.
- Bekker, A. et al., 2004. Dating the rise of atmospheric oxygen. *Nature*, 427: 117-120.
- Canfield, D.E., 1998. A new model for Proterozoic ocean chemistry. *Nature*, 396: 450-453.
- Canfield, D.E. et al., 2008. Ferruginous conditions dominated later Neoproterozoic deep-water chemistry. *Science*, 321: 949-952.
- Canfield, D.E., Poulton, S.W. and Narbonne, G.M., 2007. Late-Neoproterozoic deep-ocean oxygenation and the rise of animal life. *Science*, 315: 92-95.

- Crusius, J., Calvert, S., Pedersen, T. and Sage, D., 1996. Rhenium and molybdenum enrichments in sediments as indicators of oxic, suboxic, and sulfidic conditions of deposition. *Earth and Planetary Science Letters*, 145: 65-78.
- Dahl, T.W. et al., 2011. Molybdenum evidence for expansive sulfidic water masses in ~750 Ma oceans. *Earth and Planetary Science Letters*, 311: 264-274.
- Fischer-Gödde, M., Becker, H. and Wombacher, F., 2011. Rhodium, gold and other highly siderophile elements in orogenic peridotites and peridotite xenoliths. *Chemical Geology*, 280: 365-383.
- Goldberg, T., Archer, C., Vance, D. and Poulton, S.W., 2009. Mo isotope fractionation during adsorption to Fe (oxyhydr)oxides. *Geochimica et Cosmochimica Acta*, 73: 6502-6516.
- Goldberg, T. et al., 2012. Controls on Mo isotope fractionations in a Mn-rich anoxic marine sediment, Gullmar Fjord, Sweden. *Chemical Geology*, 296-297: 73-82.
- Greber, N.D., Hofmann, B.A., Voegelin, A.R., Villa, I.M. and Nägler, T.F., 2011. Mo isotope composition in Mo-rich high- and low-T hydrothermal systems from the Swiss Alps. *Geochimica et Cosmochimica Acta*, 75(21): 6600-6609.
- Greber, N.D., Siebert, C., Nägler, T.F. and Pettke, T., 2012. $\delta^{98/95}$ Mo values and molybdenum concentration data for NIST SRM 610, 612, and 3134: towards a common protocol for reporting Mo data. *Geostandards and Geoanalytical Research*, 36(3): 291-300.
- Johnston, D.T. et al., 2010. An emerging picture of Neoproterozoic ocean chemistry: Insights from the Chuar Group, Grand Canyon, USA. *Earth and Planetary Science Letters*, 290: 64-73.
- Kamber, B.S., Bolhar, R. and Webb, G.E., 2004. Geochemistry of late Archean stromatolites from Zimbabwe: evidence for microbial life in restricted epicontinental seas. *Precambrian Research*, 132(4): 379-399.
- Kamber, B.S., Greig, A. and Collerson, K.D., 2005. A new estimate for the composition of weathered young upper continental crust from alluvial sediments, Queensland, Australia. *Geochimica et Cosmochimica Acta*, 69(4): 1041-1058.
- Kirschvink, J.L., 1992. Late Proterozoic low-latitude global glaciation: the Snowball Earth. In: J.W. Schopf and C. Klein (Editors), *The Proterozoic biosphere: A multidisciplinary study*. Cambridge University Press, Cambridge, pp. 51-52.

- Klein, C. and Beukes, N.J., 1993. Sedimentology and geochemistry of the glaciogenic late Proterozoic Rapitan iron-formation in Canada. *Economic Geology*, 88: 542-565.
- Klein, C. and Ladeira, E.A., 2004. Geochemistry and mineralogy of Neoproterozoic banded iron-formations and some selected, siliceous manganese formations from the Urucum District, Mato Grosso Do Sul, Brazil. *Economic Geology*, 99: 1233-1244.
- Krapež, B., Barley, M.E. and Pickard, A.L., 2003. Hydrothermal and resedimented origins of the precursor sediments to banded iron formation: sedimentological evidence from the Early Palaeoproterozoic Brockman Supersequence of Western Australia. *Sedimentology*, 50(5): 979-1011.
- Li, C. et al., 2010. A stratified redox model for the Ediacaran ocean. *Science*, 328: 80-83.
- Lottermoser, B.G. and Ashley, P.M., 2000. Geochemistry, petrology and origin of Neoproterozoic ironstones in the eastern part of the Adelaide Geosyncline, South Australia. *Precambrian Research*, 101: 49-67.
- Macdonald, F.A. et al., 2010a. Calibrating the Cryogenian. *Science*, 327: 1241-1243.
- Macdonald, F.A., Strauss, J.V., Rose, C.V., Dudás, F.Ö. and Schrag, D.P., 2010b. Stratigraphy of the Port Nolloth Group of Namibia and South Africa and implications for the age of Neoproterozoic iron formations. *American Journal of Science*, 310: 862-888.
- Meisel, T., Dale, C.W., Pearson, D.G. and Sergeev, D.S., 2009. Complete sample digestions for accurate isotope measurements? The Re-Os isotope system under scrutiny. *Geochimica et Cosmochimica Acta*, 73(13): A867.
- Meisel, T. and Moser, J., 2004. Platinum-group element and rhenium concentrations in low abundance reference materials. *Geostandards and Geoanalytical Research*, 28(2): 233-250.
- Miller, C.A., Peucker-Ehrenbrink, B., Walker, B.D. and Marcantonio, F., 2011. Re-assessing the surface cycling of molybdenum and rhenium. *Geochimica et Cosmochimica Acta*, 75(22): 7146-7179.
- Morford, J.L. and Emerson, S., 1999. The geochemistry of redox sensitive trace metals in sediments. *Geochimica et Cosmochimica Acta*, 63(11/12): 1735-1750.

- Morford, J.L., Emerson, S.R., Breckel, E.J. and Kim, S.H., 2005. Diagenesis of oxyanions (V, U, Re, and Mo) in pore waters and sediments from a continental margin. *Geochimica et Cosmochimica Acta*, 69(21): 5021-5032.
- Nägler, T.F., Neubert, N., Böttcher, M.E., Dellwig, O. and Schnetger, B., 2011. Molybdenum isotope fractionation in pelagic euxinia: Evidence from the modern Black and Baltic Seas. *Chemical Geology*, 289: 1-11.
- Nakagawa, Y. et al., 2012. The molybdenum isotopic composition of the modern ocean. *Geochemical Journal*, 46(2): 131-141.
- Nameroff, T.J., Balistrieri, L.S. and Murray, J.W., 2002. Suboxic trace metal geochemistry in the eastern tropical North Pacific. *Geochimica et Cosmochimica Acta*, 66(7): 1139-1158.
- Neubert, N., Nægler, T.F. and Böttcher, M.E., 2008. Sulfidity controls molybdenum isotope fractionation into euxinic sediments: Evidence from the modern Black Sea. *Geology*, 36(10): 775-778.
- Och, L.M. and Sheilds-Zhou, G.A., 2012. The Neoproterozoic oxygenation event: Environmental perturbations and biogeochemical cycling. *Earth-Science Reviews*, 110: 26-57.
- Pattan, J.N. and Pearce, N.J.G., 2009. Bottom water oxygenation history in southeastern Arabian Sea during the past 140 ka: Results from redox-sensitive elements. *Palaeogeography, Palaeoclimatology, Palaeoecology*, 280: 396-405.
- Planavsky, N.J. et al., 2011. Widespread iron-rich conditions in the mid-Proterozoic ocean. *Nature*, 477: 448-451.
- Poulson, R.L., Siebert, C., McManus, J. and Berelson, W.M., 2006. Authigenic molybdenum isotope signatures in marine sediments. *Geology*, 34(8): 617-620.
- Poulton, S.W. and Canfield, D.E., 2011. Ferruginous conditions: a dominant feature of the ocean through Earth's history. *Elements*, 7: 107-112.
- Poulton, S.W., Fralick, P.W. and Canfield, D.E., 2004. The transition to a sulphidic ocean ~1.84 billion years ago. *Nature*, 431: 173-177.
- Poulton, S.W., Fralick, P.W. and Canfield, D.E., 2010. Spatial variability in oceanic redox structure 1.8 billion years ago. *Nature Geoscience*, 3: 486-490.
- Scott, C. et al., 2008. Tracing the stepwise oxygenation of the Proterozoic ocean. *Nature*, 452: 456-459.

- Shen, Y., Canfield, D.E. and Knoll, A.H., 2002. Middle Proterozoic ocean chemistry: evidence from the McArthur basin, Northern Australia. *American Journal of Science*, 302: 81-109.
- Siebert, C., Nägler, T.F. and Kramers, J.D., 2001. Determination of molybdenum isotope fractionation by double-spike multicollector inductively coupled plasma mass spectrometry. *Geochemistry, Geophysics, Geosystems*, 2: doi:10.1029/2000GC000124.
- Siebert, C., Nägler, T.F., von Blanckenburg, F. and Kramers, J.D., 2003. Molybdenum isotope records as a potential new proxy for paleoceanography. *Earth and Planetary Science Letters*, 211: 159-171.
- Slack, J.F., Grenne, T., Bekker, A., Rouxel, O.J. and Lindberg, P.A., 2007. Suboxic deep seawater in the late Paleoproterozoic: Evidence from hematitic chert and iron formation related to seafloor-hydrothermal sulfide deposits, central Arizona, USA. *Earth and Planetary Science Letters*, 255: 243-256.
- Wille, M. et al., 2007. Evidence for a gradual rise of oxygen between 2.6 and 2.5 Ga from Mo isotopes and Re-PGE signatures in shales. *Geochimica et Cosmochimica Acta*, 71: 2417-2435.

3.11 Supplementary Data

Table 3.S1: Mo concentrations by different techniques

Table S1: Mo concentrations by different techniques			
	[Mo] ppm		
Sample	Isotope Dilution Bern	Canada	Difference
2.31	0.24	0.23	0.01
2.42	0.95	0.93	0.02
4.50	0.41	0.37	0.04
5.00	0.44	0.43	0.02
5.10	0.40	0.38	0.02
13.50	0.03	0.03	0.00
13.60	0.09	0.09	0.01
15.50	0.07	0.07	-0.01
16.50	0.07	0.06	0.01
32.18	0.28	0.27	0.01
33.32	0.53	0.55	-0.02
33.91	0.48	0.46	0.02

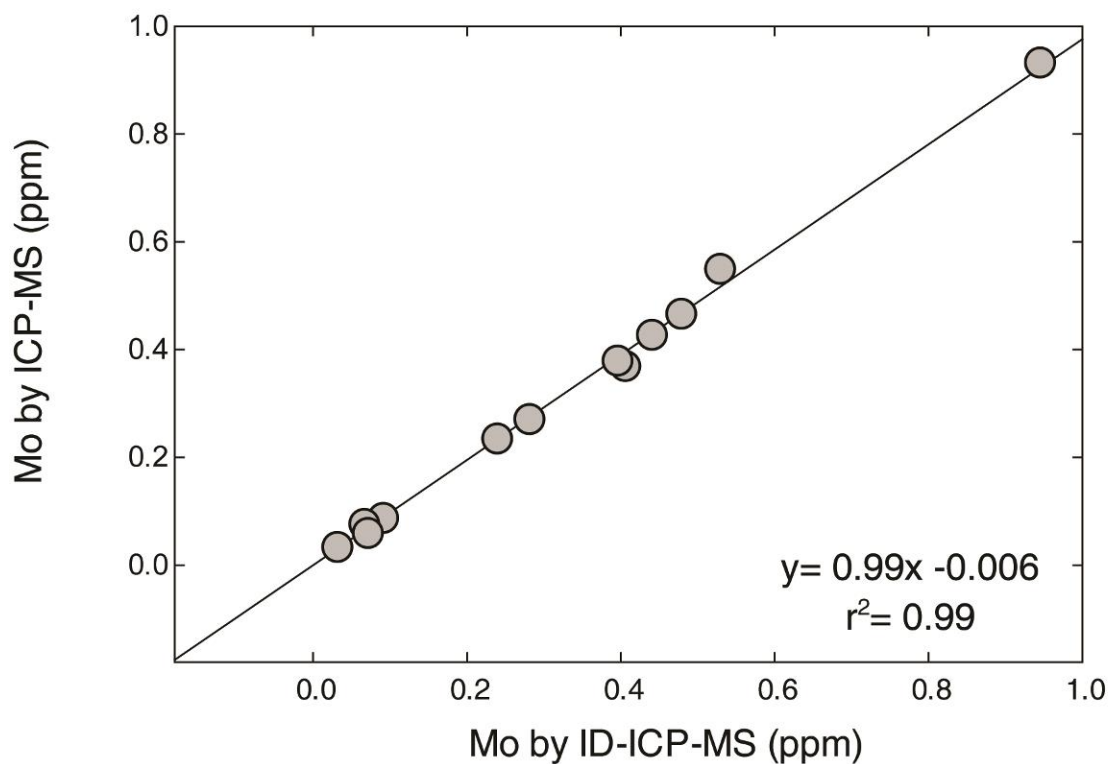


Figure 3.S1: X-Y plot of Mo concentration data obtained by quadrupole ICP-MS at Laurentian University, Canada against Mo concentration data obtained by isotope dilution ICP-MS at Universität Bern, Switzerland. The data shows an excellent correlation with a slope of 0.99 and an r^2 value of 0.99, indicating that the Mo data by quadrupole ICP-MS is of excellent accuracy, often only slightly underestimating relative to isotope dilution (Table S1).

Chapter 4: Paleogeographic controls on the distribution and sedimentological character of the Rapitan iron formation, Northwest Canada

4.1 Abstract

The Rapitan iron formation (Rapitan Group, NWT and YT, Canada) contains one of the largest undeveloped iron deposits on Earth. Formed in a rift basin during the Neoproterozoic “snowball Earth” glacial episode (ca. 711 Ma), this hematite-jasper iron formation is stratigraphically associated with glacioclastic turbidites and diamictites. The Rapitan Group overlies the extension-related Coates Lake Group but exposures of the Rapitan Group are geographically discontinuous, and appear to define two sub-basins. First, the Snake River basin (YT and NWT), which contains thick iron formation (locally >100 m thick), and second, the Redstone basin (NWT), in which the iron formation is much thinner (local maximum 35 m). Iron formation and glacioclastic strata in the two sub-basins have distinct sedimentological characteristics. In the Snake River basin, the iron formation is generally hematite-rich and contains abundant jasper nodules; in the Redstone basin the iron formation is dominated by bedded and locally silty jasper with much less hematite. Glacioclastic turbiditic rocks of the Sayunei Formation, which underlies the iron formation, consist of siliceous, hematitic mudstone and siltstone, with thin intervals of coarser clastic material in the Redstone basin; whereas much sandier and clast-rich diamictite dominates in the Snake River basin. Rare earth element plus yttrium (REE+Y) data indicate that most iron formation deposition at both localities swung between phases of domination by hydrogenous precipitation and dominance of siliciclastic input. The geochemistry indicates that at certain times there was a complete shutdown of siliciclastic sediment supply during iron formation deposition. Geographically, there is an important association between locations of crustal-scale syn-sedimentary faults and major stratigraphic changes in the thickness and distribution of the Rapitan iron formation and the Rapitan Group as a whole. These faults define extension-related sub-basins that exerted dominant control over the

distribution of the Rapitan iron formation: active subsidence in rifting basins was necessary for deposition of Neoproterozoic iron formation, and may have been critical in controlling the distribution of Sturtian-age glaciogenic deposits overall.

4.2 Introduction

The Neoproterozoic recorded a major turning point in the evolution of the Earth's surface environments. It witnessed the second major rise in oxygenation of the ocean and atmosphere (Campbell and Squire, 2010; Och and Shields-Zhou, 2012), and the subsequent appearance of the first macroscopic metazoans (Canfield et al., 2007). These significant, irreversible changes in Earth's surficial system occurred against the backdrop of the "snowball Earth" glaciations, a series of possibly global glacial events that took place between 740 and 582 Ma (Kirschvink, 1992; Hoffman et al., 1998; Hoffman and Li, 2009). It has been widely suggested that these glaciations are intimately linked to the rise in atmospheric free oxygen and the evolution of metazoans (Canfield et al., 2008; Peterson et al., 2008; Shields-Zhou and Och, 2011). Despite their obvious geological significance, there remains significant disagreement over the scale of the "snowball" glaciations. There are strong arguments for a "hard snowball Earth", with full global glaciation (Hoffman and Schrag, 2002; Hoffman, 2009), whereas others make a case for more localised, continental-rift-related events (e.g., Young, 2002; Eyles and Januszcak, 2004; Eyles, 2008). In either case, the geological implications of these glacial events are substantial.

A peculiar aspect of the "snowball Earth" glaciations is the apparent resumption of deposition of banded iron formation, a sediment type that had not been deposited in significant volumes after the latest Paleoproterozoic (Bekker et al., 2010), with some rare exceptions directly associated with hydrothermal venting (e.g., Slack et al., 2007). The Neoproterozoic resumption of iron formation deposition is a key aspect of major models for Proterozoic redox evolution and has informed most models of even Archean banded iron formation (e.g., Holland, 1984; Beukes and Klein, 1992; Canfield, 1998; Poulton and Canfield, 2011). Although the Neoproterozoic glaciogenic iron formation ("Rapitan-type" iron formation (Gross, 1993)) is not unique in its stratigraphic association with glacioclastic sediments (Smith et al., 2013), nor age (Basta et al., 2011), it does represent the most substantial evidence of Neoproterozoic and glacially associated

iron formation in the geological record. Most, if not all, of the Rapitan-type iron formations are associated with glacial deposits of the Sturtian glaciation (~720-660 Ma) (Macdonald et al., 2010b), the first of three proposed Neoproterozoic glacial episodes, although some examples have not been assigned to any specific glaciation due to the lack of geochronology and stratigraphic complications (e.g., Freitas et al., 2011). It is important to recall that iron formation is not universal in Sturtian-aged glacial deposits (Hoffman, 2009), and is commonly very localised within the glacial deposits that contain it. The Sturtian glacial deposits were deposited in young continental rifts, similar in scope to the modern Red Sea (Young, 2002), and few if any were deposited on conventional continental margins. This distribution could be a product of preservational bias, or the sheer abundance of incipiently rifting margins at 700 Ma due to the dispersal of Rodinia, or, as some have argued, indicative of a genetic link between rifting and both “snowball Earth” and Rapitan-type iron formation (e.g., Young, 2002). Although the dynamics of the link between rifting and “snowball” glaciations remain unresolved, development of partially restricted marine basins has been shown to be necessary for the deposition of iron formation (Baldwin et al., 2012b).

The archetypal glaciogenic Neoproterozoic iron formation is the Rapitan iron formation of the Mackenzie and Wernecke Mountains, Northwest Territories and Yukon, Canada. This particular iron formation was deposited after 711 Ma (Baldwin et al., 2012a) during the Sturtian glaciation, and is associated with glacioclastic turbidites and diamictites of the Rapitan Group. The Rapitan Group is preserved in a >500 km-long arcuate belt in the northern Canadian cordillera, but across that distance is exposed discontinuously: exposure is present over 370 km of strike, and defines two distinct depositional basins (Snake River basin and Redstone basin). The iron formation itself is even more discontinuous than the Rapitan Group, and for much of its strike length is very thin. Significant thicknesses (>30 m) of iron formation are limited to the Snake River basin, at the northwestern end of the exposure belt (Yeo, 1981). This sector also encompasses most of the observed textural variation. Thickness and sedimentological differences between the two basins have resulted in disputed stratigraphy and correlation at the formation level in the Snake River basin (e.g., Yeo, 1981; Klein and Beukes, 1993; Hoffman and Halverson, 2011).

The documented thickness differences in the Rapitan Group across the Mackenzie Mountains were addressed in a paleogeographic context by Eisbacher (1985), whose study placed most emphasis on implications for the distribution and deposition of the entire Windermere Supergroup, as opposed to just the Rapitan Group. This work yielded a detailed assessment of sedimentation patterns, from the incipient rifting of the basal Coates Lake Group to the much more widespread deposition of the Hay Creek Group (overlies Rapitan Group), but does not provide much explanation for the limited distribution of the Rapitan iron formation. This leaves open the question of the significance of the discontinuous nature of the iron formation.

Geochemical data from banded iron formations is crucial to aid reconstruction of depositional models. Although considerable geochemical work has been undertaken on Neoproterozoic iron formation, this has not always been presented with sufficiently detailed sedimentological and stratigraphic context. The present paper presents the first fully integrated stratigraphic-sedimentological-geochemical study of Neoproterozoic iron formation. Examining the geochemical nature of the archetypal Neoproterozoic iron formation in the context of its regional sedimentary setting is expected to advance the understanding of the geological environments and driving factors behind Neoproterozoic glaciation and iron formation deposition in particular.

4.3 Geological Background

The Neoproterozoic Rapitan Group of the lower Windermere Supergroup is exposed in an arcuate outcrop belt over 500 km long in the Mackenzie and Wernecke Mountains of the northern Canadian cordillera, Northwest Territories and Yukon (Fig. 4.1A). The Rapitan Group was deposited during the Sturtian glaciation, the first of the three globally distributed glacial episodes associated with “snowball Earth” (Kirschvink, 1992; Hoffman et al., 1998; Hoffman, 2009; Hoffman and Li, 2009), and has a maximum depositional age of 711.33 ± 0.25 Ma based on U-Pb detrital zircon geochronology (Baldwin et al., 2012a).

The Windermere Supergroup in the Mackenzie Mountains consists of the basal Coates Lake Group, the Rapitan Group, the Hay Creek Group (Yeo, 1978), and the informal “upper

group” (Aitken, 1989) (Fig. 4.2). Windermere strata in the Mackenzie Mountains have been correlated with Windermere strata in the southern Canadian cordillera (Gabrielse, 1972); the glacioclastic Rapitan Group has been considered to be temporally equivalent to the Toby conglomerate in the Kootenay Range (Ross et al., 1995), and other diamictites in the central cordillera (e.g., McMechan, 2000) are considered to be correlative with the younger glaciogenic deposit in the Mackenzie Mountains, the Ice Brook Formation. Windermere Group deposition was initiated by dispersal of the supercontinent Rodinia at approximately 770 Ma (Young, 1995), recorded in the Mackenzie Mountains in the Tsezotene sills and their presumed extrusive correlative, the “Little Dal basalt” which lies at the base of the Coates Lake Group (Armstrong et al., 1982). Regional stratigraphic patterns divide middle Neoproterozoic rocks of the Mackenzie Mountains into the Redstone basin (Mackenzie Mountains), NWT, and the Snake River basin (Mackenzie and Wernecke Mountains), NWT and YT.

The Windermere Supergroup is underlain by the Mackenzie Mountains Supergroup, a thick (~4-5 km) succession of shallow-marine carbonate rocks, fluvial sandstones, marine siltstones and shale, and evaporite rocks (Long et al., 2008; Long and Turner, 2012; Turner and Long, 2012) (Fig. 4.2). The Mackenzie Mountains Supergroup is the oldest Proterozoic unit exposed in the Mackenzie Mountains, but is underlain by the Paleo- and Mesoproterozoic Wernecke Supergroup and Pinguicula Group in the Wernecke Mountains, YT (Thorkelson et al., 2005). Some of the oldest possible evidence of metazoans is preserved in carbonate rocks of the Little Dal Group (Neuweiler et al., 2009). The Coates Lake Group, consisting of the “Little Dal basalt”, Thundercloud Formation, Redstone River Formation, and Coppercap Formation, is an early rift succession, composed of basaltic flows, alluvial conglomerates, terrestrial siltstone, gypsum, and shallow-marine carbonate rocks, and contains stratiform copper deposits in the Redstone basin of the Mackenzie Mountains (Jefferson and Ruelle, 1987). The Coates Lake Group is apparently absent in the Snake River basin. The Rapitan Group is overlain by the Hay Creek Group, consisting of the Twitya, Keele, and Ice Brook formations, as well as the “Teepee dolostone”, a cap carbonate overlying the glaciogenic Ice Brook Formation (Yeo, 1978; Aitken, 1991; James et al., 2001). The base of the Twitya Formation, which is predominantly deep-water siltstone, sandstone, and shale, features a purported carbonate-clastic cap carbonate of limited regional extent in the northern end of the Redstone basin immediately overlying the Rapitan

Group (Eisbacher, 1981b). The “Profeit dolostone” in YT may be of similar origin, based primarily on its stratigraphic position (Eisbacher, 1981b). The Twitya Formation contains disc-shaped impressions that are the oldest purported example of Ediacaran fauna (Hofmann et al., 1990). The Hay Creek Group is overlain by the informal ‘upper group’, which records a series of shallowing-upward deep-water shale and carbonate sequences from the rift-drift transition of the basin through to the Ediacaran-Cambrian boundary (Aitken, 1989; Narbonne and Aitken, 1995; Young, 2013).

The Rapitan Group is distributed from near Coates Lake, NWT, across the Mackenzie Mountains into YT, where it is truncated by the Snake River Fault (part of the Richardson Fault Array; Eisbacher, 1981b). Rocks immediately west of the Snake River Fault mapped as part of the Rapitan Group are predominantly orthoconglomerates, and are dissimilar to all other Rapitan lithologies in the region (Eisbacher, 1981b). Existing rock descriptions for this area resemble conglomerates of the Redstone River Formation member 2 (Jefferson and Ruelle, 1987), or orthoconglomerates of the Mount Berg Formation (Yeo, 1981), although neither of these formations is known to be present in the Snake River area; the identity of the putative Rapitan Group rocks west of the Snake River Fault remains uncertain. Purported correlatives to the Rapitan Group are exposed well to the west of the Snake River basin, in the central and western Ogilvie Mountains of YT (upper Mount Harper Group, Macdonald et al., 2010a), and Alaska (upper Tindir Group, Young, 1982).

The Rapitan Group is subdivided into three formations, the Mount Berg, Sayunei, and Shezal formations (Yeo, 1981). The Mount Berg Formation is a laterally discontinuous unit of diamictite and orthoconglomerate, which occurs in the vicinity of faults cross-cutting the underlying Coates Lake and Little Dal Groups. Its thickness locally exceeds 300 m, but it is typically no more than a few tens of metres thick, and is limited to the southern part of the Redstone basin (Yeo, 1981). The overlying Sayunei Formation is characterised by maroon or purple fine-grained turbidites, dominated by siltstone and mudstone, with some sandstone and diamictite interbeds. In the Snake River basin, the fine-grained turbidite lithology is absent, allowing some authors to suggest that the Sayunei Formation is entirely absent in this area (e.g., Yeo, 1981, 1986). The Sayunei Formation is capped by jasper-hematite iron formation ranging

from a few centimetres to over 100 m thick; the thickest iron formation is in the Snake River basin (Baldwin and Turner, 2012). Texturally, the iron formation has both the banded and granular types that are well known from older iron formations (Bekker et al., 2010), as well as massive hematite with jasper nodules, a texture that is unique to Neoproterozoic iron formation (Hoffman et al., 2011). Traditionally, the iron was assumed to be sourced from hydrothermal or volcanic sources (e.g., Gross, 1965; Yeo, 1981; Halverson et al., 2011), but recent work has shown that a hydrothermal iron source was geochemically improbable, and that the iron ore was derived from remineralised nanoparticulate iron derived from glacial outwash (Baldwin et al., 2012b). The Sayunei Formation is overlain by the Shezal Formation, which consists of massive, recessive-weathering grey or tan diamictite with minor sandstone and siltstone intervals, and is interpreted to be a glaciomarine outwash diamictite, with possible localised terminal moraines (Eisbacher 1978). Locally, the base of the Shezal Formation consists of reworked material from the top of the Sayunei Formation, including iron formation material.

Iron formation in the northern Canadian cordillera was known as early as the Yukon gold rush from the Snake River area, Yukon (Keele, 1906), and was later reported in the Mackenzie Mountains by Keele (1910). The clastic rocks stratigraphically associated with the iron formation were first interpreted to be of glaciogenic origin by Ziegler (1959), an interpretation that was confirmed by numerous later studies (e.g., Uppit, 1966; Eisbacher, 1976; Young, 1976; Eisbacher, 1981a; Yeo, 1981; Eisbacher, 1985). The iron formation and associated clastic rocks were later formalised as the Rapitan Group by Green and Godwin (1963) after Rapitan Creek, west of the Snake River deposit, Yukon. Extensive exploration for iron ore was conducted in the 1960s, in which up to 120 m of jasper-hematite iron formation with 5.6 billion tonnes of ore reserves at 42.7% iron was reported over a 25.9 km² area near Iron Creek, YT (Stuart, 1963). The Rapitan Group was later subdivided into the predominantly turbiditic Sayunei Formation and diamictite-rich Shezal Formation, based on stratigraphy in the Mackenzie Mountains in the Redstone area (Eisbacher, 1978), with the later addition of basal diamictite of the Mount Berg Formation (Yeo, 1981). Despite the well-defined stratigraphy in the southern Mackenzie Mountains, the formation-level stratigraphy in the Snake River area, YT, remains disputed (e.g., Yeo, 1981; Klein and Beukes, 1993; Hoffman and Halverson, 2011).

Sedimentological patterns in Proterozoic strata of the Mackenzie Mountains are controlled by basin geometry that broadly follows the arcuate shape and structural grain of the modern exposure belt (Aitken and Long, 1978). This arcuate geometry has long been understood to be controlled by pre-existing major, crustal-scale structures (Aitken and Pugh, 1984), as well as a series of northeast- trending faults that controlled basin morphology (Eisbacher, 1977, 1981b, 1985; Turner and Long, 2008). These latter faults correlate well with major changes in stratigraphic thickness and lithofacies in the Mackenzie Mountains Supergroup (Turner and Long, 2008), and define distinct sub-basins in the Coates Lake and Rapitan Groups (Eisbacher, 1981b). In addition to the NE- trending structures, a series of NNW- trending faults running roughly parallel to dykes associated with the Tsezotene sills (Aitken et al., 1973; Aitken and Cook, 1974), have been suggested to provide further control on pull-apart basins in the Coates Lake Group (Jefferson and Ruelle, 1987). Evidence of syn-sedimentary compressional tectonism has been documented in the form of localised folding and internal unconformities in the Sayunei Formation at the Nite copper prospect (Helmstaedt et al., 1979, 1981), although the timing and cause of the folding has been disputed (Aitken et al., 1981). Recent work has shown that the folding was coeval with Rapitan Group deposition, although whether it was the product of traditional compressional deformation or possible salt tectonics in older Neoproterozoic strata remains unclear (J.A. Milton, personal communication, 2012). Basin fault control became less important in controlling sedimentation patterns in the latter stages of rifting in the Hay Creek Group and the upper Windermere Supergroup during the transition from rift to drift tectonics, as sediment distribution became more widespread and less variable in thickness across the latest Proterozoic passive margin of the Mackenzie Mountains (Eisbacher, 1981b; Aitken, 1989).

4.4 Stratigraphy

Six stratigraphic sections through parts of the Rapitan Group were documented from the length of the Rapitan exposure area (Figs. 4.1B; Tables 4.1 and 4.2). Focus was placed primarily on the Sayunei Formation, and on sections reported to contain exposure of iron formation according to Yeo (1984). Regionally, exposure of the Rapitan Group is divided into two distinct basins, the Snake River basin and the Redstone basin. These two basins are separated by

approximately 135 km of strike-length in which the Rapitan Group is absent. Each of the two basins has a distinct sedimentological and stratigraphic character, particularly in the Sayunei Formation and the iron formation that caps it; characteristics of the Shezal Formation are somewhat more uniform in these two basins

4.4.1 Snake River Basin

The Snake River basin is the type area for the Rapitan iron formation, contains its thickest known exposures (Stuart, 1963), and is the smaller of the two Rapitan basins. Numerous sections were measured in this area, in the vicinities of Iron (Fig. 4.3A) and Discovery (Fig. 4.3B) Creeks (YT) and the Cranswick River (Fig. 4.3C) (NWT), although a single representative section from each locality is described here.

Previously described in detail by Baldwin and Turner (2012), the Iron Creek section is located at the Crest iron deposit (Fig. 4.1B). This section contains the thickest exposure of iron formation across the entire exposure belt of the Rapitan Group, and is within a 25.9 km² area estimated to contain 5.6 billion tonnes of iron ore at 47.2% iron (Stuart, 1963). The lowest part of the Sayunei Formation is covered in this section, but the interval from the bottom of the exposed section to the base of the iron formation consists of 65.5 m of massive, dark red to purple matrix-supported clast-poor sandy diamictite (Fig. 4.4A) (classification scheme of Moncrieff, 1989). The iron formation is exposed over a 118.7 m interval, and contains numerous interbeds of siltstone and purple diamictite up to 21 m thick. The iron formation layers consist of a mix of bedded jasper and hematite (BIF) and nodular iron formation (jasper nodules in a massive to bedded hematite matrix), but is dominantly the latter. The iron formation locally shows dramatic soft-sediment slump folds (Fig. 4.4B). The top 2.5 m of the iron formation is characterised by granular iron formation (GIF), which is medium-sand sized grains of jasper and hematite deposited above wave base (Clout and Simonson, 2005) (Fig. 4.4C). The iron formation is overlain by purple to brown siltstone, diamictite, and fine-grained sandstone of the Shezal Formation (Fig. 4.4D).

The Discovery Creek section was also described by Baldwin and Turner (2012), and is located to the east of the main Crest deposit, close to the YT-NWT border. The Sayunei Formation at this location is underlain by the Little Dal Group (formation unknown), and consists

of a basal 340 m interval of purple to red siliciclastic rocks, dominated by clast-poor and clast-rich diamictite with muddy sand matrix with interbeds of matrix- and clast-supported conglomerate. Iron formation appears in three stratigraphic levels: the lowermost is 1 m thick and dominantly BIF, the middle is 0.1 m of nodular iron formation, and the uppermost is 20.2 m thick, and is equal parts BIF and nodular iron formation (Fig. 4.4E, F). The top of the iron formation is in erosional contact with the lower Paleozoic Franklin Mountain Formation. White quartz arenite boulders containing clasts of jasper and hematite are present in nearby rivers, supporting the erosional interpretation of the upper surface of the iron formation. Furthermore, the Rapitan Group pinches out 10 km northwest of this section, with a clearly erosional upper surface (Fig. 4.4G). Several small copper showings, consisting of chalcopyrite weathering to malachite and chrysocolla are present in the Sayunei Formation, in both the iron formation and the underlying diamictite.

In the Cranswick River section, previously described by Baldwin et al., (2012b), the basal contact of the Sayunei Formation is unexposed (~5 m below the bottom of the iron formation). The main lithology underlying the iron formation in the area is friable, hematitic, purple, clast-rich muddy diamictite, which is locally cross-cut by a ≤ 5 m-thick tan, polymictic clast-supported channel-fill conglomerate that directly underlies the iron formation. The iron formation is 30 m thick and contains approximately equal parts BIF and nodular iron formation, with several thin (<50 cm) interbeds of siltstone and diamictite. The iron formation is overlain by a tan clast-poor diamictite that includes a single bed containing remobilised jasper clasts 5 m above the iron formation (Fig. 4.4H).

4.4.2 Redstone Basin

The Redstone basin is characterised by excellent exposure of the Rapitan Group in the central Mackenzie Mountains. This area is centred approximately 170 km south of Norman Wells, NWT (Fig. 4.1A,B), and spans a strike-length of roughly 320 km. Three stratigraphic sections through the Sayunei Formation from this region are described herein (Fig. 4.1B): Boomerang (Fig. 4.3F), Hayhook North (Fig. 4.3G), and Hayhook South (Fig. 4.3H).

In the northernmost measured section in the Redstone basin (Boomerang), the Sayunei Formation is underlain by the Coppercap Formation of the Coates Lake Group, and contains

patchy vein copper mineralisation directly below an erosional contact with the Sayunei Formation. The basal Sayunei Formation (0.8 m) is orange-weathering maroon clast-supported diamictite, with all clasts derived from the underlying Coppercap Formation. This interval is overlain by 90.7 m of predominantly maroon siltstone with interbeds of maroon mudstone, and blue-grey medium-grained sandstone, with scattered dropstones and diamictite interbeds (Fig. 4.5A). The siltstone is overlain by 28 m of maroon pebble diamictite with siltstone interbeds. The uppermost unit of the Sayunei Formation is silty- to sandy-matrix clast-intermediate pebble diamictite, which contains large (up to 30 cm) clasts of reworked and plastically deformed (bent) jasper and hematite (Fig. 4.5E, F). The jasper-bearing diamictite is overlain by grey clast-rich muddy diamictite of the Shezal Formation.

The remaining two measured sections in the Redstone basin are Hayhook North and Hayhook South. These sections are 5 km apart, and were measured individually because they are, respectively, the type sections for the Shezal (north), and Sayunei (south) formations (Eisbacher, 1978).

The Sayunei Formation is underlain by grey-weathering limestone of the Coppercap Formation at Hayhook North, but the contact is unexposed. The Sayunei Formation is 120 m of dominantly maroon siltstone with interbeds of sandy siltstone and sandstone, and rare interbeds of green mudstone and sandstone up to 1.4 m thick. At 120 m stratigraphic elevation, the Sayunei Formation becomes finer-grained, and is dominated by maroon to pink mudstone and siltstone (Fig. 4.5B). A 70 cm-thick interval of bedded jasper with minor bedded hematite is present at 197 m, and is immediately overlain by interbedded pale green mudstone and grey to tan diamictite (variable clast content) of the Shezal Formation.

At Hayhook South, the Sayunei Formation is underlain by grey cherty limestone of the Coppercap Formation. The basal Sayunei Formation is 5.6 m of clast-rich, muddy hematitic diamictite. This unit is overlain by 250 m of predominantly maroon siltstone, with intervals (up to 40 m) of maroon mudstone and sandy siltstone. Iron formation is present over 6.5 m, and is interbedded with hematite-rich purple siltstone. The iron formation is almost entirely BIF, with flaggy-weathering beds of jasper and hematite (Fig. 4.5C). Black chert nodules are present in the basal jasper bed, but are absent in the rest of the iron formation. Trace chalcopyrite, malachite,

and chrysocolla are present along jasper-hematite bed contacts at the top of the iron formation (Fig. 4.5D). The iron formation is immediately overlain by 4.5 m of purple to maroon siltstone, followed by a covered interval underlain by tan Shezal Formation talus.

4.4.3 Regional observations

Detailed stratigraphic documentation of the Redstone basin was focussed on a relatively small area (45 km strike length), between the Redstone and Keele rivers, but general stratigraphic observations were gathered from the rest of this basin, which spans an additional 156 km to the northwest and 117 km to the south of the Boomerang-Hayhook area. The northern margin of this basin (Fig. 4.1B, location D) shows very rapid thinning of the Rapitan and Coates Lake groups northwestward from the Stone Knife River: the Sayunei Formation's thickness diminishes from >100 m south of the Stone Knife River to <50 north of it, and quickly pinches out a few kilometres farther north (Fig. 4.6A, B). This observation is consistent with isopach maps of Sayunei Formation thickness (Yeo, 1981). The northernmost part of the Redstone basin is devoid of iron formation: no evidence for iron formation, except for minor concentrations of coarse hematite crystals in upper Sayunei Formation siltstone and mudstone, is present anywhere between the Stone Knife and Twitya rivers, an area with otherwise excellent exposure of the Rapitan Group. The northernmost exposure of iron formation is just north of the Godlin River (9.5 km S of the Twitya River and 13 km W of the Keele River; Fig. 4.1B, location E). This exposure consists of approximately 20 cm of iron formation, present as 10 cm of jasper (Fig. 4.6C) and 10 cm of massive, flaggy-weathering hematite at the contact between the underlying siltstone of the Sayunei Formation and tan diamictite of the Shezal Formation (Fig. 4.6D). South of this location, iron formation is generally present, either *in situ* (e.g., Hayhook area) or as reworked clasts in diamictite (e.g., Boomerang).

Although exposure of the Rapitan Group south of the Redstone River is less consistent than it is farther north in the Redstone basin, and the Sayunei Formation thins dramatically (e.g., Eisbacher, 1978), the Rapitan Group in this area stands out in several regards. The Mt. Berg Formation is present only in this southern region (type section south-east of Coates Lake, as well as localised occurrences in other areas, typically in close association with faults in the underlying Little Dal Group (Yeo, 1981). At Coates Lake, at the extreme southern end of the Redstone basin,

the iron formation was reported to be of substantial thickness (<30 m, Eisbacher, 1976), but at no location visited in this study is it >15 m thick. Most interesting in this area is the iron formation present at the Hidden Valley copper prospect (Fig. 4.1B, location I). This location is known for vein-type copper mineralisation in the Little Dal Group (Jory, 1962; Colpron and Augereau, 1998; Colpron and Jefferson, 1998). Here, the lower Sayunei Formation consists of maroon siltstone and mudstone turbidites, which is typical of the Sayunei Formation in the Redstone Basin (Fig. 4.16 for a generalised stratigraphy). Where it differs, is that this approximately 100 m of fine-grained siliciclastic rocks is overlain by 50 m of medium to coarse-grained purple-brown, moderately hematitic sandstone. The sandstone is overlain by a 35 m-thick interval of iron formation that is different from that known from elsewhere in the Redstone basin. In addition to its unusual thickness, the iron formation at Hidden Valley contains a considerable volume of massive hematite (Fig. 4.6 E, F), both the flaggy-weathering, slaty hematite as at Hayhook, but also the more massive, poorly bedded type common throughout the Snake River basin. Jasper nodules are common in iron formation at Hidden Valley, despite their scarcity in most of the Redstone basin. In addition to all of the similarities of the iron formation with that in the Snake River basin, the Sayunei Formation is also similar to that in the northern basin. Although diamictite is sparse in the Sayunei Formation at Hidden Valley, the sandstone underlying the iron formation more closely resembles the matrix of the clast-poor diamictite underlying the iron formation at Iron Creek. The iron formation is immediately overlain by classical, recessive, scaly-weathering tan diamictite of the Shezal Formation.

4.5 Rare earth element geochemistry

The rare earth elements plus yttrium (REE+Y) are sensitive tracers for the origins of hydrogenous sedimentary rocks such as iron formation. This is due to the fact that the marine shale or upper continental crust composite-normalised (MuQ, from Kamber et al. 2005, is used here) REE+Y pattern appears to have behaved predictably over 3.7 Ga (e.g. Kamber, 2010) and because deviations from the expected pattern can be used to define the role of other sediment sources, such as hydrothermal fluids and siliciclastic detritus. In the ocean, the REE+Y fractionate from their normal, uniform behavior due to differences in their adsorption and

complexation properties; they are not solely controlled by valence and atomic radius (Bau, 1996). This fractionation results in a distinctly positive-sloped normalised REE+Y pattern with several well-defined anomalies that are consistent across the modern ocean and vary predictably with water depth (Zhang and Nozaki, 1996). There is now a very large body of data demonstrating that hydrogenous sedimentary rocks from throughout Earth history, most notably iron formation, can record important aspects of the dissolved marine REE+Y inventory over time (e.g., Kamber, 2010; Baldwin et al., 2012b).

The positive overall REE slope is best demonstrated using a normalised Pr/Yb ratio, because Pr and Yb are the lightest and heaviest REE that do not occur in anomalous concentrations. The La and Gd anomalies (La/La^* and Gd/Gd^*), calculated here after Lawrence et al. (2006), yield values >1.0 when a normal-marine seawater was sampled (there is no documented significance for values less than 1.0 in hydrogenous sediment for either of these anomalies). The Y/Ho ratio yields values greater than the chondritic ratio of 26.1 (Pack et al., 2007) when these chemical twins fractionate in seawater or in fluorine-rich magmatic systems (Bau, 1996). Rare examples of subchondritic ($Y/Ho < 26$) ratios have been documented in basaltic weathering profiles (Hill et al., 2000), and in iron formation deposited under a water column that was stratified with respect to the redox state of Mn (Planavsky et al., 2010). Two other REE+Y anomalies are commonly used when dealing with iron formation: the Ce and Eu anomalies. Ce commonly deviates from the REE+Y in a modern, oxidised ocean, generating deep, negative Ce anomalies, whereas in anoxic settings it is generally flat. In some redox-stratified conditions, positive anomalies form (e.g., Planavsky et al., 2010) below an inferred redox chemocline. Flat to weakly negative Ce anomalies are most common in the vast majority of iron formations, including those of Neoproterozoic age (Kato et al., 2006). The positive Eu anomaly is a robust tracer of high-temperature hydrothermal fluids, and is the principal evidence of a hydrothermal iron source in Archean and Paleoproterozoic iron formations (e.g., Derry and Jacobsen, 1990). This paper focusses predominantly on Pr/Yb, Gd/Gd^* , and Y/Ho ratios, because they have been shown to be the most insightful proxies in the Rapitan iron formation (Baldwin et al., 2012b).

The REE+Y data from iron formation jasper samples from three stratigraphic sections in the Snake River basin (Iron Creek, Discovery Creek, Cranswick River) and two stratigraphic sections in the Redstone basin (Hayhook North and South) are discussed individually. Emphasis is placed on stratigraphic trends in the REE+Y, especially in the Y/Ho ratio.

4.5.1 Iron Creek

The REE+Y patterns of 21 samples from Iron Creek at first glance look highly variable, but certain characteristics are present throughout the iron formation (Fig. 4.7) and with apparent stratigraphic control. Most samples have some features of seawater-derived sedimentary rocks, most notably, consistently positive slopes, expressed as Pr_{MuQ}/Yb_{MuQ} ranging from 0.05-0.71. As can be appreciated from the stratigraphically arranged panels (Fig. 4.7; panels C to F) the patterns flatten up-section. The La/La^* values range from weakly negative to strongly positive ($La/La^*=0.9-1.38$); all strongly positive La anomalies are low in the section. Cerium behaviour is fairly uniform throughout the section, with a tight Ce/Ce^* range of 0.88 to 1.06; six samples show statistically significant negative anomalies ($Ce/Ce^* \leq 0.95$), and only one sample has a significant positive anomaly ($Ce/Ce^*=1.06$.) but the majority of samples from Iron Creek are either flat or weakly negative with respect to Ce. Europium anomalies are predominantly flat to negative ($Eu/Eu^*=0.9-1.03$), with only two weakly positive anomalies in the dataset ($Eu/Eu^*=1.09$ and 1.19). The Gd anomalies are almost all flat to positive ($Gd/Gd^*=0.99-1.18$); one sample has a slightly negative anomaly ($Gd/Gd^*=0.94$). Y/Ho ratios are highly variable and weakly subchondritic to strongly superchondritic ($Y/Ho=23.0-42.2$), with a clear, well-developed stratigraphic trend (Fig. 4.7B).

Samples from low in the iron formation at Iron Creek ($n=7$; 65.7-69.7 m) all have strongly superchondritic Y/Ho ratios, ranging from 31.5-42.2, the highest ratios from the entire section (Fig. 4.7B). These samples also all have consistently positive Gd anomalies ($Gd/Gd^*=1.05-1.18$), as well as very low Pr_{MuQ}/Yb_{MuQ} (0.05-0.25), indicating strong HREE-enrichment relative to the LREE. These samples also have positive La anomalies ($La/La^*=1.09-1.21$). All of these features are consistent with hydrogenous sediment recording normal marine REE+Y compositions, and with the exception of La/La^* , are similar to other Rapitan iron formation samples from Cranswick River (Baldwin et al., 2012b) (Fig. 4.7C).

Higher in the section (96.1-121.2 m; n=4), Y/Ho ratios are weakly to moderately subchondritic (23.0-25.7; Fig. 7B). Gd anomalies are generally flat ($Gd/Gd^* = 0.99-1.05$), with negative to positive La anomalies ($La/La^* = 0.91-1.09$). Pr_{MuQ}/Yb_{MuQ} remains low (0.1-0.32), but is generally higher than in samples from the base of the iron formation (Fig. 4.7D). The generally flat to negative Y/Ho ratios, flat Gd anomalies, and slightly flattened pattern overall indicate an elevated clastic component in the iron formation, which is sufficient to overwhelm many of the common seawater REE+Y features, but not enough to cause the patterns to resemble shale or upper continental crust. This interval has numerous interbeds of clastic material, including diamictite and siltstone (Fig. 4.7A), indicating that clastic input into the iron formation was episodically high, and may have continued at a lower background level during times dominated by iron oxide and silica deposition, as suggested by the slightly elevated Al_2O_3 concentrations in this interval relative to the bottom of the section.

From 145.7-168.8 m (n= 6), Y/Ho ratios return to superchondritic levels, although they are much lower than those in the bottom interval, ranging from 26.5-34.0 (Fig. 4.7B). Gd anomalies are flat to positive ($Gd/Gd^* = 0.99-1.11$), as are most La anomalies ($La/La^* = 0.99-1.15$); a single sample has a negative La anomaly (0.93). The slopes of the patterns still show HREE-enrichment overall, with Pr_{MuQ}/Yb_{MuQ} ranging from 0.12-0.34, in the same range as the immediately underlying interval (Fig. 4.7E). These samples all exhibit seawater-like features, but the anomalies are much more subdued than those in the bottom interval, suggesting a continued, but diminished, clastic contribution to the iron formation. Because of the thick covered section between this and the preceding interval (Fig. 4.7A), it is impossible to know whether there was sharp change or a gradual shift from subchondritic to superchondritic Y/Ho. At the top of this interval, both the Y/Ho and Gd/Gd^* ratios decrease back toward non-anomalous values, indicating a gradual shift toward the characteristics of the overlying section.

Samples from the top interval (173.7-184.4 m; n=4), are characterised by flat to subchondritic Y/Ho ratios ($Y/Ho = 23.1-26.2$), returning to the same range as samples from the second interval (Fig. 4.6B). Gd and La anomalies are both negative to flat ($Gd/Gd^* = 0.94-1.06$; $La/La^* = 0.9-1.04$). Gd anomalies generally increase upward, but La lacks any significant trend. Pr_{MuQ}/Yb_{MuQ} ratios show a strong increase up-section, from 0.16 at 173.7 m, increasing to 0.29,

0.47, and 0.71 at the stratigraphically highest sample (Fig. 4.7F). The gradual flattening of the REE+Y patterns up-section, paired with consistently flat to weakly subchondritic Y/Ho ratios, indicates that the detrital flux was increasing upward. Importantly, the two samples from the top of the section, those with the flattest REE+Y patterns, classify as GIF samples (“iron formation arenites” of Klein and Beukes, 1993), as opposed to jasper bands, and contain variable amounts of siliciclastic material. The REE+Y evidence indicates that near the iron formation, prior to the onset of strictly siliciclastic deposition, the flux of detrital material into the hydrogenous iron formation increased, and was generally independent of the type of iron formation deposited.

Overall, the REE+Y record four separate geochemical intervals within the Iron Creek section, with the lowest being strongly seawater-influenced, the next indicating a weak siliciclastic component, followed by a return to weakly seawater conditions, and ending with strongly siliciclastic-influenced iron formation. This suggests that initially the iron formation at Iron Creek underwent a steady increase in the influence of siliciclastic sediment, which briefly lessened prior to a strong influx at the end of iron formation deposition. These intervals broadly coincide with increased proportions of purely siliciclastic sediment (siltstone or diamictite) interbedded with the iron formation, as well as textural evidence of shallowing in the iron formation.

4.5.2 Discovery Creek

Variations in the REE+Y patterns in the 13 samples from Discovery Creek (Fig. 4.8) are more dramatic than those from Iron Creek. All samples have positive slopes, with Pr_{MuQ}/Yb_{MuQ} ratios ranging from 0.07 to 0.69, reflecting strong to very weak HREE-enrichment; only five samples have $Pr_{MuQ}/Yb_{MuQ} < 0.20$, showing that most of the samples have strongly positive slopes, and only two of those have $Pr_{MuQ}/Yb_{MuQ} \geq 0.30$. La anomalies are variable, ranging from negative to positive, although most samples are statistically flat ($La/La^* = 0.82-1.30$). No discernible stratigraphic trend is visible in the La/La^* data. All samples have flat to weakly negative Ce anomalies ($Ce/Ce^* = 0.86-1.02$), with a single sample showing a deeper negative anomaly ($Ce/Ce^* = 0.79$). Eu anomalies are highly variable, ranging from weakly negative to moderately strongly positive ($Eu/Eu^* = 0.87-1.34$); only 4 samples have non-anomalous Eu. Gd anomalies are consistently flat to positive, with Gd/Gd^* ranging from 1.02 to 1.16. Y/Ho ratios

fall into a wide range, from flat to strongly superchondritic ($Y/Ho= 26.5-40.6$), with the exception of a single sample with a subchondritic ratio of 23.3. Y/Ho ratios form a clear stratigraphic trend with decreasing values up-section.

The lower two iron formation horizons (340.1-369.8 m; $n=5$) have strongly superchondritic Y/Ho ratios ($Y/Ho= 34.9-40.6$) (Fig. 4.8B). No clear stratigraphic trend is evident in this sample group, despite the large stratigraphic gap between the two thin iron formation units. Gd anomalies are flat to positive ($Gd/Gd^*= 1.02-1.16$), with no meaningful stratigraphic trend. All samples show strongly positive slopes overall, with Pr_{MuQ}/Yb_{MuQ} ranging from 0.07 to 0.12. Other REE+Y systematics are more variable in this group: La anomalies are dominated by negative to flat values, except sample DC-369.8, which is strongly positive. Similarly, the Eu anomaly is highly variable, ranging from negative to moderately positive (Fig. 4.8C). Despite the variations in this group, all REE+Y patterns record well-developed seawater-type patterns. Elsewhere in the Rapitan iron formation, the REE with the greatest relative variability, La and Eu, occur in otherwise extremely coherent datasets, which reflects a combination of basin restriction and detrital input (Baldwin et al., 2012b).

The 414.5-419.1 m interval, which is the lower part of the thicker, third iron formation interval ($n=5$), also has uniformly superchondritic Y/Ho ratios. The ratios are slightly less superchondritic, and fall into a tighter range than those from the lowermost interval, spanning from 27.8 to 30.1. Gd anomalies, although uniformly positive, are generally smaller than those in lower strata, with Gd/Gd^* between 1.05 and 1.09. The HREE are less enriched in these samples than the previous interval, with Pr_{MuQ}/Yb_{MuQ} values falling between 0.11 and 0.27 (Fig. 4.8D). Both the La and Eu anomalies are variable, as in underlying strata, and show no stratigraphic trend. Overall, these samples still appear to record seawater-type REE+Y patterns, but with smaller Y/Ho , Gd/Gd^* , and Pr_{MuQ}/Yb_{MuQ} ratios, the influence of open-marine seawater was probably diminishing.

Samples from the top of the iron formation at Discovery Creek, between 422.5 and 429.8 m ($n=3$), are as dissimilar from one another as they are from the samples from lower in the section. Y/Ho ratios range from subchondritic to weakly superchondritic going up-section ($Y/Ho= 23.3, 26.5, 27.2$ respectively; Fig. 4.8B). Gd anomalies are flat to positive, and decrease

near the top of the iron formation ($Gd/Gd^* = 1.07, 1.04, \text{ and } 1.02$). The overall slope of the patterns is erratic, with Pr_{MuQ}/Yb_{MuQ} ratios of 0.29, 0.69, and 0.30 (Fig. 4.8E). Whereas all previously described samples had fairly uniform positive slopes, and vary only in their finer-scale features, each of these three patterns is distinct. The lowest of these, DC-422.5, has a uniformly positive slope, but is otherwise a fairly featureless pattern, which is probably caused by the dominance of detrital material over the marine REE+Y signal. The middle sample, DC-423.5, is has a concave-down pattern, with LREE depletion relative to the MREE and HREE. The near-chondritic Y/Ho ratio of this sample suggests that it records a primarily crustal signature, although this signature is strongly diluted by >2 orders of magnitude. The uppermost sample, DC-429.8, is the most unusual with its concave-up pattern, showing strong LREE and HREE enrichment relative to the MREE. When compared to samples from lower in the section, specifically DC-414.7, which has a very similar Y/Ho ratio, the patterns are almost identical in all elements heavier than Sm (plus Y). Thus, it can be reasonably inferred that this was primarily a weak seawater-derived pattern that was overprinted by a phase rich in the LREE (La, Ce, Pr, Nd). Normally, this might be attributed to the presence of the Ce-phosphate monazite, but this sample has half as much P_2O_5 as the average of the entire section. Consequently, the LREE enrichment is of uncertain origin.

In summary, the two low, thin intervals of iron formation at Discovery Creek have well-developed seawater-type REE+Y patterns, indicating minimal geochemical influence from siliciclastic input. The topmost and thickest iron formation interval, however, shows a marked decrease in its Y/Ho ratios and generally less seawater-like patterns overall. The upper half of the third iron formation unit has erratic REE+Y patterns with variably circum-chondritic Y/Ho ratios, suggesting the dominance of a different geochemical source than that of the lower intervals. This upward evolution, although suggesting an increase in siliciclastic input overall, may be further complicated by the presence of copper mineralisation and possible post-depositional, pre-lower-Paleozoic weathering.

4.5.3 Cranswick River

Of the 42 samples from Cranswick River (Fig. 4.9A) described by Baldwin et al. (2012b), 33 have uniformly seawater-type REE+Y patterns, and the remaining nine are removed from

discussion because of their dramatically different patterns. These nine samples were scattered randomly throughout the stratigraphy of the iron formation, interspersed with the otherwise very homogeneous samples. Interestingly, however, all of these samples have superchondritic Y/Ho, with only a single sample showing a near-chondritic ratio of 26.5. All other patterns, seawater or otherwise, are moderately to very strongly superchondritic (Y/Ho = 28.6-42.5) (Fig. 4.9B). The consistently superchondritic Y/Ho strongly suggests that even the otherwise unusual REE+Y patterns all have a substantial, if not dominant, seawater component, which is quite distinct from the other studied locations. REE+Y patterns from this section are very coherent regardless of stratigraphic position (Fig. 4.9C).

4.5.4 Hayhook North

The REE+Y patterns in six samples from the thin iron formation at Hayhook North (Fig. 10) are all very coherent throughout the 1-meter section. Pr_{MuQ}/Yb_{MuQ} ratios record a moderate degree of HREE-enrichment, ranging from 0.27-0.43. La anomalies are flat to positive ($La/La^* = 0.94-1.28$), whereas Ce is consistently fairly flat ($Ce/Ce^* = 0.98-1.06$). All samples lack any kind of Eu anomaly, with Eu/Eu^* values ranging from 0.95 to 1.06. The entire iron formation shows positive Gd anomalies, ranging from 1.09 to 1.15. Y/Ho ratios range from modestly to strongly superchondritic (Y/Ho = 28.8-35.8) (Fig. 4.10C). Due to the strong coherence of the REE+Y patterns throughout the section, there is no stratigraphic trend with respect to any of the anomalies (Fig. 4.10B). All of the REE+Y proxies, as well as the overall shape of the patterns, strongly support a seawater source for the iron formation at Hayhook North, although the fairly high Pr_{MuQ}/Yb_{MuQ} ratios and modestly superchondritic Y/Ho ratios suggest that this signal was slightly diluted as compared to seawater-derived cherts from Iron Creek, Discovery Creek, and Cranswick River.

4.5.5 Hayhook South

Samples (n = 12) from the iron formation at the top of the Hayhook South section (Fig. 11) exhibit REE+Y patterns in two distinct groups. The patterns have positive slopes, with Pr_{MuQ}/Yb_{MuQ} ratios ranging from 0.19-0.84; this is a large range from moderately strong to weak HREE-enrichment. Lanthanum anomalies show a large range from deeply negative to positive ($La/La^* = 0.68-1.16$). Cerium anomalies are variable, ranging from negative to positive (Ce/Ce^*

= 0.86-1.17), although half of the samples are have essentially no anomalies. Europium anomalies are predominantly weakly negative to flat ($\text{Eu}/\text{Eu}^* = 0.88\text{-}1.02$, $n = 10$), although two samples have $\text{Eu}/\text{Eu}^* < 1.05$. Most samples either have no Gd anomaly or a positive anomaly ($\text{Gd}/\text{Gd}^* = 1.01\text{-}1.15$, $n=11$), except a single sample with a very small negative anomaly ($\text{Gd}/\text{Gd}^* = 0.95$). The Y/Ho ratios record the most dramatic variations, ranging from deeply subchondritic to strongly superchondritic ($\text{Y}/\text{Ho} = 16.5\text{-}40.3$). The Y/Ho ratios form two very well-developed groups stratigraphically, one with superchondritic ratios, and one with chondritic to subchondritic ratios.

Samples from the lower interval of the iron formation (230.5- 233.4 m) all have superchondritic and decreasing Y/Ho ratios (Fig. 4.11B) that are between 40.3 at the base of the interval and 29.3 at the top. Similarly, the Gd anomaly decreases with increasing stratigraphic height, from 1.10 and 1.15 at the bottom to 0.95 at the top. Other seawater proxies are more erratic throughout the section, with no stratigraphic trend for either La ($\text{La}/\text{La}^* = 0.97\text{-}1.15$), or for $\text{Pr}_{\text{MuQ}}/\text{Yb}_{\text{MuQ}}$ (0.19-0.84) (Fig. 4.11C). Although $\text{Pr}_{\text{MuQ}}/\text{Yb}_{\text{MuQ}}$ ratios do not form any well-developed stratigraphic trend, the sample with the very high ratio (HS-233.4; $\text{Pr}_{\text{MuQ}}/\text{Yb}_{\text{MuQ}} = 0.84$) is the highest in this section. This pattern is very flat overall, and with generally poorly developed anomalies, relative to the rest of this group ($\text{Gd}/\text{Gd}^* = 0.95$, $\text{Y}/\text{Ho} = 29.3$). Although some resemblance with a seawater REE+Y signature is present in this sample, it is much more strongly dominated by siliciclastic input, unlike the other samples in this group. This pattern is consistent with the transition from bedded jasper and hematite to an interval of interbedded IF and siltstone at the dm-scale just above this sample (Fig. 4.11A). Overall, this interval records moderate to weakly developed seawater REE+Y patterns, with some evidence for an increase in siliciclastic input higher in the interval.

The upper interval, from 234.6 to 237.0 m, in contrast with the lower part of the iron formation, has flat to strongly subchondritic Y/Ho ratios ranging from 16.5 to 25.6. Such unusually low values in iron formation have been attributed elsewhere Mn-cycling below a redoxcline (e.g., Planavsky et al., 2010). This does not appear to be the case here, because such Mn-cycling would also produce a positive Ce anomaly, and all Rapitan samples with subchondritic Y/Ho have flat to negative Ce (0.87-0.95) (Fig. 4.11B). The only sample with a

small positive Ce anomaly ($Ce/Ce^* = 1.05$) has an approximately chondritic Y/Ho ratio of 25.6. Based on these inconsistencies, a Mn-redox shuttle can be dismissed as the cause of the subchondritic Y/Ho ratios. Alternatively, these ratios may be related to the presence of copper sulfide mineralisation (chalcopyrite) along jasper and hematite bedding contacts in some of these samples. The sulfide minerals are very weathered, and Y has been noted to be highly mobile even after mild, low-temperature alteration (e.g., Hill et al., 2000). It appears that Y loss occurred either during post-Rapitan mineralisation, or during sulfide weathering, but it is uncertain which is responsible for these negative Y anomalies

Besides the Y/Ho ratios, the patterns from the upper interval at Hayhook South differ from seawater in other ways. Superficially, their Pr_{MuQ}/Yb_{MuQ} ratios are consistent with HREE-enrichment from a seawater source ($Pr_{MuQ}/Yb_{MuQ} = 0.26-0.50$), but the overall shape of these patterns does not depict steady light to heavy enrichment, but instead shows stronger depletion of the lightest LREE relative to the MREE than it does from the MREE to the HREE. Furthermore, most samples show sharp, negative La anomalies ($La/La^* = 0.68-0.80$), except for one sample with a pronounced positive La/La^* value of 1.16. Gd anomalies are all either flat or positive; four out of six have $Gd/Gd^* = 1.01$, and the others are 1.07 and 1.15, respectively. Overall, these patterns appear to be the product of mixed sources: a siliciclastic source, which overwhelmed any primary seawater signature, was followed by the removal of Y from the system either during Cu mineralisation or weathering.

4.5.6 Sources of REE+Y variability

The considerable variability in the REE+Y ratios used as seawater proxies in samples from the Rapitan iron formation may be the result of several different influences. These include:

- 1) The presence of comparatively high volumes of REE-bearing phosphate minerals;
- 2) The development of a strong redoxcline with respect to either Mn or Fe;
- 3) The presence or absence of Cu-sulfide mineralisation;
- 4) Variations in the detrital flux into the depositional basin;
- 5) Influence of freshwater (likely melt water) admixture into restricted rift basins

Each of these has the potential to influence the REE+Y chemistry of the iron formation, and it is possible that all or several of them contributed to variability.

The presence of a significant volume of phosphate minerals is known to affect the REE+Y composition of hydrogenous rocks. The distinctly non-seawater-like patterns preserved in marine phosphates (e.g., Picard et al., 2002) stem from over-enrichment of certain REE in specific phosphate mineral species, which can mask an otherwise normal marine signature (Shields and Webb, 2004). This is an important concern in the Rapitan iron formation, because of the previously reported high P₂O₅ content of Neoproterozoic iron formation (e.g., Klein and Beukes, 1993). Regardless, phosphate overwhelming the REE+Y budget can be excluded as a main reason for REE+Y variability in the studied Rapitan iron formation samples for two reasons. Pre-screening by laser ablation ICP-MS showed that P₂O₅ in the Rapitan IF is concentrated in hematite, rather than jasper; the samples analysed in this study are exclusively jasper. Limiting analysis to jasper produced lower P₂O₅ concentrations than those in large datasets that analysed bulk Rapitan iron formation samples that included hematite. Stuart (1963) reported a range of 0.43-1.60 wt% P₂O₅, with a mean of 0.83 and a median value of 0.77, whereas samples analysed here fall between 0.001 and 1.08 wt% P₂O₅ with a mean concentration of 0.21 wt % and a median of 0.16. Thus it is apparent that analyzing only the jasper in the IF limits the data to material with inherently low phosphate present. Furthermore, no clear relationship is seen when any of the REE+Y proxies are plotted against P₂O₅.

The possibility of Mn or Fe redox cycling is compatible with the occurrence of subchondritic Y/Ho ratios, which are practically unknown in pre-GOE hydrogenous sediments (e.g. Kamber, 2010). As discussed in the preceding section, however, Mn or Fe redox-cycling also leads to well-developed positive Ce anomalies. In the present dataset, there is no correlation between Y/Ho and the polarity of the Ce anomaly ($r^2 = 0.0426$). Furthermore, there are no obvious relationships between Fe₂O₃ and MnO (not shown) concentrations and any of the REE+Y proxies.

The possible influence of mineralizing fluids on REE+Y systematics is a viable explanation for those samples that were taken in proximity of Cu sulfide and their weathering products (Hayhook South), float (Discovery Creek), or nearby iron formation outcrop (Iron

Creek; Baldwin and Turner, 2012). As discussed above, the most dramatically subchondritic Y/Ho ratios correspond to samples containing Cu minerals, or are stratigraphically associated with such samples. Although there is no correlation between Cu concentrations and any of the REE+Y anomalies, this offers an acceptable explanation for some of the unusual Y/Ho ratios, but fails to explain the variations in the slope of the REE and the Gd anomaly, which do not show any clear relationship with the presence or absence of Cu minerals.

The fourth possible cause for REE+Y variability is the influence of detritus. Given the generally low concentrations of the REE+Y in these samples, an authigenic seawater signature could be easily overwhelmed by the contribution of siliciclastic material. When this possibility is tested by comparing the seawater proxies directly to Al₂O₃ content, however, no clear pattern emerges. This discrepancy was already documented by Baldwin et al. (2012b) with Eu. These authors found that elevated Eu/Eu* values consistently occurred in samples with higher Al₂O₃, but not all samples with high Al₂O₃ had elevated Eu/Eu*. The problem was attributed to the presence of Eu-poor aluminous phases in the jasper, but may also be related to the concentration of Al *relative* to that of another, more abundant element, such as Fe. This possibility was tested by plotting the seawater proxies against the molar ratio of Fe/Al (molar ratios were used because of the dramatically different concentrations of the wt% oxides of these elements), which yields a fairly clear relationship. When plotted against the Pr_{MuQ}/Yb_{MuQ} ratio, one clear trend emerges. Without exception, the high Fe/Al samples (i.e. those low in siliciclastic material) have consistently very low, open marine Pr_{MuQ}/Yb_{MuQ} (Fig. 4.12A). Equally, all samples with high Pr_{MuQ}/Yb_{MuQ} have low Fe/Al. This reflects flatter REE+Y patterns with increasing Al content relative to Fe (increased detrital flux to the iron formation). However, there remains a group of samples with relatively steep patterns but much lower Fe/Al. Similar relationships are present with other REE+Y ratios. A weakly hyperbolic relationship exists between Fe/Al and Eu/Eu*, especially when samples with negative Eu anomalies (Eu/Eu* ≤ 0.95) are excluded (Fig. 4.12B). This highlights the previous observations of Baldwin et al. (2012b) and Klein and Beukes (1993), that positive Eu anomalies are present only in samples with elevated amounts of siliclastic material, most likely plagioclase-rich samples with relative excess in Eu. The relationships of Y/Ho and Gd/Gd* with Fe/Al, however, are less clear than those of Pr_{MuQ}/Yb_{MuQ} and Eu/Eu* (Fig. 4.12 C, D). Superchondritic Y/Ho and positive Gd anomalies occur at high and low Fe/Al

and low excesses of Y and Gd are not restricted to samples with low Fe/Al ratios. The fact that neither of these plots generates a well-developed hyperbolic relationship reflects the influence of further factors on these ratios, such as the connection between Cu mineralisation and subchondritic Y/Ho.

A final factor to be considered is the possibility of sudden freshening of ambient water in response to ice collapse. This possibility is explored for the Discovery Creek section in Figure 4.13. Here it is found that the lowermost samples have very low Ba/Sr ratios, which is a clear indication of a marine character, whereas the middle section (meters 416 to 420) shows highest Ba/Sr (Fig. 4.13B). There is a clear association of high Y/Ho ratios with the marine low Ba/Sr and equally a clear flattening of the REE+Y pattern with lowering of the Y/Ho ratio (Fig. 4.13C, D). The uppermost samples show evidence for elevated Th/U ratios, which is a clear indication of clastic sediment admixture, which also goes in hand with a flatter REE slope (Fig. 4.13D). This chemostratigraphy could thus be interpreted to reflect an initially sediment-starved marine environment, followed by substantial release of fresh (possibly melt) water, that strongly increased the Ba/Sr ratio and blurred the marine REE+Y systematics immediately followed by an increase of clastic sediment input. The latter stages could be interpreted with the concept of Pleistocene Heinrich events. The complex interplay between marine precipitation, freshwater influx and variable clastic sedimentation probably explains the absence of a well-developed hyperbola in the Gd/Gd* diagram (Fig. 4.12D). The Fe/Al ratios do not correlate well with the variations in the La/La* values, but the presence of negative La anomalies was found to be an artefact of normalisation together with felsic drainage into a restricted basin (Baldwin et al., 2012b). Renormalisation to a granitic average (as opposed to MuQ, as used here) either flattens the pattern or generates a positive La/La* in most samples, as previously established.

Overall, the results from this large, regional dataset are consistent with the conclusions reached using data from a single location (Cranswick River; Baldwin et al., 2012b), but with increased variability owing to locally and intermittently elevated siliciclastic content in the iron formation, as well as other geochemical influences that were not at work at Cranswick River. Understanding the variations in the REE+Y helps to distinguish broad depositional patterns with

respect to proximity to sediment supply across the regional expanse of the Rapitan iron formation.

4.6 Discussion

Major regional stratigraphic and geochemical differences in the Rapitan iron formation in the Snake River and Redstone basins have significant paleogeographic implications. The most significant of these is the thickness and widespread occurrence of iron formation in the former, and its limited thickness and patchy occurrence in the latter. If the precipitation rate of Fe-oxide precursors and silica was roughly constant, a complete shut-down of terrigenous clastic input is required to deposit a substantial thickness of purely hydrogenous iron formation. The Snake River basin must, therefore, have had a much more significant interval of siliciclastic sediment starvation than did the Redstone basin, where sediment starvation must have been fairly localised and brief. An argument could be made for a smaller supply of dissolved iron in the Redstone basin than the Snake River basin, based on the lower percentage of hematitic beds in the iron formation there (10-20% maximum), but the large concentration of Fe₂O₃ in the siliciclastic parts of the Sayunei Formation (average 12.1 wt%, Yeo, 1984) negates this possibility.

There are several possible explanations for why the Snake River basin was more sediment-starved than the Redstone basin. Regionally supplied sediment may have been temporarily trapped in a nearby basin-margin area in the Snake River basin during interglacial sea-level rise; sediment stranding during sea-level rise was part of the depositional model proposed by Baldwin et al. (2012b). An explanation that invokes sediment supply, however, is applicable to deposition of the Rapitan iron formation in both basins, because it can be reasonably assumed that iron formation deposition was contemporaneous across the entire basin system during a major regional sea-level rise (Klein and Beukes, 1993). A more distal position for the Snake River basin than the Redstone basin, however, appears to conflict with the observation that the Sayunei Formation in the Snake River basin is much coarser grained than in the Redstone basin. Furthermore, the steep faulted contact with the Wernecke Supergroup and Pinguicula Group on the western margin of the Snake River basin (Eisbacher 1981b) suggests that it is possible that the basin was not necessarily physically distal to sediment source, and that

sediment trapping above the basin margins made the otherwise proximal basin very distal during iron formation deposition. This is in sharp contrast with the Redstone basin, which had shallow-sloped basin margins, with significant sediment transport distances during Sayunei Formation deposition, resulting in the fine-grained turbidites. The shallow-sloped basin margins resulted in a shallower basin overall, with less sediment trapping outside of the basin margins during sea-level highstand, which combined to cause a relatively brief period of siliciclastic sediment starvation to the basin. Combined with a comparatively thin ferruginous water column in the deepest basin, this feature caused the deposition of much thinner iron formation than that deposited in the Snake River basin (Fig. 4.16).

Most of the iron formation sections analysed for their REE+Y geochemistry show clear stratigraphically controlled variability. Well-defined intervals of hydrogenous and siliciclastic-influenced iron formation (despite being sedimentologically indistinguishable) are present in the stratigraphic sections at Iron Creek, Discovery Creek, and Hayhook South. This makes the geochemically homogeneous stratigraphic sections at Cranswick River and Hayhook North unusual (particularly the thick Cranswick section). The stratigraphic patterns in each of the former three sections indicate a strongly hydrogenous, particulate-sediment-starved environment that received pure, hydrogenous iron formation, particularly at the onset of iron formation deposition. Higher in these sections, the influence of siliciclastic material on the REE+Y chemistry increases (although this pattern is complicated at Hayhook South due to the presence of copper sulfide mineralisation, as discussed above). Iron Creek is the thickest and most complete of these three sections, and contains two complete alternations between purely hydrogenous- and siliciclastic-influenced iron formation. The second alternation is more strongly siliciclastic-influenced in both the hydrogenous and siliclastic-dominated intervals (transitioning, in increasing stratigraphic order, from strongly hydrogenous to weakly siliciclastic, to weakly hydrogenous to strongly siliciclastic), which are overlain by hematitic sandstone and siltstone. The stratigraphic evolution of the REE+Y in the Iron Creek section records gradual basin filling with increasing siliciclastic input, although chemical sedimentation was still the dominant process. The combination of thick siliciclastic interbeds (up to 21 m) and increasing detritally-influenced REE+Y patterns suggests that throughout iron formation deposition, there was at least one episode of moderate sea-level lowstand, potentially caused by moderate local tectonic

activity, or perhaps a high-order Milankovitch cycle. The return to more hydrogenous-influenced REE+Y at Iron Creek higher in the succession suggests that sediment starvation was renewed partway through iron formation deposition, through either renewed subsidence or sea level rise. The return to strongly siliciclastic-influenced iron formation at the top of the section, as well as the presence of shallow-water iron formation facies (GIF) in the uppermost strata of the iron formation, suggest that sediment starvation was minimal at the end of iron formation deposition, even during predominantly hydrogenous sediment deposition. The loss of sediment starvation was probably the result of several factors, including significant sea-level lowstand and basin infill. The former was likely more important, and is consistent with the apparently more ice-proximal depositional setting of the overlying Shezal Formation, which is predominantly composed of submarine diamictite with variable clast contents (Eisbacher, 1978). Furthermore, the Shezal Formation is iron-poor in most areas (except immediately overlying the iron formation at Iron Creek), and is on average several weight percent lower in Fe_2O_3 than the Sayunei Formation (Yeo, 1981), which suggests that it was deposited in shallow water above the iron chemocline in the basin. Lastly, the presence of remobilised jasper clasts, which appear to have been deformed prior to lithification in diamictites positioned either above the iron formation (Cranswick River), or in place of it (Boomerang), indicates that relatively ice-proximal areas of iron formation deposition were susceptible to reworking by the later influx of glacioclastic sedimentation. The sedimentology and iron content clearly indicate that a significant drop in sea level followed, and possibly triggered, the shut-down of iron formation deposition in the Rapitan Group.

These stratigraphic and geochemical considerations define significant changes in the depositional patterns of the Rapitan Group across the entire region. There is a clear geographic pattern for the distribution of iron formation. Thick iron formation is clearly associated with an early-stage rift, but iron formation is thin to absent in areas with well-developed, earlier rift-associated sedimentary packages. These observations suggest that a system of faults and sub-basins may have been the primary control on the distribution and sedimentation style in the Rapitan Group.

4.6.1 Basins and faults

The considerable regional differences in the formation-level stratigraphy of the Rapitan Group, including thickness and geographic extent of the iron formation, between the Snake River and Redstone basins appear to be a depositional and not a deformational or erosional feature. Similarly, the absence of the Rapitan Group in the large area between the two sub-basins appears to record no deposition, rather than later erosion (Eisbacher 1981). Even within each of these basins, variations in the thickness and distribution of the Rapitan Group and the iron formation are considerable. Internal variations are relatively minor in the Snake River basin, but are more pronounced in the geographically much more extensive Redstone basin. A very important observation is that the margins of each of these basins, as well as changes in the stratigraphic character (e.g., major thickness changes in the Sayunei Formation, the appearance or disappearance of iron formation), correspond with the locations of mapped and inferred major, crustal-scale fault systems. The locations of inferred syndepositional faults were based on overall thickness changes in the Coates Lake and Rapitan groups (Eisbacher, 1981b, 1985), but also on unusual thickness and facies patterns for time-delimited units in the underlying Katherine and Little Dal groups of the Mackenzie Mountains Supergroup (Turner and Long, 2008). A comparison of the areal distribution of the iron formation and the proposed locations of many of these faults suggests that they may have exerted dominant control on the distribution, and even thickness, of the iron formation.

Nine faults, both documented and inferred, are present in the exposure area of the Rapitan Group (Fig. 4.14). Because most of the faults are inferred based on stratigraphic evidence from rocks that predate the Rapitan basin rather than documented directly from structural evidence (with the exception of the Snake River fault on the western margin of the Snake River basin), the relative timing of their activity and their sense of movement at any given time cannot be ascertained. Changes in stratigraphic thicknesses, however, strongly indicate their approximate positions, as well as which side was the down-thrown side of the fault. Most of the faults implicated in Rapitan basin evolution were also active prior to deposition of the Rapitan Group (Turner and Long, 2008), and some, if not all, of these structures were active throughout Rapitan deposition based on localised deformation features (e.g., Helmstaedt et al., 1979). Consequently, the only available means of categorising these faults is by their importance in basin development,

with minimal implications with regards to timing or origin. Faults are here sorted using the term ‘class’ rather than the more conventional term ‘order’, because the latter has chronological implications. The fault series are as follows: Class 1: Major basin-bounding faults; Class 2: Major basin-changing faults; and Class 3: Minor basin-changing faults. Each category is established based on its significance in defining the paleogeography of the basin: some faults define basin margins, some mark depth changes within the basin, and others mark minor changes in basin depth.

The Snake River, Cranswick, Stone Knife, and Silverberry faults are Class 1 (basin-bounding) faults. The Godlin and Raven’s Throat faults are Class 2 faults (are located where there are major changes in sedimentation, such as appearance of iron formation). The Sammon’s Creek, Mountain River and Redstone faults are Class 3 faults, across which significant thickness changes are evident in the Sayunei Formation and underlying lithologies (Yeo, 1981; Jefferson, 1983; Eisbacher, 1985; Long et al., 2008; Turner and Long, 2008). No other previously proposed structures meet any of the above criteria, but the Fort Norman structure (Aitken and Pugh, 1984), just south of the Godlin fault, may be important in the Boomerang or Nite areas. The hierarchical classification of syndepositional faults helps in understanding the sedimentological development of the Rapitan sub-basins, especially the presence and thickness of iron formation, and the presence/absence of the underlying Coates Lake Group (CLG). Three styles of sub-basin are present:

Type 1: Older rift basin with moderate subsidence and no iron formation (CLG present)

Type 2: Older rift basin with elevated subsidence and thin iron formation (CLG present)

Type 3: Young rift with substantial subsidence and thick iron formation (No CLG present).

Each of these basin types is bounded by one or more of the above fault series, and is distinct in several sedimentological and stratigraphic ways.

In Type 1 basins, the Rapitan Group is underlain by the Coates Lake Group, indicating that the basin had a recent depositional history prior to Rapitan Group deposition. The main example of this basin type is the northern part of the Redstone basin (between Stone Knife and

Twitya Rivers). Bounded to the north by the Series 1 Stone Knife fault, this sub-basin is underlain by a substantial but variable thickness of the Coates Lake Group, and contains both the Sayunei and Shezal Formations. Iron formation is absent throughout this area, and this basin type is in general. The absence of iron formation indicates that the basin floor in this basin type was at or above the iron chemocline at the time of iron formation deposition. The absence of iron formation, the presence of pre-Rapitan rift deposits, and the apparent pinch-out of the Rapitan and Coates Lake Groups north of the Stone Knife River suggests that this was a shallower basin than other areas of the greater Rapitan basin, on the margin between the Redstone basin and the area to the northwest of the basin, which remained above base level until the post-Rapitan Twitya Formation was deposited. Because this basin type is apparently the oldest and most marginal of the listed types, it can contain sub-basins of Types 2 or 3 within it, if they are subdivided by faults of Class 2. Thickness changes in Type 1 basins are controlled by either Class 3 faults, such as the Mountain River Fault, in the case of substantial thickness changes, or by more minor structures that had an influence on the paleobathymetry of the basin, but have not been documented here (Fig. 4.15A).

Type 2 basins, in which both the Coates Lake Group and iron formation are present, include most of the Redstone basin south of the Twitya River, where the northern limit of thin iron formation is immediately north of the Godlin River. Increased fault movement, and consequently the creation of additional accommodation space, allowed for this part of the basin to become particularly deep, which allowed for a prolonged interval of siliciclastic sediment starvation at the end of Sayunei Formation deposition. Sedimentological isolation of a deep basin depocentre permitted deposition of iron formation throughout most of this basin, but limited its thickness to no more than 10-15 metres. Although this part of the basin had undergone more subsidence than the Type 1 basin to the north, it did not starve the basin of siliciclastic material for a time that was long enough for accumulation of thicker iron formation, as in the Snake River basin. The limitations of sediment starvation are also shown by the REE+Y patterns from the iron formation at each of the Hayhook measured sections. Hayhook North has consistently seawater-type REE+Y patterns, with high Gd/Gd* and Y/Ho ratios, and low Pr/Yb. The iron formation is only 0.7 m thick in this section, however, indicating that the sediment starvation at this location, although complete, was also brief. The short duration of sediment starvation is corroborated by

the relative paucity of pure seawater-type REE+Y patterns from the much thicker (6 metre) iron formation a short distance away in the Hayhook South section, where even the most-seawater like patterns are more poorly developed than at Hayhook North. This variation over such a short lateral distance probably reflects a complex paleobathymetry, across which the iron formation was discontinuous. The entire Redstone Basin is thus best visualised as a complex of subaqueous lows and highs, which controlled where iron formation deposition was possible (Fig. 4.15A). The presence of plastically deformed, reworked iron formation clasts in the lowermost Shezal Formation in the Boomerang section and other nearby locations indicates that parts of the basin had been sufficiently starved at some time to accumulate iron formation, but were later shallow enough to have that iron formation completely reworked during later diamictite deposition. This sub-basin is bounded by a Class 2 fault (Godlin fault) to the north, which separates it from the Type 1 part of the Redstone basin, and is bounded to the south by the Class 1 Silverberry fault. Like the Type 1 basin, this basin type can contain smaller, deeper sub-basins of Type 3, specifically the Hidden Valley area.

Type 3 basins are the youngest, and at the time of deposition, were the deepest and most distal of the Rapitan basin system. These basins are characterised by ≥ 30 m of iron formation, and are not underlain by Coates Lake Group strata, instead lying in unconformable contact with the older Little Dal Group. There are two examples of this in the greater Rapitan basin: the entire Snake River basin, and the very small Hidden Valley basin (Fig. 4.15A). Both of these basins are directly fault-bounded, and are in angular unconformable contact with the Little Dal Group. The absence of the Coates Lake Group beneath each of these Type 3 basins indicates that they were not areas with a depositional history that closely predated deposition of the Rapitan Group, and suggests that they began receiving Rapitan Group sediment very soon after their development. This interpretation of recent and dramatic basin initiation in areas underlain by Little Dal Group strata rather than Coates Lake Group strata is further supported by the coarseness of the siliciclastic rocks below the iron formation in Type 3 basins, which probably reflects proximity to a faulted basin margin. In both Type 3 basins the Sayunei Formation contains significant thicknesses (≥ 50 m) of much coarser material than the fine-grained turbidites that dominate this formation in the other basin types. In the Snake River basin, the iron formation is underlain by red to purple diamictite with a sandy matrix. Likewise, the iron formation at Hidden Valley has

several coarse clastic units underlying it. In immediate contact with the Little Dal Group is an orange to tan boulder diamictite, similar to the Mt. Berg Formation in the region, which is irregularly overlain by purple fine-grained turbidites typical of the Sayunei Formation. The top 50 metres of the Sayunei Formation (below the iron formation), however, is medium- to coarse-grained purple-brown sandstone, a feature not documented elsewhere. The grain size of the coarse material from each of these two Type 3 basins is dramatically different, but the reason the coarse sediments are present is the same. As newly developed rift basins at the time of deposition, these basins were both bounded by relatively high-angled basin margins, which would have been prone to collapse, supplying coarser siliciclastic material to the distal parts of the basin than would otherwise get there. Once the basin margins had stabilised, the basin remained deep enough to be starved of siliciclastic sediment during protracted highstand, allowing for thick iron formation to be deposited. This also resulted in some other differences in the sedimentology of the iron formation. Massive hematite, as opposed to slaty (or flaggy) hematite, is present in both of these basins, whereas it is completely absent in Type 2 areas. Likewise, the iron formation in the Type 3 basins contains abundant jasper nodules, which are rare in thinner iron formation exposures, where the jasper is exclusively bedded. This suggests that the deeper basins had a thicker ferruginous, or iron-rich, water column, allowing for the deposition of much larger amounts of hematite relative to silica, and that the siliciclastic input into the deepest basins was low enough to not affect the sedimentological character of the iron formation. The relatively thick iron formation at Hidden Valley contains characteristics of iron formation from both Type 2 and Type 3 basins, suggesting that this small Type 3 basin was not nearly as deep as the Snake River basin.

Sediment infilling of the Snake River and Redstone basins differed markedly. In both basins, the siliciclastic portion of the Sayunei Formation was deposited during a glacial period with relatively low sea level, which allowed the delivery of significant amounts of siliciclastic material to the distal parts of the basin in each (Fig. 4.16A, B). Sediments in the Snake River basin was sourced from the north, resulting in even sedimentation of diamictite with a sandy to muddy matrix across the east-west axis of the basin, whereas different paleocurrent directions in different parts of the Redstone basin suggest multiple sediment sources in different parts of that basin (Eisbacher 1981b). Broadly, paleocurrent directions in the Redstone basin indicate two

differently sourced areas: one that was situated between the Stone Knife and Mountain River faults, and another between the Godlin and Silverberry faults. In the former area, paleocurrents indicate the dominant sediment source was from the northeast (coming out of Fig. 4.16B), whereas sediment sources for the latter area were sourced from the southeast. These basins were separated by an elevated horst between the Mountain River and Godlin faults, where the Sayunei Formation was not deposited (Yeo, 1981). Towards the end of Sayunei Formation deposition, an interglacial period began, with a concomitant rise in sea-level. This sea-level rise flooded the basin margins of both the Snake River and Redstone basins, resulting in significant siliciclastic sediment trapping outside of the basins, and starving the distal basin of sedimentation. In the Snake River basin, this allowed the deposition of a significant thickness of iron formation with only periodic interruption by siliciclastic sedimentation during intervals of moderate sea-level lowstand (Fig. 4.16C). In the Redstone basin, the end-Sayunei Formation highstand only permitted the deposition of iron formation to the south of the Godlin fault. This is because the areas to the north had undergone sufficient sediment infilling that the basin floor was above the iron chemocline, making iron formation deposition impossible. Irregular basin floor topography south of the Godlin fault (Fig. 4.15A) resulted in variable iron formation thickness across this basin (0-30 m) (Fig. 4.16D). Iron formation deposition continued in both basins until either the iron supply was exhausted, or the iron chemocline was intersected by the sediment-seawater interface. In the case of the Snake River basin, the chemocline was above wave base, resulting in the deposition of GIF at the top of the iron formation, which was overlain by mildly hematitic siliciclastic sediments in some localities (e.g., Iron Creek) (Fig. 4.16E). Iron formation deposition was quickly followed by a drop in sea-level due to glacial re-advance, depositing the Shezal Formation. Importantly, the local occurrence of clasts of iron formation that have undergone soft-sediment folding in the base of the Shezal Formation (e.g., Cranswick River and Boomerang) indicates that Shezal Formation sedimentation started soon after the end of iron formation deposition, and corresponded with a sharp change in seawater chemistry (Baldwin et al., 2012b; 2013). The Shezal Formation was deposited evenly across both the Snake River and Redstone basins, including across the horst between the Mountain River and Godlin faults in the Redstone basin (Fig. 4.16F). The deep water mudstone and siltstone of the overlying Twitya Formation

(Yeo, 1978) were deposited across the entire region following total glacial withdrawal and a major rise in sea-level associated with the end of the Sturtian glaciation.

4.6.2 A revised correlation scheme for the Rapitan Group

The substantial differences in the Rapitan Group between the Redstone and Snake River basins have resulted in a highly disputed stratigraphy in the latter basin. This is in large part because of two factors; firstly, the considerable thickness of iron formation in the Snake River basin, and secondly, the absence of fine-grained (silty and muddy) maroon turbidites characteristic of the Sayunei Formation at its type section (Eisbacher 1978) and elsewhere in the Redstone basin. This latter issue has proved to be more troublesome factor, and has resulted in at least two different formation-level stratigraphic interpretations for the Rapitan Group in the Snake River basin. The original interpretation suggested that the Sayunei Formation is completely absent in the Snake River basin, due to the lack of the characteristic turbidites (Yeo 1981). In that interpretation, the diamictites and other siliciclastic rocks in this basin are all attributed to the Shezal Formation, and the iron formation is positioned midway in that formation. Although there are textural similarities between the diamictite that underlies the iron formation, and hematitic strata in the Shezal Formation in the Redstone basin, this interpretation requires the assumption that the iron formation was not a time horizon across the entire exposure belt. Klein and Beukes (1993) preferred a more parsimonious stratigraphic interpretation, wherein the iron formation in the Snake River basin was a time horizon with that in the Redstone basin. They only equate the diamictite immediately underlying the iron formation in the Snake River basin with the Sayunei Formation in the Redstone basin, instead correlating the lowermost diamictite with the Mt. Berg Formation. This correlation scheme is also favored by Hoffman and Halverson (2011). Where this correlation scheme fails, is that the diamictites underlying the iron formation in the Snake River basin are sedimentologically similar throughout their thickness, and are hematitic. Mapped exposures of the Mt. Berg Formation are geographically limited to the southern end of the Redstone basin, are universally directly associated with fault margins, and are exclusively non-hematitic (Yeo 1981). Consequently, from a sedimentological and geographic standpoint, the presence of the Mt. Berg in the Snake River basin can be eliminated, although certain elements of this latter interpretation remain valid.

Based on the detailed stratigraphic study presented here, a clearer picture of the formation-level stratigraphy of the Rapitan Group can be made. All Rapitan Group siliciclastic rocks underlying the iron formation in the Snake River basin are part of the Sayunei Formation. They are, however, a coarse-grained facies of the Sayunei Formation. A parallel with respect to grain size is the presence of the 50 m unit of medium-grained sandstone at the top of the Sayunei Formation in the Hidden Valley area. This indicates that, in addition to the iron formation, the Sayunei Formation, broadly speaking, has three different facies; the fine-grained turbidites of the Redstone basin, and two different coarse-grained facies, the sandstone at Hidden Valley, and sandy-matrix turbidites of the Snake River basin. In the interpretation proposed here, the coarse-grained facies are localised in isolated basins (Snake River and Hidden Valley), whereas the fine-grained turbidites are more widespread (Fig. 4.17). Iron formation was deposited at the top of the Sayunei Formation contemporaneously across both basins as a time horizon most likely corresponding to an interglacial sea-level highstand, although the thickest deposits correspond to the basins in which the coarse facies Sayunei Formation were also deposited. Iron formation was not deposited in the northern Redstone basin, and is thin throughout much of the southern Redstone basin, except for localised areas where it is thicker, such as Hidden Valley and (possibly) Coates Lake. The Shezal Formation was deposited evenly across both basins, but ‘Red Shezal’ as described by Yeo (1984) is a local feature where the uppermost Sayunei Formation was reworked during Shezal Formation deposition. This new correlation scheme should resolve the longstanding disagreement about the stratigraphic context of the Rapitan iron formation.

4.6.3 Implications for the rifting of northwestern Laurentia

The rifting of the western margin of Laurentia during Rodinia’s dispersal has been established as diachronous at the regional scale (Colpron et al., 2002), which explains the laterally discontinuous Sturtian-age record along the Cordillera. The sedimentological evidence presented here further suggests that rifting was staggered at a more local scale, with the development of several sub-basins at slightly different times across the Mackenzie, Wernecke, and Ogilvie mountains.

Rifting began much earlier in the Redstone basin than in the Snake River basin, as indicated by the presence of continental-rift-associated rocks (basalt, red beds, evaporites) of the

Coates Lake Group underlying the Rapitan Group in the Redstone basin, and their absence in the Snake River basin. Furthermore, there is evidence that rifting was temporally staggered within the Redstone basin as well. Thickness profiles of the Sayunei Formation, the Coates Lake Group, and the Ram Head Formation (Little Dal Group) support the notion of staggered rifting (Fig. 4.15C, D, E, F). Broadly speaking, areas where the Ram Head Formation and the Coates Lake Group are thickest do not correspond with areas where the Sayunei Formation is thickest. With few exceptions (notably in the vicinity of Coates Lake in the far south), the thickest developments of the Sayunei Formation are where the Coates Lake Group is fairly thin. This suggests that rifting within the Redstone basin system was more pronounced in different areas at different times. Namely, areas that underwent less subsidence during Coates Lake Group deposition subsided more prior to and during deposition of the Sayunei Formation. This suggests that the earliest stages of rifting were very localised across the region.

Overall, rifting of the Redstone basin progressed as follows: (1) A pre-history during which the Little Dal Group was deposited. Subsidence was comparatively even along strike during deposition of the uppermost part of the group, resulting in minimal thickness differences along strike in the Ram Head Formation units 1-5 (Jefferson, 1983) (Fig. 4.15C). (2) During deposition of the upper Ram Head Formation, subsidence was becoming less even, resulting in larger along-strike thickness changes than those evident in units 1-5 (Fig. 4.15D). (3) Rifting began in earnest following the emplacement of the “Little Dal basalt”, with deposition of the Coates Lake Group. Thicknesses of the Coates Lake Group were highly variable along strike. The variability in thickness is interpreted to outline sub-basins or embayments through uneven, early-stage rifting (Fig. 4.15E) (Jefferson and Ruelle, 1987). (4) Rifting and subsidence continued through deposition of the Sayunei Formation, which is thicker where the Coates Lake Group is thin, resulting from the combination of basin fill and enhanced subsidence of areas where the Coates Lake Group had not been deposited (Fig. 4.15F). Continued subsidence resulted in a more regular thickness profile for the Sayunei Formation across the Redstone basin than that exhibited by the Coates Lake Group. (5) Successive formations higher in the Windermere Supergroup became more evenly distributed along strike as extension progressed, eventually connecting the Redstone and Snake River basins. Smaller rifts, more akin to the Snake River basin in areal extent, simultaneously developed to the northwest, in the Hart River and Tatonduk inliers,

western Yukon and eastern Alaska (Young, 1982; Macdonald et al., 2010a). Extension progressed towards the full development of a passive margin in the latest Neoproterozoic - Cambrian, with deposition of the ‘upper group’ of the Windermere Supergroup and its putative time-equivalent Hyland Group in the Selwyn Basin (e.g., Fritz et al., 1983; Aitken, 1989; Gordey and Anderson, 1993; Cecile, 2000).

The observation that the progressive rifting stages of a supercontinent correlate directly with depositional patterns in Rapitan Group glacial strata has significant implications for late Neoproterozoic, putatively global glaciations. The evidence is consistent with the “zipper-rift” hypothesis for “snowball Earth” proposed by Eyles and Januszcak (2004). Such lithostratigraphic evidence may also be present in other Sturtian-aged basins worldwide, which have not yet been subjected to rigorous regional stratigraphic analysis. Determining the global implications of the profound relationship between tectonics and Neoproterozoic glacial dynamics, documented in detail here for the first time, will require a large-scale interdisciplinary approach, integrating sedimentology, detailed stratigraphy of numerous sections, and geochemistry, applied to other Neoproterozoic glacial basins.

4.7 Conclusions

Stratigraphic sections through the Sayunei Formation from throughout the exposure of the Rapitan Group show that Rapitan iron formation is highly variable in both thickness and character over fairly short distances. Major changes in iron formation thickness are further reflected by the changing character of the underlying Sayunei Formation, which is very fine-grained in areas where iron formation is <30 m thick, but contains significant thicknesses of coarse clastic material (either sandstone or sandy diamictite) where iron formation is thicker. Thicker iron formation successions commonly contain several distinct chemostratigraphic zones, as defined by the REE+Y signatures that are dominated by either hydrogenous or siliciclastic components. Chemical zones in the thickest iron formation show several cycles of shallowing-upward and subsequent deepening of the basin, and coincide with sedimentary evidence for basin infill and subsequent subsidence. The geochemical signatures of iron formation units that were consistently isolated from siliciclastic sedimentation remained purely hydrogenous over their

entire thickness. These lines of evidence collectively indicate that the thickest and most iron-rich iron formation intervals were deposited in the deepest and most tectonically active sub-basins.

The locations of major stratigraphic and sedimentological changes in the Rapitan iron formation and the Rapitan Group as a whole correspond with the estimated locations of crustal-scale basin-forming faults proposed by Eisbacher (1985) and Turner and Long (2008). This pre-existing context, considered in conjunction with the presence of extensive soft-sediment deformation in thick iron formation intervals, suggests active subsidence in a relatively young rift basin, an interpretation that is supported by the absence of the Coates Lake Group in areas with thick iron formation (Snake River area and Hidden Valley). Older, more evolved basins, such as most of the Redstone basin, contain much thinner iron formation. The presence of thick units of red Shezal (reworked Sayunei) and remobilised, plastically deformed jasper clasts in the lower Shezal Formation at Boomerang Lake indicate that the basin was probably at or near the ice-grounding line in this area, and was thus probably too shallow at the end of Sayunei Formation deposition to generate great thicknesses of iron formation. Iron formation is even thinner and more patchily distributed in the central part of the Redstone basin, and exposures in the northwestern Redstone basin do not contain iron formation, regardless of the thickness of the Sayunei Formation overall, due to the relatively shallow-water conditions, the stratigraphically evolved nature of the basin in this area, and the absence of siliciclastic sediment trapping on the basin margins. This basin then shallowed rapidly to the northwest, and the Rapitan Group pinches out depositionally in this direction. In the Snake River area, the basin has a fairly steep western fault margin and a gradual, shelf-like eastern margin, resulting in a small, deep basin, which allowed for the deposition of coarse clastic rocks in the deep basin prior to iron formation deposition, but the limitation of siliciclastic input later, allowing for deposition of thick iron formation. Consequently, economically viable iron formation could only be deposited in the most distal parts of the basin, with sufficient depth to a significant water mass below the iron chemocline, and with active subsidence to maintain basin depth and accommodation space.

Together with previous, related papers on the Rapitan iron formation, this study represents the first comprehensive sedimentological-stratigraphic-geochemical treatment of late Neoproterozoic glacial strata containing iron formation. The history of the Sayunei Formation's

basin is geographically complex in terms of its subsidence, sediment budget, and geochemistry. The overall picture is of a profoundly unstable rift environment containing erratically subsiding, geochemically isolated sub-basins that had distinct geochemical and sedimentological histories. An improved understanding of the tectonostratigraphic controls on the depositional environment of the Rapitan Group has resulted in a resolution of the long disputed stratigraphy in the vicinity of the Crest iron deposit. Although no conclusive statement can be made regarding the possibility of a ‘global’ glaciation, the combined evidence points to regional glaciation that developed along the margins of a rift system in northwestern Laurentia during early dispersal of Rodinia. Sea water in each of the rift’s sub-basins evolved independently, suggesting that Neoproterozoic iron formation deposition may not have required a global driver.

4.8 Acknowledgments

Field work for this project was jointly funded by the Northwest Territories Geoscience Office (NTGO) and the Yukon Geological Survey (YGS). Additional field support was provided by Aurora Geosciences Ltd., Coltstar Ventures, and Copper North Mining Corp. Funding was also provided by a Society of Economic Geologists Student Research Grant to GJB, and National Science and Engineering Research Council (NSERC) Discovery Grants to ECT and BSK. E Martel, J. Ketchum, and C. Ozyer of the NTGO, C. Relf, V. Bennet, and J. Chakungal of the YGS, D. White, G. Vivien, and R. Wyllie of Aurora Geosciences, D. Dupre of Coltstar Ventures, and S. Eyre of Copper North Mining Corp are thanked for arranging field support. Lab assistance at Laurentian University was provided by J. Petrus, A Gladu, and T.S. Chevrier. Major element analysis was performed at the Ontario Geoscience Laboratories by N. Chrétien and expedited by N. Remeikis. T.S. Chevrier, S.P. O’Hare, H. Ngo, K. Medig, P. Schachtel, and B. Webster are all thanked for their assistance in the field. J.A. Milton, D.G.F. Long, and L. Ootes are all thanked for their helpful discussions in the field, in person, and in correspondence.

4.9 Figures

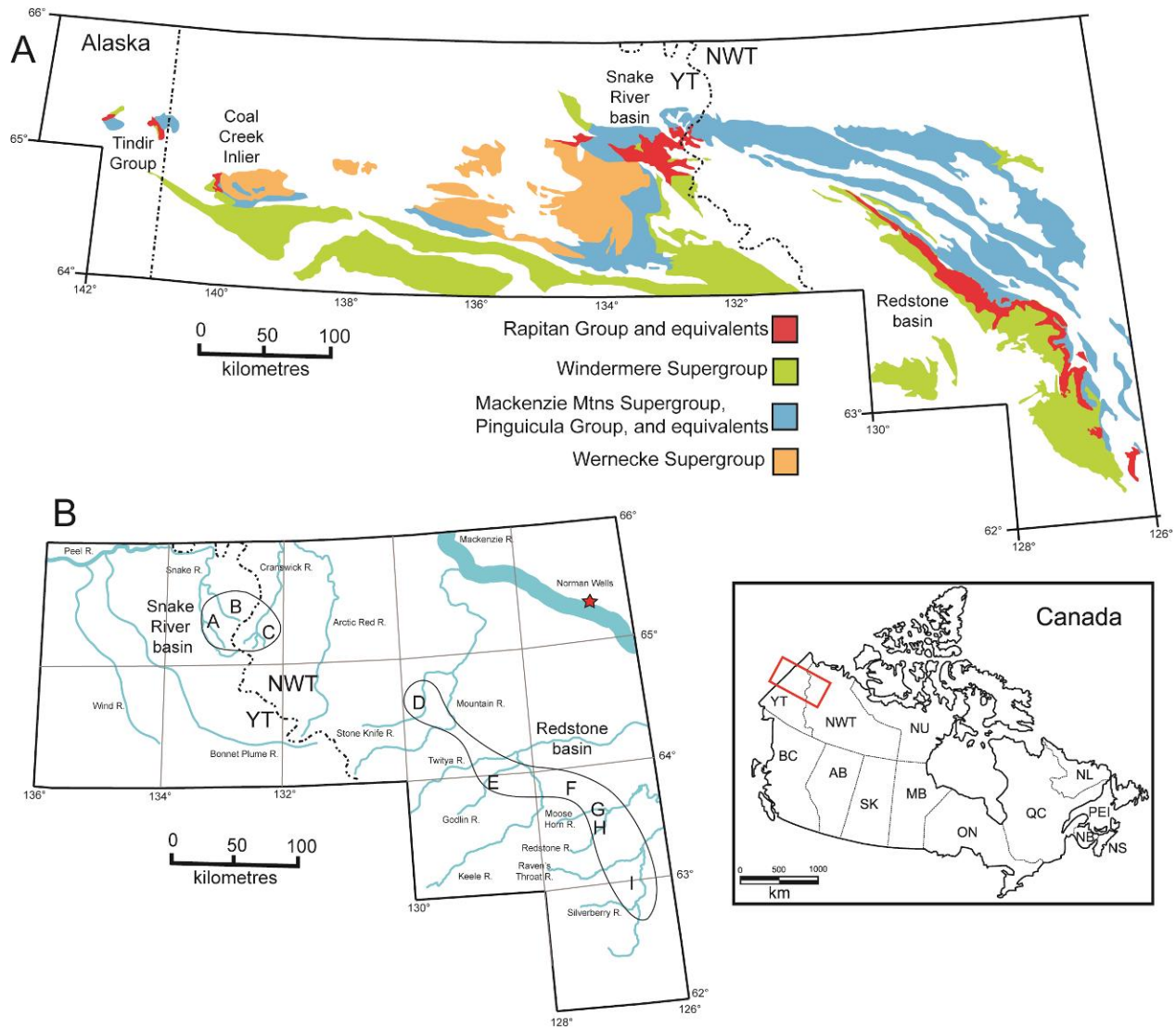
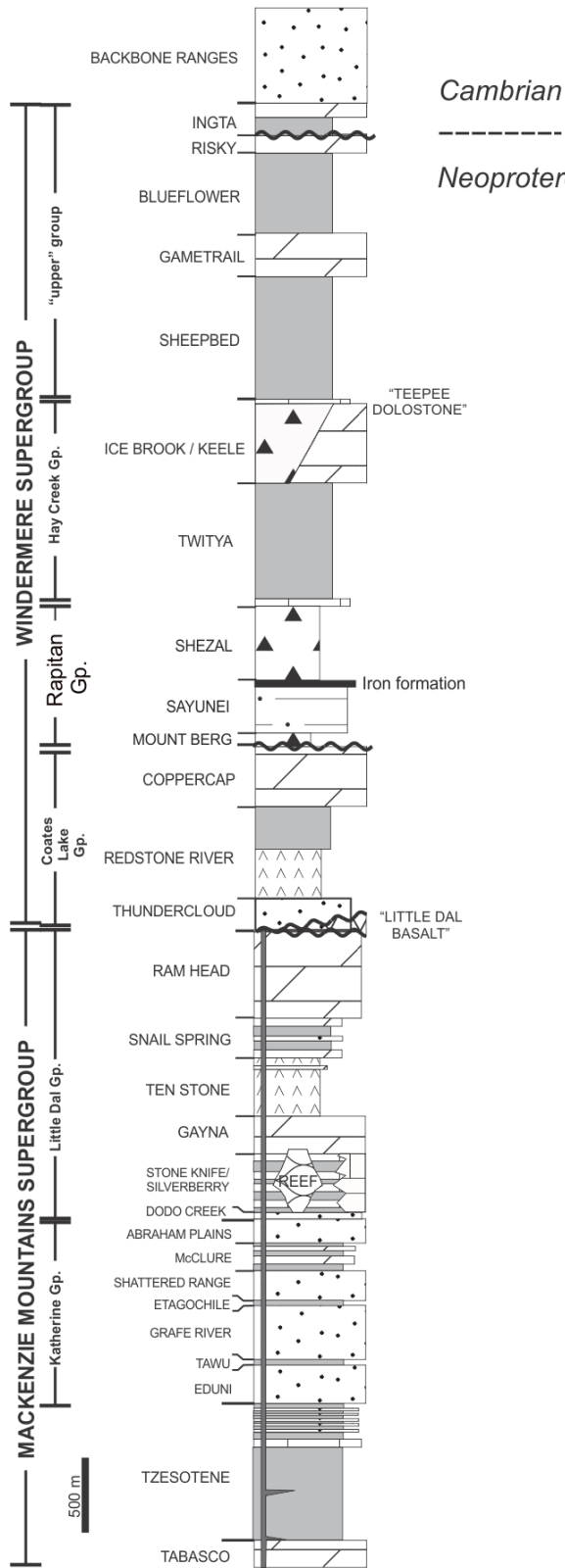


Figure 4.1: (A) Regional geology map showing the distribution of Proterozoic rocks in the northern Canadian cordillera (after Yeo, 1981; Baldwin et al., 2012b) inset in bottom left shows study location in Canada. (B) Location map of stratigraphic sections and locations discussed in the text. A- Iron Creek (IC); B- Discovery Creek (DC); C- Cranswick River (CR); D- Stone Knife River; E- Godlin River; F- Boomerang; G- Hayhook North (HN), H- Hayhook South (HS); I- Hidden Valley.



Cambrian

 Neoproterozoic

Figure 4.2: Formation-level stratigraphy of Proterozoic rocks of the Mackenzie Mountains (after Baldwin et al., 2012).

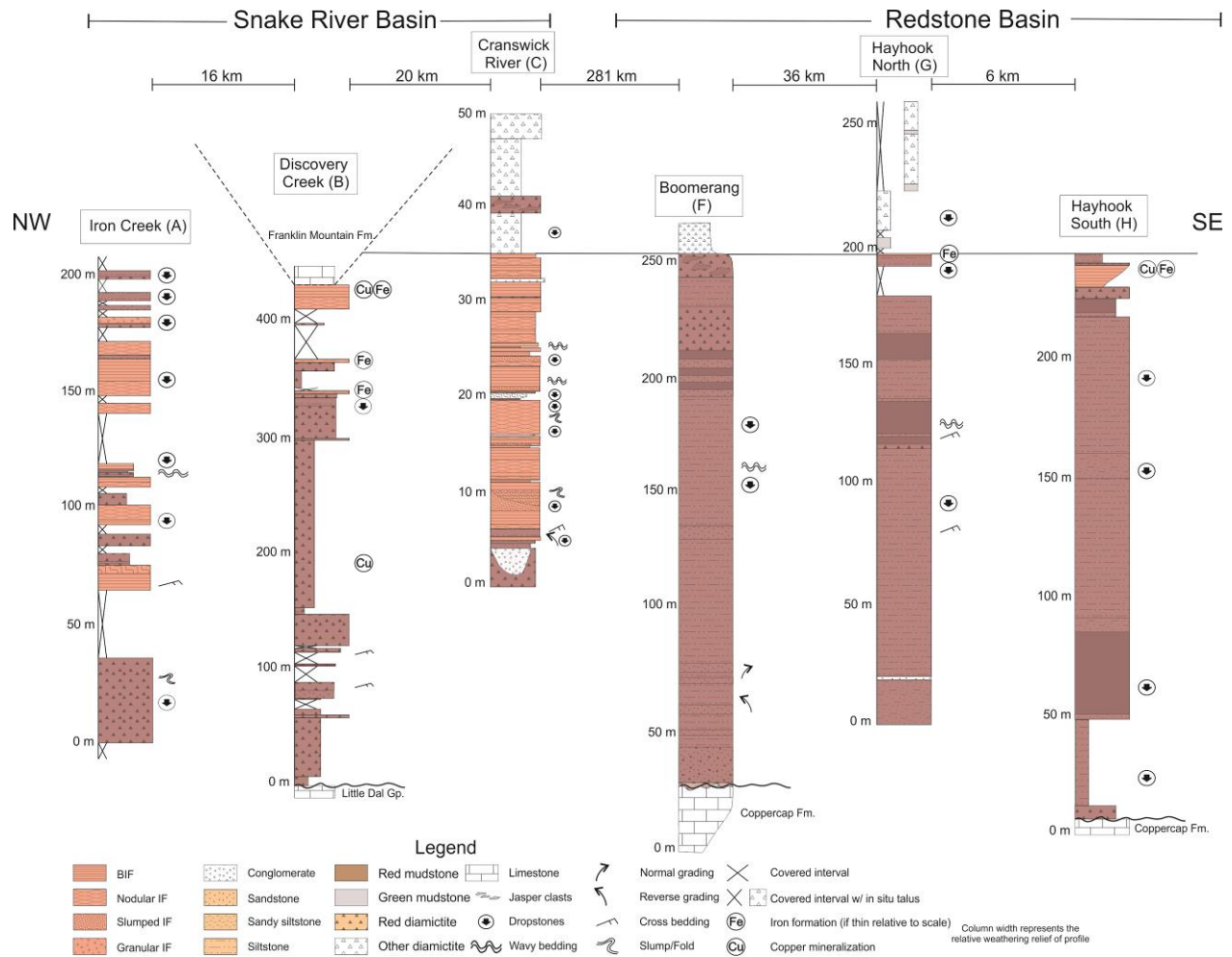


Figure 4.3: Stratigraphic sections of six measured sections of the Sayunei Formation and Rapitan iron formation. All sections have been hung from the contact between the Sayunei and Shezal Formations, where this contact was documented. Sections from left to right are as follows: Iron Creek (A), Discovery Creek (B), Cranswick River (C), Boomerang (D), Hayhook North (E), and Hayhook South (F). Close-up sections of the iron formation at each section are present in later figures. Iron formation is highlighted in red, hematitic siliciclastic rocks in orange.

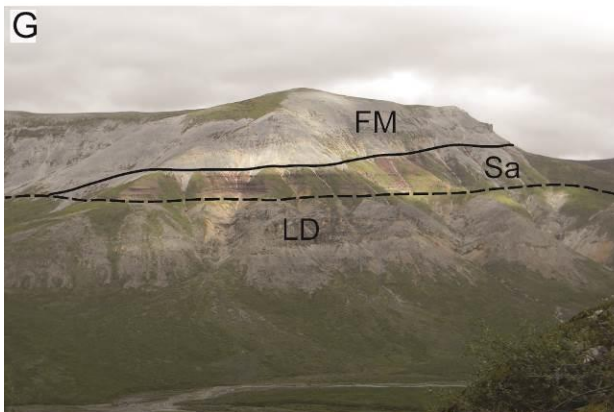
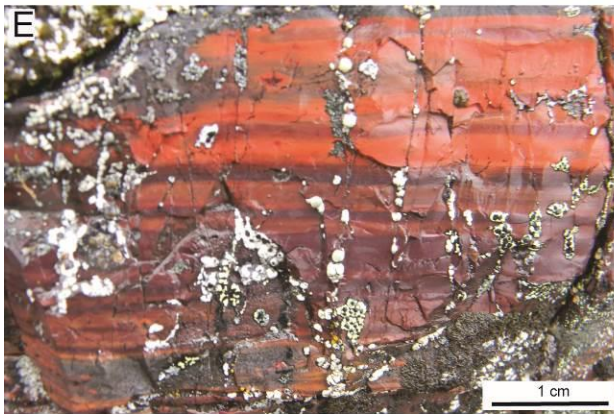


Figure 4.4: Photographs from the Snake River basin. (A) Sandy, clast-intermediate, red diamictite underlying the iron formation at Iron Creek. (B) Major syn-sedimentary slump structure seen at Iron Creek. Photo is only a part of the slump structure. (C) Granular iron formation (GIF), the top of the Iron formation at Iron Creek indicates deposition above wave-base at the end of iron formation deposition. Arrow indicates way up. (D) Hematitic sandy siltstone immediately overlying the iron formation at Iron Creek. (E) Bedded, varicoloured jasper in thin, lower strata of iron formation at Discovery Creek. (F) Hematite-rich iron formation with minor jasper nodules seen in the main iron formation horizon at Discovery Creek. (G) Rapitan Group pinches out to the northwest near Discovery Creek, down to zero metres thickness (in the photograph) from over 400 m (10 km to the southeast). Field of view is approximately 2 km. Contacts between the Rapitan Group and the Little Dal Group (underlying) and the Franklin Mountain Formation (overlying) are marked in black, showing the pinch-out of the Rapitan Group. (H) Non-hematitic glacioclastic strata immediately overlying the iron formation at Cranswick River, which is unlike other sites visited in the Snake River basin. Arrow indicates a horizon of reworked iron formation clasts in diamictite several metres above the top of the iron formation.

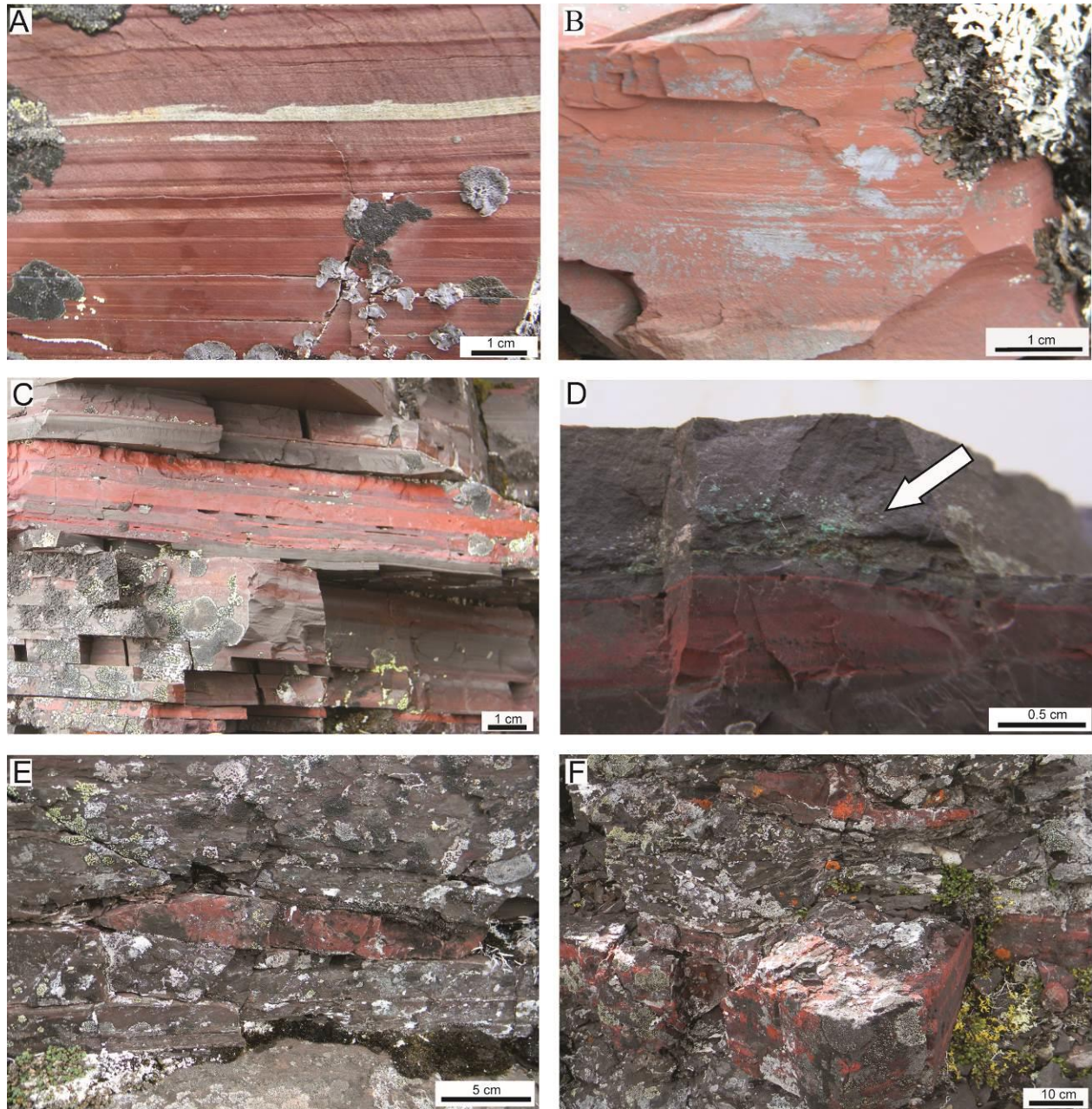


Figure 4.5: Photographs from the Redstone basin. (A) Fine-grained hematitic turbidites (interbedded mudstone and siltstone) typical of the Sayunei Formation in the Redstone basin. (B) Bright red, massive mudstone with grey hematite on fracture surfaces is found high in the Sayunei Formation close to the iron formation. (C) ‘Slaty’ iron formation typical of the Redstone basin, it lacks significant massive hematite, and is dominated slaty to flaggy weathering jasper, with bedding-plane parallel fracture. (D) Copper mineralisation associated with iron formation at

Hayhook South. The arrow indicates malachite/chrysocolla as a weathering product after chalcopyrite (visible on fresh surfaces). (E) Plastically deformed, reworked jasper clast in basal hematitic diamictite of the Shezal Formation and blockier reworked iron formation clasts from Boomerang (F).

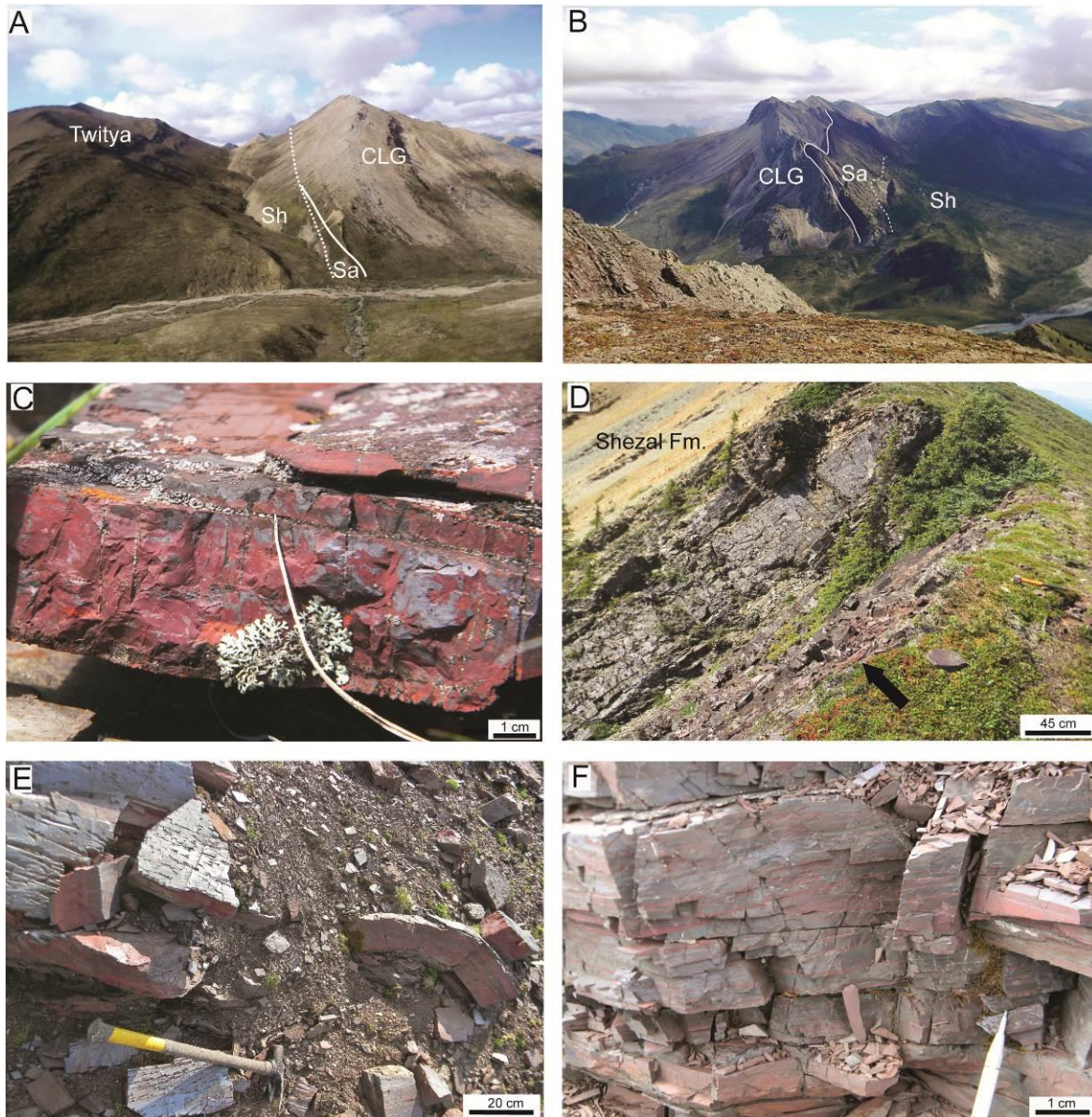


Figure 4.6: Photographs from other regional sites visited. View to the north (A) near Stone Knife River, where the Sayunei Formation pinches out. The Shezal Formation also thins to the north. View to south across the Stone Knife River (B), showing a significant southward thickness increase in Sayunei Formation. (C) Thin jasper-iron formation unit at Godlin River, which consists of a pair of 5 cm jasper and hematite beds directly below the contact of the Sayunei and Shezal formations (D, arrow). Iron formation at the Hidden Valley copper prospect (E, F) which contains bedded jasper with massive hematite, which can occur as thin platy beds (E), or thicker, blockier beds (F). CLG- Coates Lake Group; Sa- Sayunei Formation; Sh- Shezal Formation.

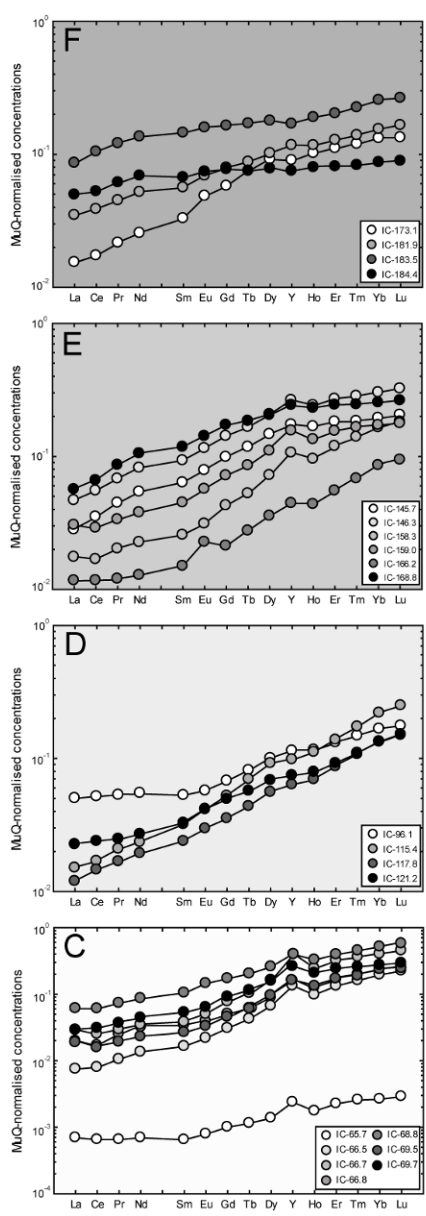
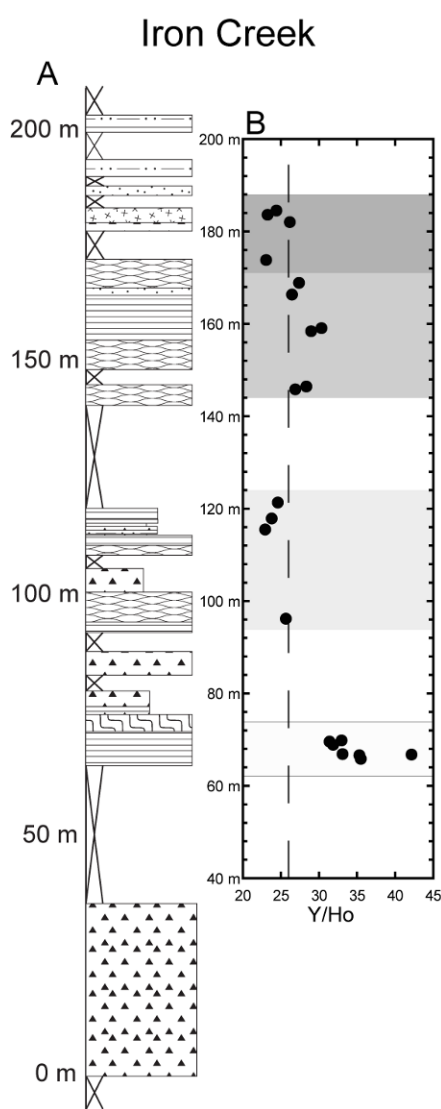


Figure 4.7: REE+Y chemostratigraphy of the iron formation at Iron Creek. (A) Stratigraphic column from Iron Creek; legend is same as figure 2. (B) Stratigraphic distribution of Y/Ho ratios. Dashed line is the chondritic/crustal ratio of 26. The iron formation consists of four intervals based on the Y/Ho ratios—strongly superchondritic (C), with well-developed seawater-type REE+Y patterns; weakly subchondritic (D), with flat, HREE-enriched

patterns; weakly superchondritic (E), with moderately to poorly developed seawater-type REE+Y patterns; and weakly subchondritic (F), with flat to moderately HREE-enriched REE+Y patterns. This suggests an overall up-section increase in siliciclastic contribution to the iron formation. Background colours on panels C-F correspond with the stratigraphic intervals marked in the same shade in (B).

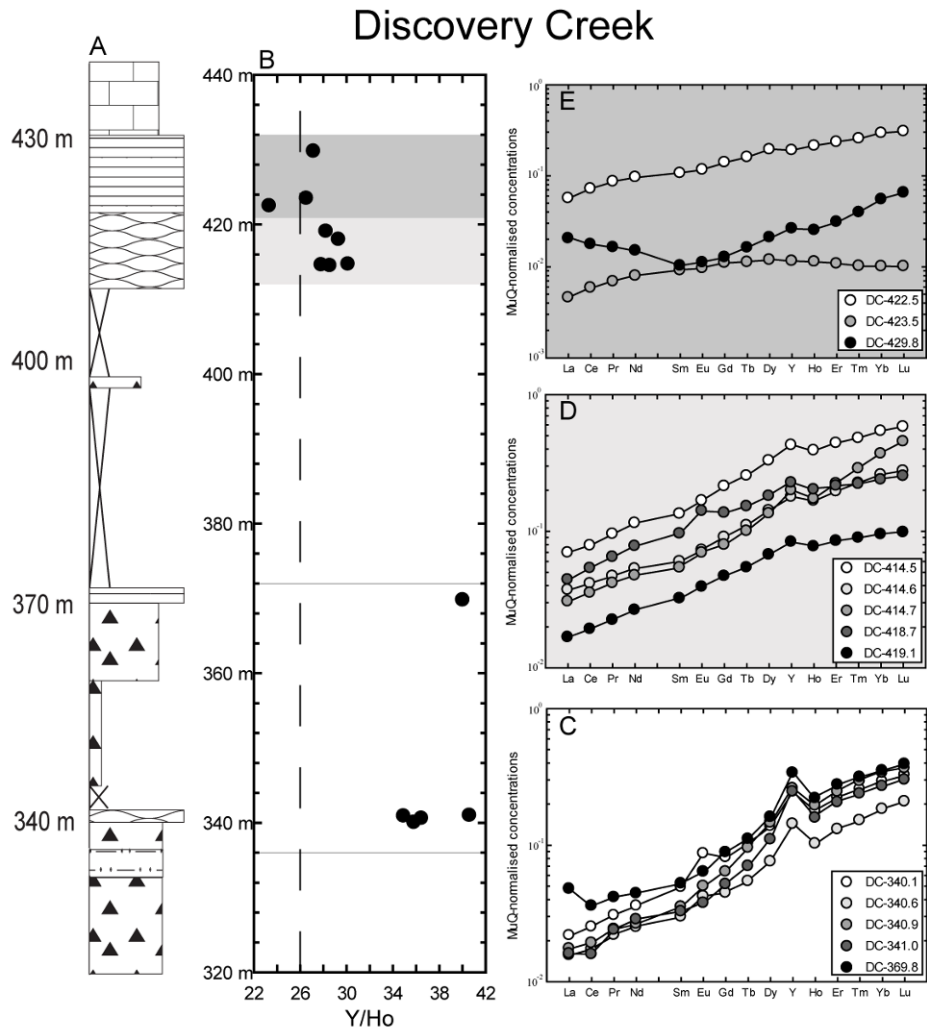


Figure 4.8: REE+Y chemostratigraphy of the iron formation at Discovery Creek. (A) Stratigraphic of the iron formation (only) at Discovery Creek, legend is the same as figure 2. (B) Stratigraphic distribution of Y/Ho ratios. Dashed line is the chondritic ratio of 26. The iron formation is broken into three different intervals based on the Y/Ho ratios and REE+Y patterns. The lowest (C) has strongly superchondritic Y/Ho ratios and distinct seawater-type REE+Y patterns, whereas the middle interval (D) has more weakly superchondritic Y/Ho ratios and still-well developed, but less dramatic seawater-type REE+Y patterns. The topmost interval (E) has variable Y/Ho ratios ranging from subchondritic to essentially chondritic, with highly variable patterns that suggest that post-depositional weathering may have affected the REE+Y chemistry (see text). Background colours on panels C-E correspond with the stratigraphic intervals marked in the same shade in (B).

Cranswick River

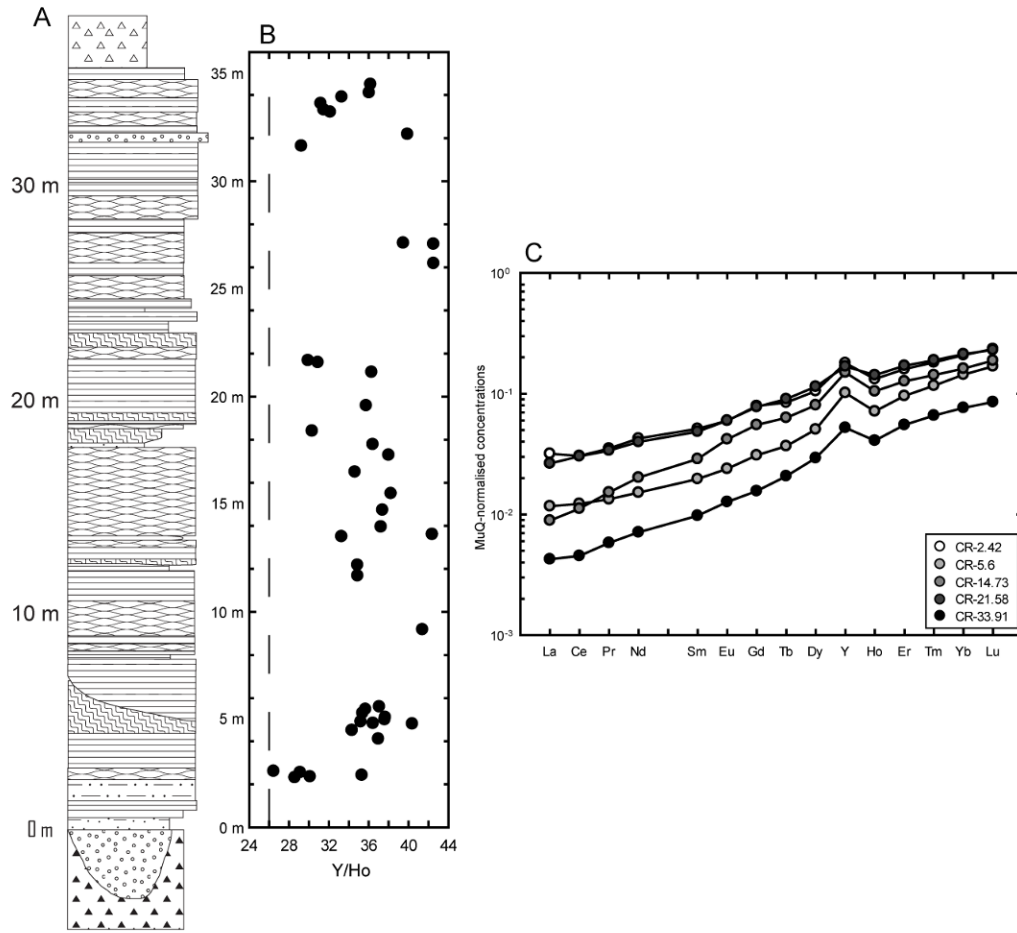


Figure 4.9: REE+Y chemostratigraphy of the iron formation at Cranswick River. (A) Stratigraphic column of the iron formation at Cranswick River, legend is the same as figure 2. (B) Stratigraphic distribution of the Y/Ho ratios. Dashed line is the chondritic ratio of 26. The entirety of the iron formation except a single sample has superchondritic Y/Ho ratios and distinctly seawater-type REE+Y patterns (C) (select data from Baldwin et al., 2012).

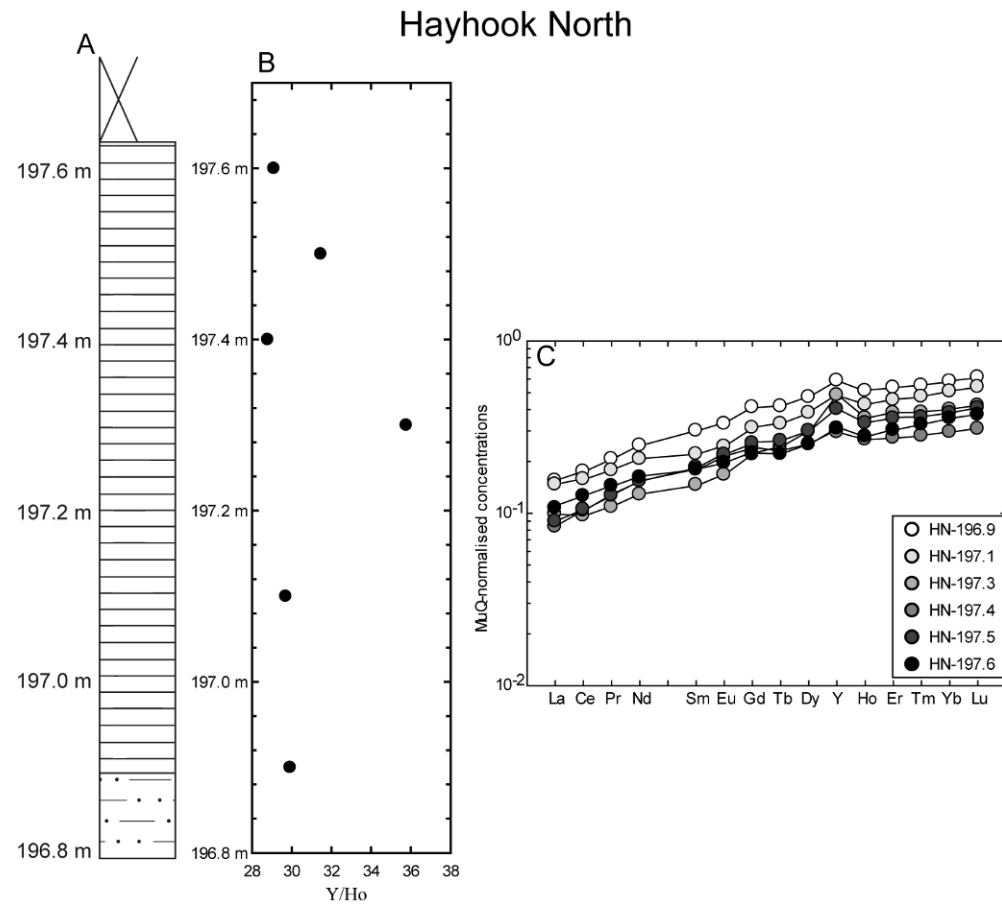


Figure 4.10: REE+Y chemostratigraphy of the iron formation at Hayhook North. (A) Stratigraphic column of the iron formation at Hayhook North (legend as in figure 2). (B) Stratigraphic distribution of Y/Ho ratios, all of which are strongly superchondritic, and correspond with seawater-type REE+Y patterns (C).

Hayhook South

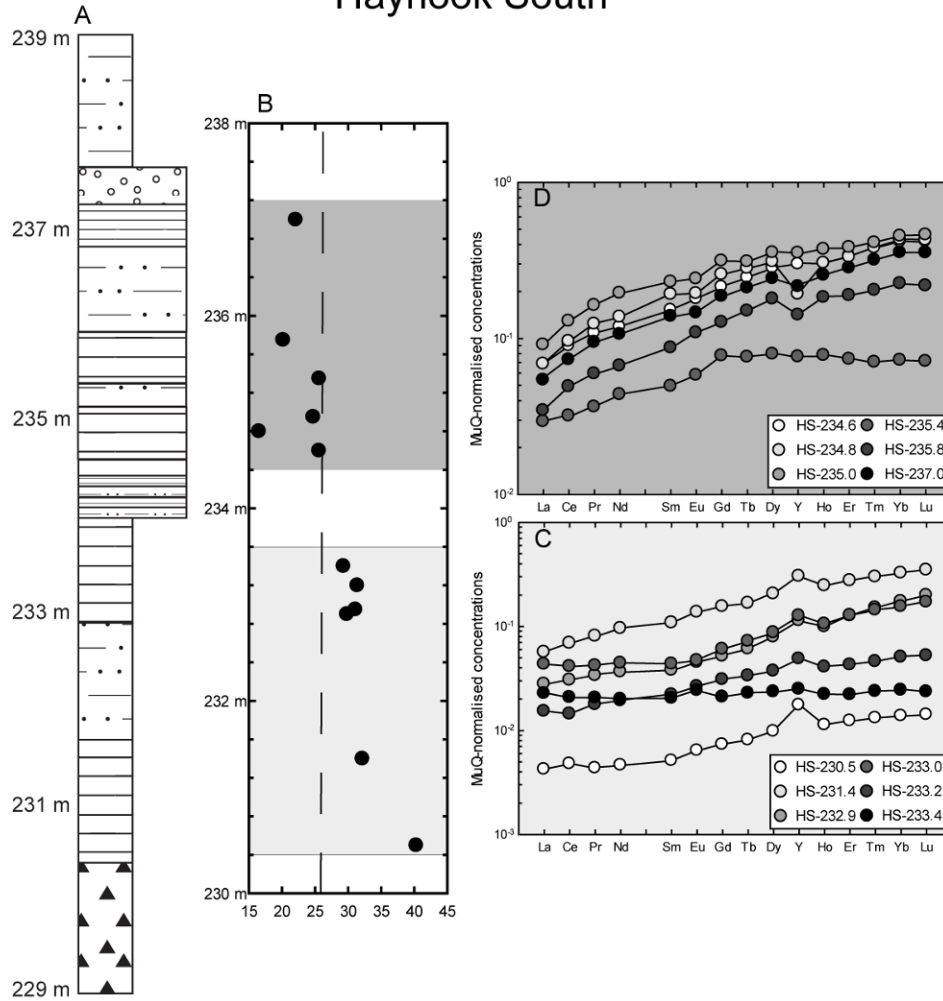


Figure 4.11: REE+Y chemostratigraphy of the iron formation at Hayhook South. (A) stratigraphic column of the iron formation at Hayhook South, legend as in figure 2. (B) Stratigraphic distribution of Y/Ho ratios. Dashed line is the chondritic ratio of 26. The Y/Ho ratios define two separate intervals in the iron formation, the lower (C) has consistently superchondritic Y/Ho ratio and well-developed seawater-type REE+Y patterns. The upper interval has chondritic to subchondritic Y/Ho ratios, and REE+Y patterns that have some features similar to seawater, but with some major differences. See text for discussion.

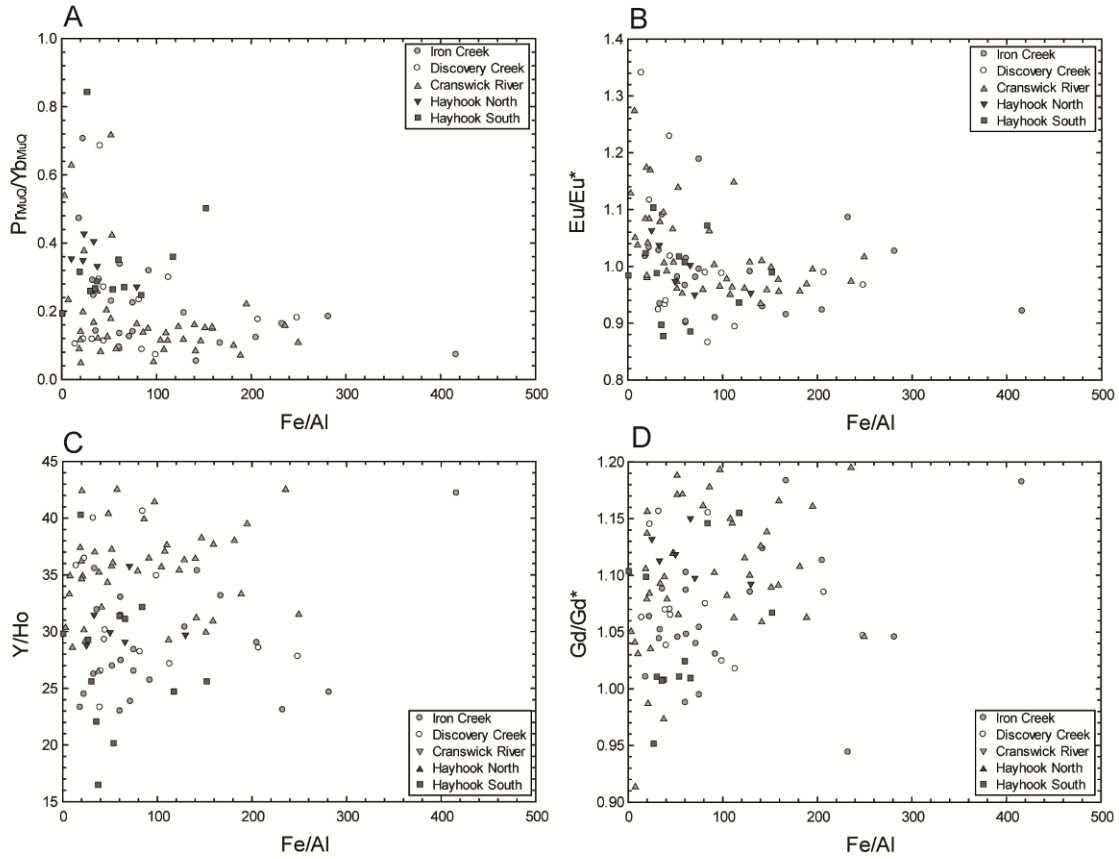


Figure 4.12: Covariance plots of several different REE+Y ratios with the molar Fe/Al ratio. Weak hyperbolic relationships are present between Pr_{MUCO}/Yb_{MUCO} (A) and Eu/Eu^* (B) and Fe/Al. More scattered patterns occur when Fe/Al is plotted against Y/Ho (C) and Gd/Gd* (D), but importantly no samples from any site have both high Fe/Al and low Y/Ho and Gd/Gd*. Data for Cranswick River is from Baldwin et al., (2012).

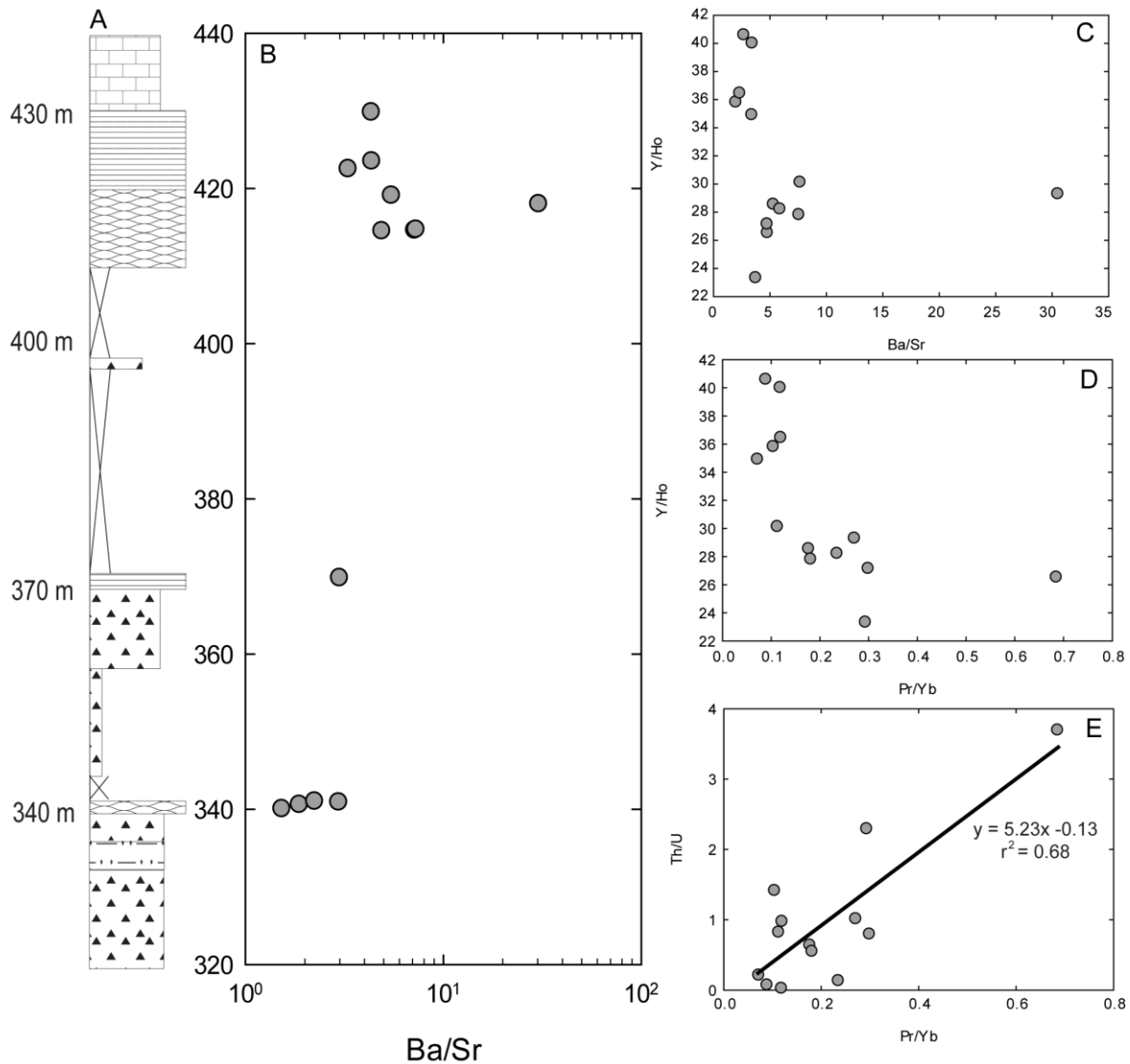


Figure 4.13: Trace element geochemistry from Discovery Creek. (A) Stratigraphic column of the iron formation (only) at Discovery Creek. (B) stratigraphic distribution of Ba/Sr ratios (log scale), showing an increase upsection, reflecting an increase in the flux of fresh water to the basin. (C) Y/Ho vs Ba/Sr, showing that increased Ba/Sr ratios correspond with samples with subchondritic to weakly superchondritic Y/Ho ratios. (D) Y/Ho vs Pr_{MuQ}/Yb_{MuQ}, wherein lower Y/Ho ratios correspond to strongly flattened (elevated Pr_{MuQ}/Yb_{MuQ}) REE+Y patterns. (E) Th/U vs Pr_{MuQ}/Yb_{MuQ} show a moderately strong positive correlation ($r^2 = 0.68$), reflecting an increase in the immobile element Th with flattened REE+Y patterns. This indicates that the flattening was dominantly the result of siliciclastic input to the iron formation.

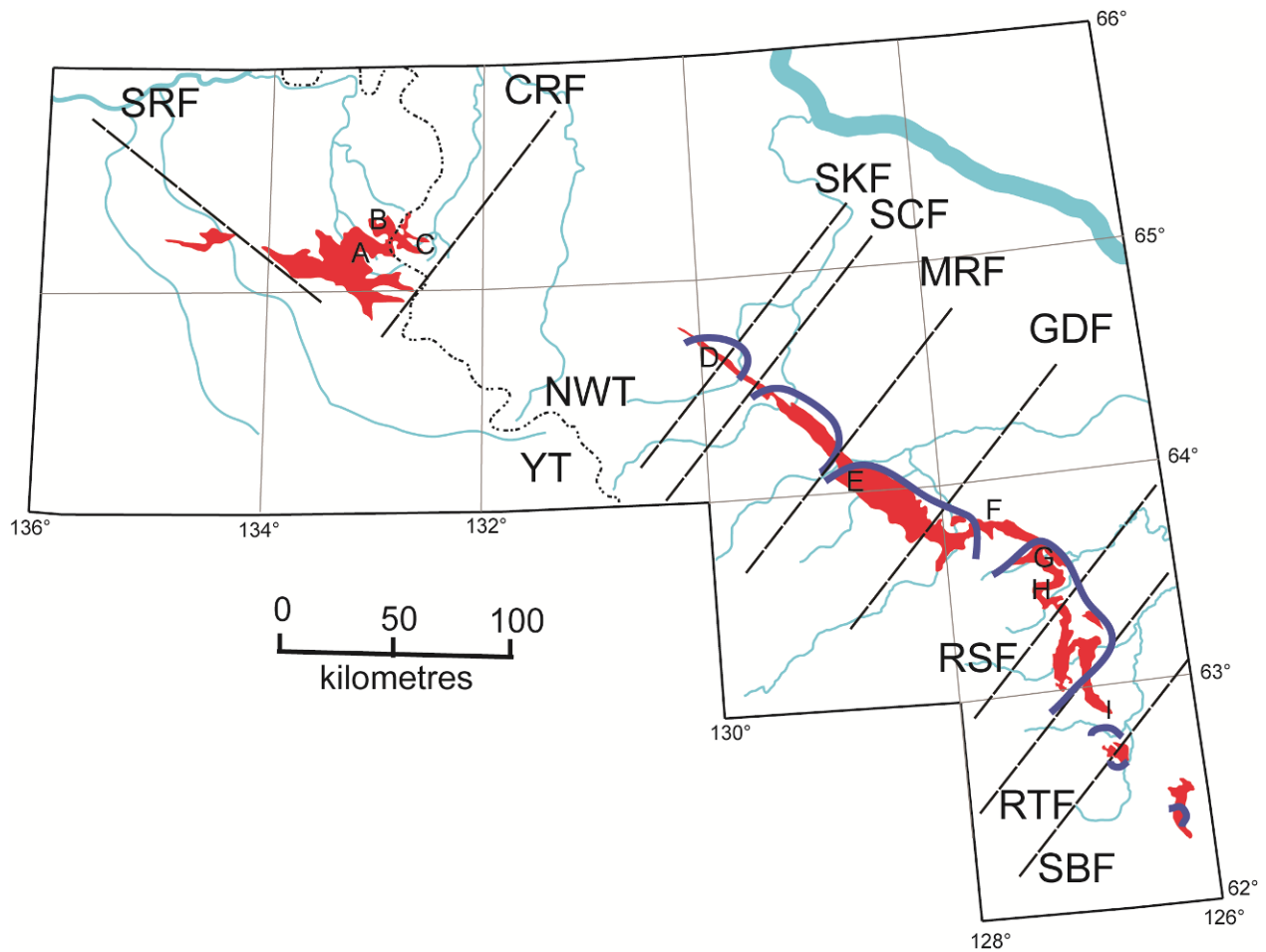


Figure 4.14: Map showing the inferred position of basin-defining faults (dashed lines) and their position relative to mapped exposures of the Rapitan Group. From northwest to southeast, they are as follows: SRF- Snake River fault; CRF- Cranswick fault; SKF- Stone Knife fault; SCF – Sammon’s Creek fault; MRF- Mountain River fault; GDF- Godlin fault; RSE- Redstone fault; RTF- Raven’s Throat fault; SBF- Silverberry fault. Blue lines approximate the locations of Coates Lake Group embayments (from Jefferson and Ruelle, 1987). Fault locations are after (Turner and Long, 2008) and (Eisbacher, 1985). Rapitan Group distribution (red) after Yeo (1981).

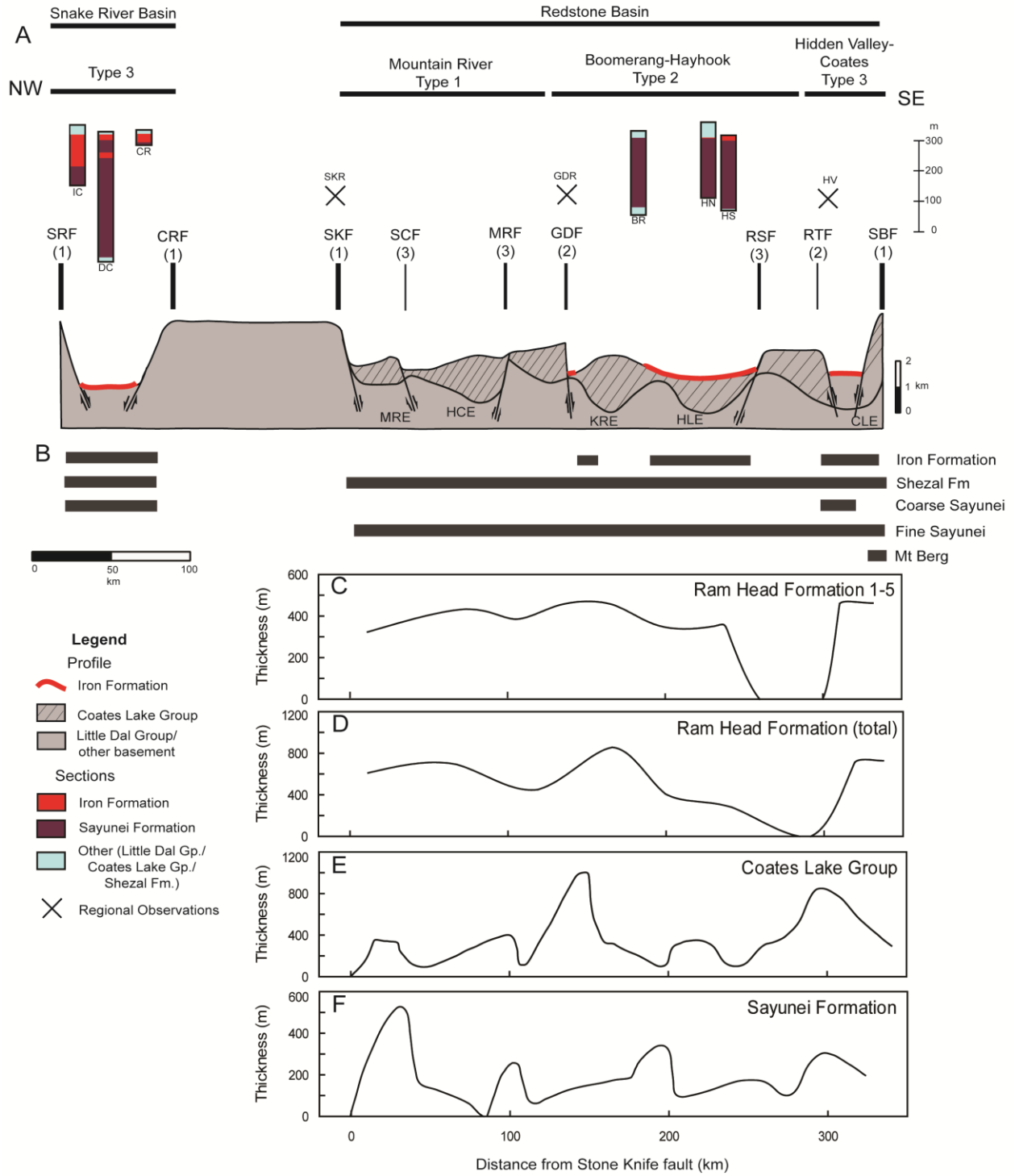


Figure 4.15: Proposed along-strike basin profile for the Rapitan basin during deposition of the Sayunei Formation, with corresponding fault positions; acronyms correspond to the preceding figure (profile after Eisbacher, 1985). Red lines indicate documented distribution of the iron formation. Only the Snake River basin and the southern half of the Redstone basin were sufficiently distal from siliciclastic sediment sources to deposit iron formation. Cross-hatched areas in the profile indicate the approximate distribution of the Coates Lake Group and Coates Lake Group embayments, after Jefferson and Ruelle (1987) (MRE- Mountain River embayment; HCE- Hay Creek embayment; KRE- Keele River embayment; HLE- Hayhook Lake embayment; CLE- Coates Lake embayment), indicating their relationships with Sayunei Formation and iron formation distribution in the Redstone basin. Fault positions are after Turner and Long (2008) and Eisbacher (1985) with the most important (Class 1) faults (SRF, CRF, SKF, and SBF) bounding the Snake River and Redstone basins, respectively, the Class 2 faults marking major changes in the depth of the basin (GDF and RTF), and the Class 3 minor faults (SCF, MRF, RSF) marking more subtle changes in basin depth, with relatively minor implications for iron formation deposition. (B) The distribution of the iron formation, Shezal Fm., coarse-grained Sayunei Fm., and fine-grained Sayunei Formation across the Mackenzie Mountains, showing their relationships to the faults, and the different sub-basin types (Type 1- Mountain River sub-basin; Type 2- Boomerang-Hayhook sub-basin; Type 3- Snake River basin, Hidden Valley-Coates sub-basin. (C) Thickness profile for the Ram Head Formation units 1-5 (from Jefferson, 1983 and Long et al., 2008). (D) Thickness profile for the entire Ram Head Formation (from Jefferson, 1983 and Long et al., 2008). (E) Thickness profile for the Coates Lake Group (from Jefferson, 1983). (F) Thickness profile of the Sayunei Formation (from Yeo, 1984). The four thickness profiles show the gradual evolution of the Mackenzie tectonic arc through the early stages of the rifting of northwestern Laurentia, and the gradual development of the depositional sub-basins documented in the Redstone basin in the Sayunei Formation.

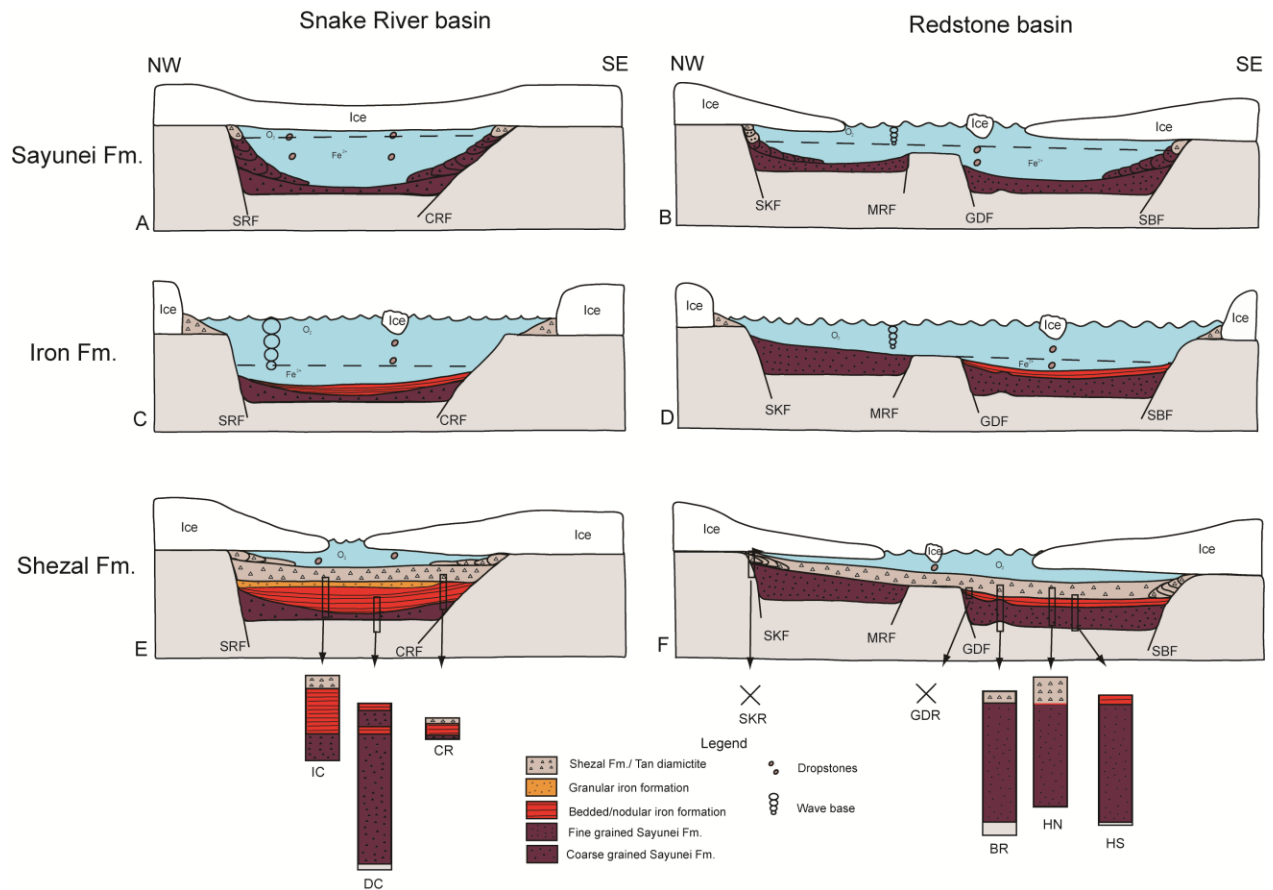


Figure 4.16: Interpreted history of basin fill at the formation-level in the Snake River (A, C, E) and Redstone (B, D, F) basins, based on stratigraphic data. Figure is not to scale. (A) Coarse clastic turbidites of the Sayunei Formation were deposited in the Snake River basin, in a proximal, steep-margined basin. Deposition was below the iron chemocline, resulting in purple diamictite. The comparatively coarse, sandy matrix of the diamictite near the western margin of the basin was due to a steeper, faulted margin, whereas the shallower margin in the east resulted in a muddier matrix in Sayunei Fm. diamictite. (B) Distal exposures of the broader sub-basins of the Redstone basin consist of fine-grained turbidites deposited in the Sayunei Formation, with the occasional deposition of dropstones and other ice-rafted debris into the deep basin below the iron chemocline. Paleocurrent measurements (Eisbacher 1981b) indicate sediment sources from opposite directions, on either side of a paleogeographic high (Yeo 1981) between the Mountain River and Godlin Faults. (C) Iron formation deposition in the Snake River basin was characterised by the trapping of most siliciclastic sediment near the basin margins during sea-level highstand following glacial withdrawal (Baldwin et al., 2012b). This allowed substantial

iron formation to be deposited in the distal parts of this basin below wave-base. Encroachment of the sediment-seawater interface on wave-base (through basin-fill and/or sea-level lowstand) produced shallow-water GIF facies locally deposited at the top of the iron formation (Baldwin and Turner 2012; Baldwin et al. 2013). (D) During glacial withdrawal and sea-level highstand, only part of the southern Redstone basin was deep enough for iron formation deposition below the iron chemocline; north of the Godlin Fault the basin was too shallow for iron formation deposition, due to sediment trapping on the basin margins (with the exception of ice-rafted debris), a hiatus may be inferred north of the Godlin fault during iron formation deposition. (E) Following glacial re-advance, the submarine diamictite of the Shezal Formation in the Snake River basin were deposited. Initially this occurred at or below the iron chemocline, as indicated by the presence of purple-brown diamictites and siltstones above the iron formation at Iron Creek, but deposition eventually aggraded to a position above this chemocline, resulting in deposition of the tan to grey diamictites characteristic of the Shezal Fm. (F) the Shezal Formation was deposited with relatively even thickness and geographic coverage across the Redstone basin. Hematitic facies of the Shezal Formation are present only locally in the Redstone basin, and only at the contact with the underlying Sayunei Formation or iron formation, whereas tan to grey diamictite is ubiquitous. The resultant stratigraphy in areas studied here is shown at the bottom of the figure.

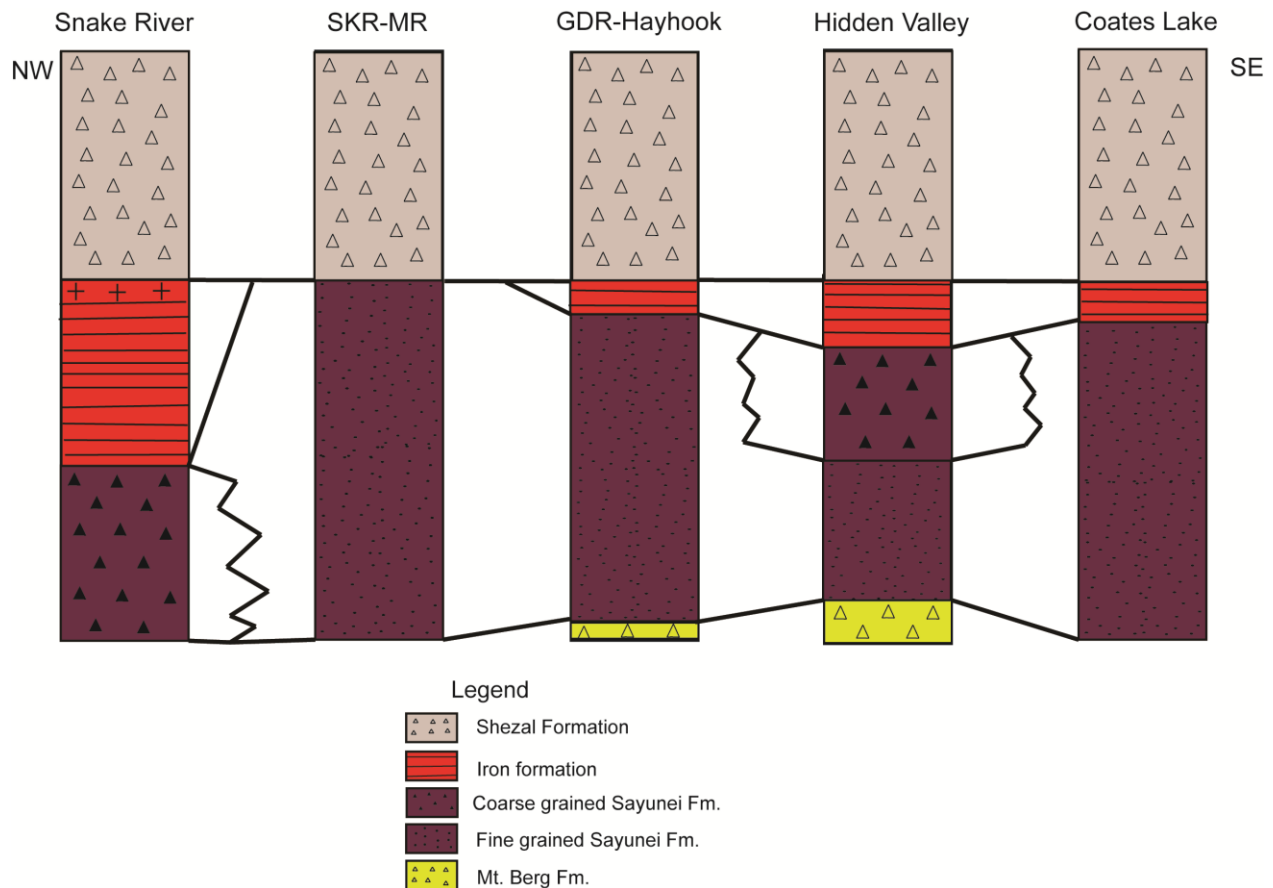


Figure 4.17: Proposed formation-level correlation scheme for the Rapitan Group across five areas in the Mackenzie Mountains. The earliest sedimentation in the Rapitan Group was the localised deposition of the Mt. Berg Fm. in local basins in the Godlin-Hayhook and Hidden Valley areas in the southern Redstone basin. This was contemporaneous with the initial deposition of the Sayunei Fm. in the northern Redstone basin (Stone Knife and Mountain river areas) and in the Snake River basin. Across the entirety of the Redstone basin, initial deposition of the Sayunei Fm. was characterised by fine-grained silty to muddy maroon turbidites with scattered dropstones, whereas in the Snake River basin, the siliciclastic portion of the Sayunei Fm. consists of sandy to muddy matrix maroon diamictite, much coarser than the classical Sayunei Fm. observed in the Redstone basin. Similarly, at Hidden Valley, the uppermost Sayunei Fm. is a maroon to brown medium-grained sandstone, which is absent elsewhere in the Redstone basin. Iron formation was deposited simultaneously in all locations where it is present in the Rapitan Group, but is much thicker in the Snake River basin, and locally at Hidden Valley and (reportedly, Eisbacher 1976) Coates Lake than in the majority of the Redstone basin (Stone Knife and Mountain rivers and the

Godlin-Hayhook areas). The base of the Shezal Fm. records a time horizon, and is deposited evenly across all five regions studied. In this correlation scheme, the iron formation is the top of the Sayunei Fm. in all areas. The siliciclastic portion of the Sayunei Formation consists, broadly, of two different facies; fine-grained, which consists of silty turbidites, found throughout the Redstone basin, and coarse-grained, which is characterized by diamictite with a sandy matrix in the Snake River basin, and by massive, medium-grained sandstone in the Hidden Valley area.

4.10 Tables

Table 4.1: Study site locations

Table 4.1: Study site locations					
Location	Section Type	Latitude	Longitude	NTS Map Sheet	Location Description
A-Iron Creek (Crest iron deposit)	Ridge	65° 16' 12.1" N	133° 02' 56.8" W	106F	18 km W of the NWT-YT border; 16 km E of the Snake River about 145 km upstream of its convergence with the Peele River
B-Discovery Creek	Ridge	65° 18' 55.9" N	132° 44' 2.4" W	106F	Headwaters of Discovery Creek, YT, 7.4 km west of the border with NWT, and 32 km east of the Snake River
C-Cranswick River	Creek	65° 12' 51.3" N	132° 22' 6.1" W	106F	East side of the Cranswick River, 126 km upstream of its convergence with the Arctic Red River; 18 km E of NWT-YT border
D-Stone Knife River		64° 37' 35.6" N	129° 43' 30.5" W	106A	Ridge a few kilometres north of the Stone Knife River
E-Godlin River		64° 3' 31" N	128° 21' 57" W	106A	Ridge directly north of the Godlin River, upstream of its convergence with the Ekwi River
F-Boomerang	Ridge	63° 47' 33.6" N	127° 32' 32.4" W	95M	4.1 km WSW of Boomerang Lake; 16.7 km E of the Keele River
G-Hayhook North	Ridge	63° 32' 44.5" N	127° 3' 57" W	95M	14.5 km WNW of Hayhook Lake; 8.5 km S of the Moose Horn River (formerly North Redstone River)
H-Hayhook South	Ridge	63° 30' 34.8" N	126° 59' 18" W	95M	11 km W of Hayhook Lake; 4 km N of the Redstone River
I-Hidden Valley		62° 59' 3.1" N	126° 39' 1.4" W	95L	8.25 km W of Silverberry River; 21.75 km S of Raven's Throat River

Table 4.2: Stratigraphic descriptions of the Rapitan iron formation and Sayunei Formation

Table 4.2: Stratigraphic Descriptions of the Rapitan iron formation and Sayunei Formation							
	Underlying rocks and basal contact of Sayunei Formation	Iron formation thickness	Sayunei Formation stratigraphy and characteristics	Iron formation characteristics	Overlying strata	Local relationships	Comment
Snake River Basin							
A- Iron Creek (Crest iron deposit) ¹ (measured)	Basal contact unexposed	118.7 m	Iron formation underlain by ≥ 65.5 m of massive, dark red to purple matrix-supported, clast-poor sandy cobble to boulder diamictite; clasts are limestone, dolostone, and minor sandstone, basalt, and granite porphyry clasts	Basal iron formation is dominantly BIF, with minor nodular iron formation; hematite beds vary from massive to well-bedded with flaggy weathering; at 9m the BIF is extensively shumped and syn-sedimentary folded; shumped IF overlain by 21m siliciclastic interval of purple siltstone and purple matrix-supported clast-poor diamictite; above siliciclastics the IF is more hematite-rich and dominated by nodular iron formation, with scattered jasper beds and diamictite/siltstone interbeds; topmost IF is granular iron formation (wave-reworked hematite and jasper granules); IF is overlain by purple-brown siltstone with interbeds of fine sandstone and clast-poor diamictite	Shezal Formation (red)		Siliciclastic units underlying the iron formation are coarse-grained, with sandy matrix, as opposed to muddy; other sections measured in the area are overlain by >200m of red diamictite and siltstone with similar weathering characteristics to the Shezal Formation in other areas.
B- Discovery Creek ¹ (measured)	Basal contact unexposed; Little Dal Group observed locally	21.3 m (total over 3 intervals)	Sayunei Fm below IF is 340 m of dark red to purple clast-poor to clast-rich diamictite with a muddy sand matrix. Interbeds of matrix and clast-supported pebble conglomerate present; clasts consist of limestone and dolostone with minor granitic, gabbroic, and basaltic clasts; IF occurs at three stratigraphic levels near top of section separated by intervals of clast-poor pebble diamictite.	Iron formation occurs in 3 horizons – the lowermost is 1 m thick bedded jasper and hematite; middle horizon is a thin exposure (0.1 m) of nodular IF with a single jasper bed; upper unit is 15.3 m IF over 20.2 m of section; top horizon consists of equal parts bedded and nodular IF; nodules range from elongate to lenticular and rarely spherical; chalcopryite and malachite-chrysocolla found in near <i>in situ</i> float; top of IF is eroded away.	Inferred erosive contact (unexposed) with the Franklin Mountain Formation	White quartz arenite boulders containing jasper and hematite clasts present in nearby rivers, but not seen in outcrop; the Rapitan Group thins and pinches out 10 km NW of the section, where a clear erosional contact is seen between the Rapitan Group and the overlying carbonates of the Franklin Mountain Fm.	Only location where the Sayunei Formation observed without the Shezal Formation; also the only location where the IF is the uppermost unit of the Rapitan Group; significant post-Sayunei erosion is inferred from the map and stratigraphic observations.
C- Cranwick River ² (measured)	Basal contact unexposed	30 m	IF is underlain by 2 different lithologies: most common is a friable, hematitic purple, clast-rich muddy diamictite; diamictite is cut by up to 5 m thick tan, polyminic, clast-supported channel-fill conglomerate, which immediately underlies the IF	IF is roughly equal parts bedded and nodular, with nodules ranging from very elongate (to 50 cm long) to slightly lenticular; spherical nodules are rare; hematite is mostly poorly bedded and massive, with rare slaty or flaggy intervals present; several thin (<20 cm) hematitic siltstone and sandy siltstone interbeds are present throughout; major sharp structure cross-cuts several metres low in the IF, with dramatically contorted bedding along strike from the shump.	Shezal Formation (grey/tan)	Thin interval of hematite-bearing diamictite containing reworked jasper and IF clasts occurs 4 m above upper contact of IF with the tan to grey clast-poor diamictite of the Shezal Formation	GIF at the top of iron formation exposures 14 km W
Redstone Basin							
D- Stone Kaife River (observed)	Coppercap Formation	Absent	Fine-grained muddy; red to purple turbidites with sandy interbeds and scattered dropstones	Absent	Shezal Formation (grey/tan)	Sayunei Formation thins to the north from ~100 m thick south of the river to 0m in roughly 10 km; Shezal Formation thins slightly farther north	
E- Godin River (observed)		0.3 m	Fine-grained muddy; red to purple turbidites with sandy interbeds and scattered dropstones	2 discrete beds, one of jasper, and the other of slaty, massive hematite just below the Sayunei-Shezal contact	Shezal Formation (grey/tan)	Northernmost appearance of iron formation in the Redstone basin	
F- Boomerang (measured)	Erosional contact with the Coppercap Formation. Basal Sayunei Formation is clast-rich diamictite of reworked Coppercap Formation	0 m	Basal Sayunei Fm is an orange-weathering maroon clast supported pebble to cobble diamictite (0.8m); lower Sayunei Fm is bedded, grey, fine-grained sandstone, with red to maroon siltstone interbeds, that increase upsection, above 75 m, dominantly siltstone with rare sandstone interbeds and scattered dropstones; top of fine-grained Sayunei is interbedded maroon hematitic mudstone and blue-grey fine- to medium-grained sandstone; sharp contact with maroon pebble diamictite grading upwards to boulder diamictite; top of Sayunei Fm is maroon siltstone with up to 40% interbeds of diamictite; uppermost unit is silty to sandy clast-intermediate red pebble diamictite with clasts coarsening upward; reworked jasper clasts present in top diamictite below sharp contact with grey Shezal diamictite.	No intact, IF, but plastically deformed, reworked jasper and (rare) jasper-hematite clasts up to 30 cm in diameter present in red clast-rich, muddy diamictite at or above Sayunei-Shezal contact	Shezal Formation (grey/tan)	IF occurs intermittently immediately south of this section; with distances of 1-3 km of strike it can change from remobilized jasper clasts, to IF being present, to neither, with no regularity to this pattern north of the Moose Horn River.	
G- Hayhook North (measured)	Basal contact unexposed; Coppercap Formation is exposed below a covered interval	0.7 m	Dominantly maroon siltstone with interbeds of sandy siltstone and sandstone; dropstones up to 10-15 cm present throughout; rare interbeds of pale green sandstone and mudstone to 1.4 m thick; high in section is interbedded maroon mudstone and siltstone at 10-15 m intervals, with minor cross-bedded sandstone beds (to 30 cm).	IF is thin and poorly exposed; contains >80 jasper with very little hematite; hematite is exclusively flaggy weathering and slaty; all jasper is bedded	Shezal Formation (grey/tan)		Type section for the Shezal Formation (Eisbacher, 1978)
H- Hayhook South (measured)	Erosional contact with the Coppercap Formation. Basal Sayunei Formation is clast-rich diamictite of reworked Coppercap Formation	6.5 m	Basal diamictite is 5.6 m clast-rich muddy hematitic diamictite consisting of clasts from the directly underlying limestone; overlain by recessive maroon siltstone and hematitic mudstone; dropstones are abundant in lower strata; mudstone grades upwards into siltstone with sandy siltstone interbeds, which are dominantly maroon, with rare pale green interbeds; mudstone becomes more common up-section and is increasingly hematitic and siliceous closer to the base of the IF.	IF is dominantly bedded jasper, with minor slaty hematite; jasper nodules are absent, except for black nodules in basal jasper bed; IF consists of jasper and purple siltstone units interbedded at 0.1-1.8 m intervals; some jasper beds are brecciated with tabular jasper clasts in siltstone and hematite matrix in uppermost 20 cm; entire IF has flaggy weathering with partings along jasper bed contacts; chalcopryite, malachite, and chrysocolla are present along jasper and hematite bed contacts in upper half of IF; commonly heavily weathered and vuggy.	Shezal Formation (grey/tan)		Type section for the Sayunei Formation (Eisbacher, 1978)
I- Hidden Valley (observed)	Little Dal Group (Silverberry Formation?)	Estimated 35 m	Sayunei Formation composed predominantly of maroon siltstone with sandstone and mudstone interbeds, but capped by a 50 m interval of medium- to coarse-grained, massive purple-brown sandstone directly underlying the IF.	IF is mostly bedded jasper and hematite, with ~20% nodular IF; hematite is approximately 40% of the IF; hematite occurs as both poorly bedded massive and flaggy-weathering, slaty hematite	Shezal Formation (grey/tan)	Only known occurrence of iron formation thicker than 15 m in Redstone basin; in a very small, localized area; Rapitan Group in steeply faulted contact with underlying Little Dal Group	The thick sandstone in the Sayunei Formation is unique to this location; coarse-grained facies of the Sayunei Fm in this basin usually thin and restricted to muddy diamictites or thin sandy interbeds in siltstone or mudstone

¹From Baldwin and Turner, 2012
²From Baldwin et al., 2012

Table 4.3: Major and Trace Element Geochemical results

Table 4.3: Geochemical Results													
Strat Height	units	Iron Creek (IC)											
	metres	65.7	66.5	66.65	66.75	68.75	69.45	69.7	96.05	115.35	117.75	121.2	145.7
SiO2	wt%	98.56	74.88	55.91	42.54	61.22	65.23	62.90	32.36	65.84	55.78	66.10	68.06
TiO2	wt%	0.01	0.01	0.01	0.01	0.03	0.01	0.02	0.06	0.02	0.04	0.01	0.04
Al2O3	wt%	0.03	0.10	0.05	0.10	0.61	0.25	0.36	0.46	0.34	0.36	0.07	0.37
Fe2O3	wt%	1.59	22.27	32.61	26.18	34.57	23.95	34.54	66.30	32.24	40.30	30.87	30.45
MnO	wt%	0.01	0.05	0.20	0.47	0.10	0.33	0.03	0.03	0.03	0.05	0.02	0.02
MgO	wt%	0.03	0.03	0.03	0.10	0.16	0.13	0.03	0.07	0.06	0.03	0.02	0.06
CaO	wt%	0.10	0.96	5.90	16.15	1.64	4.85	0.41	0.32	0.53	1.66	1.30	0.35
K2O	wt%	0.01	0.03	0.01	0.01	0.08	0.04	0.03	0.02	0.03	0.03	0.01	0.04
Na2O	wt%	0.07	0.09	0.09	0.08	0.10	0.12	0.10	0.12	0.10	0.12	0.11	0.10
P2O5	wt%	0.00	0.14	0.31	0.30	0.20	0.08	0.16	0.05	0.05	0.11	0.82	0.27
LOI	wt%	0.46	1.49	5.15	13.85	1.94	4.70	0.68	0.94	1.10	1.91	1.02	0.87
Total	wt%	100.84	100.05	100.27	99.79	100.67	99.68	99.27	100.73	100.35	100.40	100.35	100.61
Li	ppb	872	2767	2114	3984	1457	1855	1366	820	2657	2823	2302	1789
Be	ppb	34	527	195	447	1521	462	226	481	638	743	729	468
Sc	ppb	-82	1572	1259	1611	3110	913	2202	2737	3177	1994	1193	2586
Ti	ppb	3618	97282	70556	78817	164222	76990	158878	423957	129129	110322	91454	232934
V	ppb	665	20102	20912	16228	28965	13226	34023	67877	27336	15856	19601	33668
Cr	ppb	686	9746	8446	8304	17618	4595	9350	18718	12493	8550	12293	19531
Co	ppb	38	439	456	355	1304	346	424	523	869	650	584	425
Ni	ppb	105	788	931	674	6229	1478	1245	1595	4940	3316	1160	1414
Cu	ppb	804	5990	84236	8956	6219	6580	1215	489	10942	1739	3146	995
Zn	ppb	-562	784	394	403	2207	333	463	1408	1851	694	202	2319
Ga	ppb	71	539	145	404	4874	530	667	830	1185	1017	589	1245
As	ppb	194	1870	2739	1470	3641	3121	2622	4632	1513	1716	1381	2498
Rb	ppb	220	264	255	244	2384	673	1032	564	765	725	164	979
Sr	ppb	1960	9594	53733	17921	19823	43791	16024	13962	11739	13144	11989	12549
Y	ppb	76	4214	12470	5045	12705	5109	8286	3626	3118	2018	2371	5502
Zr	ppb	325	3758	2699	3194	8189	2625	5008	14972	8990	6451	1841	7556
Nb	ppb	4	237	160	268	461	159	332	1557	341	276	188	419
Mo	ppb	9	349	297	169	160	71	228	303	108	61	102	51
Ag	ppb	-17	-10	19	-20	-17	-22	-25	-18	-23	-27	-31	-15
Cd	ppb	1	5	48	8	24	20	11	14	7	5	3	8
In	ppb	0	1	2	1	5	1	5	6	2	2	1	3
Sn	ppb	11	19	29	36	47	18	39	164	38	8	7	34
Sb	ppb	6	19	43	14	59	66	43	94	31	46	18	26
Cs	ppb	90	91	141	83	270	157	435	361	215	141	50	239
Ba	ppb	1498	10031	9265	11000	27527	16920	15911	37190	13264	4765	6715	8271
La	ppb	22	242	937	508	1962	604	942	1623	488	387	734	912
Ce	ppb	46	563	1775	1186	4276	1218	2181	3662	1197	1032	1692	2494
Pr	ppb	6	88	246	212	615	170	308	448	176	142	209	377
Nd	ppb	23	442	1130	1089	2817	751	1445	1797	769	635	886	1776
Sm	ppb	4	112	260	235	714	182	362	362	219	164	224	436
Eu	ppb	1	34	79	61	226	52	99	89	65	46	65	123
Gd	ppb	6	194	491	318	1086	287	575	430	331	224	313	626
Tb	ppb	1	42	102	60	199	62	113	80	69	43	56	116
Dy	ppb	8	390	952	516	1515	558	915	589	540	328	402	859
Ho	ppb	2	119	295	152	398	162	251	141	136	85	96	204
Er	ppb	8	443	1071	555	1322	582	811	443	463	293	308	611
Tm	ppb	1	81	183	100	228	101	129	76	88	55	56	93
Yb	ppb	9	632	1297	763	1662	730	879	539	711	432	434	629
Lu	ppb	1	109	219	127	279	121	142	86	122	74	73	100
Hf	ppb	5	50	31	43	97	39	81	287	65	57	26	100
Ta	ppb	0	5	3	4	14	5	12	32	9	4	3	11
W	ppb	50	90	25	153	252	26	75	101	200	150	84	65
Tl	ppb	3	4	5	4	15	11	10	4	6	12	3	6
Pb	ppb	94	599	1008	532	1820	1868	1775	2250	497	609	757	2239
Th	ppb	2	108	59	94	233	66	166	377	148	79	137	183
U	ppb	14	54	95	50	93	40	63	124	98	48	43	37

Table 4.3: Geochemical Results (cont)										
Strat Height	metres	Iron Creek (IC)								
		146.3	158.3	158.95	166.2	168.75	173.7	181.9	183.5	184.4
SiO2	wt%	69.25	69.44	75.72	62.44	49.71	76.74	66.46	76.86	80.66
TiO2	wt%	0.05	0.02	0.01	0.03	0.04	0.01	0.02	0.14	0.05
Al2O3	wt%	0.23	0.09	0.11	0.31	0.48	0.06	0.58	0.62	0.48
Fe2O3	wt%	27.07	28.92	22.25	36.48	46.31	21.86	29.74	17.95	16.96
MnO	wt%	0.07	0.03	0.06	0.03	0.04	0.03	0.01	0.04	0.05
MgO	wt%	0.31	0.05	0.07	0.09	0.16	0.01	0.23	0.20	0.08
CaO	wt%	0.92	0.37	0.63	0.18	1.64	0.53	0.63	1.59	0.70
K2O	wt%	0.03	0.02	0.04	0.02	0.04	0.02	0.04	0.07	0.16
Na2O	wt%	0.14	0.11	0.10	0.09	0.12	0.08	0.11	0.15	0.10
P2O5	wt%	0.30	0.20	0.35	0.07	0.89	0.29	0.30	0.45	0.49
LOI	wt%	1.42	0.70	0.65	0.75	0.91	0.62	1.07	1.92	0.68
Total	wt%	99.79	99.94	99.99	100.48	100.34	100.24	99.20	99.99	100.41
Li	ppb	3584	757	1563	1380	1319	680	2218	2981	1848
Be	ppb	215	460	225	586	257	463	1346	1343	397
Sc	ppb	1574	1062	758	3412	3306	831	2157	7038	1092
Ti	ppb	181003	45259	91484	159797	127103	54378	130964	761008	192360
V	ppb	13499	25161	16378	38724	17508	20995	49676	60106	37002
Cr	ppb	13210	8111	11497	3043	7208	8891	5397	27471	8673
Co	ppb	707	639	257	434	374	127	598	429	403
Ni	ppb	1685	1802	576	703	845	982	1414	1017	910
Cu	ppb	824	2624	399	739	828	199	6030	4061	94913
Zn	ppb	1594	530	24	1214	231	-140	1648	1286	382
Ga	ppb	201	423	152	1756	188	282	1311	1114	270
As	ppb	1169	2588	2163	1705	1959	3300	4020	2592	3058
Rb	ppb	705	351	531	2183	922	291	1405	1632	572
Sr	ppb	26525	17152	20512	16032	34700	17675	19916	35249	15409
Y	ppb	8357	3376	4951	1407	7699	2856	3718	5367	2375
Zr	ppb	4606	2812	3398	9904	6261	2396	6810	31966	10015
Nb	ppb	419	173	267	802	421	165	398	2770	761
Mo	ppb	49	187	61	104	166	827	578	273	980
Ag	ppb	-26	-19	-32	-18	-18	-36	-18	-11	-20
Cd	ppb	10	6	5	14	20	4	144	56	76
In	ppb	4	1	3	2	4	2	4	12	2
Sn	ppb	44	7	41	51	17	7	38	154	30
Sb	ppb	27	51	42	29	44	130	108	67	53
Cs	ppb	191	82	129	248	289	70	146	172	121
Ba	ppb	15270	7665	15368	19553	21516	5063	46582	31210	28410
La	ppb	1512	569	989	378	1829	499	1128	2782	1607
Ce	ppb	3899	1193	2061	828	4682	1226	2742	7391	3720
Pr	ppb	572	171	283	101	723	182	379	1015	518
Nd	ppb	2685	743	1237	420	3447	839	1705	4435	2256
Sm	ppb	638	176	308	103	806	226	386	992	460
Eu	ppb	180	49	89	36	221	76	108	248	116
Gd	ppb	901	271	456	135	1092	367	500	1037	487
Tb	ppb	164	52	84	27	182	74	86	168	74
Dy	ppb	1198	423	645	210	1215	536	596	1049	458
Ho	ppb	294	116	163	53	280	124	142	230	97
Er	ppb	907	400	521	185	819	372	430	680	272
Tm	ppb	144	71	84	35	125	61	71	114	42
Yb	ppb	978	533	556	277	820	428	500	825	281
Lu	ppb	158	89	86	46	128	65	81	129	43
Hf	ppb	79	22	46	112	73	19	77	522	124
Ta	ppb	16	2	7	7	6	2	11	57	11
W	ppb	33	110	32	84	54	211	184	139	171
Tl	ppb	16	7	9	12	16	6	22	29	9
Pb	ppb	1715	4321	652	3129	25342	1668	19875	1701	3071
Th	ppb	204	44	103	106	119	64	159	565	149
U	ppb	19	101	50	54	30	9	60	71	39

Table 4.3: Geochemical Results (cont)

Strat Height	metres	Discovery Creek (DC)												
		340.05	340.6	340.9	341	369.8	414.5	414.6	414.7	418	419.1	422.5	423.5	429.8
SiO2	wt%	75.37	74.58	54.38	70.81	71.28	62.61	55.76	69.10	48.98	73.18	51.71	95.61	80.93
TiO2	wt%	0.01	0.01	0.01	0.01	0.02	0.02	0.03	0.02	0.03	0.03	0.05	0.01	0.01
Al2O3	wt%	0.95	0.64	0.27	0.21	0.50	0.11	0.11	0.42	0.64	0.14	0.73	0.06	0.10
Fe2O3	wt%	21.30	23.02	41.92	27.81	25.28	35.66	42.82	29.40	44.18	17.92	44.79	3.78	17.69
MnO	wt%	0.04	0.10	0.32	0.08	0.22	0.01	0.02	0.01	0.07	0.10	0.02	0.02	0.01
MgO	wt%	0.71	0.31	0.39	0.09	0.28	0.02	0.03	0.13	0.79	1.37	0.27	0.07	0.02
CaO	wt%	0.16	0.20	0.80	0.13	0.28	0.33	0.33	0.15	1.82	2.50	0.75	0.11	0.08
K2O	wt%	0.05	0.07	0.04	0.02	0.04	0.02	0.01	0.03	0.02	0.02	0.04	0.01	0.01
Na2O	wt%	0.10	0.13	0.11	0.10	0.11	0.10	0.10	0.09	0.10	0.08	0.11	0.07	0.07
P2O5	wt%	0.05	0.08	0.02	0.07	0.03	0.22	0.18	0.03	0.12	0.09	0.50	0.03	0.06
LOI	wt%	1.83	1.16	2.28	0.96	1.63	0.60	0.61	0.63	3.38	4.29	1.34	0.52	0.61
Total	wt%	100.56	100.29	100.53	100.29	99.68	99.70	100.00	100.01	100.13	99.73	100.30	100.28	99.59
Li	ppb	3659	2873	1409	634	2600	3064	3126	6073	7431	1068	1303	833	1507
Be	ppb	1282	275	710	1089	1580	978	560	471	742	257	1252	95	194
Sc	ppb	2759	2702	1821	1312	1824	3180	1898	5333	4636	596	2939	278	495
Ti	ppb	62629	86770	62724	63000	71340	213874	118529	238277	230661	71507	148358	19983	68607
V	ppb	32209	29796	76246	47562	62522	51250	31409	59920	111424	32113	32760	5076	19981
Cr	ppb	22640	20726	18608	20528	26772	33739	27186	30265	16451	17539	28651	9673	19275
Co	ppb	8052	6028	8188	1836	5384	2784	1662	4199	1464	558	721	206	330
Ni	ppb	11298	4772	4936	3986	9020	6721	4372	6634	6812	1860	2640	1136	1406
Cu	ppb	4977	30921	8136	20265	4477	6213	4912	5870	3353	34453	10828	1050	4645
Zn	ppb	17056	5579	3115	52070	6254	3147	1801	11480	4970	914	3120	393	436
Ga	ppb	5430	1186	1258	1442	5040	1197	426	1891	2066	296	1537	152	168
As	ppb	6299	5071	11426	9894	9143	10827	8769	9866	7733	2738	4589	481	2860
Rb	ppb	496	1003	598	269	609	516	941	1590	688	418	582	287	223
Sr	ppb	19214	16885	17134	19207	27366	25911	18804	19274	13799	7414	16321	2241	4174
Y	ppb	7810	4550	8279	7848	10759	13587	5674	6339	7220	2663	6076	368	835
Zr	ppb	6612	7195	3889	2668	6604	8309	6131	20819	23709	2351	6950	1284	2348
Nb	ppb	180	363	179	177	225	582	376	962	446	177	460	47	189
Mo	ppb	1937	2244	4264	4766	3707	2496	1728	1274	902	1084	683	403	599
Ag	ppb	8	28	12	13	8	22	13	19	8	30	38	4	21
Cd	ppb	9	16	9	12	17	11	8	11	12	4	8	2	2
In	ppb	7	3	2	1	2	3	3	5	12	1	6	1	0
Sn	ppb	70	92	64	71	72	131	95	148	69	56	68	48	58
Sb	ppb	429	169	313	398	589	496	389	303	202	178	146	35	103
Cs	ppb	205	432	329	107	196	211	381	990	469	170	189	72	77
Ba	ppb	29482	31784	50912	43148	82158	127104	135279	140684	420002	40689	54151	9789	18135
La	ppb	711	509	569	521	1554	2265	1210	993	1437	544	1843	149	665
Ce	ppb	1795	1225	1363	1128	2548	5579	2946	2515	3815	1368	5089	418	1254
Pr	ppb	259	186	205	203	351	807	397	352	547	189	728	58	138
Nd	ppb	1180	825	873	940	1454	3766	1743	1555	2556	872	3162	262	494
Sm	ppb	339	206	243	225	359	923	412	373	662	221	733	63	71
Eu	ppb	136	66	79	59	100	263	115	109	221	61	182	15	18
Gd	ppb	517	285	407	328	564	1357	576	505	866	299	891	70	81
Tb	ppb	102	54	94	69	110	252	109	99	150	54	158	11	16
Dy	ppb	810	446	859	647	945	1940	832	793	1068	396	1141	70	124
Ho	ppb	218	125	237	193	269	476	204	210	246	94	260	14	31
Er	ppb	753	440	828	693	933	1491	660	751	724	286	788	36	105
Tm	ppb	131	78	150	121	160	245	115	147	113	46	131	5	20
Yb	ppb	954	598	1099	878	1140	1756	841	1202	776	309	953	33	178
Lu	ppb	160	102	179	148	192	284	135	222	124	48	151	5	32
Hf	ppb	42	87	30	24	46	88	68	211	125	29	63	13	34
Ta	ppb	3	4	3	2	3	13	6	13	17	3	8	2	4
W	ppb	7789	8030	6955	9835	7637	11533	11953	7154	2220	7493	6829	5663	6725
Tl	ppb	15	23	37	36	41	16	16	14	5	7	10	2	4
Pb	ppb	2100	1425	2619	3692	4518	6015	4221	2771	2274	1355	4482	395	663
Th	ppb	138	110	105	49	72	138	88	237	190	62	193	30	97
U	ppb	98	113	493	668	2748	215	160	287	187	460	84	8	122

Table 4.3: Geochemical Results (cont)							
Strat Height	metres	Hayhook North (HN)					
		196.9	197.1	197.3	197.4	197.5	197.6
SiO2	wt%	65.83	63.09	84.35	81.54	80.75	75.12
TiO2	wt%	0.01	0.03	0.01	0.02	0.01	0.02
Al2O3	wt%	0.40	0.17	0.13	0.42	0.34	0.23
Fe2O3	wt%	31.29	34.54	14.36	16.48	17.64	23.70
MnO	wt%	0.06	0.02	0.01	0.02	0.02	0.02
MgO	wt%	0.05	0.04	0.03	0.09	0.03	0.04
CaO	wt%	0.18	0.39	0.20	0.23	0.24	0.10
K2O	wt%	0.03	0.01	0.02	0.06	0.05	0.01
Na2O	wt%	0.11	0.10	0.07	0.11	0.07	0.08
P2O5	wt%	0.20	0.32	0.17	0.13	0.23	0.10
LOI	wt%	2.26	1.31	0.82	1.15	0.89	1.11
Total	wt%	100.41	100.02	100.16	100.24	100.27	100.52
Li	ppb	2317	3066	1304	1480	1533	1902
Be	ppb	1203	925	613	549	643	919
Sc	ppb	3233	2455	1214	2167	2678	2283
Ti	ppb	80094	103521	47346	50356	59350	75391
V	ppb	22471	24457	16639	18933	22029	19470
Cr	ppb	9544	11392	8348	8777	7144	8526
Co	ppb	1614	2977	1228	1491	1500	1091
Ni	ppb	6009	8314	4600	4745	4932	4710
Cu	ppb	21036	6199	6361	9961	11018	7716
Zn	ppb	3032	2593	2491	1620	2211	2459
Ga	ppb	1830	847	681	868	1017	1389
As	ppb	6211	4777	7098	3333	4703	4440
Rb	ppb	1666	184	265	1159	1370	229
Sr	ppb	59379	31164	20316	76011	72220	46000
Y	ppb	18714	15401	15454	9388	12807	9882
Zr	ppb	19478	7791	2267	7495	9167	9441
Nb	ppb	309	314	146	231	277	399
Mo	ppb	6309	13669	5012	4279	4429	4768
Ag	ppb	8	6	5	9	5	49
Cd	ppb	25	14	11	13	14	9
In	ppb	3	1	1	1	1	1
Sn	ppb	51	59	46	46	44	52
Sb	ppb	219	177	158	128	137	169
Cs	ppb	150	92	64	118	111	104
Ba	ppb	40285	58152	30727	20873	16928	21599
La	ppb	5013	4763	3220	2718	2910	3485
Ce	ppb	12405	11190	6886	7354	7475	8955
Pr	ppb	1743	1502	917	1069	1072	1219
Nd	ppb	8115	6798	4215	5055	5036	5317
Sm	ppb	2074	1515	1002	1234	1269	1232
Eu	ppb	519	382	262	330	343	307
Gd	ppb	2619	1988	1393	1517	1622	1416
Tb	ppb	412	327	241	227	260	218
Dy	ppb	2776	2250	1748	1473	1768	1479
Ho	ppb	626	519	432	326	407	340
Er	ppb	1799	1528	1287	924	1196	1023
Tm	ppb	280	242	196	143	184	167
Yb	ppb	1891	1652	1296	961	1240	1156
Lu	ppb	301	264	207	151	199	183
Hf	ppb	129	46	18	42	53	57
Ta	ppb	7	10	4	4	5	5
W	ppb	5102	6019	5424	6373	4835	5957
Tl	ppb	11	2	2	9	10	4
Pb	ppb	735	826	386	441	497	746
Th	ppb	171	168	72	91	114	130
U	ppb	224	175	225	184	258	229

Table 4.3: Geochemical Results (cont)

Strat Height	metres	Hayhook South (HS)												
		229.6	230.5	231.4	232.9	232.95	233.2	233.4	234.6	234.8	234.95	235.35	235.75	237
SiO2	wt%	55.43	93.95	80.52	54.52	84.36	78.05	92.18	73.89	79.10	68.74	85.87	63.10	56.69
TiO2	wt%	0.67	0.01	0.01	1.14	0.01	0.03	0.01	0.03	0.01	0.04	0.01	0.02	0.05
Al2O3	wt%	8.16	0.19	0.14	13.91	0.12	0.23	0.17	0.43	0.32	0.15	0.05	0.41	0.73
Fe2O3	wt%	25.78	5.63	18.40	12.93	12.40	21.60	7.13	20.44	18.76	27.59	11.92	34.55	40.37
MnO	wt%	0.32	0.02	0.02	0.19	0.09	0.03	0.06	0.08	0.04	0.04	0.02	0.02	0.03
MgO	wt%	3.66	0.11	0.07	4.88	0.06	0.08	0.09	0.11	0.13	0.04	0.03	0.12	0.29
CaO	wt%	0.24	0.13	0.21	8.08	1.04	0.09	0.02	2.06	0.82	1.46	0.67	0.59	0.62
K2O	wt%	0.97	0.04	0.03	1.36	0.05	0.03	0.03	0.09	0.05	0.03	0.01	0.03	0.09
Na2O	wt%	1.65	0.05	0.09	2.74	0.09	0.08	0.06	0.09	0.07	0.08	0.06	0.09	0.10
P2O5	wt%	0.13	0.10	0.15	0.13	0.07	0.06	0.01	0.17	0.14	0.35	0.13	0.19	0.15
LOI	wt%	3.10	0.31	0.56	0.39	0.89	0.30	0.38	2.20	0.94	1.18	0.90	1.12	1.11
Total	wt%	100.11	100.56	100.21	100.25	99.16	100.57	100.13	99.58	100.38	99.71	99.67	100.23	100.22
Li	ppb	36543	531	838	661	281	490	2236	1529	845	564	781	2532	839
Be	ppb	1136	52	403	316	236	113	164	517	613	580	525	792	810
Sc	ppb	14893	399	2057	973	942	819	1384	9047	5596	3053	977	2713	4324
Ti	ppb	2654477	19820	38022	21962	24184	41023	63824	174872	84135	74483	31244	117562	77218
V	ppb	126096	4114	11196	9397	9133	5527	27739	24620	20204	16796	9994	22368	17973
Cr	ppb	33391	7773	8478	6373	8058	7009	7287	15860	15857	11149	8971	8160	11435
Co	ppb	20693	294	1101	260	386	405	605	1171	681	1059	439	753	904
Ni	ppb	22472	950	3370	1294	1807	1615	1487	7441	6954	6200	2971	5180	5997
Cu	ppb	234186	9682	4605	3432	5957	72358	3524	15791	7737	26030	1613	4357	4468
Zn	ppb	68535	1795	1030	678	580	813	2435	3588	2137	2730	963	3753	5820
Ga	ppb	9467	174	403	254	247	253	753	2052	869	670	554	2291	1710
As	ppb	2157	278	1741	1163	933	656	500	1410	1718	1709	1082	2193	1972
Rb	ppb	27662	1067	1228	1124	998	933	833	3896	1416	934	272	456	1861
Sr	ppb	50443	3871	18667	14798	13850	5309	4455	49037	34079	32960	22877	42226	34504
Y	ppb	20655	557	9660	3610	4020	1557	792	9527	6112	11225	2429	4508	6835
Zr	ppb	77415	1331	5931	7422	2941	17222	7186	30294	67661	18868	4385	6631	34908
Nb	ppb	10744	45	130	83	53	361	513	708	514	330	101	445	326
Mo	ppb	286	336	657	425	131	273	353	623	677	1003	1116	1048	990
Ag	ppb	65	51	19	11	4	9	2	19	32	16	0	27	15
Cd	ppb	94	3	12	5	23	13	12	88	65	47	14	31	44
In	ppb	78	1	1	0	0	1	2	2	1	0	2	1	1
Sn	ppb	1723	46	48	32	40	40	57	58	55	57	44	61	59
Sb	ppb	172	16	50	23	35	24	69	76	168	192	89	162	163
Cs	ppb	1644	123	257	219	194	127	145	205	124	118	74	179	140
Ba	ppb	156481	9406	68662	12640	24046	13172	8952	232972	15694	12349	5745	27502	20949
La	ppb	21761	138	1829	908	1408	498	738	2238	2234	2959	952	1123	1758
Ce	ppb	46295	340	4904	2165	2930	1021	1475	6368	6810	9158	2264	3486	5187
Pr	ppb	5506	37	681	286	355	150	174	914	1047	1378	308	501	799
Nd	ppb	20241	152	3146	1205	1455	635	659	3904	4499	6417	1438	2192	3499
Sm	ppb	4074	35	745	260	300	151	140	1046	1318	1579	340	600	952
Eu	ppb	955	10	215	71	74	41	38	281	305	378	91	171	228
Gd	ppb	3856	47	987	330	383	196	133	1362	1631	1999	492	805	1181
Tb	ppb	633	8	165	60	71	33	23	242	278	308	75	148	209
Dy	ppb	3871	58	1211	465	512	219	139	1667	1829	2089	468	1052	1423
Ho	ppb	803	14	300	121	129	50	27	372	370	454	95	224	310
Er	ppb	2191	42	927	425	431	144	74	1140	1120	1291	248	635	953
Tm	ppb	317	7	153	77	73	23	12	195	194	209	36	104	162
Yb	ppb	1891	45	1056	567	504	164	79	1353	1398	1472	235	729	1152
Lu	ppb	261	7	170	98	84	26	11	206	209	226	35	106	173
Hf	ppb	2119	18	23	23	16	270	119	155	232	50	14	61	78
Ta	ppb	505	2	2	1	1	2	9	11	6	5	2	14	5
W	ppb	389	2415	5104	4466	295	1943	1582	4121	2424	5297	6004	4866	6188
Tl	ppb	130	6	9	7	6	6	6	23	9	6	2	3	12
Pb	ppb	35256	482	808	465	513	695	763	1483	1695	1131	651	1221	1249
Th	ppb	2602	20	50	41	44	42	128	310	182	112	38	162	143
U	ppb	827	36	274	290	410	41	37	95	235	158	131	367	165

4.11 References

- Aitken, J. D., 1989, Uppermost Proterozoic formations in central Mackenzie Mountains, Northwest Territories: Geological Survey of Canada, Bulletin 368, p. 1-26.
- Aitken, J. D., 1991, Two late Proterozoic glaciations, Mackenzie Mountains, northwestern Canada: *Geology*, v. 19, p. 445-448.
- Aitken, J. D., and Cook, D. G., 1974, Effect of antecedent faults on "Laramide" structure, Mackenzie Arc: Geological Survey of Canada Paper, v. 74-1 Part B, p. 259-264.
- Aitken, J. D., and Long, D. G. F., 1978, Mackenzie tectonic arc- reflection of early basin configuration?: *Geology*, v. 6, p. 626-629.
- Aitken, J. D., Macqueen, R. W., and Usher, J. L., 1973, Reconnaissance studies of Proterozoic and Cambrian stratigraphy, lower Mackenzie River area (Operation Norman), District of Mackenzie: Geological Survey of Canada Paper, v. 73-9.
- Aitken, J. D., and Pugh, D. C., 1984, The Fort Norman and Leith Ridge structures: major, buried, Precambrian features underlying Franklin Mountains and Great Bear and Mackenzie Plains: *Bulletin of Canadian Petroleum Geology*, v. 32, no. 2, p. 139-146.
- Aitken, J. D., Ruelle, J. C., and Cook, D. G., 1981, Copper mineralization near an intra-Rapitan unconformity, Nite copper prospect, Mackenzie Mountains, Northwest Territories, Canada: Discussion: *Canadian Journal of Earth Sciences*, v. 18, p. 410-413.
- Armstrong, R. L., Eisbacher, G. H., and Evans, P. D., 1982, Age and stratigraphic-tectonic significance of Proterozoic diabase sheets, Mackenzie Mountains, northwestern Canada: *Canadian Journal of Earth Sciences*, v. 19, p. 316-323.
- Baldwin, G. J., and Turner, E. C., 2012, Lithofacies and lithostratigraphic correlation potential of the Rapitan iron formation, Snake River area (NTS 106F), Yukon, *in* Macfarlane, K. E., and Sack, P. J., eds., *Yukon Exploration and Geology 2011*, Yukon Geological Survey, p. 1-15.
- Baldwin, G. J., Turner, E. C., and Kamber, B. S., 2012a, Ice, but no fire: a new depositional age for the Rapitan Group, Canada (*in* Goldschmidt 2012 abstract volume): *Mineralogical Magazine*, v. 76, no. 6.

- Baldwin, G. J., Turner, E. C., and Kamber, B. S., 2012b, A new depositional model for glaciogenic Neoproterozoic iron formation: insights from the chemostratigraphy and basin configuration of the Rapitan iron formation: *Canadian Journal of Earth Sciences*, v. 49, p. 455-476.
- Basta, F. F., Maurice, A. E., Fontbote, L., and Favarger, P.-Y., 2011, Petrology and geochemistry of the Banded Iron Formation (BIF) of Wadi Karim and Um Anab, Eastern Desert, Egypt: Implications for the origin of Neoproterozoic BIF: *Precambrian Research*, v. 187, p. 277-292.
- Bau, M., 1996, Controls on the fractionation of isovalent trace elements in magmatic and aqueous systems: Evidence from Y/Ho, Zr/Hf, and lanthanide tetrad effect: *Contributions to Mineralogy and Petrology*, v. 123, no. 3, p. 323-333.
- Bekker, A., Slack, J. F., Planavsky, N., Krapež, B., Hofmann, A., Konhauser, K. O., and Rouxel, O. J., 2010, Iron formation: The sedimentary product of a complex interplay among mantle, tectonic, oceanic, and biospheric processes: *Economic Geology*, v. 105, p. 467-508.
- Beukes, N. J., and Klein, C., 1992, Models for iron-formation deposition, *in* Schopf, J. W., and Klein, C., eds., *The Proterozoic biosphere: a multidisciplinary approach*: Cambridge, Cambridge University Press, p. 147-151.
- Campbell, I. H., and Squire, R. J., 2010, The mountains that triggered the Late Neoproterozoic increase in oxygen: the second Great Oxygenation Event: *Geochimica et Cosmochimica Acta*, v. 74, p. 4187-4206.
- Canfield, D. E., 1998, A new model for Proterozoic ocean chemistry: *Nature*, v. 396, p. 450-453.
- Canfield, D. E., Poulton, S. W., Knoll, A. H., Narbonne, G. M., Ross, G., Goldberg, T., and Strauss, H., 2008, Ferruginous conditions dominated later Neoproterozoic deep-water chemistry: *Science*, v. 321, p. 949-952.
- Canfield, D. E., Poulton, S. W., and Narbonne, G. M., 2007, Late-Neoproterozoic deep-ocean oxygenation and the rise of animal life: *Science*, v. 315, p. 92-95.
- Cecile, M. P., 2000, Geology of the northeastern Nidderly Lake map area, east-central Yukon and adjacent Northwest Territories: *Geological Survey of Canada Bulletin*, v. 553, p. 119 p.

- Clout, J. M. F., and Simonson, B. M., 2005, Precambrian Iron Formations and Iron Formation-Hosted Iron Ore Deposits: Economic Geology 100th Anniversary Volume, p. 643-680.
- Colpron, M., and Augereau, C. M., 1998, Preliminary geological map of the Dal Lake area, Mackenzie Mountains, Northwest Territories (NTS 95M/2): NWT Geology Division, Indian and Northern Affairs Canada, v. EGS 1998-03, p. 1:50,000.
- Colpron, M., and Jefferson, C. W., 1998, Geological map and cross sections of the Mount Kraft area, Mackenzie Mountains, Northwest Territories (NTS 95L/15): NWT Geology Division, Indian and Northern Affairs Canada, v. EGS 1998-02, p. 1:50,000.
- Colpron, M., Logan, J. M., and Mortensen, J. K., 2002, U-Pb zircon age constraint for late Neoproterozoic rifting and initiation of the lower Paleozoic passive margin of western Laurentia: Canadian Journal of Earth Sciences, v. 39, p. 133-143.
- Derry, L. A., and Jacobsen, S. B., 1990, The chemical evolution of Precambrian seawater: Evidence from REEs in banded iron formations: *Geochimica et Cosmochimica Acta*, v. 54, no. 11, p. 2965-2977.
- Eisbacher, G. H., 1976, Proterozoic Rapitan Group and Related Rocks, Redstone River Area, District of Mackenzie: Geological Survey of Canada Paper, v. 76, no. 1A, p. 117-125.
- Eisbacher, G. H., 1977, Tectono-stratigraphic framework of the Redstone copper belt, District of Mackenzie: Geological Survey of Canada Paper, v. 77-1A, p. 229-234.
- Eisbacher, G. H., 1978, Re-definition and subdivision of the Rapitan Group, Mackenzie Mountains: Geological Survey of Canada Paper, v. 77, no. 35, p. 1-21.
- Eisbacher, G. H., 1981a, Late Precambrian tillites of the northern Yukon-Northwest Territories region, Canada, *in* Hambrey, M. J., and Harland, W. B., eds., *Earth's pre-Pleistocene glacial record*: Cambridge, Cambridge University Press, p. 724-727.
- Eisbacher, G. H., 1981b, Sedimentary tectonics and glacial record in the Windermere Supergroup, Mackenzie Mountains, Northwestern Canada: Geological Survey of Canada Paper, v. 80, no. 27, p. 1-41.
- Eisbacher, G. H., 1985, Late Proterozoic rifting, glacial sedimentation, and sedimentary cycles in the light of Windermere deposition, western Canada: *Palaeogeography, Palaeoclimatology, Palaeoecology*, v. 51, p. 231-254.

- Eyles, N., 2008, Glacio-epochs and the supercontinent cycle after ~3.0 Ga: Tectonic boundary conditions for glaciation: *Palaeogeography, Palaeoclimatology, Palaeoecology*, v. 258, p. 89-129.
- Eyles, N., and Januszczak, N., 2004, 'Zipper-rift': a tectonic model for Neoproterozoic glaciations during the breakup of Rodinia after 750 Ma: *Earth-Science Reviews*, v. 65, p. 1-73.
- Freitas, B. T., Warren, L. V., Boggiani, P. C., Paes De Almeida, R., and Piacentini, T., 2011, Tectono-sedimentary evolution of the Neoproterozoic BIF-bearing Jacadigo Group, SW-Brazil: *Sedimentary Geology*, v. 238, p. 48-70.
- Fritz, W. H., Narbonne, G. M., and Gordey, S. P., 1983, Strata and trace fossils near the Precambrian-Cambrian boundary, Mackenzie, Selwyn, and Wernecke Mountains, Yukon and Northwest Territories: Current Research Part B, Geological Survey of Canada Paper, v. 83-1B, p. 365-375.
- Gabrielse, H., 1972, Younger Precambrian of the Canadian cordillera: *American Journal of Science*, v. 272, p. 521-536.
- Gordey, S. P., and Anderson, R. G., 1993, Evolution of the northern Cordilleran miogeocline, Nahanni map area (105I), Yukon and Northwest Territories: Geological Survey of Canada Memoir, v. 428, p. 214 p.
- Green, L. H., and Godwin, C. I., 1963, Mineral Industry of Yukon Territory and southwestern District of Mackenzie, 1962.: Geological Survey of Canada Paper, v. 63, no. 38, p. 15-18.
- Gross, G. A., 1965, Iron-formation, Snake River area, Yukon and Northwest Territories, *in* Jenness, S. E., ed., Report of Activities: Field, 1964, Geological Survey of Canada paper 65-1, p. 143.
- Gross, G. A., 1993, Industrial and genetic models for iron ore in iron-formations, *in* Kirkham, R. V., Sinclair, W. D., Thorpe, R. I., and Duke, J. M., eds., Mineral deposit modelling: Geological Association of Canada, Special Paper no. 40: Ottawa, p. 151-170.
- Halverson, G. P., Poitrasson, F., Hoffman, P. F., Nédélec, A., Montel, J.-M., and Kirby, J., 2011, Fe isotope and trace element geochemistry of the Neoproterozoic syn-glacial Rapitan iron formation: *Earth and Planetary Science Letters*, v. 309, no. 1-2, p. 100-112.

- Helmstaedt, H., Eisbacher, G. H., and McGregor, J. A., 1979, Copper mineralization near an intra-Rapitan unconformity, Nite copper prospect, Mackenzie Mountains, Northwest Territories, Canada: *Canadian Journal of Earth Sciences*, v. 16, p. 50-59.
- Helmstaedt, H., Eisbacher, G. H., and McGregor, J. A., 1981, Copper mineralization near an intra-Rapitan unconformity, Nite copper prospect, Mackenzie Mountains, Northwest Territories, Canada: Reply: *Canadian Journal of Earth Sciences*, v. 18, p. 414-418.
- Hill, I. G., Worden, R. H., and Meighan, I. G., 2000, Yttrium: the immobility-mobility transition during basaltic weathering: *Geology*, v. 28, no. 10, p. 923-926.
- Hoffman, P. F., 2009, Pan-glacial- a third state in the climate system: *Geology Today*, v. 25, no. 3, p. 100-107.
- Hoffman, P. F., and Halverson, G. P., 2011, Chapter 36 Neoproterozoic glacial record in the Mackenzie Mountains, northern Canadian Cordillera, *in* Arnaud, E., Halverson, G. P., and Shields-Zhou, G., eds., *The geological record of Neoproterozoic glaciations*: London, Geological Society of London, p. 397-411.
- Hoffman, P. F., Kaufman, A. J., Halverson, G. P., and Schrag, D. P., 1998, A Neoproterozoic Snowball Earth: *Science*, v. 281, p. 1342-1346.
- Hoffman, P. F., and Li, Z. X., 2009, A paleogeographic context for Neoproterozoic glaciation: *Palaeogeography, Palaeoclimatology, Palaeoecology*, v. 277, p. 158-172.
- Hoffman, P. F., Macdonald, F. A., and Halverson, G. P., 2011, Chapter 5 Chemical sediments associated with Neoproterozoic glaciation: iron formation, cap carbonate, barite, and phosphate, *in* Arnaud, E., Halverson, G. P., and Shields-Zhou, G., eds., *The geological record of Neoproterozoic Glaciations*: London, Geological Society of London, p. 67-80.
- Hoffman, P. F., and Schrag, D. P., 2002, The snowball Earth hypothesis: testing the limits of global change: *Terra Nova*, v. 14, p. 129-155.
- Hofmann, H. J., Narbonne, G. M., and Aitken, J. D., 1990, Ediacaran remains from intertillite beds in northwestern Canada: *Geology*, v. 18, p. 1199-1202.
- Holland, H. D., 1984, *The chemical evolution of the atmosphere and oceans*: Princeton, Princeton University Press, 598 p.

- James, N. P., Narbonne, G. M., and Kyser, T. K., 2001, Late Neoproterozoic cap carbonates: Mackenzie Mountains, northwestern Canada: precipitation and global glacial meltdown: *Canadian Journal of Earth Sciences*, v. 38, p. 1229-1262.
- Jefferson, C. W., 1983, The upper Proterozoic Redstone copper belt, Mackenzie Mountains, N.W.T.: University of Western Ontario, 445 p.
- Jefferson, C. W., and Ruelle, J. C. L., 1987, The late Proterozoic Redstone copper belt, Mackenzie Mountains, Northwest Territories, *in* Morin, J. A., ed., *Mineral Deposits of the northern Cordillera*, Canadian Institute of Mining and Metallurgy Special Vol. 37, p. 154-168.
- Jory, L. T., 1962, Geological mapping and trenching, North Redstone claim group, Dal Lake, NWT: Department of Indian Affairs and Northern Development, Assessment Report, v. 017596.
- Kamber, B. S., 2010, Archean mafic-ultramafic volcanic landmasses and their effect on ocean atmosphere chemistry *Chemical Geology*, v. 274, no. 1-2, p. 19-28.
- Kamber, B. S., Greig, A., and Collerson, K. D., 2005, A new estimate for the composition of weathered young upper continental crust from alluvial sediments, Queensland, Australia: *Geochimica et Cosmochimica Acta*, v. 69, no. 4, p. 1041-1058.
- Kato, Y., Yamaguchi, K. E., and Ohmoto, H., 2006, Rare earth elements in Precambrian banded iron formations: Secular changes of Ce and Eu anomalies and evolution of atmospheric oxygen, *in* Kesler, S. E., and Ohmoto, H., eds., *GSA Memoir 198: Evolution of Earth Earth's Atmosphere, Hydrosphere, and Biosphere- Constraints from Ore Deposits*: Boulder, The Geological Society of America, p. 269-289.
- Keele, J., 1906, Upper Stewart River region, Yukon: Geological Survey of Canada Annual Report 1904, v. 16, p. 5-23.
- Keele, J., 1910, Reconnaissance across the Mackenzie Mountains on the Pelly, Ross, and Gravel Rivers, Yukon and Northwest Territories: Geological Survey of Canada Report No. 1097.
- Kirschvink, J. L., 1992, Late Proterozoic low-latitude global glaciation: the Snowball Earth, *in* Schopf, J. W., and Klein, C., eds., *The Proterozoic biosphere: A multidisciplinary study*: Cambridge, Cambridge University Press, p. 51-52.

- Klein, C., and Beukes, N. J., 1993, Sedimentology and geochemistry of the glaciogenic late Proterozoic Rapitan iron-formation in Canada: *Economic Geology*, v. 88, p. 542-565.
- Lawrence, M. G., Greig, A., Collerson, K. D., and Kamber, B. S., 2006, Rare earth element and yttrium variability in South East Queensland waterways: *Aquatic Geochemistry*, v. 12, no. 1, p. 39-72.
- Long, D. G. F., Rainbird, R. H., Turner, E. C., and MacNaughton, R. B., 2008, Early Neoproterozoic strata (Sequence B) of mainland northern Canada and Victoria and Banks islands: a contribution to the Geological Atlas of the North Canadian Mainland Sedimentary Basin: Geological Survey of Canada, Open File 5700, p. 24 p.
- Long, D. G. F., and Turner, E. C., 2012, Formal definition of the Neoproterozoic Mackenzie Mountains Supergroup (Northwest Territories), and formal stratigraphic nomenclature for terrigenous clastic units of the Katherine Group: Geological Survey of Canada Open File, v. 7713, p. 1-40.
- Macdonald, F. A., Schmitz, M. D., Crowley, J. L., Roots, C. F., Jones, D. S., Maloof, A. C., Strauss, J. V., Cohen, P. A., Johnston, D. T., and Schrag, D. P., 2010a, Calibrating the Cryogenian: *Science*, v. 327, p. 1241-1243.
- Macdonald, F. A., Strauss, J. V., Rose, C. V., Dudás, F. Ö., and Schrag, D. P., 2010b, Stratigraphy of the Port Nolloth Group of Namibia and South Africa and implications for the age of Neoproterozoic iron formations: *American Journal of Science*, v. 310, p. 862-888.
- McMechan, M. E., 2000, Vreeland diamictites- Neoproterozoic glaciogenic slope deposits, Rocky Mountains, northeast British Columbia: *Bulletin of Canadian Petroleum Geology*, v. 48, no. 3, p. 246-261.
- Moncrieff, A. C. M., 1989, Classification of poorly sorted sedimentary rocks: *Sedimentary Geology*, v. 65, p. 191-194.
- Narbonne, G. M., and Aitken, J. D., 1995, Neoproterozoic of the Mackenzie Mountains, northwestern Canada: *Precambrian Research*, v. 73, p. 101-121.
- Neuweiler, F., Turner, E. C., and Burdige, D. J., 2009, Early Neoproterozoic origin of the metazoan clade recorded in carbonate rock texture: *Geology*, v. 37, no. 5, p. 475-478.

- Och, L. M., and Shields-Zhou, G. A., 2012, The Neoproterozoic oxygenation event: Environmental perturbations and biogeochemical cycling: *Earth-Science Reviews*, v. 110, p. 26-57.
- Pack, A., Russell, S. S., Shelley, J. M. G., and van Zuilen, M., 2007, Geo- and cosmochemistry of the twin elements yttrium and holmium: *Geochimica et Cosmochimica Acta*, v. 71, p. 4592-4608.
- Peterson, K. J., Cotton, J. A., Gehling, J. G., and Pisani, D., 2008, The Ediacaran emergence of bilaterians: Congruence between their genetic and the geological fossil records: *Philosophical Transactions of the Royal Society B: Biological Sciences*, v. 363, no. 1496, p. 1435-1443.
- Picard, S., Lécuyer, C., Barrat, J.-A., Garcia, J. P., Dromart, G., and Sheppard, S. M. F., 2002, Rare-earth element contents of Jurassic fish and reptile teeth and their potential relation to seawater composition (Anglo-Paris basin, France and England): *Chemical Geology*, v. 186, p. 1-16.
- Planavsky, N., Bekker, A., Rouxel, O. J., Kamber, B., Hofmann, A., Knudsen, A., and Lyons, T. W., 2010, Rare earth element and yttrium compositions of Archean and Paleoproterozoic Fe formations revisited: New perspectives on the significance and mechanisms of deposition: *Geochimica et Cosmochimica Acta*, v. 74, p. 6387-6405.
- Poulton, S. W., and Canfield, D. E., 2011, Ferruginous conditions: a dominant feature of the ocean through Earth's history: *Elements*, v. 7, p. 107-112.
- Ross, G. M., Bloch, J. D., and Krouse, H. R., 1995, Neoproterozoic strata of the southern Canadian Cordillera and the isotopic evolution of seawater sulfate: *Precambrian Research*, v. 73, p. 71-99.
- Shields-Zhou, G., and Och, L., 2011, The case for a Neoproterozoic oxygenation event: geochemical evidence and biological consequences: *GSA Today*, v. 21, no. 3, p. 4-11.
- Shields, G. A., and Webb, G. E., 2004, Has the REE composition of seawater changed over geological time?: *Chemical Geology*, v. 204, p. 103-107.
- Slack, J. F., Grenne, T., Bekker, A., Rouxel, O. J., and Lindberg, P. A., 2007, Suboxic deep seawater in the late Paleoproterozoic: Evidence from hematitic chert and iron formation

- related to seafloor-hydrothermal sulfide deposits, central Arizona, USA: *Earth and Planetary Science Letters*, v. 255, p. 243-256.
- Smith, A. J. B., Beukes, N. J., and Gutzmer, J., 2013, The composition and depositional environments of Mesoproterozoic iron formations of the West Rand Group of the Witwatersrand Supergroup, South Africa: *Economic Geology*, v. 108, p. 111-134.
- Stuart, R. A., 1963, Geology of the Snake River Iron deposit: D.I.A.N.D. Assessment Files, Yellowknife, N.W.T., p. 18 p.
- Thorkelson, D. J., Abbott, J. G., Mortensen, J. K., Creaser, R. A., Villeneuve, M. E., McNicoll, V. J., and Layer, P. W., 2005, Early and Middle Proterozoic evolution of Yukon, Canada: *Canadian Journal of Earth Sciences*, v. 42, p. 1045-1071.
- Turner, E. C., and Long, D. G. F., 2008, Basin architecture and syndepositional fault activity during deposition of the Neoproterozoic Mackenzie Mountains supergroup, Northwest Territories, Canada: *Canadian Journal of Earth Sciences*, v. 45, p. 1159-1184.
- Turner, E. C., and Long, D. G. F., 2012, Formal definition of the Neoproterozoic Mackenzie Mountains Supergroup (Northwest Territories), and formal stratigraphic nomenclature for its carbonate and evaporite formations: *Geological Survey of Canada Open File*, v. 7712, no. 1-57.
- Upitis, U., 1966, The Rapitan Group, southeastern Mackenzie Mountains, Northwest Territories [M.S. thesis]: McGill University, 70 p.
- Yeo, G. M., 1978, Iron-formation in the Rapitan Group, Mackenzie Mountains, Yukon and Northwest Territories: DIAND Mineral Industry Report 1975, v. NWT Economic Geology Series 1978-5, p. 170-175.
- Yeo, G. M., 1981, The late Proterozoic Rapitan glaciation in the northern Cordillera, *in* Campbell, F. H. A., ed., *Proterozoic Basins of Canada*, Geological Survey of Canada Paper 81-10, p. 25-46.
- Yeo, G. M., 1984, The Rapitan Group: Relevance to the global association of late Proterozoic glaciation and iron-formation [Ph.D. thesis]: University of Western Ontario, 603 p.
- Yeo, G. M., 1986, Iron-formation in the late Proterozoic Rapitan Group, Yukon and Northwest Territories, *in* Morin, J. A., ed., *Mineral Deposits of the Northern Cordillera*: Canadian Institute of Mining and Metallurgy Special Vol. 37, p. 142-153.

- Young, G. M., 1976, Iron-formation and glaciogenic rocks of the Rapitan Group, Northwest Territories, Canada: *Precambrian Research*, v. 3, p. 137-158.
- Young, G. M., 1982, The late Proterozoic Tindir Group, east-central Alaska: evolution of a continental margin: *Geological Society of America Bulletin*, v. 93, p. 759-783.
- Young, G. M., 1995, Are Neoproterozoic glacial deposits preserved on the margins of Laurentian related to the fragmentation of two supercontinents?: *Geology*, v. 23, no. 2, p. 153-156.
- Young, G. M., 2002, Stratigraphic and tectonic settings of Proterozoic glaciogenic rocks and banded iron-formations: relevance to the snowball Earth debate: *Journal of African Earth Sciences*, v. 35, p. 451-466.
- Young, G. M., 2013, Climatic catastrophes in Earth history: two great Proterozoic glacial episodes: *Geological Journal*, v. 48, p. 1-21.
- Zhang, J., and Nozaki, Y., 1996, Rare earth elements and yttrium in seawater: ICP-MS determinations in the East Caroline, Coral Sea, and South Fiji basins of the western South Pacific Ocean: *Geochimica et Cosmochimica Acta*, v. 60, p. 4631-4644.
- Ziegler, P. A., 1959, Frühpaläozoische Tillite im östlichen Yukon-Territorium (Kanada): *Ecologiae Geologicae Helveticae*, v. 52, p. 735-741.

Chapter 5: Conclusions

The Rapitan iron formation is the archetypical example of Neoproterozoic iron formation, and consequently is one of the most important units for understanding the changes in the Earth's surficial processes during this enigmatic time. The Rapitan Group has not previously been studied using modern geochemical or basin analysis techniques, and thus its role in models for Neoproterozoic iron formation, "snowball Earth", and the evolution of the redox state of the Proterozoic ocean was flawed. The work presented in this dissertation is intended to improve the understanding of the geochemical, stratigraphic, and basinal constraints on the deposition of the Rapitan iron formation.

The initial approach, a detailed stratigraphic and trace element study of a single stratigraphic section of the iron formation, is outlined in Chapter 2 (published as a paper in *Canadian Journal of Earth Sciences* in 2012). Using the REE+Y and the redox-sensitive trace elements Mo and U, it was established that the Rapitan iron formation was deposited in a partially restricted or 'silled' basin. Furthermore, it was shown that the iron was not ultimately derived from a hydrothermal source, and that the basin was redox-stratified, with oxic shallow waters, sulfidic mid-depths, and ferruginous water in the deep basin. These factors were used to construct a depositional model for the iron formation, in which glacially derived nanoparticulate iron was biogenically reduced under glacial ice cover of the basin. During an interglacial interval, the aqueous reduced iron was oxidized, depositing the iron formation, while high, post-glacial primary productivity drove the development of mid-depth sulfidic conditions. The apparent absence of a positive Eu anomaly in the iron formation samples was also presented as evidence for a fully oxygenated open ocean, which differed from previous models for the mid-Neoproterozoic.

Several questions emerged from the findings presented in Chapter 2, foremost among them being how hematite-facies iron formation could be deposited at the same time as sulfidic conditions in the water column. In an effort to further explore these these apparently incompatible conditions, a selection of samples from Chapter 2 was analysed for ultra-sensitive, non-traditional redox proxies, specifically elemental Re and Mo isotopes, the results from which are presented in

Chapter 3 (published as a paper in *Precambrian Research* in 2013). Chapter 3 demonstrates, based on sulfidic Re/Mo ratios and elevated $\delta^{98}\text{Mo}$, that the sulfidic conditions inferred from Mo enrichment were real. It also showed that there was a strong interplay between the fractionation of Mo due to sulfidic conditions and adsorption of Mo onto hematite, which is consistent with contemporaneous sulfidic conditions and hematite deposition. That this was only documented at the top of the iron formation suggests that it may have been a driving factor in the termination of iron formation deposition, although the presence of shallow-water iron formation facies elsewhere in the basin indicates that sulfidic conditions were localised. Finally, it was observed that the $\delta^{98}\text{Mo}$ values preserved in the top of the iron formation ($\sim 1\%$) under the observed conditions indicate that the open ocean Mo isotopic composition was most likely in the vicinity of 1.8% , which is much higher than had been suggested in recent literature. This shows that the Neoproterozoic ocean was more oxygenated than previously assumed, which is in agreement with the conclusions from Chapter 2.

Whereas Chapter 2 addressed the depositional controls on the Rapitan iron formation overall, major questions regarding the distribution and thickness of the iron formation across the Mackenzie Mountains, as well as variations in the character of the iron formation, are answered in Chapter 4. Sedimentological and REE+Y data show that the most distal parts of basins, which were mostly protected from significant siliciclastic input during iron formation accumulation, contain the thickest iron formation. Furthermore, coarse clastic sediment underlying the iron formation in areas where it is thickest indicates that these basins were steep-margined, whereas thick units of mudstone and siltstone occur in areas where the iron formation is thin or absent. Based on iron formation thickness, as well as the thickness of the Sayunei and Shezal Formations, the Rapitan basin as a whole was subdivided into three different types of basins, based on the presence or absence of iron formation, the presence or absence of the underlying Coates Lake Group, and the relative thickness of iron formation. Changes in the type of basin, as well as inflection points within these types of basin correspond to the inferred position of proposed crustal-scale faults that dictated the depth and geography of the developing rift basin. Furthermore, a re-evaluated tectonostratigraphic context for the Sayunei Formation and iron formation helps resolve the disputed stratigraphy in the Snake River basin by demonstrating that the Sayunei Formation has both coarse and fine-grained lithofacies occurring in different areas.

These three chapters together create a geotectonic and geochemical regime for the deposition of the Rapitan iron formation. This regime can be summarized thusly:

- 1) Early stage continental rift basin with marine incursion.
- 2) Young, deep sub-basins with partial restriction at depth from the open ocean and limited post-rift sediment infill to allow for
- 3) The development of a biogenically-induced ferruginous basin under glacial ice cover
- 4) Limited sulfidic conditions in the water column following ice withdrawal and strong primary productivity
- 5) An oxygenated open-marine system, potentially with slightly more expansive near-coastal or mid-depth euxinia than the modern ocean.

Sedimentological descriptions, as well as the available (albeit limited) geochemical dataset for other Neoproterozoic iron formations indicate that this lithology is very similar in different localities worldwide. Consequently, the geotectonic and geochemical regime described above may be applicable to other examples. This could potentially aid in improved understanding of the Neoproterozoic surficial environment, the “snowball Earth” glaciations, and improved exploration models for Neoproterozoic iron deposits.

5.1 Unanswered questions and suggestions for future work

The most unusual element of Neoproterozoic iron formations (besides their age), is their unusual texture. A significant proportion of the jasper in the Rapitan iron formation is in the form of nodules, as opposed to laterally continuous beds. The nodules are rounded to elongate, but are predominantly lenticular, and are especially common in the thickest and most hematite-rich iron formation occurrences, such as Iron Creek. Sampling in this dissertation was focussed on the jasper bands, as opposed to the nodules, for several reasons: preliminary LA-ICP-MS analysis of the nodules showed that they have a complex chemical zonation, which does not always coincide with the visible zonation in thin section and hand specimen. Furthermore, some chemical

zonation was found to be discordant to nodule zonation, appearing as relict bedding through LA-ICP-MS geochemical mapping. This complexity is in sharp contrast with the chemical homogeneity documented in jasper bands using the same technique. Consequently, as outlined in the methods for Chapter 2, the nodules were not subjected to further analysis. As a result, at this stage, all that is known about the nodules' origin is that they formed early and sufficiently close to the sediment-seawater interface to be disturbed by dropstones (Fig. 3.2A), and that subtle bedding relationships suggest some may have formed on the seafloor, as opposed to below it (Fig. 3.2B). Some nodules are perfectly spherical, however, and are probably of a later, post-compaction diagenetic origin. A more in-depth petrographic and *in situ* geochemical investigation would help to explain the origins of these nodules, and determine their implications for the depositional model presented here.

Another question raised in the course of completing this dissertation is the aqueous redox behavior of tungsten (W). In chapter 2 it is discussed that W behaves similarly to Mo in microbiological systems (Kletzin and Adams, 1996), and under oxic marine conditions, but lacks an affinity for forming thiotungstate under sulfidic conditions, which is distinctly unlike Mo, which readily forms thiomolybdate when sufficient H₂S is present (Arnórsson and Óskarsson, 2007). In this respect, W is more like V, another redox-sensitive transition metal with similar behavior under oxic conditions to W and Mo (Johannesson et al., 2000). Tungsten enrichment in samples from the Rapitan iron formation appears at similar stratigraphic horizons as Mo and U, and it is suggested that its redox behavior may be transitional between the two (similar to that of V). Unfortunately, very little work has been done on the aqueous redox behavior of W, and it has not been developed as a possible trace element redox proxy. The observations presented here, however, suggest that research into this behavior could be useful. It needs to be established at what redox level is W removed from the water column, and by what mechanism does the tungstate compound change in a way that promotes adsorption onto other material, such as organic carbon, Mn oxides, or iron oxy-hydroxides, or does it get fixed as U does, by transfer across the sediment-seawater interface? Developing the practical use of W as a marine redox proxy would require a combination of experimental and empirical studies of both modern and ancient redox systems, which was well beyond the scope of this dissertation.

5.2 References

- Arnórsson, S. and Óskarsson, N., 2007. Molybdenum and tungsten in volcanic rocks and in surface and <100°C ground waters in Iceland. *Geochimica et Cosmochimica Acta*, 71: 284-304.
- Johannesson, K.H., Lyons, W.B., Graham, E.Y. and Welch, K.A., 2000. Oxyanion concentrations in eastern Sierra Nevada Rivers- 3. Boron, molybdenum, vanadium, and tungsten. *Aquatic Geochemistry*, 6: 19-46.
- Kletzin, A. and Adams, M.W.W., 1996. Tungsten in biological systems. *FEMS Microbiology Reviews*, 18: 5-63.

Appendix A: Lithofacies and lithostratigraphic correlation potential of the Rapitan iron formation, Snake River area (NTS 106F), Yukon

A.1 Abstract

The Neoproterozoic Rapitan iron formation in the Mackenzie Mountains of Yukon and NWT is one of the largest iron deposits in North America. The Rapitan Group can be traced along strike for several hundred kilometres, but the thickest and most extensive part of this unit is located on the border between NWT and Yukon in NTS 106F. Several stratigraphic sections in the areas of Discovery and Iron creeks were measured as part of a larger effort to understand basin architecture marine redox history during deposition of the Rapitan Group, with special emphasis on attributes of the thick interval of iron formation. The iron formation contains diverse textures including a wide variety of jasper nodules and beds. Due to the variable presence of these diverse textures, long-distance correlation of iron formation correlation is challenging. Minor copper mineralization of probable post-depositional origin was found in local float at Discovery Creek and in situ at Iron Creek.

A.2 Introduction

The Rapitan iron formation of the Mackenzie and Wernecke Mountains (NWT and YT) is the archetype of Neoproterozoic ‘Rapitan-type’ iron formations, and was deposited in a dynamic early rift setting. Although this iron formation has been a major component in models for the surficial and oceanic evolution of the Precambrian Earth, and despite several excellent studies in the 1980s and early 1990s, it remains relatively poorly understood. This paper reports on one component of a larger study attempt to resolve the stratigraphy, geochemistry, and basin

architecture of the Rapitan iron formation in NWT and YT, in an effort to explain its role in the geochemical evolution of Earth's surface environments and the tectonic history of the northern Canadian Cordillera.

One of the more controversial questions about the Rapitan Group are the disputed temporal relationships among the major lithostratigraphic units exposed in different areas along its more than 200 hundred kilometres of strike length. Although several regional correlation schemes have been proposed, no true consensus has emerged regarding the temporal relationships among the depositional units in the two main Rapitan basins (Snake River and Redstone-Keele-Mountain Rivers). The ability to correlate at a broad, regional scale (hundreds of kms), as well as at a comparatively local scale (kms to tens of kms) is highly desirable, because it would enable predictions about the possible presence and composition of Rapitan strata in the subsurface, permit the tracing of particularly economic units (iron, and to a lesser extent, copper), and provide marker beds that can provide the basis for interpretations regarding basin evolution. This paper provides detailed descriptions of stratigraphic sections of this iron formation in Yukon, assesses the potential for local-scale correlation within the Snake River basin, offers a preliminary solution to long-standing problems in regional stratigraphic correlation of the Rapitan Group, and discusses the implications of minor copper mineralization occurrences in the area.

A.3 Previous Work

The Neoproterozoic Rapitan iron formation in the Snake River area, Yukon, was the subject of extensive work in past decades. Iron formation was first identified in the Snake River area during the Klondike gold rush (Keele 1906). Associated diamictite was first interpreted as glaciogenic by Ziegler (1959). Extensive exploration for iron ore at the Crest deposit was undertaken in the 1960s, and up to 18.6 billion tonnes of iron reserves were estimated, including 5.6 billion tonnes at 47.2% iron along Iron Creek in Yukon (Stuart 1963). Extensive research into the stratigraphy and sedimentology of the Rapitan Group was conducted through the 1970s, with

focus on assessing basin architecture and glacial sedimentology (e.g., Eisbacher 1976; 1978; 1981a; 1981b; Young 1976); this research resulted in designation of the Mount Berg, Sayunei, and Shezal formations (Green and Godwin 1963; Upitis 1966; Eisbacher, 1981). Further study of the stratigraphy, geochemistry, and depositional setting followed, leading to the suggestion that hydrothermal and glacial processes combined to form the iron deposit (Yeo 1981; 1984; 1986). This was complemented by an intensive geochemical study of drill-core archived from earlier exploration (Klein and Beukes 1993). The latter authors produced an elegant depositional model for the iron formation, in which a low-oxygen, subglacial water mass became enriched in ferrous iron (Fe^{2+}) and was subsequently oxidized upon glacial retreat and reventilation of the ocean. At the time, this was a plausible depositional model in the context of the early iterations of the “snowball” Earth model (e.g. Kirschvink 1992), but since then new developments in the understanding of basin analysis, redox geochemistry (e.g. Tribovillard et al. 2006), and Proterozoic oceanic chemistry (e.g., Lyons et al. 2009) have necessitated a renewed stratigraphic and geochemical examination of the Rapitan iron formation.

The Crest deposit of the Rapitan iron formation straddles the border between Yukon and Northwest Territories (NWT) in NTS map sheet 106F, with the bulk of the thick iron formation in the vicinity of Iron Creek, a tributary of the Snake River. Another thick exposure of the iron formation is present along the Cranswick River, and thinner exposures are present between these main localities, such as along Discovery Creek. This paper presents selected stratigraphic sections measured along Discovery Creek and Iron Creek (Fig. 1).

A.4 Rapitan iron formation stratigraphy

A.4.1 Discovery Creek

Stratigraphic section Discovery Creek 2 (DC-2 on Fig. 1) was measured near the headwaters of Discovery Creek, Yukon. This section includes the entire exposure of the Rapitan Group at this location, with a measured thickness of ~430 m. At this locality, the Rapitan Group overlies carbonate rocks of the Little Dal Group, and is unconformably overlain by the Cambro-

Ordovician Franklin Mountain Formation. This is the thickest exposure of the Rapitan Group in the Discovery Creek area; other sections to the northwest record pronounced thinning down to zero thickness.

The lowermost 340 m of the section are siliciclastic rocks that have been interpreted to be glaciogenic in origin (Fig.2; Eisbacher 1978; Yeo 1981). The dominant rock types in this section are dark red to purple, clast-poor to clast-rich intermediate diamictites (classification scheme of Moncrieff 1989) (Fig. 3A), with a broad spectrum of clast sizes (pebble to boulder) and weathering characteristics. Previous authors (e.g., Yeo 1981) have interpreted the entirety of the Rapitan Group in the Snake River to belong to the Shezal formation, based on the sedimentological character and weathering patterns of the diamictites in the region. Diamictites of the Shezal Formation are typically massive, clast-poor to clast-rich, intermediate pebble to boulder diamictites with characteristic fissile to platy weathering that has been referred to by the informal descriptive term “scaly” weathering, and is common in diamictites of the Discovery Creek area. The diamictites of this section are locally interbedded with matrix-supported and rare framework-supported conglomerate (Fig. 3B) and siltstone units, although in terms of overall character, each of these may be extremely clast-rich and clast-poor end-members of the diamictite spectrum, in that the clasts and/or matrix are nearly identical in all reported lithologies. The presence of dropstones in some of the siltstone units indicates that such rocks may be a variety of clast-poor diamictite, but at a minimum demonstrates their glacial association.

Iron formation is present at three distinct levels in the uppermost 67 m of the Discovery Creek section, representing about 16.5 m of this interval. The two lower iron formation units are thin (0.1 to 1 m thick). They are characterized by dark grey to blue, massive hematite bands with bright red-orange to wine-red jasper (Fig. 3C). Jasper layers are both bedded and nodular; adjacent jasper layers are commonly distinguished only by colour. The nodular jasper is typically lenticular and predominantly bright red (Fig. 3D). The lenticular shape, coupled with the deformation of hematite beds around the nodules, suggests that the nodules are early diagenetic, pre-compactional features that developed in the upper metre or so of the sedimentary column. The two lower iron formation units form resistantly weathering prominences.

As much as 15.3 m of the upper iron formation is exposed in a 20.2 m-thick unit. Unlike the lower, (thinner) iron formation units, this unit has a greater range of textures and colours. Jasper beds are bright red-orange to wine-red, with shades of orange that are not present in lower units. Nodule shape in this unit is also more varied: subspherical nodules indicate minimal compaction, whereas lenticular and ellipsoidal nodules indicate considerable bedding-parallel flattening. The more spherical nodules do not cross-cut bedding in the hematite, and so are probably of very early diagenetic origin and formed pre-compaction, much like the more flattened (lensoidal) nodules. There is no apparent relationship between stratigraphic position and the degree of nodule compaction, and so the cause for variation in nodule shape remains unknown. Contacts between jasper and hematite beds are commonly planar, although irregular contacts are also present. Some jasper beds pinch and swell; these are typically associated with units that have wavy bed contacts. This iron-formation-bearing interval forms the uppermost exposure of the Rapitan Group in the Discovery Creek area and is overlain by a 1 metre-thick covered interval below the first exposure of the overlying Franklin Mountain Formation. The contact is not exposed, but is inferred to be erosional, because the entire Rapitan Group pinches out beneath the Franklin Mountain Formation less than 10 km to the northwest and because of the presence of iron formation clasts in a white quartz arenite boulder, necessarily from a younger formation, in the streambed of Discovery Creek. Unfortunately, rocks such as these were not documented in outcrop.

The most unusual finding in this field study was the discovery of two occurrences of copper mineralization in the Rapitan Group section at Discovery Creek. Copper has not been previously reported in the Rapitan Group in this area, but it is associated with the underlying Coates Lake Group in the NWT (e.g., Jefferson and Ruelle, 1987). Both copper occurrences at DC-2 are in float, but are interpreted to be approximately *in situ* due to the knife-edge geometry of the ridge on which they were found, which would prevent samples that had been transported more than a few metres from remaining on the ridge crest. The lower copper occurrence is in a diamictite unit at 209.3 m, although its exact original stratigraphic position is uncertain. The occurrence consists of malachite-stained pebbles that have weathered out completely from the host rock. The upper occurrence was in a boulder of iron formation associated with the upper iron

formation interval and consists of a ~2 cm diameter piece of malachite-coated chalcopyrite within a ~5 cm diameter vug in the iron formation.

A.4.2 Iron Creek

The entire thickness of the Rapitan iron formation is not exposed in any one location in the Iron Creek area owing to abundant vegetation, colluvial cover, and the pervasive coating of the rocks by a modern calcite and gypsum leachate. Four stratigraphic sections were measured in order to generate a composite section covering the entire thickness of the unit. Two of these sections, covering the majority of the thickness of the iron formation, are described below.

A.4.2.1 Iron Creek 1 (IC-1)

Iron Creek section 1 (IC-1) covers the greatest thickness of the Rapitan iron formation in the area (Fig. 1). Although several intervals are covered, including the base of the iron formation, this is the only section that spans the entire thickness of the Rapitan iron formation and includes both underlying and overlying strata (Fig. 4). The base of the measured section is in a thick package of massive, matrix-supported cobble to boulder diamictite, which is underlain by a covered interval of unknown thickness. This diamictite is dark red to purple, with clasts consisting predominantly of limestone and dolostone (Fig. 5A). The lower part of the unit is well indurated and cliff-forming, but higher units are increasingly recessive. The exposed thickness of the unit is 36.5 m, although it may be thicker because it is overlain by a 29 m-thick covered interval, above which is the lowermost exposure of iron formation.

Iron formation at this location includes a wide variety of colours and textures. Bedded jasper-hematite units are thinly to thickly laminated (Fig. 5B). Colours are similar to those at Discovery Creek, with the addition of thin bands of pink jasper. Jasper is predominantly nodular (2 mm - 5 cm in diameter). The nodules are common in both hematite, and to a lesser degree, jasper bands, and locally form the bulk of the host jasper band. The largest nodules commonly

are cored by a variety of materials including carbonate clasts, hematite particles, and rip-up clasts of jasper beds (Fig. 5C, D), which results in more complicated nodule shapes that range from tabular to spheroidal to irregular. Some irregular nodules contain multiple nuclei and are interpreted to have resulted from intergrowth of two or more nodules. Some irregular nodules exhibit continuous growth zones around a single nucleus, suggesting irregular, uneven growth patterns. In a layer at 158 m, nodules consist of white chert in a jasper band; this is the only known example of white nodules in the Rapitan Group, although tan chert nodules have been reported from the vicinity of Cranswick River, NWT (Baldwin et al. *in press*; Fig. 4F). Bedded jasper exhibits a wide range of characteristics. Layer thicknesses vary from 1 mm to several centimetres (thick laminated to thin bedded). Faint micro-laminae are locally evident in some of the thicker jasper beds. Contorted bedding, load structures, and wavy bedding are all common. In rare cases, hematite lenses are present in the thickest jasper bands, mimicking the relationship of the jasper nodules that are so common in the hematite beds.

The iron formation at section IC-1 is interbedded with intervals of siltstone and diamictite. Siltstone intervals are typically less than 1 m thick, whereas diamictite units are up to 5 m thick. These siliciclastic units are most common between 75 and ~100 m, but they may make up a significant proportion of the recessively weathering, covered intervals of the section (diamictite exposures are commonly immediately overlain by covered or vegetated intervals). At the top of the iron formation, two thin units of granular iron formation (GIF) are present (Fig. 5F). Previously referred to as 'iron formation arenite' by Klein and Beukes (1993), granular iron formation consists of sand-sized particles of chert and hematite that are typically peloidal or oolitic (Clout and Simonson 2005). This type of iron formation is common in late Palaeoproterozoic 'Superior-type' iron formations, such as the Gunflint (Lake Superior region) or Sokomon (Labrador Trough) iron formations. Granular iron formation is considered to indicate iron formation deposition above storm wave-base, where shoaling can occur, allowing the chemogenic material to form granules. The iron formation is overlain by a thick succession of interbedded pebble- to cobble-bearing diamictite and maroon siltstone, the lower 17.4 m of which was measured in IC-1. The presence of the GIF in direct contact with the transition to clastic sediment suggests that in this area, iron formation deposition was terminated by a loss of

accommodation space, which initially caused shoaling of the iron formation in shallow water, but soon led to an influx of clastic sediment.

The GIF lithofacies at the top of IC-1 is also present near the tops of several other measured stratigraphic sections in the Iron Creek area, specifically IC-2 and IC-4, but is not exposed in section IC-3 (described below), probably due to colluvial and vegetation cover. The GIF is overlain by an unmeasured thickness of interbedded purple siltstone and diamictite, with a minimum thickness of 40 m, based on other sections measured in the area (IC-2).

A.4.2.2 Iron Creek 3 (IC-3)

Iron Creek section 3 (IC-3) was selected because the contact of the iron formation with underlying diamictite is exposed, even though exposure of the iron formation itself is limited (Figs. 1, 6). The base of the iron formation lies conformably on the underlying red pebble- and cobble-bearing diamictite that is common in the area, which has been attributed to the Shezal Formation despite its sharp differences in both colour and texture from classic Shezal Formation to the southeast in NWT (Eisbacher 1981). The diamictite here is roughly 100 m thick but was not measured. The lowermost iron formation unit is 5.4 m thick, and includes alternating layers of bedded iron formation (Fig. 7A), nodular iron formation, and a thin interval of what is referred to here as ‘hematitic mudstone’. The latter lithofacies is a thinly bedded, very fine-grained hematitic mudstone lacking jasper and was referred to as ‘massive hematite’ in other publications (e.g., Klein and Beukes 1993). The top unit of this basal iron formation contains minor copper mineralization: a vug containing copper minerals oxidized to malachite. This mineralization is significant because unlike other copper occurrences in the area (e.g., the upper mineralization at DC-2), it was documented in outcrop.

The basal iron formation at IC-3 is overlain by ~7 m of recessively weathering diamictite that is texturally identical to the underlying siliciclastic rocks except for its weathering profile. This is succeeded by a 14 m covered interval. This covered interval is overlain by 83 m of iron formation with less than 50% exposure in the upper 50 m. The iron formation is in places

interbedded with siliciclastic rocks, including sandstone, siltstone, conglomerate and diamictite. Iron formation that is under or overlain by these clastic intervals, particularly diamictite, commonly shows evidence of slumping and reworking marked by intense folding and convolution of jasper beds. In section IC-3, the unit is dominated by nodular iron formation, with a smaller proportion of bedded iron formation. Nodule and jasper bands exhibit a similar range of colour and morphology to beds in section IC-1. Jasper nodules are lenticular to highly spheroidal (Fig. 7C). Rare hematite nodules in jasper bands are a textural reversal from the norm but have been documented at Cranswick River, NWT (Figs. 1 and 7D). The section was terminated at this point due to very poor exposure above the top of the measured iron formation, as well as an apparent shift towards siltstone and diamictite based on the scattered boulders present.

Despite their similarity and relatively close proximity (~6 km apart), correlation of individual iron formation units between sections IC-1 and IC-3 using jasper textures does not appear to be possible. This problem is compounded by the absence from section IC-3 of any obvious marker units documented in other sections, such as the GIF unit; the absence of the GIF unit is probably a function of incomplete exposure at the top of the section. This limitation notwithstanding, it appears that a high degree of lateral variability existed at the time of deposition, a feature that has also been documented by the author in sections measured in the NWT.

A.5 Discussion

A.5.1 Correlation

Long-distance correlation between different regions where the Rapitan iron formation is exposed in NTS sheet 106F appears to be impossible. Although ostensibly coeval iron formation in other regions of the world commonly include laterally persistent marker beds, no such layers have been documented in the Rapitan iron formation. Although the iron formation overall is a geographically extensive unit deposited during a single, limited time interval in the Snake River area, its internal stratigraphy and relationships with sub- and superjacent strata demonstrate

considerable local variability, making more detailed correlation difficult. The absence of the upper diamictite at Discovery Creek may simply be a result of erosion, as indicated by the rapid pinch-out of the Rapitan Group to the northwest. This erosion occurred post-lithification, as indicated by the presence of iron formation clasts in conglomerate boulders with white sandstone matrix observed in the creek bed, but before the deposition of the Franklin Mountain Formation during the Late Cambrian to Early Ordovician, although these boulders themselves may alternatively be the product of post-Franklin Mountain Formation erosion. Furthermore, this erosion makes it impossible to determine whether or how much of the upper Windermere Supergroup (e.g. Hay Creek Group and the informal 'upper group'; Yeo et al., 1978; Aitken 1989) was originally deposited in this area prior to erosion.

It is possible that the thinner exposure of iron formation at Discovery Creek than Iron Creek is in part a primary feature. Based on the sections measured at Iron Creek and data reported at Cranswick River, NWT (Baldwin et al., *in press*) lateral facies variation is common in the Rapitan Group. For example, 30 metres of iron formation pinches out to no more than 3 metres over a strike-length of less than a kilometre along the Cranswick River. This suggests that small-scale facies variations may have existed in the Snake River basin, complicating stratigraphic correlation across large distances. At a very local scale, this phenomenon is expressed most obviously as lateral discontinuity of distinctive individual units in the iron formation. At a larger scale, the phenomenon is expressed as localized to regional variations in the sedimentological character of associated clastic rocks, which show considerable variability in the relative proportions of sand, mud, and coarse clasts (pebbles, cobbles, and boulders) at apparently similar stratigraphic levels over very short distances (<1 km). Apparent variations in the iron content (and therefore colour) of the same clastic rocks are also visible over relatively short distances. Such variability in glacioclastic rocks is not uncommon, because local topography, glaciology, hydrodynamics, and sediment sources can profoundly influence their sedimentological character. This does not, however, imply that deposition of the iron formation at Discovery Creek, Iron Creek, and Cranswick River was asynchronous, but merely that the textural details of each area's strata may be too different to permit definitive correlations. As discussed in the previous section, this difficulty in correlation is exacerbated by the lack of any truly distinctive marker horizons across all measured sections in the region (e.g., GIF, a

distinctive conglomerate bed, or an easily identifiable, texturally distinct nodule layer). Each of these features has enabled correlation within geographically limited areas, but none has extended across all three localities (Discovery Creek, Iron Creek, Cranswick River) nor conclusively across any two.

The difficulty in local to regional correlation is best interpreted as a symptom of the dynamic tectonic environment in which the Rapitan Group was deposited. The preponderance of evidence suggests that the Rapitan Group was deposited in a relatively young rift basin (Yeo, 1981), probably related to the rifting of Rodinia (Young 1992), with ample evidence for active tectonic subsidence during deposition (Helmstaedt et al., 1979). An active rift graben system would have provided considerable paleobathymetric variability, featuring bathymetric highs or 'sills', as well as highly compartmentalized sub-basins. Consequently, in addition to the larger regional Rapitan sub-basins (Snake River basin and Redstone-Keele-Mountain River basin), each of these sub-basins would have been internally subdivided and would therefore have possessed extensive sedimentological and stratigraphic variation over short distances, as is recorded in both the clastic and hydrogenous (iron formation) records. This has already been shown to be a major control on the overall distribution and thickness of iron formation across the Mackenzie Mountains (Baldwin et al. 2011), and may have provided considerable local control on the stratigraphy of iron formation in any given locality. Consequently, only the top and base of the iron formation are liable to be the only consistently correlateable stratigraphic horizons, both sedimentologically and temporally, and even these probably varied geographically.

A.5.2 Copper mineralization

Although copper mineralization has been described in the Rapitan Group (e.g., Helmstaedt et al., 1979, 1981; Aitken et al., 1981), it has not previously been reported in the Snake River area, instead being restricted to isolated showings in the Redstone-Keele-Mountain River area (e.g., Nite and June showings). Previous workers have suggested several mechanisms for copper paragenesis, including the remobilization of copper from the Coates Lake Group,

which underlies the Rapitan Group in the Redstone-Keele-Mountain River area (Baldwin et al, in press, Fig. 2), or through the resedimentation of carbonate and siltstone clasts of similar origin (Helmstaedt et al, 1979). Neither of these explanations is especially plausible for the minor copper mineralization here reported in the Snake River area, however, because the Coates Lake Group is not present in this area, making any copper unlikely to be derived by either remobilisation or resedimentation from such a source. However, the occurrence of minor copper mineralization at numerous stratigraphic levels in the Rapitan Group, across its geographic extent (Baldwin, unpublished data 2010), together with field relationships, suggest that simple remobilization of Coates Lake Group copper is less probable, and that Rapitan-hosted copper may be paragenetically related to the more genetically complex deposits in the Coates Lake Group (J.E. Milton, pers. comm. 2011).

The minor copper mineralization of the Snake River area probably had an authigenic, post-depositional origin similar to that found to the southeast, but the copper source and fluid conduits were undoubtedly distinct. This relates back to the issue of overall basin architecture, in that the Snake River area was a separate sub-basin from areas to the southeast. Consequently, it is probable that the fluids responsible for precipitating copper minerals did not pass through the same source rocks as those responsible for the Coates Lake deposit, nor its related deposits (e.g., Nite, June) hosted in the Rapitan Group. The most probable explanation for the minor copper mineralization reported here is through precipitation in chemical traps formed at the interface between carbonate dropstones and the surrounding iron formation or diamictite matrix, while the original copper source remains uncertain. A dropstone weathers out of the rock leaving an open vug, may leave behind a crust of copper minerals that once shrouded the clast inside the iron formation, as is seen in sections DC2 and IC3.

A.5.3 Comparison with previous work

Several previous authors have made significant efforts to resolve the controversial stratigraphy of the Rapitan Group in the Snake River area. Yeo (1981; 1984), measured

numerous stratigraphic sections in the region in an effort to resolve both the map distribution and stratigraphy of the entire Rapitan Group, whereas Klein and Beukes (1993) reported details of diamond drill core logs for drill holes from both the Iron Creek and Cranswick River (NWT) areas. Comparing the stratigraphy and sedimentology of the sections documented in this paper measured with those provided in earlier publications is difficult. The details of original stratigraphic sections from some studies that favoured generalised stratigraphic composites remain unavailable (e.g. Yeo, 1981), which inhibits the direct comparison of the originally observed stratigraphy and sedimentology to other work, such as the detailed work on core by Klein and Beukes (1993). The present paper describes many of iron formation units as hybrids of bedded iron formation and nodular iron formation, which is distinct from the practice in both previous studies, which leaned toward identification of lithofacies as either one end-member or the other, which resulted in fewer and less-variable units in the iron formation, and complicated efforts to compare the stratigraphy. The best study available for direct comparison was conducted using archived drill core, with a minimal field component (Klein and Beukes, 1993). Although this core-based study had the advantage of fresh, unweathered surfaces, it lacked the small-scale lateral spatial data available in detailed field studies that is necessary to characterize the well-developed lateral variability that is expressed on a scale of metres to hundreds of metres throughout the region, despite well-reported well thicknesses and approximate drill collar locations. As a consequence of stratigraphic simplification, the core-based study inferred direct correlations between the Iron Creek area and the Cranswick River area in the NWT (Klein and Beukes, 1993, fig. 7). The proposed correlations were based exclusively on the composition and vertical distribution of siliciclastic intervals in the iron formation, which were used as regional marker units. The present study shows that such units are probably not meaningful markers, based on major differences in sediment colour and matrix composition, among other features. Based on the observations reported here and by Baldwin et al. (*in press*), most sedimentary units within and associated with the iron formation are not laterally traceable due to dramatic lateral facies changes related to the tectonically influenced paleobathymetric variability of the rift basin at the time of deposition. Previous authors may have been in error in attempting to correlate across the basin based on anything more detailed than the (probable) time-marker horizons of the top and bottom of the iron formation.

A.6 Future Work

Future work on the Rapitan iron formation will focus on the geochemistry of the measured sections and the possible use of chemostratigraphy for regional correlation. A pilot study on samples from Cranswick River (NWT) is currently in press (Baldwin et al. *in press*). Work to date has focused on developing a working model for basin configuration and characterizing the redox stratification of the Snake River basin, using rare earth elements and redox-sensitive metals such as molybdenum and uranium, and on implications for the depositional processes and iron source for the Rapitan iron formation. The principles established in the pilot study will be applied to samples collected elsewhere in the Rapitan iron formation, including the exposures in Yukon. It is possible that the chemostratigraphy of Mo and U may help resolve the sedimentological limitations on long-distance correlation, because water-mass chemistry may have been significantly less susceptible to lateral variability than was physical sedimentology; alternatively, each sub-basin may have been influenced by a chemically distinct water mass. If this approach fails to permit high-quality stratigraphic correlation, it will probably demonstrate instead that basin morphology was characterized by chemically and sedimentologically distinct sub-basins. Ongoing detrital U-Pb zircon studies on samples from across the belt may help provide further insight into basin architecture.

A.7 Acknowledgements

The subject matter of this paper is part of GJB's PhD research. Yukon Geological Survey and Northwest Territories Geoscience Office are gratefully acknowledged for their support of the field work. Further funding for this project was provided by a SEG student grant to GJB, and an NSERC Discovery Grant to ECT. Minor additional field support was provided by Aurora Geosciences. Joyia Chakungal and Venessa Bennet are thanked for their helpful comments in the

field. Tiffany Chevrier and Kirsti Medig are also thanked for their assistance in the field. Special thanks go out to Darrel G.F. Long for his helpful comments and critical review of the text.

A.8 Figures

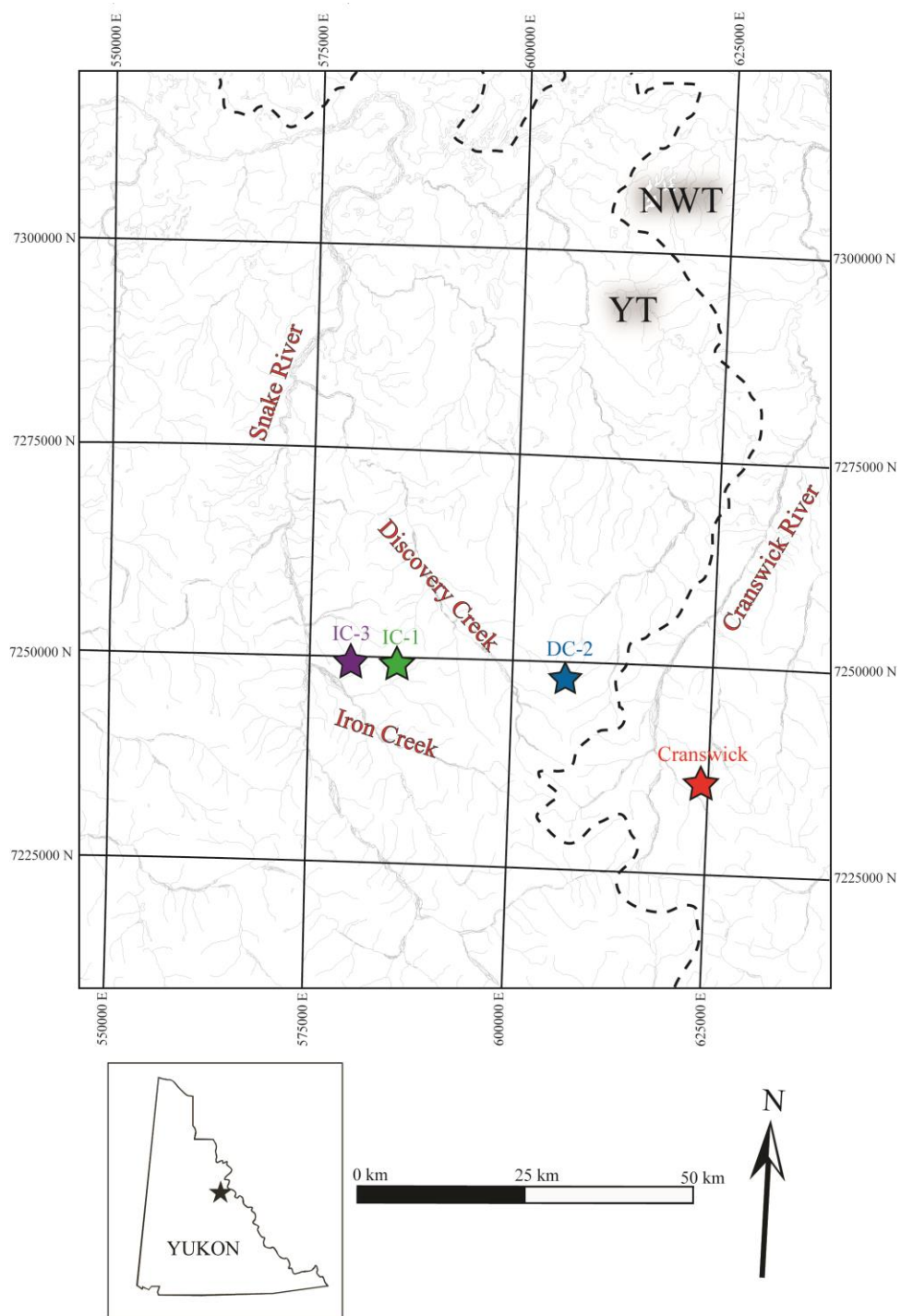


Figure A1: Study location map in NTS 106F. Section DC-2 is marked in blue, IC-1 in green, and IC-3 in purple. A location on the Cranswick River, NWT (mentioned in text) is marked in red. Major rivers and creeks in the area are also labelled.

Discovery Creek 2 (DC-2)

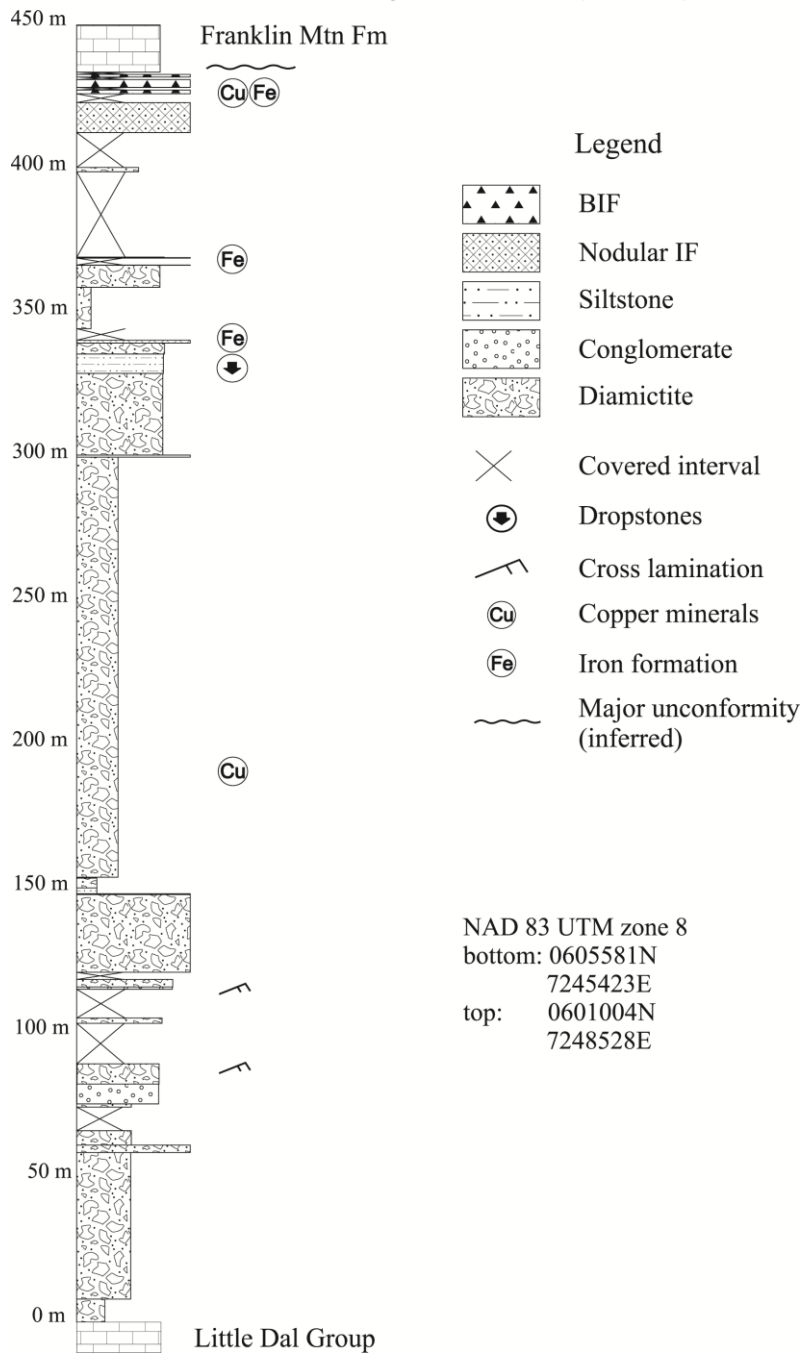


Figure A2: Stratigraphic column of Discovery Creek 2 section (DC-2). Box widths depict the relative weathering profile of natural exposures. Iron formation units are marked by circled Fe due to the very thin exposure of this lithofacies relative to the thickness of the measured section, causing them to appear as thin black bands on the section. Copper showings are marked with a circled Cu. Base of measured section is at the contact between the underlying Little Dal Group and the base of the Rapitan Group. Above the top of the section are unmeasured carbonates of the Franklin Mountain Formation.

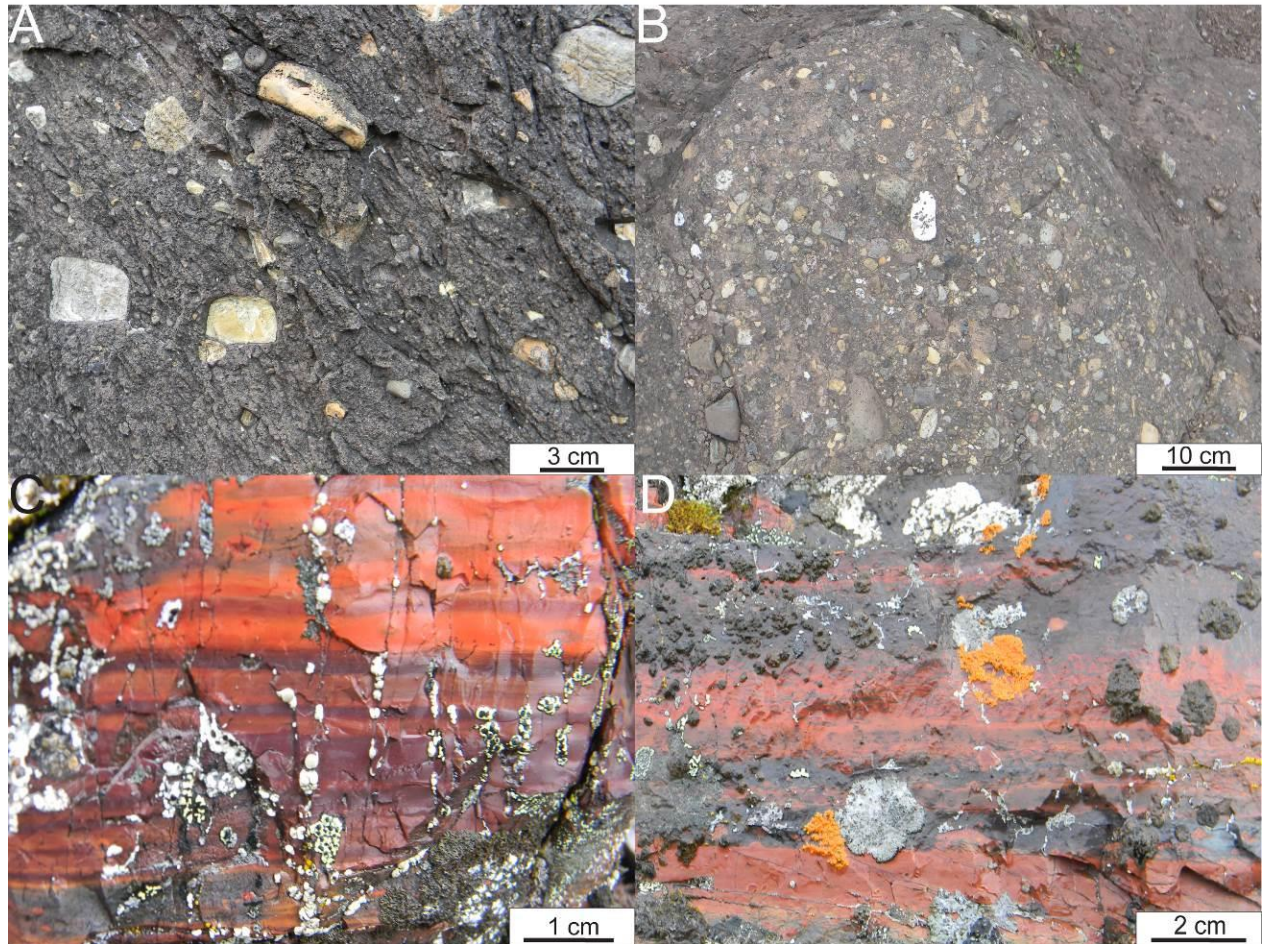


Figure A3: Photographs of typical lithofacies from section DC-2. (A) Pebble-bearing clast-poor intermediate diamictite dominates the lower part of the section. (B) Pebble conglomerate, the framework-supported end-member of the range of siliciclastic material (siltstone to conglomerate) present in this section. (C) Bedded iron formation exhibiting interbedded jasper of different colours. This style of bedding was suggested to be of diagenetic origin by Klein and Beukes (1993). (D) Iron formation with both bedded and nodular types. Some jasper bands appear to be transitional between nodules and beds, a common texture throughout the region.

Iron Creek 1 (IC-1)

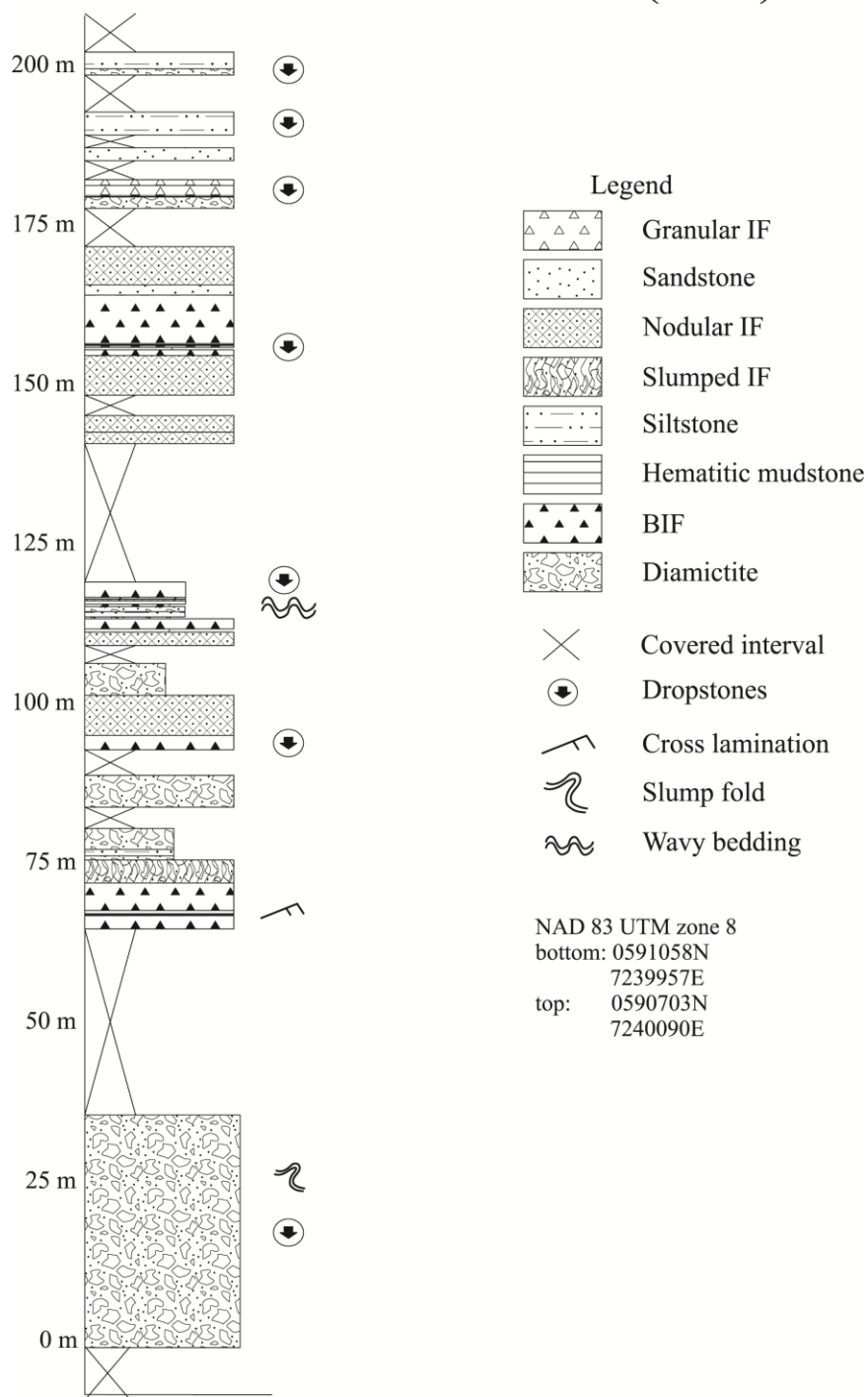


Figure A4: Stratigraphic column of Iron Creek 1 section (IC-1). Box widths depict the relative weathering profile of natural exposures. The section base is the lowest exposed stratigraphic level at the location, and overlying the top of the section is minor outcrop of the same siltstone and diamictite exposed at the top of the section.

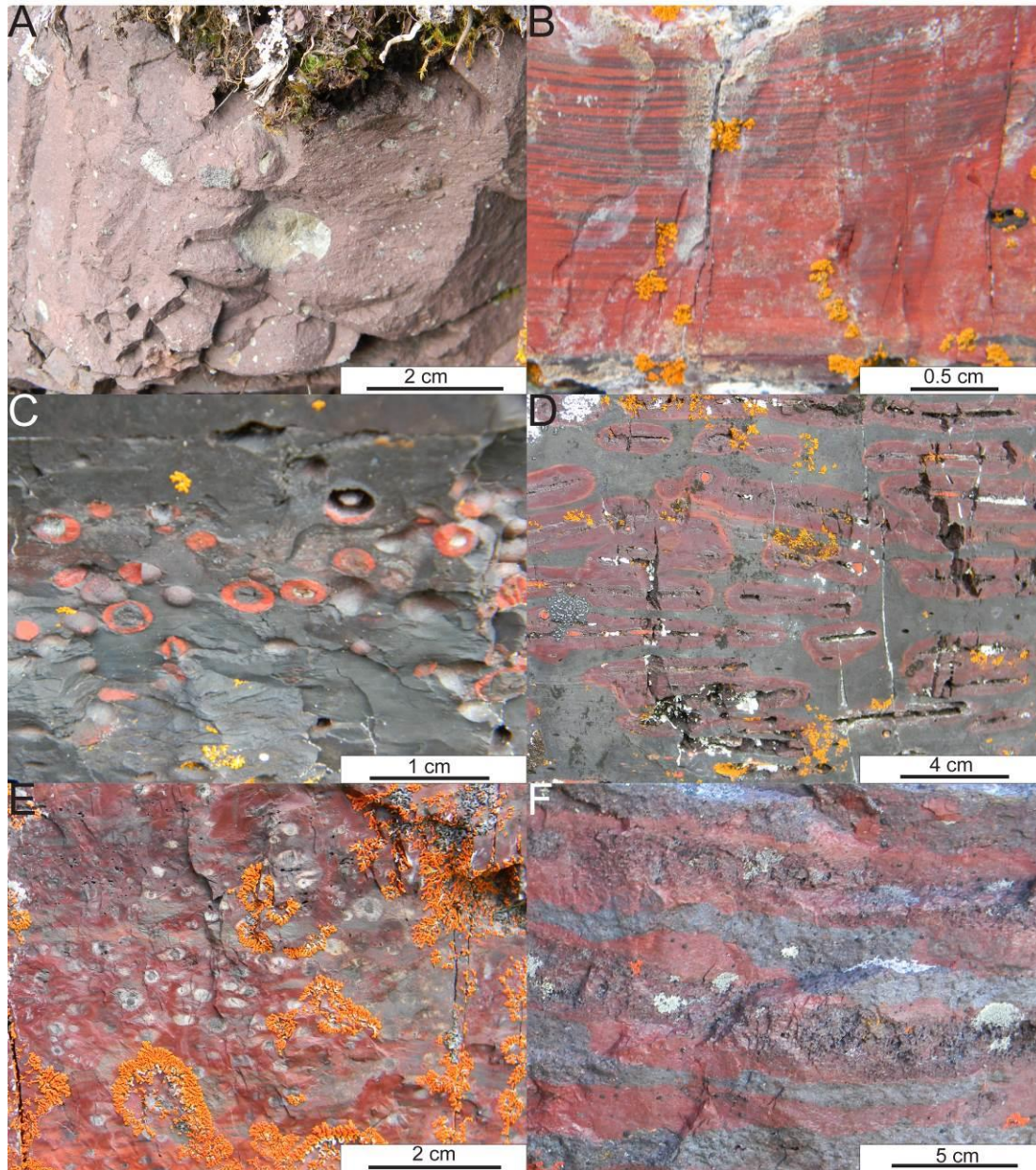


Figure A5: Photographs of typical and unusual lithofacies from section IC-1. (A) Non-stratified clast-poor intermediate diamictite from below the iron formation, at ~0 m. (B) Thinly bedded jasper and hematite iron formation. (C) Compound hematite-jasper nodules. (D) Oblate jasper nodules, with tabular hematite-jasper cores that may represent rip-up clasts of bedded iron formation. (E) White chert nodules are present only in this thin unit at ~158 m. (F) Granular iron formation (GIF), consisting of coarse sand-sized grains of jasper and hematite.

Iron Creek 3 (IC-3)

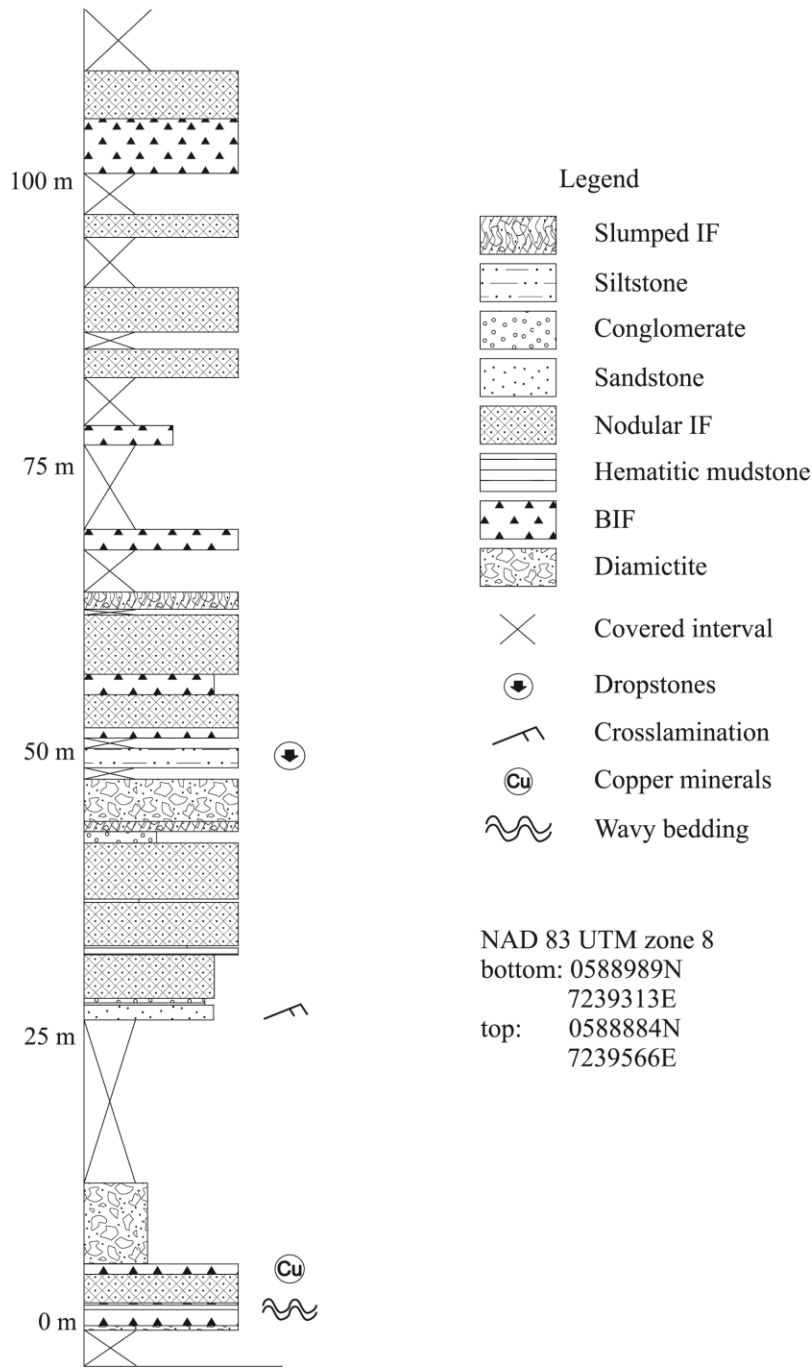


Figure A6: Stratigraphic column of Iron Creek section 3 (IC-3). Box widths depict the relative weathering profile of natural exposures.

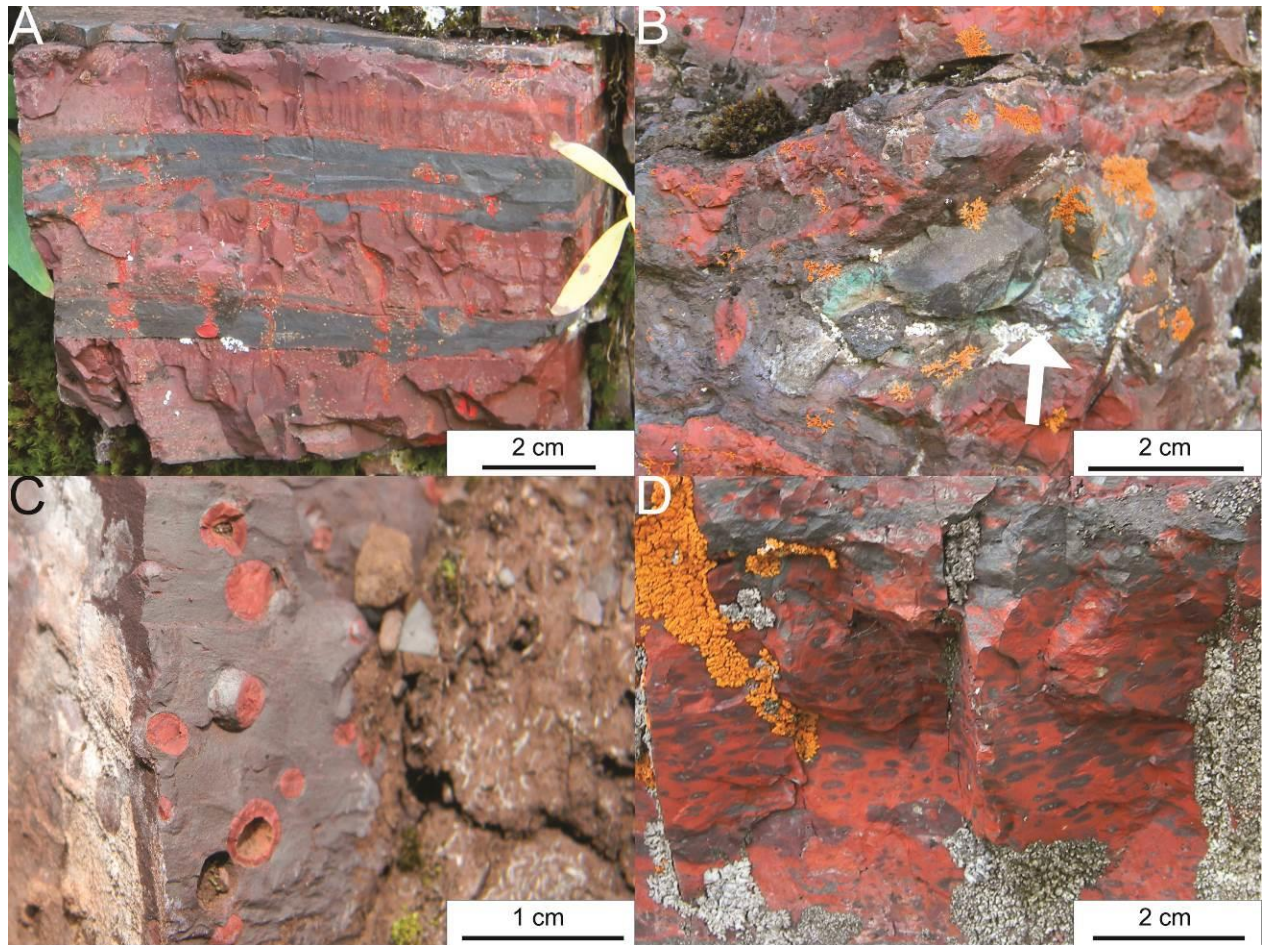


Figure A7: Photographs of typical lithofacies from section IC-3. (A) Interbedded jasper and hematite from just above the basal iron formation at ~5 m. (B) Copper mineralization, characterized by malachite (arrow). (C) Highly sphaeroidal nodules. (D) Hematite nodules in jasper (the reverse of the normal nodule-host rock compositional relationship).

A.9 References

- Aitken, J.D., Ruelle, J.C. and Cook, D.G. 1981. Copper mineralization near an intra-Rapitan unconformity, Nite copper prospect, Mackenzie Mountains, Northwest Territories, Canada: Discussion. *Canadian Journal of Earth Sciences*, 18, p. 410-413.
- Baldwin, G.J., Turner, E.C., and Kamber, B.S. 2011. Reevaluating the depositional model and iron source of the Rapitan iron formation. *in* 39th Annual Yellowknife Geoscience Forum Abstracts. Compiled by B.J. Fischer and D.M. Watson. Northwest Territories Geoscience Office, Yellowknife. pp. 20.
- Baldwin, G.J., Turner, E.C., and Kamber B.S. in press. A new depositional model for Neoproterozoic iron formation: Insights from the chemostratigraphy and basin configuration of the Rapitan iron formation. *Canadian Journal of Earth Sciences*. 2011.
- Clout, J.M.F. and Simonson, B.M. 2005. Precambrian Iron Formations and Iron Formation-Hosted Iron Ore Deposits. *Economic Geology 100th Anniversary Volume*, p. 643-680.
- Eisbacher, G.H. 1976. Proterozoic Rapitan Group and Related Rocks, Redstone River Area, District of Mackenzie. *Geological Survey of Canada Paper 76*, p. 117-125.
- Eisbacher, G.H. 1978. Re-definition and subdivision of the Rapitan Group, Mackenzie Mountains. *Geological Survey of Canada Paper 77*, p. 1-21.
- Eisbacher, G.H. 1981a. Sedimentary tectonics and glacial record in the Windermere Supergroup, Mackenzie Mountains, Northwestern Canada. *Geological Survey of Canada Paper 80*, p. 1-41.
- Eisbacher, G.H. 1981b. Late Precambrian tillites of the northern Yukon-Northwest Territories region, Canada. *In* Earth's pre-Pleistocene glacial record. *Edited by* M.J. Hambrey and W.B. Harland. Cambridge University Press, Cambridge. pp. 724-727.
- Green, L.H. and Godwin, C.I. 1963. Mineral Industry of Yukon Territory and southwestern District of Mackenzie, 1962. *Geological Survey of Canada Paper*, 63: 15-18.
- Helmstaedt, H., Eisbacher, G.H. and McGregor, J.A. 1979. Copper mineralization near an intra-Rapitan unconformity, Nite copper prospect, Mackenzie Mountains, Northwest Territories, Canada. *Canadian Journal of Earth Sciences*, 16, p. 50-59.

- Helmstaedt, H., Eisbacher, G.H. and McGregor, J.A. 1981. Copper mineralization near an intra-Rapitan unconformity, Nite copper prospect, Mackenzie Mountains, Northwest Territories, Canada: Reply. *Canadian Journal of Earth Sciences*, 18, p. 414-418.
- Jefferson, C.W. and Ruelle, J.C.L., 1987. The late Proterozoic Redstone copper belt. In *Mineral Deposits of the northern Cordillera*, edited by J.A. Morin. Canadian Institute of Mining and Metallurgy Special Vol. 37, p. 154-168
- Keele, J. 1906. Upper Stewart River region, Yukon. *Geological Survey of Canada Annual Report 1904*, vol. 16, p. 5-23.
- Kirschvink, J.L. 1992. Late Proterozoic low-latitude global glaciation: the Snowball Earth. *In The Proterozoic biosphere: A multidisciplinary study. Edited by J.W. Schopf and C. Klein.* Cambridge University Press, Cambridge. pp. 51-52.
- Klein, C. and Beukes, N.J. 1993. Sedimentology and Geochemistry of the Glaciogenic Late Proterozoic Rapitan Iron-Formation in Canada. *Economic Geology*, vol. 88, p. 542-565.
- Lyons, T.W., Anbar, A.D., Severmann, S., Scott, C. and Gill, B.C. 2009. Tracking euxinia in the ancient ocean: A multiproxy perspective and Proterozoic case study. *Annual Reviews in Earth and Planetary Science*, 37: 507-534.
- Moncrieff, A.C.M. 1989. Classification of poorly sorted sedimentary rocks. *Sedimentary Geology*, 65: 191-194.
- Stuart, R.A. 1963. Geology of the Snake River Iron deposit. DIAND Assessment Files, Yellowknife, NWT, p. 18.
- Tribouillard, N., Algeo, T.J., Lyons, T. and Riboulleau, A. 2006. Trace metals as paleoredox and paleoproductivity proxies: An update. *Chemical Geology*, 232: 12-32.
- Upitis, U. 1966. The Rapitan Group, southeastern Mackenzie Mountains, Northwest Territories. M.S. thesis, Department of Geological Sciences, McGill University, Montreal. 70 p.
- Yeo, G.M. 1981. The late Proterozoic Rapitan glaciation in the northern Cordillera. *In Proterozoic Basins of Canada. Edited by F.H.A. Campbell.* Geological Survey of Canada Paper 81-10, p. 25-46.
- Yeo, G.M. 1984. The Rapitan Group: Relevance to the global association of late Proterozoic glaciation and iron formation. Ph.D. thesis, Department of Geology, University of Western Ontario, London. 603 p.

- Yeo, G.M. 1986. Iron-formation in the late Proterozoic Rapitan Group, Yukon and Northwest Territories. *In Mineral Deposits of the Northern Cordillera: Canadian Institute of Mining and Metallurgy Special Vol. 37. Edited by J.A. Morin.* p. 142-153.
- Young, G.M. 1976. Iron-formation and glaciogenic rocks of the Rapitan Group, Northwest Territories, Canada. *Precambrian Research*, vol. 3: p. 137-158.
- Young, G.M. 1992. Late Proterozoic stratigraphy and the Canada-Australia connection. *Geology*, 20: 215-218.
- Ziegler, P.A. 1959. Frühpaläozoische Tillite im östlichen Yukon-Territorium (Kanada). *Ecologiae Geologicae Helveticae*, vol. 52, p. 735-741.